Nuclear Science

OECD

Shielding Aspects of Accelerators, Targets and Irradiation Facilities – SATIF 7

Workshop Proceedings
Sacavém, Portugal
17-18 May 2004

AEN
NEA

NUCLEAR • ENERGY • AGENCY

Nuclear Science

Shielding Aspects of Accelerators, Targets and Irradiation Facilities – SATIF 7

Proceedings of the Seventh Meeting held at
Instituto Tecnológico e Nuclear (ITN)
Sacavém, Portugal
17-18 May 2004

Jointly organised by

Organisation of Economic Co-operation and Development
Instituto Tecnológico e Nuclear (ITN)
Radiation Safety Information Computational Center (RSICC)
The Division of Radiation Science and Technology of Atomic Energy Society of Japan

NEA No. 6005

NUCLEAR ENERGY AGENCY
ORGANISATION FOR ECONOMIC CO-OPERATION AND DEVELOPMENT

ORGANISATION FOR ECONOMIC CO-OPERATION AND DEVELOPMENT

The OECD is a unique forum where the governments of 30 democracies work together to address the economic, social and environmental challenges of globalisation. The OECD is also at the forefront of efforts to understand and to help governments respond to new developments and concerns, such as corporate governance, the information economy and the challenges of an ageing population. The Organisation provides a setting where governments can compare policy experiences, seek answers to common problems, identify good practice and work to co-ordinate domestic and international policies.

The OECD member countries are: Australia, Austria, Belgium, Canada, the Czech Republic, Denmark, Finland, France, Germany, Greece, Hungary, Iceland, Ireland, Italy, Japan, Korea, Luxembourg, Mexico, the Netherlands, New Zealand, Norway, Poland, Portugal, the Slovak Republic, Spain, Sweden, Switzerland, Turkey, the United Kingdom and the United States. The Commission of the European Communities takes part in the work of the OECD.

OECD Publishing disseminates widely the results of the Organisation's statistics gathering and research on economic, social and environmental issues, as well as the conventions, guidelines and standards agreed by its members.

* * *

NUCLEAR ENERGY AGENCY

The OECD Nuclear Energy Agency (NEA) was established on 1st February 1958 under the name of the OEEC European Nuclear Energy Agency. It received its present designation on 20th April 1972, when Japan became its first non-European full member. NEA membership today consists of 28 OECD member countries: Australia, Austria, Belgium, Canada, the Czech Republic, Denmark, Finland, France, Germany, Greece, Hungary, Iceland, Ireland, Italy, Japan, Luxembourg, Mexico, the Netherlands, Norway, Portugal, Republic of Korea, the Slovak Republic, Spain, Sweden, Switzerland, Turkey, the United Kingdom and the United States. The Commission of the European Communities also takes part in the work of the Agency.

The mission of the NEA is:

- to assist its member countries in maintaining and further developing, through international co-operation, the scientific, technological and legal bases required for a safe, environmentally friendly and economical use of nuclear energy for peaceful purposes, as well as
- to provide authoritative assessments and to forge common understandings on key issues, as input to government decisions on nuclear energy policy and to broader OECD policy analyses in areas such as energy and sustainable development.

Specific areas of competence of the NEA include safety and regulation of nuclear activities, radioactive waste management, radiological protection, nuclear science, economic and technical analyses of the nuclear fuel cycle, nuclear law and liability, and public information. The NEA Data Bank provides nuclear data and computer program services for participating countries.

In these and related tasks, the NEA works in close collaboration with the International Atomic Energy Agency in Vienna, with which it has a Co-operation Agreement, as well as with other international organisations in the nuclear field.

FOREWORD

Atomic and nuclear energy applications involve a large range of scientific and technological activities using a variety of machines and analytical techniques. Activities in this area have increased over the years and consequently the OECD/NEA Nuclear Science Committee sponsors an increasing amount of work in this domain.

One of these activities concerns Shielding Aspects of Accelerators, Targets and Irradiation Facilities (SATIF). A series of workshops has been held over the last decade:

- SATIF 1 was held on 28-29 April 1994 in Arlington, Texas;
- SATIF 2 on 12-13 October 1995 at CERN in Geneva, Switzerland;
- SATIF 3 on 12-13 May 1997 at Tohoku University in Sendai, Japan;
- SATIF 4 on 17-18 September 1998 in Knoxville, Tennessee;
- SATIF 5 on 17-21 July 2000 at the OECD in Paris, France;
- SATIF 6 on 10-12 April 2002 at the Stanford Linear Accelerator Center (SLAC), Menlo Park, California;
- SATIF 7 on 17-18 May 2004 at ITN, Sacavém, Portugal.

SATIF 8 is planned for 22-24 May 2006 at the Pohang Accelerator Laboratory in the Republic of Korea.

SATIF 7 was jointly organised by the following bodies:

- OECD Nuclear Energy Agency;
- Instituto Tecnológico e Nuclear (ITN);
- Radiation Safety Information Computational Center (RSICC);
- Division of Radiation Science and Technology of the Atomic Energy Society of Japan.

The current proceedings provide a summary of the discussions, decisions and conclusions as well as the text of the presentations made at the seventh SATIF meeting. Many of the graphics printed in the report are in colour in their original version; interested readers can request a colour copy of the report on CD-ROM from the NEA.

The proceedings are published on the responsibility of the OECD Secretary-General. The views expressed are those of the authors and do not necessarily correspond to those of the national authorities concerned.

Acknowledgements

Acknowledgements are due to the members of the SATIF-7 Technical Programme Committee: P. Vaz (ITN, Chairman), T. Gabriel (ORNL), H. Hirayama (KEK), B.L. Kirk (RSICC), A. Leuschner (DESY), S. Rokni (SLAC), N. Mokhov (FNAL), T. Nakamura (U. Tohoku, Vice-Chair), M. Silari (CERN) and E. Sartori (OECD/NEA, Secretary) for their contribution in shaping the technical programme, and to all participants who contributed the valuable work and ideas described in these proceedings. Special thanks go to Andrea Griffin-Chahid for her dedication in preparing these proceedings for publication.

TABLE OF CONTENTS

EXECUTIVE SUMMARY

Scope

The Expert Group on Shielding of Accelerators, Targets and Irradiation Facilities (SATIF) deals with multiple aspects related to the modelling and design of accelerator shielding systems including electron accelerators, proton accelerators, ion accelerators, spallation sources and several different types of facilities, such as synchrotron radiation facilities, transmutation sources including accelerator driven systems, very-high-energy radiation facilities, free electron lasers, high-power targets and dumps.

Objectives

Objectives of the SATIF-7 meeting include:

- to promote the exchange of information among scientists in this particular field;
- to identify areas in which international co-operation could be fruitful;
- to carry on a programme of work in order to achieve progress in specific priority areas.

Deliverables

Deliverables emerging from the SATIF-7 meeting include:

- assessment of needs in experimental data for the validation of models and codes;
- organisation of shielding experiments;
- collection and compilation of experimental data sets;
- assessment of models, computer codes, parametrisations and techniques available for accelerator shielding design purposes;
- validation of computer codes and models available to perform particle transport simulation;
- organisation of international benchmark and intercomparison exercises;
- organisation of workshops and co-organisation of conferences relevant in the area of its scope and computing radiation dosimetry;
- publication of workshop proceedings;
- editing of an “Accelerator Shielding Handbook”;
- maintenance of the SATIF listserver and archive of technical discussion between members.

SATIF-7 workshop

Summary

The seventh SATIF workshop was hosted by the Instituto Tecnológico e Nuclear (ITN), of Sacavém, Lisbon, Portugal. The objectives were to present and assess achievements on actions agreed upon at the previous meeting held at Stanford, California in 2002, and to discuss and recommend actions where a strong need is identified for further work in theoretical model development, experimental work and benchmarking for model validation.

The workshop was opened by Professor Manuel Leite de Almeida, Vice President of ITN, who welcomed the participants along with the General Chair, Pedro Vaz (ITN). He reminded participants of the history of SATIF and that the occasion marked the 10th anniversary of the first SATIF meeting, which was held at Arlington, TX, and chaired by Dr. Shun-ichi Tanaka, now Vice President of JAERI.

Enrico Sartori welcomed participants on behalf of the OECD/NEA and thanked ITN for hosting this workshop.

The workshop was attended by 36 participants from 9 countries, representing 24 organisations. Twenty-five (25) presentations were made, organised into five topical sessions:

- source term and related data – electron, proton and ion accelerators and spallation source;
- measurements and calculations of induced radioactivity and activation data;
- benchmark experiments and calculations;
- dose and related issues;
- status of computer codes, cross-sections and shielding data libraries.

The abstracts of the presentations from this proceeding are accessible via Internet at the following address: http://www.nea.fr/html/science/meetings/SATIF-7/satif7-programme.html.

The complete set of presentations was indexed and made available to participants on CD-ROM. The workshop proceedings are being edited and published in hard copy by the OECD. Details about the programme and its participants are provided in the Annex to the Executive Summary and the List of Participants.

The workshop was concluded with sessions on follow-up of past SATIF agreements and actions, and discussion/summary and future actions.

Concerning future directions, the following topics were proposed for discussion.

- The visibility of the SATIF group activities needs to be enhanced through:
  - a book on "State-of-the-art on Accelerator Shielding";
  - publication in archival journals.

- New applications should be targeted, such as:
  - medical radiation applications;
  - dosimetry-related calculations for different applications;
  - shielding of transmutation facilities;
  - applications involving high-energy radiations.
- Increased interaction with other groups should be implemented via:
  - QUADOS-like initiatives (quality assurance and benchmarking);
  - EURADOS (dosimetry).

During Sessions VI and VII, which were concerned with follow-up, future actions and recommendations, Pedro Vaz, co-ordinator of the NEA/NSC activities in Radiation Shielding and Dosimetry, reported on the scheduled in-depth discussion that will tackle the subject with emphasis on accelerators at the next NSC meeting (10 June 2004).

The mandate of this expert group had been extended in 2003 through 2005. As this group meets only every two years, a period judged appropriate for consistent progress, and as the mandate expires before the next meeting, a discussion as to justification for continuing the SATIF activities was initiated.

Aspects for future studies were then discussed by all participants, the most important ones being:

1. Activation and dose rate estimations for facility maintenance planning are requested. It is particularly crucial if the targets are changed to identify "hot spots" and how to prevent them.

2. Dismantling of facilities requires estimation of remanent dose for dose management in order that the waste can be declared free from radiation. Lack of such capability may lead to very expensive solutions.

3. Relevant data on activation and corresponding evaluation were presented in several papers of SATIF-7 (e.g. induced radioactivity and remanent doses at CERN, production of radioactive isotopes at GT, an important/comprehensive set of experiments carried out within the ISTC programme in the Russian Federation by ITEP, and the HINDAS project, which has produced large sets of data at GSI, Darmstadt). These data contribute to waste disposal and hazard classification of accelerators. The SINBAD database should be expanded to include such compilations as EXFOR; however, this database does not seem to be an adequate format. In addition, more basic data on mass distribution and spallation products are needed and should be integrated into the databases.

4. The activities of SATIF can provide reliable, evaluated data and guidance for model selection; however, there should be strong support for making such data available. These experimental data should be presented at the SATIF meetings.

5. The group does not just meet and hold workshops, it also co-ordinates analysis and proposes action items (e.g. the collaboration on attenuation length up to 10 GeV for which codes now agree). Consensus on certain parameters, reached though independent but co-ordinated work, is of high value.

6. Comparison between codes creates a challenge for code developers to show which ones perform better. This creates important insight for users and code developers.

7. For the energy region where it becomes difficult to distinguish phenomena such as fission and spallation, additional development of models is needed as the discrepancies are still very high. SATIF should devote a certain amount of effort to resolve such issues by proposing experiments that help in choosing the right model.

8. In accelerator shield design, simple codes are often used. This tends to lead to overdesign. With today's state-of-the-art methods only a few safety factors need to be applied.

9. Experimental databases and benchmarking are key elements for building confidence in utilized data and codes; SATIF encourages objective comparison and facilitates access to needed information. Official endorsement of benchmarks by NEA/NSC is essential.

10. The discussions and exchange of views at SATIF relative to mechanisms that are not well-understood provide new ideas for designing experiments that lead to solution of problems.

11. The provision of a gamma beam line for nuclear physics and applications at the AURORA facility were reported. It was noted that there is a lack of photonuclear data available for light elements and that those available involve a limited range and poor quality. Data for the production of *d*, *t* and alphas with their spectra are required. Relevant work on photonuclear data is going to be presented and published by A. Fassó at the International Conference on Nuclear Data for Science and Technology (ND-2004) in September 2004 at Santa Fe, NM, USA. This work could form the basis for identifying the need for experiments to be carried out at this new facility. The availability of such a facility would be most welcome.

12. Concerning computer programs, it is essential that all responsible developers of the relevant codes contribute to the discussion and share their model. The developers should also generate a table describing the quality (good and bad aspects) of their features. This should be presented and discussed by authors at SATIF-8. A session should be devoted to "event generators" in order to facilitate common ways of solving problems. The release of standard routines and tools for geometry conversion from one code input to another should be strongly encouraged to minimise benchmarking efforts and cost.

13. A very valuable contribution is the "Heavy Ion Handbook", presented at SATIF-7. Preparation of additional specialised handbooks should be encouraged.

14. At SATIF-6 it was agreed that the know-how and experience gathered by the SATIF group over recent years should be synthesised into an "Accelerator Shielding Handbook" for the benefit of an increasingly large community of accelerator shielders. Since no current handbook exists on this subject and a strong need for it has been expressed, its production was agreed upon. The importance of such a work was underlined during SATIF-7 and stronger co-ordination of the effort is required. The editors of the handbook were designated among SATIF members with editing experience and time to realise the project. Those chosen include: Pedro Vaz and Nikolai Mokhov (co-ordinators and authors); Takashi Nakamura, Stepan Mashnik, Phillip Ferguson and Franz Gallmeier (authors); and others who will confirm their availability. The handbook should be prepared over the next two years and be available in draft form for the next SATIF workshop. The chapters will cover physics basics for accelerator shielding, facilities and their shielding and dosimetry approaches, simple fast methods for estimating orders of magnitude, existing state-of-the-art transport codes (MC and deterministic), data for accelerator shielding and experimental benchmark data.

It was noted that many of the actions agreed on in previous meetings have been carried out to the benefit of participants and the shielding community in general.

Members concluded that in view of the number of large accelerator facilities in planning or under construction within the OECD area, there is a growing need for extended and improved databases, methods and codes on accelerator and target shielding. The present scope and objectives of SATIF define well and represent current needs in this field as well as the deliverables (e.g. experimental benchmarks, adequate computer codes and code comparison reports, preparation of special handbooks, etc.). SATIF will be a major contribution to progress in this area.

Over the past 10 years, the radiation shielding community has benefited from the co-operation that takes place under the aegis of SATIF and the group has established itself as the international forum for addressing priority issues in this area. SATIF will further contribute by sharing its research results on emerging priority areas; the members recommend that SATIF's mandate be extended for a period of two years until 2007.

B. Kirk presented the Technical Group in Computational Medical Physics (TGCoMP), recently set-up within ANS for the promotion of advancement of computational tools, experimental data and enabling technologies, which are applicable to problems in medical and health physics. The group has a multidisciplinary approach (nuclear engineering, medical physics and health physics) to the studies of radiation effects on human and animal life. The applications include computational benchmarks on phantoms and detectors, large-scale optimisation and deterministic/stochastic approaches to radiation therapy problems. This area is separate from the other two ANS divisions – Isotopes and Radiation, Biology and Medicine. She presented their proposed future activities. From the subsequent discussion, it was clear that these activities are of interest to SATIF, who agreed to co-operate with this group.

H-S. Lee introduced the Pohang Accelerator Laboratory (PAL) of the Republic of Korea, which is operated by the Pohang University of Science and Technology (POSTECH). PAL has a third generation light source (PLS) 160 m long with a 2.5 GeV S-band PLS linac. He briefly described the plans for construction of future facilities. Interest in accelerator radiation research is increasing in Korea and efforts are made to encourage young students to work in the field of nuclear science and accelerator radiation. PAL offers to host the NSC meeting on Shielding Aspects of Accelerators, Targets and Irradiation Facilities (SATIF-8) from 22-24 May 2006, in conjunction with the Synchrotron Radiation Instrumentation Conference that will be held at Gyeongju the following week. Members of SATIF welcomed the offer because of the opportunity for discussion with the experts at PAL.

Sponsors

This event was jointly organised by the following:

- OECD Nuclear Energy Agency;
- Instituto Tecnológico e Nuclear (ITN);
- Radiation Safety Information Computational Center (RSICC);
- Division of Radiation Science and Technology of the Atomic Energy Society of Japan.

Scientific Committee

The members of the Scientific Committee of SATIF-7 were:

T. Gabriel (ORNL)	T. Nakamura (U. Tohoku, Vice-chair)
H. Hirayama (KEK)	S. Rokni (SLAC)
B. Kirk (RSICC)	E. Sartori (OECD/NEA, Secretary)
A. Leuschner (DESY)	M. Silari (CERN)
N. Mokhov (FNAL)	P. Vaz (ITN, Chair)

Executive Committee

The members of the Executive Committee in charge of preparing the Technical Programme for SATIF-7 and submitting it to the Scientific Committee were:

B. Kirk (RSICC)	M. Silari (CERN)
T. Nakamura (U. Tohoku, Vice-chair)	E. Sartori (OECD/NEA, Secretary)
S. Rokni (SLAC)	P. Vaz (ITN, Chair)

Annex

SATIF-7 PROGRAMME

17-18 May 2004
Instituto Tecnológico e Nuclear (ITN)
Sacavém, Portugal

General Chair: Pedro Vaz • General Vice-chair: Takashi Nakamura

Monday, 17 May

Registration

Welcome and introductory remarks (*P. Vaz*)

Objectives of the workshop (*E. Sartori*)

SESSION I.1 Source Term and Related Data – Electron, Proton and Ion Accelerators and Spallation Sources

Chair: H. Hirayama

Photo-neutron Production

H-S. Lee, S. Ban, T. Sanami, K. Takahashi, T. Sato, K. Shin, C. Chung
Photo-neutron Yields from Thin and Thick Targets Irradiated by 2.0 GeV Electrons

S. Bartalucci, V. Angelov, K. Drozdowicz, G. Tracz
A Linac-based Neutron Source for Time-of-flight (TOF) Measurements

Electron-photon Production

J.L. Tain
A Gamma-ray Beam Line for Nuclear Physics and Applications
at the Spanish Synchrotron ALBA

J.E. Fernandez
Scattering in Two Targets with the Vector Code MCSHAPE

SESSION I.2 Source Term and Related Data – Electron, Proton and Ion Accelerators and Spallation Sources

Chair: N. Hertel

High-energy Proton and Heavy Ion Machines

N. Mokhov
Benchmarking Possibilities at Fermilab: Accelerators, Experiments and Irradiation Facilities

T. Nakamura, L. Heilbronn
Handbook on Secondary Particle Production and Transport by Heavy Ions of Energies above 100 MeV/nucleon – General View and Contents

Spallation Neutron Sources

K. Nünighoff, N. Bayer, W. Bernnat, V. Bollini, A. Bubak, H. Conrad, D. Filges, P. Ferguson, F.X. Gallmeier, F. Goldenbaum, H-K. Hinssen, E.B. Iverson, R-D. Neef, W. Ninaus, K. Pyzs, J. Keinert, S. Kulikov, B. Lensing, M. Mattes, Th. Matzerath, N. Paul, Ch. Pohl, H. Schaal, A. Smirnov, H. Soltner, H. Stelzer, H. Tietze-Jaensch, M. Wohlmuther, J. Wolters
Experimental Investigations of Advanced Cold Moderators at JESSICA of COSY-Jülich and Comparison with MCNPX Simulations

SESSION II Measurements and Calculations of Induced Radioactivity and Activation Data

Chair: T. Nakamura

K. Kelley, M. Devlin, E. Pitcher, S. Mashnik, N.E. Hertel
Gadolinium-148 Production Cross-section Measurements for 600 and 800-MeV Protons

V. Bollini, A. Bubak, D. Filges, F. Goldenbaum, P. Kulessa, H. Machner, K. Nünighoff, H. Ohm, N. Paul, K. Pysz, H. Schaal, R. Siudak, A. Heczko, L. Jarczyk, B. Kamys, St. Kistryn, A. Kowalczyk, A. Magiera, W. Migdal, B. Piskor-Ignatowicz, Z. Rudy, R. Sworst, M. Wojciechowski, A. Budzanowski, M. Kistryn, St. Kliczewski, J. Kisiel, E. Stephan, W. Zipper, R. Barna, D. DePasquale, A. Italiano, S. Förtsch, D. Steyn, T. Thovhogi, J. Cugnon, H. Hodde
Latest Results of PISA – LCP and IMF Cross-sections in p+Ni at 1.9 GeV Reactions

Yu.E. Titarenko, V.F. Batyaev, V.M. Zhivun, R.D. Mulambetov, S.V. Mulambetova, K.A. Lipatov, S.L. Zaitsev, S.G. Mashnik
Experimental Study of Independent and Cumulative Product Yields in ^{208,207,206,nat}Pb and ^{209}Bi Targets Irradiated with 0.04-2.6 GeV Protons

SESSION III.1 Benchmark Experiments and Calculations

Chair: B. Kirk

Neutron Attenuation Length

H. Hirayama
Intercomparison of Neutron Attenuation in Iron and Concrete (5)

T. Nakamura
Summarised Experimental Results of Neutron Shielding
and Attenuation Length

SESSION III.2 Benchmark Experiments and Calculations

Chair: A. Leuschner

Deep Penetration

H. Nakashima, N. Matsuda, H. Nakano, Y. Iwamoto, K. Niita, T. Miura, M. Numajiri, N. Nakao
Benchmark Calculation on Neutron Streaming of Labyrinth at Proton Accelerator Facilities

K. Oishi, K. Kosako, Y. Kobayashi, H. Yamakawa, T. Nakamura
Measurement and Analysis on Radiation Shielding of 18 MeV Electron Linac for Medical Use

S. Taniguchi, M. Sasaki, T. Nunomiya, H. Iwase, S. Yonai, T. Nakamura, S.H. Rokni, J.C. Liu, S. Roesler, K. Kase
Measurement of Neutron Energy Spectra Behind the Lateral Shield
of a High-energy Electron Beam Dump

Tuesday, 18 May

SESSION IV Dose and Related Issues

Chair: S. Rokni

W. Dittrich, W. Hofmann
Use of Isodose Rate Pictures for the Shielding Design
of a Proton Therapy Centre

M. Brugger, S. Mayer, S. Roesler, L. Ulrici, H. Khater, A. Prinz, H. Vincke
Measurement and Simulation of Induced Radioactivity and Remanent Dose Rates at the CERN-EU High-energy Reference Field Facility

B. Mukherjee, E. Sartori
A Database on Health Physics and Radiological Safety
of Cyclotrons 10-250 MeV

SESSION V Status of Computer Codes, Cross-sections and Shielding Data Libraries

Chair: N. Mokhov

Status of Computer Codes, Cross-sections and Data Libraries

J.M. Galán, I. Kodeli, E. Sartori, B.L. Kirk
Acquisition of Computer Codes, Cross-section Libraries
and Accelerator Shielding Experiments – Status 2004

Accelerator Shielding Modelling

R. Tayama, K. Hayashi, H. Hirayama, N. Ohtani
Development of Radiation Shielding Tool for Proton
Accelerators Facilities (BULK-I)

S.G. Mashnik, V.S. Pronskih, J. Adam, A. Balabekyan, V.S. Barashenkov,
V.P. Filinova, A.A. Solnyshkin, V.M. Tsoupko-Sitnikov, R. Brandt, R. Odoj,
A.J. Sierk, R.E. Prael, K.K. Gudima, M.I. Baznat
Analysis of the JINR p(660 MeV) + ^{129}I, ^{237}Np and ^{241}Am Measurements
with Eleven Different Models

Discussions

SESSION VI Follow-up of Past SATIF Agreements and Actions

Present Status of Data Collection on Dose Conversion Coefficients
for High-energy Radiation (*Y. Sakamoto*)

SESSION VII Discussion/Summary and Future Actions

Review of Actions (*E. Sartori*)

Technical Group on Computational Medical Physics – TGCoMP (*B.L. Kirk*)

Introduction to the Pohang Accelerator Laboratory for SATIF-8 (*H-S. Lee*)

Closing remarks (*P. Vaz*)

SESSION I.1

Source Term and Related Data – Electron, Proton and Ion Accelerators and Spallation Sources

Chair: H. Hirayama

PHOTO-NEUTRON YIELDS FROM THIN AND THICK TARGETS IRRADIATED BY 2.0 GeV ELECTRONS

Hee-Seock Lee
Pohang Accelerator Laboratory, POSTECH, Nam-gu, Pohang, 790-784, Korea
E-mail: lee@postech.ac.kr

Syuichi Ban, Toshiya Sanami, Kazutoshi Takahashi
High Energy Accelerator Research Organization, Oho, Tsukuba, Ibaraki, 305-0801, Japan

Tatsuhiko Sato
Japan Atomic Energy Research Institute, Tokai, Ibaraki, 319-1195, Japan

Kazuo Shin
Department of Nuclear Engineering, Kyoto University, Sakyo-ku, Kyoto 606-8501, Japan

Abstract

The photo-neutron yields from thin and thick targets irradiated by high energy electrons were studied. The photo-neutron spectra at 90° relative to the incident 2.0 GeV electrons were measured by the pulsed beam time-of-flight technique using the Pilot-U plastic scintillator and the NE213 liquid scintillator with 2 inches in length and 2 inches in diameter. Targets, from low-Z element (carbon) to high-Z element (bismuth) and with thin (0.5 Xo) and thick (10 Xo) thickness, were used in this study. The differential photo-neutron yields between 2 MeV (mainly 8 MeV) and 400 MeV were obtained. The systematics was studied to make empirical yield terms for shielding application. Recently, the study of the angular distributed yields was conducted at two other observing angles, 48° and 140°. The photo-neutron yields between 8 MeV and 250 MeV were obtained for thick targets. The experimental data were compared with results calculated using the EGS4+PICA3 or the MCNPX 2.5d code.

Introduction

Information on photo-neutron yields for high-energy electron accelerator has been a constant requirement for many constructions and great uses of synchrotron facility, X-FEL, and Linear Collider. In every SATIF meeting, this subject is requested. The photo-neutron measurements have been conducted using an electron linac at the Pohang Accelerator Laboratory (PAL) since 1998 as a collaborative work between PAL, KEK and Kyoto University [1-7]. Early in the measurements, the photo-neutron spectra at 90° relative to the incident 2.0 GeV electrons were measured by the pulsed beam time-of-flight technique [1-5]. To study the photonuclear reaction, measurements of radionuclides produced in a dump target and the improvement of the PICA95 code were carried out [8,9]. Both represented an improved approach of a study, which had been undertaken at KEK and SLAC prior to 1998. The differential photo-neutron yields between 2 MeV (mainly 8 MeV) and 400 MeV were obtained. The systematics of production yields were studied to generate empirical source terms for shielding applications [3,4,7]. Recently, the same measurements were conducted at two other angles, 48° and 140° [6]. The spectral yields of charged particles produced from thin targets by a photonuclear reaction were also studied.

Experimental procedure

Experimental set-up

The spectral measurements of photo-neutrons produced from thin and thick targets by incident 2.0 GeV electrons were carried out around the beam dump area of the electron linac of the Pohang Light Source. The experimental area was shown in Figure 1 (a horizontal view) and Figure 2 (a vertical view). The experimental set-ups in Figure 1 and Figure 2 are for 48° and 140° measurements and for a 90° measurement, respectively. The position of Target 1 is the same as that in Figure 2. During the measurements, the linac was run with a beam pulse width of 1 nsec, a repetition rate of 10 Hz, and a fixed beam energy of 2.0 GeV. The normal beam intensity was approximately 0.5 nC/pulse. Each target was located downstream about 20 cm from the vacuum-end window of 200 μm-thick stainless steel. The BC418 (Pilot-U) plastic scintillator and the NE213 liquid scintillator with 2 inches in length and 2 inches in diameter were used as neutron detectors. Targets, from low-Z element (carbon) to high-Z element (bismuth), with 5×5 cm^2 cross-sections and thin (0.5 Xo) and thick (10 Xo) thicknesses, were used in this study. The flight distances were 6.8 m (48°), 10.4 m (90°) and 8.1 m (140°).

Time-of-flight spectra and data reduction

A high resolution multi-channel scaler and a CAMAC TDC with 0.5 nec per channel were used to measure the flight time of neutrons. The start signal of the time-of-flight electronics was given from the beam current monitor in Figure 1 and Figure 2. The discrimination level was set to 4.2 MeVee (electron equivalent), which corresponded to about 9 MeV. This limitation results from the very intense X-ray shower background. In the n-γ discrimination using NE213 detector, we were able to get the neutron energy down to 2 MeV, which is 1.15 MeVee [5].

Typical TOF spectra were shown in Figure 3. Because of the huge number of photons mentioned above, thick Pb attenuators were set on the path of neutron flight to suppress it. Two spectra were obtained in the cases of 15-cm thick and 25-cm thick Pb attenuators, respectively. The background spectrum was measured using 100-cm thick iron cylinder and 30-cm thick Pb as a shadow bar (shown in Figure 2). For the compensation of the attenuator effect, the removal cross-sections were calculated by

A LINAC-BASED NEUTRON SOURCE FOR TIME-OF-FLIGHT (TOF) MEASUREMENTS

Sergio Bartalucci
INFN – Laboratori Nazionali di Frascati, Via Enrico Fermi 40, I-00044 Frascati (Roma), Italy
Sergio.Bartalucci@lnf.infn.it

Vladimir Angelov
Institute for Nucl. Res. and Nucl. Energy, 72 Tzarigradsko Chaussee Blvd., 1784 Sofia, Bulgaria
angelvl@inrne.bas.bg

Krzysztof Drozdowicz, Grzegorz Tracz
The Henryk Niewodniczaski Institute of Nucl. Phys. – Polish Academy of Sciences
ul. Radzikowskiego 152, 31-342 Kraków, Poland
Krzysztof.Drozdowicz@ifj.edu.pl, Grzegorz.Tracz@ifj.edu.pl

Abstract

High-power, low-energy electron linear accelerators (linacs) are widely used to produce high neutron fluxes via *bremsstrahlung* and (γ,n) reaction. Such neutron sources, although of much lower intensity than nuclear reactors and spallation sources, have interesting applications in high precision nuclear cross-section measurements and others. The research programme consists of: 1) the optimisation study of a target-moderator assembly in its physical and engineering aspects with extensive simulations; 2) the construction of a prototype and its testing on the linac at the INFN Laboratory in Frascati; 3) the realisation of a neutron beam line and the implementation of a neutron detector for energy measurement with the time-of-flight technique; and 4) the feasibility study involving the installation of a neutron source on a future normal- or preferably super-conducting linac, which is to be built in the Rome Research Area.

Introduction

Among the various kinds of neutron sources (reactors, accelerator-based sources and radio-isotopic neutron emitters), the accelerator-based neutron source is the most efficient for high resolution measurements of microscopic neutron cross-sections. It produces short bursts of neutrons with a broad continuous energy spectrum via nuclear reactions of energetic photons or charged particles. Linac is an especially powerful tool for the production of intense pulsed neutrons. Pulsed neutrons based on an electron linac are effective for measuring energy-dependent cross-sections with high resolution using the time-of-flight (TOF) technique, covering the energy range from thermal neutrons to a few tens of MeV. The measurement of neutron cross-sections provides basic information for the study of neutron interactions with nuclei.

Precise measurements of neutron cross-sections are of great importance for the safety design of nuclear reactors and for the evaluation of neutron flux density and energy spectrum around a reactor. The same holds true for fusion reactors, where the interaction of neutron and photon fields from D-T fusion with the surrounding medium (first wall, blanket and vacuum vessel) is still poorly understood. As a result, fusion neutronic experiments using a “white” spectrum below the 14 MeV-peak would be welcome as well as investigations of the elementary nuclear and atomic processes.

The contribution of neutron physics to the evolutionary process of understanding the basic laws of nature has been enormous, ranging from astrophysics and cosmology (understanding of element formation and phase transitions in the history of our universe) to fundamental forces (strong, electroweak and gravitation). Neutron beta decay measurements provided us with various data to fix the number of particle families at three. There is still a long list of fundamental physics questions that could be answered by neutron experiments in the near future. The exploration of the proposed neutron source is certainly worthwhile, especially in view of the primary mission of the Italian Institute for Nuclear Physics (INFN).

Characteristics of the source

The neutron source is modulated as an end product of an electron beam whose main purpose is research and development towards the realisation of an X-FEL facility in the Rome Research Area. Driven by the large interest that X-ray SASE (Self-amplified Spontaneous Emission)-FEL’s sources have raised world-wide in the synchrotron light scientific community, as well as in the particle accelerator community and in several Italian national research institutions, the Italian government launched a long-term initiative in 2001. The initiative is devoted to Italy’s realisation of a large-scale, ultra-brilliant and coherent X-ray source. The allocation of considerable resources in the Italian National Research Plan (PNR) brought about the formation of a CNR-ENEA-INFN-University of Roma “Tor Vergata” study group. A conceptual design has been developed and two possible schemes for the linac structure (normal- and super-conducting; at an electron energy, $E = 2.5$ GeV, which is sufficient for an X-ray λ as short as 1.5 nm) have been investigated. This has lead to the SPARX proposal [1,2]. A competing initiative named FERMI was proposed by other institutions and is to be located in Trieste on the site of the ELETTRA Synchrotron Radiation Facility.

While the final decision on the location of the future accelerator is still pending, a self-standing R&D programme for the realisation of a SASE-FEL Facility (SPARC) [3] was funded independently by INFN and the Italian Ministry of University and Research (MIUR). The programme was recently begun in Frascati. The scientific and technological issues of this programme are: 1) A high-brightness electron injector at 150 MeV; 2) a SASE-FEL visible VUV experiment at an undulator wavelength of λ ~500 nm; 3) activity on X-ray optics/monochromators; and 4) a soft X-ray table-top source.

Another area that is currently being explored is the integration of the high-brightness SPARC injector with the existing DAΦNE linac (SPARXINO Test Facility [4]), in order to achieve a λ ~ 10 nm at E ≈ 1.2 GeV. The linac is presently devoted to the injection of the double-annular 510 MeV electron-positron storage ring DAΦNE, which is the main part of the INFN accelerator complex in Frascati and is also feeding a test beam facility (BTF). A feasibility study is in progress on the possible energy upgrade of the machine beyond 1 GeV, having as the main focus a realistic improvement in energy and luminosity (DAΦNE2). The evolutionary SPARX programme can benefit from this work without too much overlap in schedules. The next step (SPARX-II), which is dependent on further allocation of funds by MIUR, aims at pushing the linac energy up to the original design value of 2.5 GeV. A possible layout of the machine complex with the neutron source is depicted in Figure 1, which also shows the BTF area where the first tests of the target/radiator system are to take place.

Figure 1. The Frascati accelerator complex involving the SPARXINO scenario and the neutron source

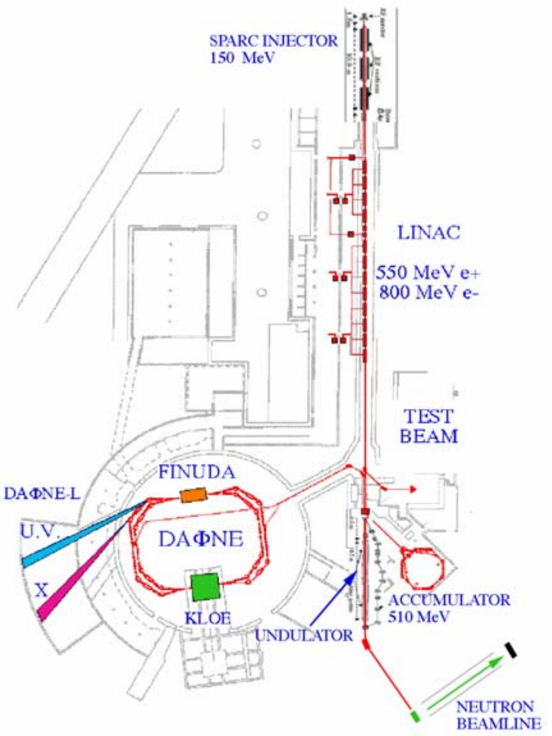

Due to the loose constraints that the primary electron beam places on the secondary neutron beam, its implementation and testing on a different machine appear feasible. Possible machines include the existing injector linac of DAΦNE at LNF or an intermediate version of the X-FEL driving linac as envisaged in the SPARX project. The fundamental feature is that the source will not interfere in any way with the main operation of the linac, being located downstream the FEL interaction region. Furthermore, it will not be affected by the degradation of beam quality (emittance dilution) unlike other sources, such as the one currently being implemented at the ELBE facility of Rossendorf, Dresden. At the ELBE facility, the large divergence after the FEL oscillation forces the neutron radiator to be integrated into the beam dump and prevents the simultaneous operation of the linac in FEL and neutron production [5]. The latter property results from high beam energy, which makes it unique among the older and newer linac-based neutron sources. A comparison of the various options for this neutron source at ELBE and another “new” (2002) linac-based facility, the Pohang Neutron Facility in South Korea [6], is shown in below in Table 1.

Table 1. Various implementations of a neutron source at INFN and certain new facilities

ACCELERATOR	ELBE-FZR DRESDEN	POHANG S.KOREA	SPARC	SPARX NC	SPARX SC	SPARC+DAΦNE LINAC
Energy (MeV)	40	100	150	2 500	2 500	~1 000
Beam power (kW)	Max. 40	Max. 10	0.008	8.3	144	0.060
Bunch charge (pC)	77		~1 000	~1 000	~1 000	~1 600
Bunches/pulse	1 176 ÷ $4 \bullet 10^5$			35	11 500	
Bunch length (ps)	2 ÷ 10		10	10	10	10
Bunch distance (ns)	77			10	87	
Rep. rate (Hz)	25 ÷ 100	12	50	100	5	50
Mean current (μA)	1 000	Max. 100	0.05	3.3	58	0.08
Pulse length (ms)	~0.09 ÷ 36.3	0.006		$350 \bullet 10^{-6}$	11	
Neutron yield n/s	$6 \bullet 10^{13}$	$2.0 \bullet 10^{13}$	$1.6 \bullet 10^{10}$	$1.7 \bullet 10^{13}$	$3.0 \bullet 10^{14}$	$1.2 \bullet 10^{11}$

Organisation of the work

The work for the first year (starting October 2003) consists mainly of a feasibility study, which will address the following basic points:

1. The general structure of the neutron radiator as regards to the choice of the neutron-producing material(s) (solid metal, liquid metal, etc.) and its geometrical design.

2. An estimate of particle background that is expected from the target and how to cope with it.

3. The choice of proper moderating material(s) and resultant effects on the neutron beam.

4. The impact of induced radioactivity on the BTF experimental hall and the evaluation of any special shielding, if needed.

5. Impact of beam degradation due to FEL oscillation on the neutron source.

6. A comparison of the various options mentioned in the first point and the resultant construction and acquisition costs.

The purpose of testing various neutron-producing materials is to maximise the neutron flux for a given energy (TOF) resolution while keeping the thermo-mechanical stress to a sustainable level as well as guaranteeing long-term stability against radiation damage. Thus complete calculations of neutron flux, energy spectrum and time structure are required and are expected from the tentative designs.

These studies shall be performed for certain reference energies of the primary electron beam (e.g. 140 MeV, 1 and 2.5 GeV), which will allow for an experimental check at BTF or will provide insights for future programmes.

The traditional nuclear physics transport codes of EGS4, MCNP, GEANT and FLUKA will be used for extensive simulations, which require much computer time (e.g. a typical FLUKA run with 10^7 events requires ~15 h CPU time on a 1.2 GHz personal computer). Therefore, the job must be carried out by several people who will be working in parallel for a co-ordinated effort. As soon as a tentative choice for the target material and geometry is made, simulations on its thermo-mechanical behaviour will be performed. The main limitation to the electron current (hence neutron flux) has always been the difficulty in handling the beam power dissipation and thus a careful optimisation of target geometry, materials and cooling system would be essential. This is also important given the pulsed nature of this source. In Figure 2, an example of preliminary calculations using MCNP with non-optimised targets is shown. The energy is 1 GeV, which corresponds to an intermediate step in the SPARX programme [1].

Figure 2. The neutron spectrum from MCNP simulations for three different target configurations. The flux is 2.4 · 10^{-6} n/e^- for a sphere with a 1 m radius for Ta + Hg.

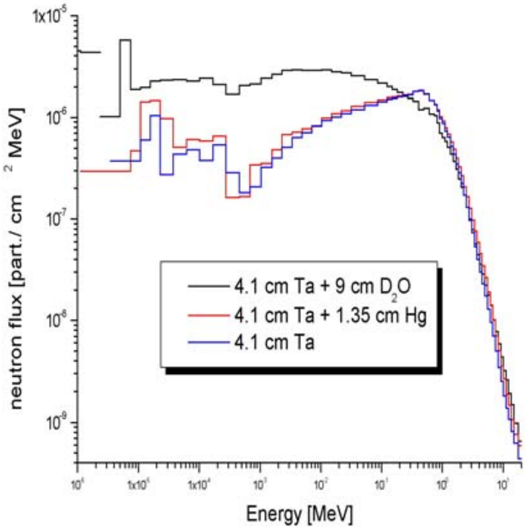

The distribution of the deposited energy in the symmetry plane of a pure tantalum target, whose length equals 10 radiations, is shown in Figure 3.

Figure 3. The distribution of energy deposited by a 1 GeV electron in a pure Ta target

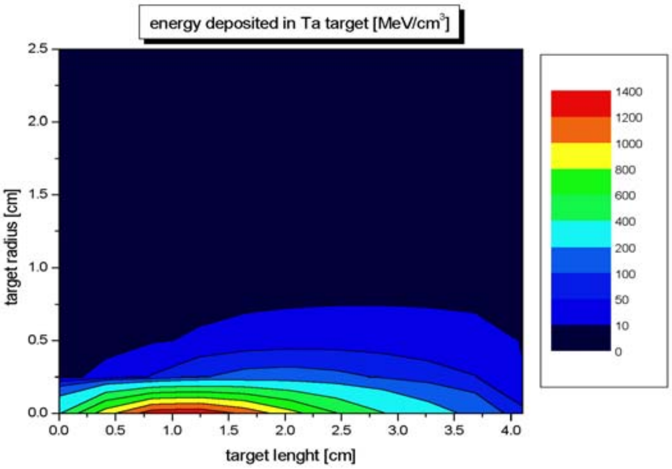

The work for the second year will address the following points:

1. Engineering design and construction of a prototype target/moderator.
2. Tests at BTF with a low current and variable energy beam to validate simulation results.
3. Design of the neutron beam line and choice of its main elements.
4. Implementation of detectors.

Acknowledgements

This work was partially supported by the European Commission under TARI Contract No. HPRI-CT-1999-00088.

REFERENCES

[1] SPARX Proposal, http://www.frascati.enea.it/SPARX/sparx.pdf.

[2] Alesini, D., *et al.*, “Conceptual Design of a High-brightness Linac for Soft X-ray SASE-FEL Source”, *Nucl. Instr. and Meth. in Phys. Res.*, A 507, 502-506 (2003).

[3] Alesini, D., *et al.*, “The SPARC Project: A High-brightness Electron Beam Source at LNF to Drive a SASE-FEL Experiment”, *Nucl. Instr. and Meth. in Phys. Res.*, A 507, 345-349 (2003).

[4] Ferrario, M., Private Communication.

[5] Gabriel, F., *et al.*, “The Rossendorf Radiation Source ELBE and its FEL Projects”, *Nucl. Instr. and Meth. in Phys. Res.*, B 161-163, 1143-1147 (2000).

[6] Kim, G.N., *et al.*, “Measurement of Photoneutron Spectrum at Pohang Neutron Facility”, *Nucl. Instr. and Meth. in Phys. Res.*, A 485, 458-467 (2002).

A GAMMA-RAY BEAM LINE FOR NUCLEAR PHYSICS AND APPLICATIONS AT THE SPANISH SYNCHROTRON ALBA

J.L. Tain
Instituto de Física Corpuscular, CSIC/Universitat de València
Apartado de Correos 22085, E-46071 València, Spain

Abstract

We will present the concept of the proposed gamma-ray beam line for the ALBA synchrotron light source, which is to be built near Barcelona. The gamma-rays will be produced by Compton backscattering of laser light from the ring electrons. Without affecting machine performance it will be possible to produce high-intensity beams with energies up to 500 MeV. In the new set-up, the beam is naturally focused and easily polarised. The beam energy could be defined by collimation at the lower energies and by internal tagging at high energies. Such gamma-ray beams could be used to study photonuclear processes of interest in basic nuclear physics, ranging from nuclear structure at low energies to sub-nucleonic degrees of freedom at high energies, as well as astrophysics. In addition, the gamma-ray beams could be used to obtain nuclear data relevant to the fields of dosimetry, radiation shielding and radiation therapy. Other applications include the non-destructive inspection of objects and their elemental analysis.

Introduction

The construction of a third generation synchrotron light source in Spain was recently approved and will commence soon at the Laboratorio de Luz Sincrotrón (LLS) near Barcelona. The machine, which is named ALBA, will provide radiation in energies ranges up to soft X-rays for research in fields such as biology, materials science, chemistry, pharmacology, etc. However, it is possible/desirable for both scientific and resource optimisation reasons to extend the energy of the radiation into the range of intermediate energy γ-rays (500 MeV). The generation of such energies is possible through the process of Compton scattering of laser photons from the highly energetic electrons circulating in the synchrotron ring. This is an alternative method to the generation of γ-rays through the electron *bremsstrahlung* process and has specific advantages. The characteristics of the γ-ray beam (energy, intensity, etc.) depend on the parameters of the colliding electron and laser beams, and will be explored in the next section. The availability of γ-rays, from a few MeV up to 500 MeV for example, expands the range of research fields for LLS into basic and applied nuclear physics. Some examples of these applications will be presented. Currently, a proposal to build a γ-ray beam line at ALBA is being prepared by a collaboration of several national groups.

Gamma-ray beam characterisation

Compton scattering on energetic electrons

Back in 1963, the possibility was put forth [1,2] to produce an energetic and highly polarised gamma-ray beam through the Compton scattering of polarised laser light with electrons accelerated in a high-energy machine. The first experimental installation was built at Frascati [3] and at present, installations of this type exist at several locations (see Ref. [4]).

The kinematics of the collision is described by the modified Compton formula [5]:

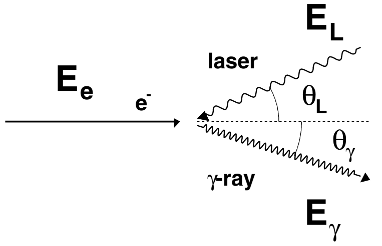

$$E_\gamma = \frac{(1-\beta_e\cos\theta_L)E_L}{1-\beta_e\cos\theta_\gamma + \frac{E_L}{E_e}\left[1-\cos(\theta_\gamma-\theta_L)\right]} \tag{1}$$

Here E_e, E_L and E_γ are the electron, laser photon and γ-ray energies, respectively; β_e is the electron velocity in units of c; and θ_γ (θ_L) is the angle of the outgoing (incoming) photon with respect to the incident electron direction (not necessarily in the same plane). For fixed E_e and E_L, the maximum possible γ-ray energy is obtained for the backscattered photon (θ_γ = 0°) in a head-on collision (θ_L = 0°). In Figure 1, we represent the maximum γ-ray energy obtainable for E_e = 3 GeV (the nominal energy of ALBA) as a function of laser wavelength. All γ-ray energies are possible between the minimum E_L and the maximum. Due to the relativistic "boost", the scattered gamma-rays are strongly forward focused, thus forming a beam. This can be deduced from Figure 2, which shows the angle θ_γ as a function of $z = E_\gamma / E_\gamma^{max}$, the energy of the gamma-ray normalised to maximum energy. We see that the top 90% range of γ energies is contained within a cone of angle 0.55 mrad. Figures 2 and 3 were calculated for E_e = 3 GeV and E_L = 1.17 eV (Nd:YAG laser). However, the range of energies for practical high-power lasers will change little over time when the universal variable z is used.

Figure 1. Maximum γ-ray energy as a function of the laser photon energy

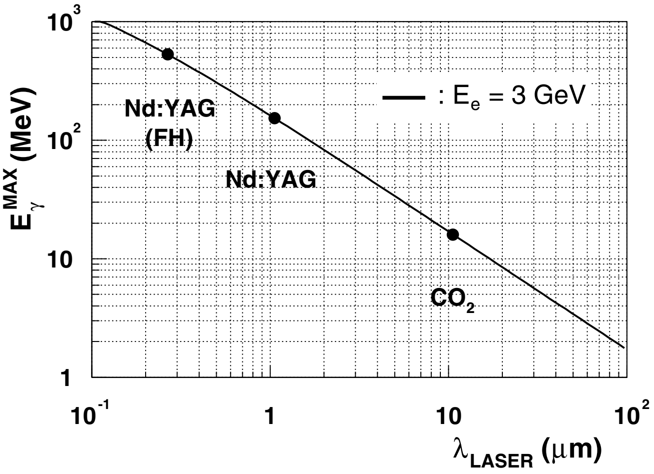

Figure 2. γ-ray energy as a function of the scattering angle

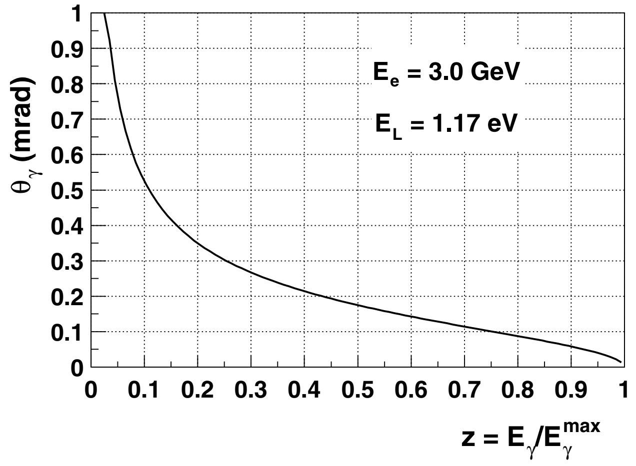

Figure 3. γ-ray relative intensity as a function of energy

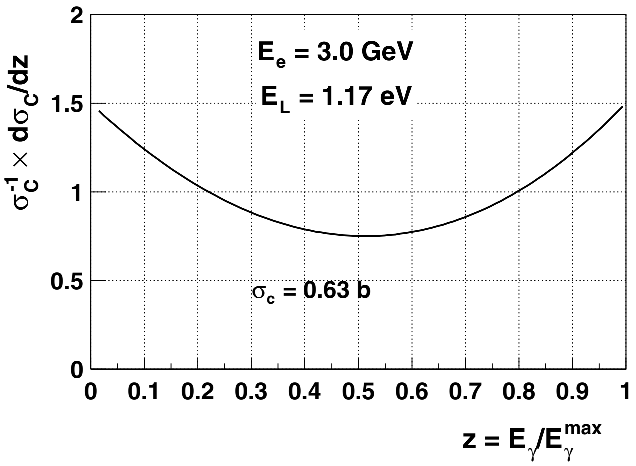

The gamma-ray energy spectrum can be obtained through the proper integration of the differential cross-section angular distribution. The expression can be written as follows [6]:

$$\frac{d\sigma_C}{dz} = \frac{1}{2(1+x)} C_{00} = \frac{1}{2(1+x)}\left[1 - y + \frac{1}{1-y} - \frac{4y}{x(1-y)} + \frac{4y^2}{x^2(1-y)^2}\right] \tag{2}$$

where $x = 4E_e E_L / m_e^2 c^4, y = E_\gamma / E_e$. Again, $d\sigma_C/dz$ does not vary much with E_e and E_L, and Figure 3 represents the normalised (by σ_C) values. The distribution has a saddle shape, with the maxima at the energy extremes being twice that of the middle. The total cross-section is a slowly varying function of electron and laser energies, and has a value of approximately $\sigma_C = 0.6$b.

If the laser beam is polarised, either linearly or circularly, the polarisation is transferred to the backward scattered gamma. For fully polarised laser photons, the degree of linear P_γ^L or circular P_γ^C polarisation of the scattered γ-ray is given by [6]:

$$P_\gamma^L = \frac{1}{C_{00}} \frac{2y^2}{x^2(1-y)^2} \tag{3}$$

$$P_\gamma^C = -\frac{1}{C_{00}}\left(\frac{2y}{x(1-y)} - 1\right)\left(1 - y + \frac{1}{1-y}\right) \tag{4}$$

In Figure 4, the degree of polarisation of the γ-ray as a function of $z = E_\gamma / E_\gamma^{max}$ is represented. It is observed that the sign of the circular polarisation is inverted for the backscattered photon. In addition, the degree of polarisation decreased with decreasing energy. Polarisations in excess of 80% are obtained for the top 30% energy range.

Figure 4. γ-ray polarisation as a function of energy

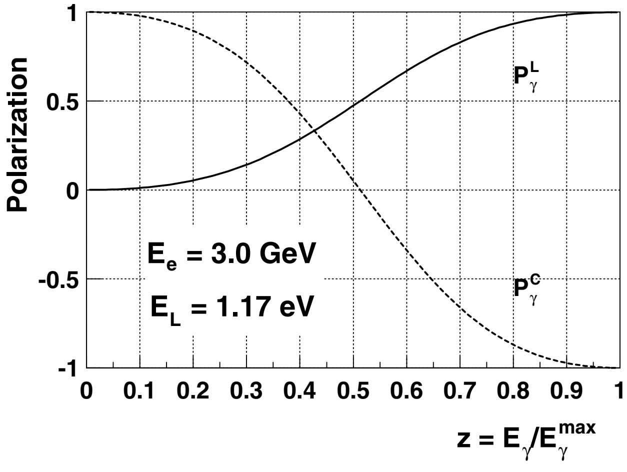

Characteristics of the installation

The accelerator parameters of the original design [7] for the synchrotron at LLS are presently being reconsidered [8], with the purpose of achieving a unique performance in terms of the light source luminosity. The exact characteristics of the γ-ray beam will depend on the final machine parameters but its main characteristics can already be estimated. For this purpose, we will use the parameters from one of the synchrotron lattice structures under consideration (of the so-called QBA-type), which are summarised in Table 1.

Table 1. Electron ring parameters used in the calculations

Ring	
Intensity I_e	0.250 A
Energy E_e	3.0 GeV
Resolution σ_{E_e}/E_e	0.001
Horizontal emittance $\in_x$	5.0 nmrad
Vertical emittance $\in_y$	0.05 nmrad
Momentum acceptance $\Delta p/p_0$	0.015
Straight section	
Length L_{int}	5 m
Horizontal beam envelope σ_X	0.250 mm
Vertical beam envelope σ_Y	0.015 mm
Horizontal slope envelope $\sigma_{X'}$	0.020 mrad
Vertical slope envelope $\sigma_{Y'}$	0.004 mrad

The accelerator complex includes a 100 MeV linac, which contains a booster (bringing the energy up to the nominal value of 3.0 GeV) and the ring itself. The booster and the ring will share the same shielding tunnel. The ring is a four-fold structure with a circumference length of ~255 m. Sixteen straight sections will be available for insertion devices. In the normal operation mode, the ring is filled with ~1.4×10^{12} electrons grouped in bunches 20-ps long separated by 2 ns, which can be regarded as a continuous beam in practice. The nominal intensity of 250 mA will be maintained within ~1% by frequent refilling (topping-up mode). One of the straight sections, which is ~5-m long between bending magnets, could be used to produce the Compton scattered γ-rays. For this purpose, a well-focused and aligned laser beam will be injected into the vacuum chamber using an adequate mirror. The obtained γ-ray beam traverses the mirror and continues up to a measuring station, located some 20-30 m away.

Figure 1 shows the maximum γ-ray energies, which can be obtained with some of the commercially available high-power lasers. With a CO_2 laser, E_γ^{max} would equal 16.0 MeV. With an Nd:YAG laser, E_γ^{max} would equal 152.5 MeV, 290.3 MeV, 415.0 MeV and 529.3 MeV in the fundamental, second harmonic (SH), third harmonic (TH) and fourth harmonic (FH) modes, respectively. Use of the higher harmonics allows one to obtain a high degree (> 80%) of polarisation in the energy range of 200-530 MeV (see Figure 4). For reasons that will be explained later, in order to cover the region of γ-ray energies from 15-150 MeV, we are considering the use of a continuously tuneable laser source. This laser source would be based on an optical parameter oscillator (OPO) [9] and pumped by the Nd:YAG laser. In this case, the polarisation would be essentially 100%.

The intensity of the γ-ray beam depends on the overlap of the colliding electron and laser photon densities and on the Compton cross-section [6]:

$$I_\gamma = 2c\sigma_C \int n_e n_L dV \qquad (5)$$

The electron density n_e is adequately represented by a transverse Gaussian distribution in both X and Y directions with parameters σ_X and σ_Y constant along Z. The laser photon density n_L is assumed to be that of a diffraction-limited circular Gaussian beam. In this case, the RMS width has a minimum σ_0 at the centre of the interaction region and diverges with z [10]: $\sigma_L = \sigma_0\sqrt{1+\left(\lambda z/\pi\sigma_0^2\right)^2}$. Using the parameters of Table 1 and assuming $\sigma_L = 0.5$ mm for the laser beam, intensity obtained is $I\gamma = 4$ - 5×10^6 s^{-1} per Watt of laser power and wavelengths in the range $\lambda = 1$-100 μm. It should be noted that although the number of laser photons per Watt is proportional to the wavelength, this effect is counterbalanced by the increase in the divergence of the laser beam. Nd:YAG laser devices with 100 W CW power are readily available, with conversion efficiencies of about 40%, 30% and 10% for the second, third and fourth harmonics, which would provide beams of 10^7-10^8 rays per second. Still higher powers are available for CO_2 lasers, and intensities larger than 10^9 s^{-1} can be expected. In the case of the OPO source, powers of ~5 W are foreseen giving intensities in excess of 10^7 s^{-1}.

One possible limit to the ultimately obtainable γ-ray intensity is the removal of electrons from the beam in the scattering process. In principle, electrons that lose less than 45 MeV, which is equivalent to the ring acceptance $\Delta p/p_0$ (see Table 1), are kept in the ring (with the exception of multiple scattering effects for very high laser powers). For γ-rays above that energy, the electron eventually hits the vacuum chamber and is lost. In the topping-up mode, electrons are frequently replenished to compensate for usual losses of intensity in the ring. Assuming a refilling time period of 100 s and that the new source of losses should be limited to a fraction of 1%, a limit is imposed of a few times 10^7 in the γ-ray intensity.

As mentioned earlier, the spectrum of γ-rays arriving at the measuring station is rather flat (see Figure 3). Most of the measurements performed will require a determination of the γ-ray energy. There are two possible methods to define the energy – collimation and tagging.

The tagging technique requires the determination of electron energy dispersed in the collision in coincidence with the γ-ray or its reaction products. Given the energies involved, the use of magnetic analysis for the electron is implied. For cost reasons, it would be convenient to make use of the ring itself for this purpose. In so-called internal tagging, a position-sensitive counter is placed at the exit of the next bending magnet after the laser electron interaction region in order to measure electron energy loss. Si microstrip detectors have been successfully employed for this purpose [11]. The obtainable energy resolution depends on the ring optics [12] (dispersion and magnification). Given the uncertainty in the ring parameters, at present we are unable to evaluate the expected resolution at ALBA. In a study performed for the original ring design, we showed [13] that resolutions (FWHM) on the order of 4 MeV or 7 MeV (independent of γ-ray energy) could be obtained depending on the configuration. The tagging technique is another source of limitation for achievable γ-ray intensity [14]. At high rates, pile-up signals in the tagger and random coincidences with the measuring detectors introduce spurious events for which correction must be performed. The maximum admissible rate equals approximately 10^7-10^8 s^{-1}; however, it depends on the time resolution and the type of experiment.

There is a minimum γ-ray energy that can be tagged, which is related to the synchrotron ring dispersion at the position of the detector and the distance of the closest possible approach of the detector to the electron beam envelope. Given the uncertainty in the ring parameters, we can only provide a rough estimate of ~150 MeV for the minimum tagged energy. For energies below this limit, the alternative method of collimation can be used to define the γ-ray energy, which exploits the angle-energy relation of the scattered photons (see Figure 2). It is obvious that smaller opening angles procure better energy resolution at the cost of intensity, so a balance between the two must be reached for actual experiments. Since the angular definition also depends on the directions of the colliding electron/photon and the position of their interaction, there is a minimum energy resolution that can be obtained. This minimum energy resolution depends on the electron and laser beam parameters as well as the collimation geometry. It is possible to obtain an estimate of the uncertainty in the γ-ray energy due to the uncertainty in the angles and energies, applying the error propagation formula to Eq. 1. We can then deduce that the collimation method gives too rough an energy resolution except when the collimator is placed at 0°. In this case, a variation of the γ-ray energy requires a variation of the electron energy (not feasible at ALBA) or the laser photon energy. As previously mentioned, we plan to use an OPO source with a wavelength range of $\lambda = 1\text{-}12\ \mu\text{m}$ to cover the energy range $E_\gamma = 15\text{-}150$ MeV. We are also considering the possibility of using a Free Electron Laser (FEL) to extend the collimated energy range to lower energies [15].

An accurate estimate of the resolution and intensity obtained requires consideration of possible variations of the parameters in Eq. 1. We chose the Monte Carlo method for this purpose. The electron and laser photon beam spatial distributions are modelled in the same way as previously explained. In addition, the momentum distributions will need to be modelled. For electrons, they are adequately represented by Gaussian distributions of the slopes in both X and Y directions with parameters $\sigma_{X'}$ and $\sigma_{Y'}$ constant along Z, and by a Gaussian distribution in the energy with parameter σ_{E_e}. For laser photons, we assume a well-defined energy in a direction perpendicular to the laser wave front, characterised by the radius [10] $R_L = z\sqrt{1+\left(\pi\sigma_0^2/\lambda z\right)^2}$. For each scattering event, the differential angular Compton cross-section is sampled to obtain the γ-ray momentum and the energy of those traversing the collimator opening is accumulated.

Figure 5 shows the results of the Monte Carlo simulation for the laser photon energy $E_L = 1.17$ eV (Nd:YAG laser) when a collimator of radius $r_{col} = 0.5$ mm is placed at $\theta_{col} = 0°$ and at a distance $d_{col} = 25$ m from the centre of the 5-m long interaction region. As can be observed, the energy distribution is characterised by a low-energy tail coming from the distribution of angles, most of the effect being due to the horizontal divergence of the electron beam ($\sigma_{X'} = 20\ \mu$rad). The electron energy resolution has a small smearing effect. The FWHM resolution amounts to $\Delta E_\gamma / E_\gamma = 1.7\%$ and the collimated intensity is $7.3 \times 10^4\ \text{s}^{-1}$ per Watt of laser power (uncollimated intensity is $4.0 \times 10^6\ \text{s}^{-1}$). The simulations were repeated for several collimator openings and laser photon energies. Figure 6 shows the relation between γ-ray energy resolution and intensity for two different laser photon energies and collimator radii of 0.25, 0.35, 0.50, 0.75 and 1.0 mm. The chosen laser photon energies $E_L = 1.17$ eV (Nd:YAG laser) and $E_L = 0.117$ eV (CO_2 laser) would provide γ-ray energies of $E_\gamma = 152$ MeV and $E_\gamma = 16$ MeV, respectively. As can be observed, the relation-intensity resolution is approximately linear except when the intrinsic resolution limit is approached. For a given collimator radius, the energy resolution is nearly independent of the laser photon energy. Given the foreseen 5 W power of the OPO source, intensities in excess of $10^5\ \text{s}^{-1}$ can be expected for a beam collimated to an energy resolution $\Delta E_\gamma / E_\gamma = 1.5\%$ in the energy range of 15-150 MeV.

Applications

Availability of intense highly polarised photon beams in the range of a few MeV to 500 MeV at LLS opens the possibility for a broad range of studies in basic or applied nuclear physics. We are currently working on the definition of an experimental programme. In addition, some general ideas on applications are discussed below.

Figure 5. Collimated γ-ray energy distribution

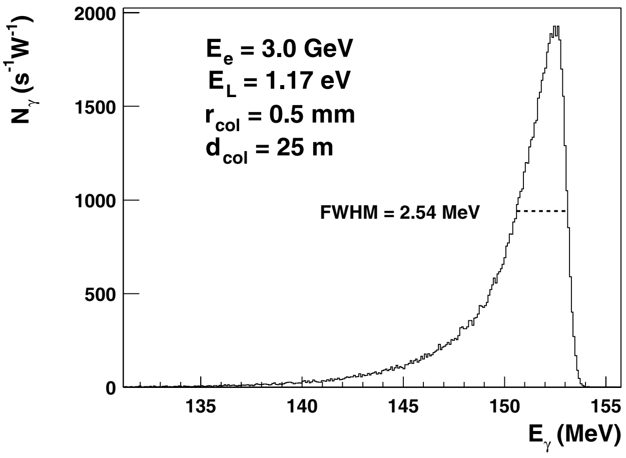

Figure 6. Collimated intensity and resolution

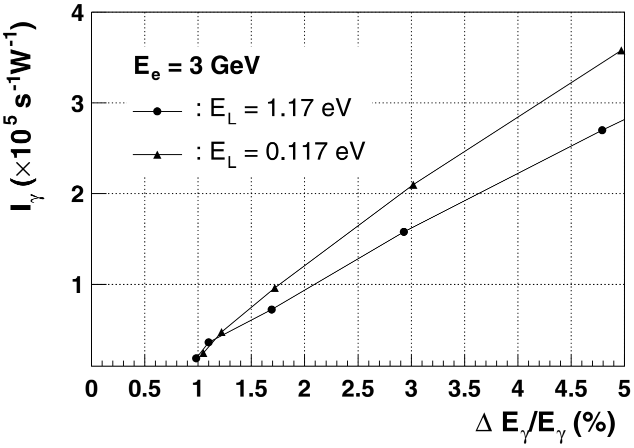

Studies in basic nuclear physics

Low-energy and highly polarised gamma-rays can be used to study the structure of bound nuclear states and to map the dipole electromagnetic strength using the nuclear resonance fluorescence (NRF) technique. At higher energies, photon-induced particle emission will give important information on the structure and damping of the collective giant dipole resonance (GDR). Reactions of this type are also of interest in nuclear astrophysics, either directly since they are responsible for the nucleosynthesis of proton-rich nuclei, or indirectly to determine the cross-section of the inverse capture reaction (for example). The latter is otherwise very difficult to measure in the laboratory, or to get information on neutrino-induced reactions governed by similar operators. At still higher energies, reactions of the one or two nucleon emission type give important information on short range correlations and meson exchange currents in nuclei. The elastic scattering of photons on nucleons will provide information regarding their internal structure while photon-induced fission can be used to investigate the evolution of fission barriers and the viscosity of nuclear matter. The study of the production of pions near the threshold gives insight into the sub-nucleonic structure. Pionic atoms could be produced in order to study the relevant pion-nucleus interaction. Further up in energy, the delta resonance can be excited and its interaction in the nuclear medium could be studied.

Nuclear data for applications

Besides more basic interests, nuclear data is relevant for fields such as nuclear technology, therapy, dosimetry and radiation shielding. It is important to fill in missing information in photonuclear databases.

Industrial applications

Intense collimated beams of ~10 MeV would be an important tool for the non-destructive inspection of objects using radiographic techniques such as gammagraphy and Computerised Tomography (CT). Intense white beams of up to ~10 MeV can be used for non-destructive elemental analysis using the NRF technique.

Instrumentation

Photon beams of this type and quality can be used for precise calibration of specialised detectors such as dosimeters, gamma-ray lenses, etc.

Conclusions

We have shown that it will be possible to produce, without affecting the synchrotron performance, γ-ray beams at LLS with intensities in excess of 10^7 s^{-1} and energies up to 500 MeV. For energies below 45 MeV, much larger (× 10^2) intensities will be possible. In the range of 15-150 MeV, collimation could be used to obtain a resolution of 1.5% or better, essentially 100% polarisation and intensities larger than 10^5 s^{-1}. Above these energies, internal tagging could be used to obtain resolutions on the order of 5 MeV, a high degree (> 80%) of polarisation and intensities larger than 10^5 s^{-1} in a 5 MeV energy bin. If we compare such an installation with existing backscattering facilities [4], the LEGS facility [14] comes closer in the tagged energy range (110-450 MeV) and has an order of magnitude less intensity. In the energy range $E_\gamma < 220$ MeV, the HIGS facility [15] when completed is expected to have comparable intensity at the higher end of the range and one order of magnitude larger intensity at the lower end. (The HIGS facility has a dedicated synchrotron and uses collimation.) In comparison with a *bremsstrahlung* installation, a backscattering installation would have a reduced low-energy background and an easily changeable and potentially higher polarisation degree. No backscattering installation covering the proposed energy range exists in Europe. At present, a proposal is being prepared by several national groups. International collaboration would be welcome.

REFERENCES

[1] Milburn, R.H., “Electron Scattering by an Intense Polarized Photon Field”, *Phys. Rev. Lett.*, 10, 75 (1963).

[2] Arutyunian, F.R., V.A. Tumanian, “The Compton Effect on Relativistic Electrons and the Possibility of Obtaining High Energy Beams”, *Phys. Rev. Lett.*, 4, 176 (1963).

[3] Federici, I., *et al.*, “Backward Compton Scattering of Laser Light against High-energy Electrons: the LADON Photon Beam at Frascati”, *Nuovo Cim.*, 59B, 247 (1980).

[4] D’Angelo, A., *et al.*, “Generation of Compton Backscattering γ-ray Beams”, *Nucl. Instr. and Meth.*, A455, 1 (2000).

[5] Feenberg, E., H. Primakoff, “Interaction of Cosmic-ray Primaries with Sunlight and Starlight”, *Phys. Rev.*, 73, 449 (1948).

[6] Ginzburg, I.F., *et al.*, “Colliding γe and $\gamma\gamma$ Beams Based on the Single-pass e^+e^- Colliders (VLEPP Type)”, *Nucl. Instr. and Meth.*, 205, 47 (1983); I.F. Ginzburg, *et al.*, “Colliding γe and $\gamma\gamma$ Beams Based on Single-pass e^+e^- Accelerators. II. Polarization Effects. Monochromatization Improvement”, *Nucl. Instr. and Meth.*, 219, 5 (1984).

[7] *LLS Detailed Design Report*, http://www.lls.cells.es/report/report2.html.

[8] Einfield, D., “The Accelerator Complex at AURORA”, *Scientific and Technological Opportunities in the Future Synchrotron of El Valles*, Mahon, 1-3 October 2003.

[9] Ebrahimzadeh, M., “Parametric Light Generation”, *Phil. Trans. Roy. Soc. Lond.*, A361, 2731 (2003).

[10] Siegman, A.E., “Lasers”, Oxford University Press (1986).

[11] Schaerf, C., *et al.*, “GRAAL Experiment at ESRF”, *Nucl. Phys. News*, 8, 24 (1998).

[12] Preger, M., *et al.*, “Monochromatic and Polarized Tagged LADON Gamma Ray Beams”, *Nucl. Instr. and Meth.*, A249, 299 (1986).

[13] Tain, J.L., *A Photo-nuclear Physics Facility for the Laboratory of the Synchrotron at Barcelona*, Report IFIC/96-57 (1996).

[14] Sandorfi, A.M., *et al.*, “High Energy Gamma Ray Beams from Compton Backscattered Laser Light”, *IEEE Trans. Nucl. Sci.*, 30, 3083 (1983).

[15] Carman, T.S., *et al.*, “The TUNL-FELL Inverse Compton γ-ray Source as a Nuclear Physics Facility”, *Nucl. Instr. and Meth.*, A378, 1 (1996).

SCATTERING IN TWO TARGETS WITH THE VECTOR CODE MCSHAPE

J.E. Fernandez and V. Scot
National Institute of Physics of Matter (INFM) and Laboratory of Montecuccolino
Department of Energetic, Nuclear and Environmental Control Engineering (DIENCA)
Alma Mater Studiorum – University of Bologna, via dei Colli,16, I-40136, Bologna, Italy
E-mail: jorge.fernandez@unibo.it

Abstract

Using the Monte Carlo code, MCSHAPE [1], simulations were performed by varying the angle between the scattering plane with the incident beam (defined by the incident beam and beam 1) and the scattering plane of the collision with the second target (defined by beam 1 and the outgoing beam). The code, MCSHAPE, is able to simulate the behaviour of arbitrarily polarised photons and to follow the evolution of their polarisation state after the interaction with atoms. The polarisation state of the photons is described using the Stokes parameters *I, Q*, *U* and *V*, which have the dimension of an intensity and contain all the physical information about the polarisation state. Simulated experiments with a monochromatic unpolarised source of 59.54 keV (main gamma line of ^{241}Am) and an X-ray tube source have been considered. In the first case, the results of the simulations show that after the 90° scattering in the first target, a part of the scattered beam (beam 1) is polarised. The degree of polarisation is a function of energy and, for some energies, 90% of the beam is polarised. However, scattered beam is not fully polarised in the case of the single scattering. This is an effect of the multiple scattering in the target. The intensity collected by the detector after the scattering in the second target depends on the rotation between the first and the second pieces of the tube. The scattering is drastically reduced with a rotation angle around 90°, even if it is not able to be reduced zero due to the multiple scattering. This behaviour was also tested with polychromatic excitation.

Introduction

It is well known that the polarisation state of source radiation influences the behaviour of photons and their interaction with the matter. The most important phenomena in the energy range of X-rays [photoelectric effect, coherent (or Rayleigh) scattering and incoherent (or Compton) scattering] are differently influenced by such a polarisation state. The photoelectric effect does not feel the effects of polarisation and has an isotropic cross-section. In contrast, the Rayleigh and Compton scatterings are strongly influenced by both the polarisation state and the scattering geometry. In particular, when a linearly polarised beam whose electric field is parallel to the scattering plane scatters at 90°, both the Rayleigh and Compton scatterings tend to vanish for a single scattering. Moreover, in spectrometry experiments this paradigmatic behaviour allows us to eliminate the "noise" due to the scattering and to collect only the signal produced by the photoelectric effect. These phenomena are more complex in the presence of the multiple scattering. That is to say that for the same geometry, the total scattering is no longer zero even if it remains considerably reduced. In order to study this phenomenon, the following configuration is proposed.

Figure 1. Set-up used in the MCSHAPE simulation

Both targets are water. The incident beam, beam 1 and the outgoing beam are narrowly collimated. The source is monochromatic (59.54 keV; ^{241}Am γ-line).

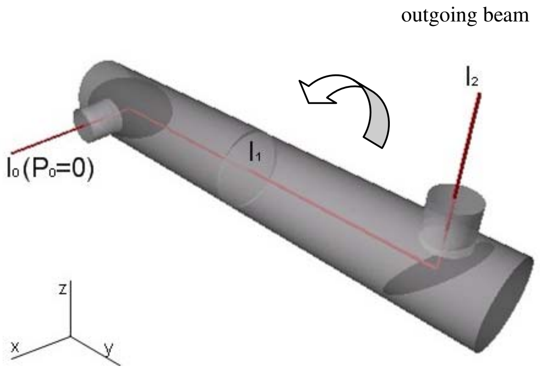

Using the Monte Carlo code, MCSHAPE [1], simulations were performed by varying the angle between the scattering plane with the incident beam (defined by the incident beam and beam 1) and the scattering plane of the collision with the second target (defined by beam 1 and the outgoing beam). The code, MCSHAPE, is able to simulate the behaviour of arbitrarily polarised photons and to follow the evolution of their polarisation state after the interaction with atoms. The polarisation state of the photons is described using the Stokes parameters I, Q, U and V, which have the dimension of an intensity and contain all the physical information about the polarisation state. In the simulated experiment, both targets are water and the energy of the unpolarised source is assumed to be 59.54 keV (^{241}Am γ-line). The simulations illustrate that after the 90° scattering in the first target, a part of the scattered beam (beam 1) is polarised. The degree of polarisation is a function of energy and, for some energies, 90% of the beam is polarised. However, the scattered beam is not fully polarised in the case of the single Rayleigh scattering. This is an effect of the multiple scattering in the target. The intensity collected by the detector after the scattering at the second target depends on the rotation between the first and second pieces of the tube. The scattering is drastically reduced for a rotation angle around 90°, even if it is not reduced to zero due to multiple scattering. An experimental apparatus is being developed in order to investigate in detail the rotational dependence of this configuration.

Representation of polarised radiation

To describe the evolution of the state of polarisation in the photons, four parameters are needed. The first is the intensity of the beam, which is the only quantity considered in scalar transport models. Second, it is important to analyse the fraction of polarised X-rays, or the degree of polarisation. In fact, at each space point and for a given wavelength and direction of propagation, the most general beam of X-rays can be regarded as a mixture of elliptically polarised and unpolarised X-rays. The remaining two parameters are necessary to describe the ellipse associated with the polarised component. These include the orientation of the polarisation ellipse (the angle between the major axes of the ellipse and a fixed co-ordinate axis in the space) and the ellipticity (the ratio of the two axes of the ellipse).

To follow the evolution of these four quantities, MCSHAPE uses the parameters I, Q, U and V, which have the dimension of intensity (introduced by Stokes). These quantities are defined as:

$$\begin{aligned} Q &= I\cos 2\beta \cos 2\chi \\ U &= I\cos 2\beta \sin 2\chi \\ V &= I\sin 2\beta \end{aligned}$$

and in terms of the rotation angle χ, which refers to the scattering plane, and of the angle β, whose tangent is equal to the ellipticity. The degree of polarisation of a partially polarised beam is generally expressed as:

$$P = \frac{\left(Q^2 + U^2 + V^2\right)^{1/2}}{I}$$

In the Stokes representation, modification of the polarisation state due to a collision is expressed below, where H_a is the scattering matrix [2] of the event (its meaning will be explained in the next section).

$$\begin{pmatrix} I_{(n+1)} \\ Q_{(n+1)} \\ U_{(n+1)} \\ V_{(n+1)} \end{pmatrix} = \mathrm{H}_a\left(\vec{r}, \vec{\omega}^{(n+1)}, \lambda^{(n+1)}, \vec{\omega}^{(n)}, \lambda^{(n)}\right) \begin{pmatrix} I_{(n)} \\ Q_{(n)} \\ U_{(n)} \\ V_{(n)} \end{pmatrix}$$

The vector transport equation

So far the scalar transport equation has not rigorously included the state of polarisation in the description of the radiation field. However, in some cases polarisation can be taken into account in the scalar kernels by appropriately defining the interactions between photons and matter. For instance, it is current practice to consider scattering kernels for unpolarised radiation depending on the average state of polarisation. The result is valid results for the first collision of the incident radiation, assuming a polarisation-insensitive detector. However, it has been shown [5] that the subsequent collisions have improper intensities because the equation is not able to describe the polarisation acquired or lost through the scattering collisions.

The transport equation, which formally describes the vector flux $\vec{f}(\vec{r},\vec{\omega},\lambda)d\lambda d\vec{\omega}$ of polarised photons in the Stokes system (having components $f_I(\vec{r},\vec{\omega},\lambda)$, $f_Q(\vec{r},\vec{\omega},\lambda)$, $f_U(\vec{r},\vec{\omega},\lambda)$ and $f_V(\vec{r},\vec{\omega},\lambda)$) for a 1-D backscattering framework [5], can be written as:

$$\eta\frac{\partial}{\partial z}\vec{f}^{(s)}(z,\vec{\omega},\lambda)=-\mu(\lambda)\vec{f}^{(s)}(z,\vec{\omega},\lambda)+\int_{4\pi}d\omega'\int_0^\infty d\lambda'\mathrm{U}(z)\mathrm{H}^{(s)}(\vec{\omega},\lambda,\vec{\omega}',\lambda')\vec{f}^{(s)}(z,\vec{\omega}',\lambda')+\delta(z)\vec{S}^{(s)}(\vec{\omega},\lambda) \tag{1}$$

where:

$$\mathrm{H}^{(s)}(\vec{\omega},\lambda,\vec{\omega}',\lambda')=\mathsf{L}^{(s)}(\pi-\Psi)\mathsf{K}^{(s)}(\vec{\omega},\lambda,\vec{\omega}',\lambda')\mathsf{L}^{(s)}(-\Psi')$$

is the kernel matrix in the meridian plane of reference; $\mathsf{K}^{(s)}(\vec{\omega},\lambda,\vec{\omega}',\lambda')$ is the scattering matrix in the scattering plane of reference; and L is the four-by-four rotation matrix, which transforms the scattered flux from the scattering plane to the meridian plane of reference. Primed magnitudes denote incidence. $\mu(\lambda)$ is the narrow-beam attenuation coefficient, which is independent of the state of polarisation in the photons (assuming the matter is isotropic), and $\vec{S}^{(s)}(\vec{\omega}',\lambda)$ is the source vector flux with components $[S_I,S_Q,S_U,S_V]$. Rotation angles Ψ and Ψ' in Eq. (1) are defined by the following relationships.

$$\cos\Psi=\frac{\eta'\sqrt{1-\eta^2}-\eta\sqrt{1-\eta'^2}\cos(\varphi-\varphi')}{\left[1-(\vec{\omega}\cdot\vec{\omega}')^2\right]^{1/2}} \qquad \cos\Psi'=\frac{\eta\sqrt{1-\eta'^2}-\eta'\sqrt{1-\eta^2}\cos(\varphi-\varphi')}{\left[1-(\vec{\omega}\cdot\vec{\omega}')^2\right]^{1/2}}$$

where η and η' are the cosines of the polar angles in spherical geometry, and φ and φ' are the azimuthal angles. For an axis rotation through an angle Φ in the clockwise direction, the matrix L is defined as:

$$\mathsf{L}(\Phi)=\begin{pmatrix}1 & 0 & 0 & 0\\ 0 & \cos2\Phi & \sin2\Phi & 0\\ 0 & -\sin2\Phi & \cos2\Phi & 0\\ 0 & 0 & 0 & 1\end{pmatrix}$$

Eq. (2) represents a system of four integro-differential equations:

$$\eta\frac{\partial}{\partial z}f_i(z,\vec{\omega},\lambda)=-\mu(\lambda)f_i(z,\vec{\omega},\lambda)+\int_{4\pi}d\omega'\int_0^\infty d\lambda'\mathrm{U}(z)H_{ij}(\vec{\omega},\lambda,\vec{\omega}',\lambda')f_j(z,\vec{\omega}',\lambda')+\delta(z)S_i(\vec{\omega},\lambda), \quad (i,j=I,Q,U,V) \tag{2}$$

where H_{ij} denotes the corresponding matrix element of H. It is noteworthy that the interaction term introduces coupling between the components of the angular flux as long as H is non-diagonal.

The solution of the proposed model can be carried out through an orders-of-interaction solution [5] or through a vector Monte Carlo approach [1]. Intensity is obtained (component by component) through adding the contributions from the different collisions, similar to the scalar model:

$$I_i(\vec{\omega},\lambda)=|\eta|f_i(0,\vec{\omega},\lambda)=|\eta|\sum_{k=0}^{\infty}f_i^{(k)}(0,\vec{\omega},\lambda)$$

Figure 2 contains a schematic representation of the orders-of-interaction solution obtained with the vector equation. Each collision contributes a term to the overall spectrum. All the terms are formed by the four components of the Stokes intensity. This makes it possible to determine the contribution of each term to the spectrum's state of polarisation as a function of the energy. Each term can then be evaluated by its contributions regarding different collision chains of the participating interactions.

Figure 2. Schematic representation of the orders-of-interaction solution obtained with the vector equation

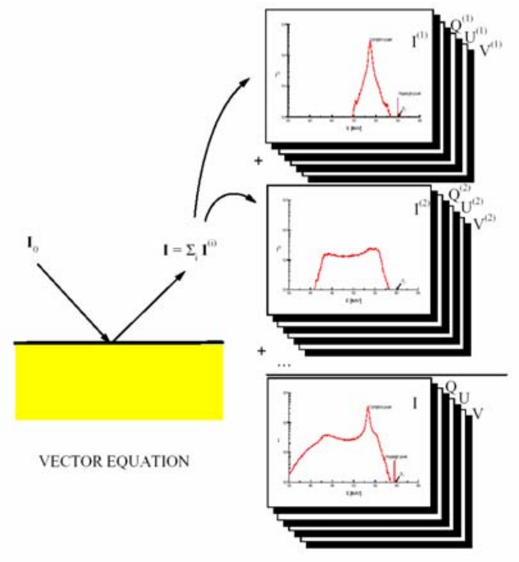

Features of the vector model

The ideas introduced by Eq. (1) are responsible for substantial differences in the solution of the scalar equation. We obtain the four coupled equations as noted in Eq. (2), which give the Stokes components of intensity. These components are a means to determine how the state of polarisation changes after every collision, thus providing a wealth of information on the entire transport process. The first Stokes component represents the detected intensity, and can be compared with the solution of the scalar equation. Although the vector equation is linear, the single equation for intensity is non-linear if considered alone, due to the coupling terms. This fact has two important consequences. First, it is not possible to separately solve the equation for intensity without considering the remaining coupled equations. This prevents us from seeking a solution with a single scalar equation and thus considering the evolution of the full polarisation state (even when using Monte Carlo). Second, the solution obtained for intensity is different from the one predicted, which uses the scalar equation for unpolarised excitation except in the case of the first collision (gives the same result in both cases). This allows to hypothesise that scalar Monte Carlo programs [6,7] employing polarisation-dependent differential cross-sections will never produce equivalent results to the vector solution because they cannot appropriately describe (i.e. at every collision) the exchange between polarised and unpolarised states produced by scattering events (see [8] for a formal demonstration).

A comparison (limited to intensity) that involves the solutions shown in Figure 3 is possible for unpolarised excitation (the extent of the difference is low in this case because polarisation is a second-order effect). Curiously, it can be seen that the average kernel is closer to the vector approach than the solution, which claims to consider a polarised scalar kernel.

Figure 3. Comparison of intensities computed with scalar and vector models

Simulated spectrum of carbon excited with an unpolarised 59.54 keV line of ^{241}*Am. The geometry is 45/135 such that the scattering angle is 90°. The continuous blue line denotes the spectrum obtained with MCSHAPE [1]. The black dashed line denotes the spectrum obtained with Namito's model [6], which is used to patch EGS4. The red dashed line corresponds to the scalar solution, which assigns an average polarisation state to the scattering interactions but neglects the polarisation in the transport equation.*

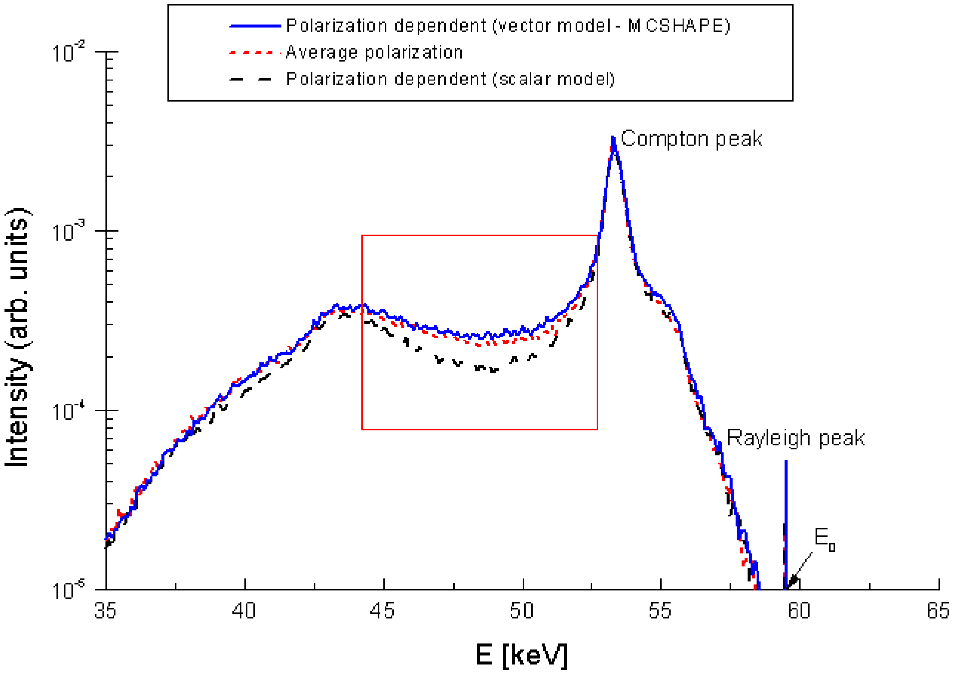

Set-up of the simulation using the Monte Carlo vector code MCSHAPE

The Monte Carlo code, MCSHAPE [1], was developed in order to properly study the transport of photons with an arbitrary state of polarisation. The adopted model is derived from the "vector transport equation" [3-5]. Using this code, simulations have been made in order to investigate in detail the rotational dependence of detected intensity for the configuration shown in Figure 1. It is possible to independently rotate the two pieces of the tube (Figure 1 shows a rotation of 90°).

Results and discussion

MCSHAPE is a FORTRAN code that can be used under both Windows and LINUX platforms. All the simulations were made on a personal computer with the following characteristics: AMD Athlon 2.0 GHz, 1 Gb RAM and LINUX kernel 2.4.20. The computational time was about two minutes for the 90° scattering in the first target (monochromatic source and 5×10^5 photons). For each scattering in the second target, the computational time was longer due to the polychromatic spectrum, which was generated in the first target (~300 energy channels). The computation time equalled nine hours for the same number of histories.

Figure 4 shows the angle χ_1, the degree of polarisation P_1 and the intensity I_1 of the beam S_1 obtained after 90° scatter with the first target. The linear polarisation state created by the collision and the different state of each energy are apparent. The polarisation distribution of the scattered beam S_1

Figure 4. Effect of multiple scattering at the first target: a) angle χ, b) polarisation degree, c) intensity spectrum – Rayleigh peak, Compton peak and double Compton shoulder

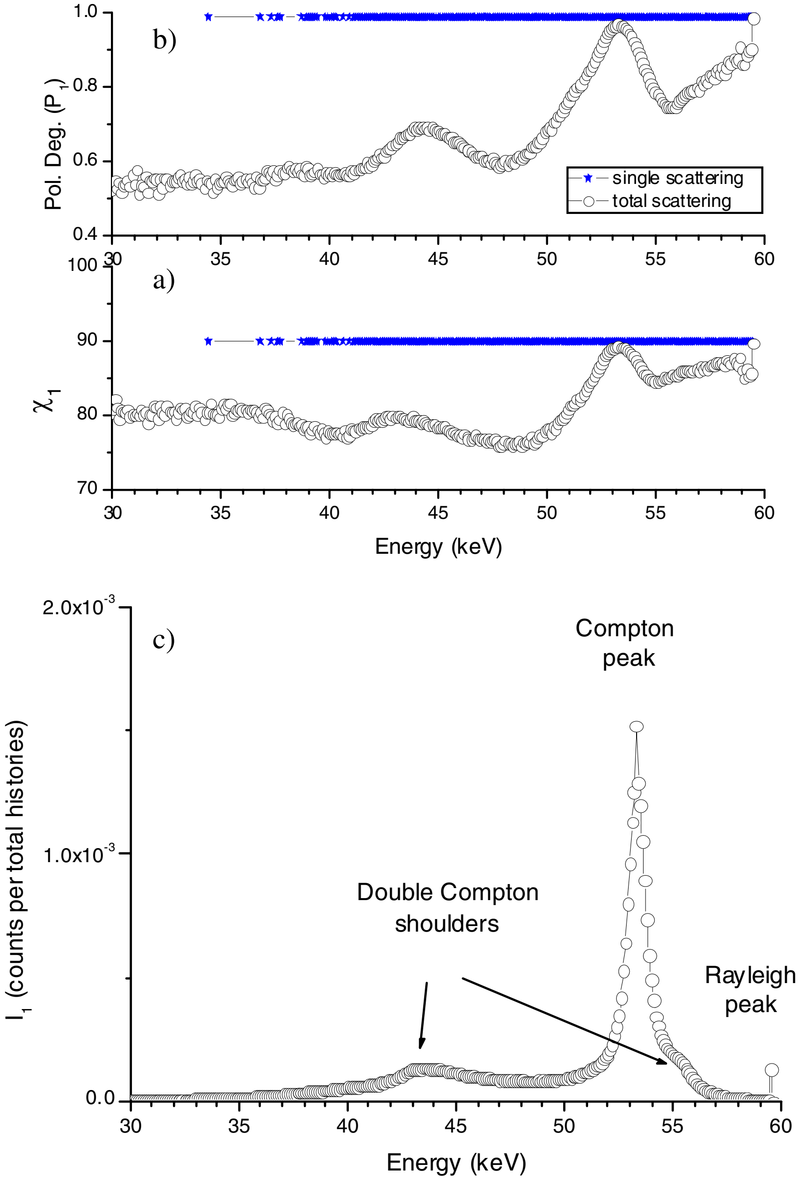

influences any further interaction undergone by the same beam. Figure 5 shows the polarisation state of S_2 (angle χ_2, polarisation degree P_2 and intensity I_2) obtained after the scatter of S_1 in a second target. The relative orientation is important of the scattering plane at the second target with respect to the orientation of the electric field vector defined by the scattering geometry at the first target (see Figures 4a and 4b). Figure 6 shows the rotational dependence of the detected intensity for angles near 90°. The scattering is drastically reduced for a rotation around 90°. For some energies, the scattering's minimum is not at 90° but at a larger value of the rotation angle. The effect on water is small but it should be investigated for other targets and for different spectra of the incident beam.

An experimental apparatus is being developed in order to investigate in detail the rotational dependence of this configuration.

Figure 5. Effect of multiple scattering at the second target: a) rotational dependence of angle χ; b) rotational dependence of the polarisation degree; c) detected intensity for a ~90° rotation the scattering is considerably reduced. For a 0° rotation: 1) Compton scattering of first target Rayleigh peak, 2) Compton scattering of first target Compton peak, 3) Compton scattering of first target double Compton shoulder.

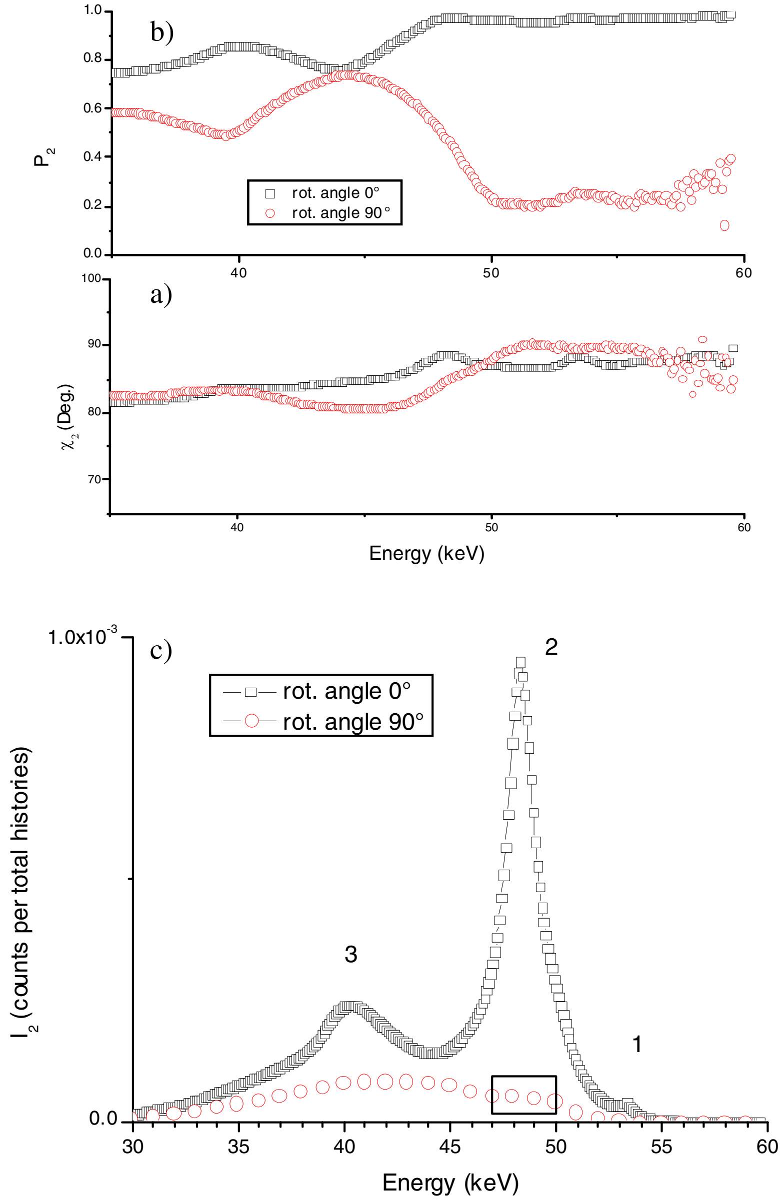

Figure 6. Detail of intensity at the second target for rotational angles near 90°. For certain energies, the scattering reaches a minimum for a rotational angle other than 90°.

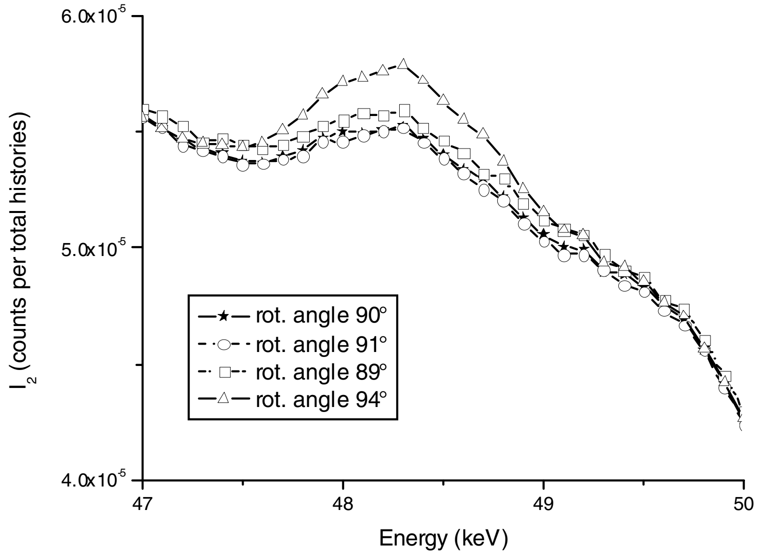

REFERENCES

[1] Fernandez, J.E., V.G. Molinari, M. Bastiano, V. Scot, "Diffusion of Photons with Arbitrary State of Polarisation: The Monte Carlo Code MCSHAPE", *Nuclear Instruments and Methods B*, 213, 105-107 (2004); see also http://shape.ing.unibo.it.

[2] Pomraning, G.C., *The Equation of Radiation Hydrodynamics*, Pergamon Press, Oxford (1973).

[3] Chandrasekhar, S., *Radiative Transfer*, Chap. 1, Section 15, Clarendon Press, Oxford (1950).

[4] Fernandez, J.E., V.G. Molinari, "Diffusion of Polarized Photons in the Frame of the Transport Theory", *Nuclear Instruments and Methods in Physics Research B,* 73, 341 (1993).

[5] Fernandez, J.E., J.H. Hubbell, A.L. Hanson, L.V. Spencer, "Polarization Effects on Multiple Scattering Gamma Transport", *Radiation Physics and Chemistry*, 41, 579-630 (1993).

[6] Namito, Y., S. Ban, H. Hirayama, "Implementation of Linearly-polarized Photon Scattering into the EGS4 Code, *Nucl. Instr. Meth. Phys. Res.,* A332, 277-283 (1993).

[7] Vincze, L., K. Janssens, F. Adams, "A General Monte Carlo Simulation of ED-XRF Spectrometers. Part I: Unpolarized Radiation, Homogeneous Samples", *Spectrochim. Acta.,* B48, 553-573 (1993).

[8] Fernández, J.E., "Non-linear Effects in Polarised Photon Transport", *Appl. Rad. Isot.,* 49, 83 (1998).

SESSION I.2

Source Term and Related Data – Electron, Proton and Ion Accelerators and Spallation Sources

Chair: N. Hertel

BENCHMARKING POSSIBILITIES AT FERMILAB: ACCELERATORS, EXPERIMENTS AND IRRADIATION FACILITIES

N.V. Mokhov
Fermi National Accelerator Laboratory, P.O. Box 500
Batavia, IL 60510 USA

Abstract

Possibilities for transport code and physics model benchmarking at the Fermilab complex are described. The facilities include: a 400 MeV linac, an 8 GeV booster, a 150 GeV main injector, a 980 × 980 GeV proton-antiproton Tevatron collider, CDF and D∅ collider detectors, fixed-target particle production and neutrino experiments, and two special irradiation facilities at the booster and antiproton target station. The complex provides a variety of conditions for particle spectra (ranging from an electron volt to 1 000 GeV) and a variety of possibilities to study source terms, the deep penetration shielding problem, induced radioactivity, radiation damage, etc. Results are presented of recent calculational and experimental radiation studies performed at these facilities, including beam-induced damage to the Tevatron collimators (December 2003).

Introduction

There are numerous possibilities for transport code and physics model benchmarking, and for materials and electronics component tests at the Fermilab complex (Figure 1) in a broad range of irradiation conditions. The facilities include: a 400 MeV linac, an 8 GeV booster, a 150 GeV main injector, a 980 × 980 GeV proton-antiproton Tevatron collider, CDF and D∅ collider detectors, fixed-target particle production and neutrino experiments and two special irradiation facilities at the booster and antiproton target station. The complex provides a variety of conditions for particle spectra (ranging from one electron volt to 1 000 GeV) and a variety of possibilities to study source terms, the deep penetration shielding problem, induced radioactivity, radiation damage, etc.

Figure 1. The Fermilab accelerator complex

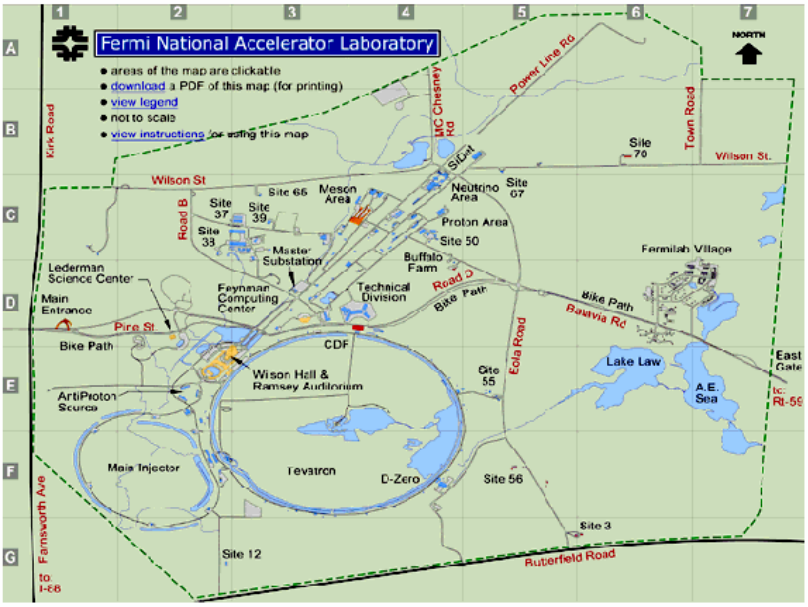

Linac, booster and MiniBooNE

The Fermilab linac

The Fermilab linac is a negative hydrogen ion, 400 MeV accelerator ~170-m long. It includes a 25 keV H-minus ion source, a 750 keV electrostatic accelerating column, a 116 MeV drift-tube (Alverez) linac operating at 201.25 MHz and a 401 MeV side-coupled cavity linac operating at 805 MHz. It provides a beam for booster operation at frequencies of 0.1-5 Hz, typically at 40 mA. Several times per week, it provides 66 MeV protons to the Fermilab Neutron Therapy Facility (NTF). Linac provides the following possibilities for radiation studies and benchmarking: beam loss and residual dose rates on machine components, dose and neutron fluxes/spectra in the machine and NTF enclosures, and neutron spectrum modification with NTF collimators.

The Fermilab booster

The Fermilab booster is an 8 GeV proton synchrotron, 474 m in circumference. It has a 15 Hz resonant magnetic cycle. It provides the 8 GeV proton beam (up to 5×10^{12} ppp) for the main injector (0.7 Hz) and the MiniBooNE experiment (4 Hz, demand 8 Hz), up to 6.4 µA for 51 kW. The Fermilab booster provides the following possibilities: beam loss distributions with/without a new collimation system, fully documented activation data for machine components and prompt dose rates on the shielding outside, groundwater activation and migration. Note that close collaboration has existed between the Energy Deposition Group (MARS code) and the Booster team since about 1998, with a complete MARS model of the entire machine, its components and shielding that makes benchmarking easy. Figure 2 provides two examples of the MARS code benchmarking at the booster.

Figure 2. Dose equivalent per 7.1 GeV proton lost in magnets after a 5.3 m dirt shielding above the booster tunnel as calculated with MARS and measured with an ionisation chamber (left). Specific activity of five isotopes at a 15 cm dirt depth underneath the concrete floor of the booster tunnel as calculated with MARS and measured (right).

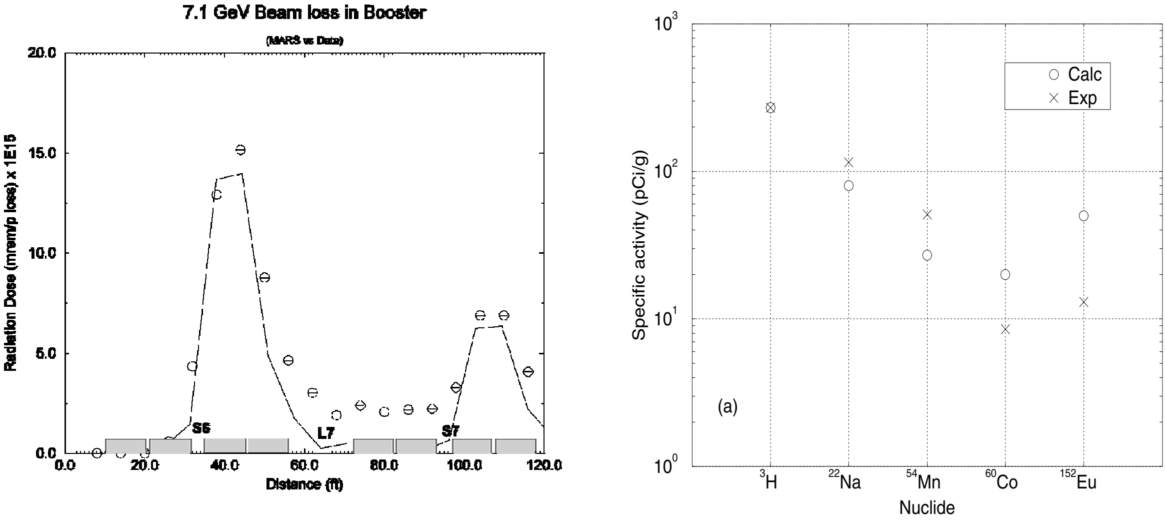

MiniBooNE neutrino experiment

The MiniBooNE neutrino experiment provides numerous possibilities for radiation benchmarking with its target station, shielding and particle production measurements. Recent comparisons of readings on the chipmunk detector in MI-12 showed that the levels agree exactly with the MARS14 calculations for the shielding assessment.

Main injector, NuMI and MIPP

The Fermilab main injector

The Fermilab main injector is a 150 GeV proton synchrotron with a circumference of 3.3 km and a magnetic cycle of 0.7 Hz. It provides the proton beam (up to 3×10^{13} ppp) for the Tevatron collider, the antiproton production target, the MIPP particle production experiment and the NuMI/MINOS neutrino experiment. There are many benchmarking possibilities at the main injector and the NuMI primary beam line including: beam loss distributions, shielding, groundwater activation and prompt and residual dose. Detailed 3-D MARS models of the extraction system (with 2% of beam loss), a NuMI primary beam line and a target station have been built over the last few years. Numerous radiological data will be available for benchmarking starting next year.

MIPP (FNAL E-907)

MIPP (FNAL E-907) stands for Main Injector Particle Production Experiment. Its purpose is to measure cross-sections for hadron production from nuclear interactions using pions, kaons and proton beams in the momentum range from 5-90 GeV/c and secondary momenta down to 0.1 GeV/c, with excellent initial and final state particle identification. Light-to-heavy targets will be used to study the scaling laws of hadronic fragmentation and light meson and baryon spectroscopy as well as specific issues of thick neutrino production targets and benchmark simulation programs (data available in 1-2 years). A detailed 3-D MARS14 model has recently been built starting from the primary target through the entire beam line, and including collimators, shielding and detectors. Numerous radiological data will be available for benchmarking next year.

Tevatron collider and detectors

The Tevatron collider and its experiments

The Tevatron collider and its experiments provide unique possibilities for code benchmarking from the highest energies available at accelerators (1 000 GeV) down to thermal neutron energies. This includes but is not limited to the following: operational and accidental beam loss in the 6.3 km ring, multi-component collimation system performance to protect superconducting magnets and collider detectors, conventional radiological issues and radiation loads on detector and electronic components.

A unique example is the damage to the collider components caused in December 2003 by a failure in the CDF Roman Pot detector positioning at the end of a 980 × 980 GeV proton-antiproton colliding beam store. Two-thirds of the 6.3 km superconducting ring quenched and two collimators were destroyed. In addition, a cryogenic spool piece that houses correction elements was damaged as a result of helium evaporation and a rise in pressure during the quench, requiring 10 days of Tevatron downtime for repairs. The misbehaved 980 GeV proton beam drilled a 2 mm hole in a primary collimator (5 mm tungsten) and created a slot (3 × 250 mm) in a secondary stainless steel collimator as shown in Figure 3. Results of this unintentional benchmarking of beam dynamics, energy deposition and ablation processes modelled using the STRUCT and MARS14 codes are in an excellent agreement with the observations in the damaged collimators.

Figure 3. Damage to the tungsten primary collimator (left) and stainless steel secondary collimator (right) induced by a beam accident in the Tevatron collider in December 2003

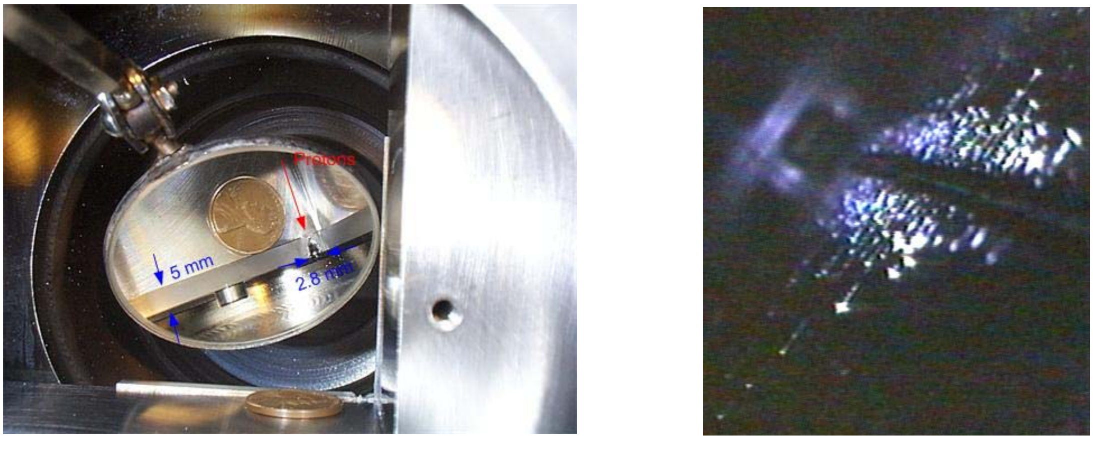

The Radiation Damage Facility

The Radiation Damage Facility (RDF) is arranged with an 8 GeV proton beam in front of the booster beam dump and with 5×10^{11} to 4.5×10^{12} protons per pulse at 1 Hz in a 25 mm diameter spot (Figure 4). The dose limit is set by the RDF Review Committee and the Accelerator Division ES&H, with dump and area activation in mind for personnel safety. The RDF is a separate radiation area from the booster, thus personnel access is relatively easy. While HEP is running, RDF is basically unavailable.

Figure 4. The Radiation Damage Facility

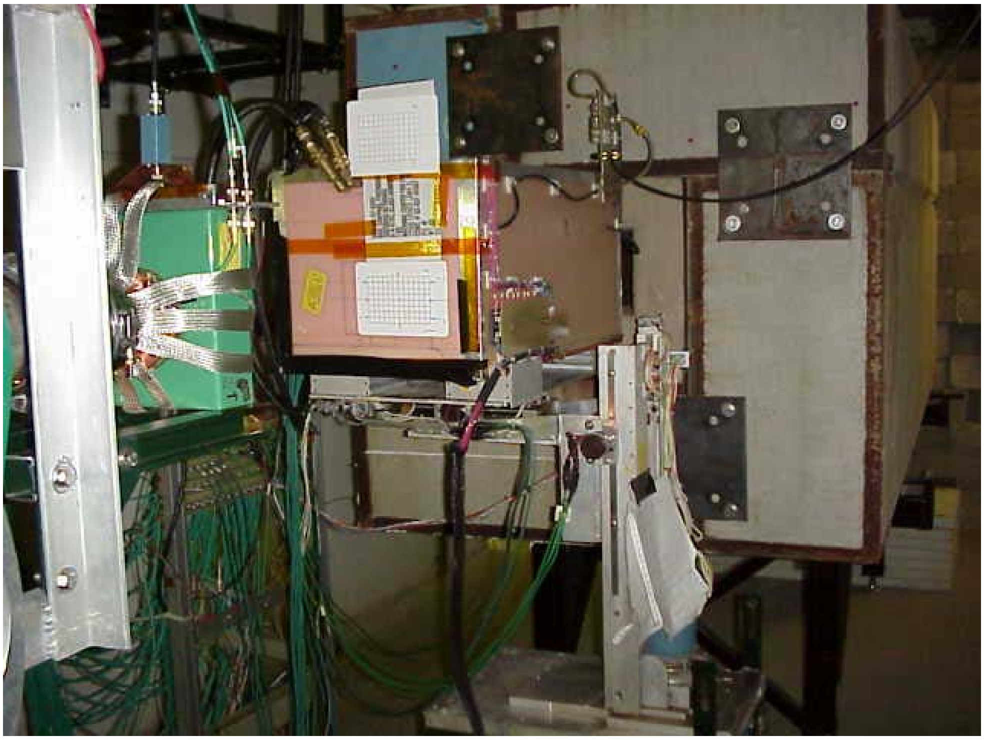

The Operations and Safety department requires that all beams to the RDF be dedicated – parasitic running is not permitted unless special monitoring/safety equipment has been developed and installed. The only time a beam can be run to the RDF is when it is not required by one of the other machines or MiniBooNE. At such times, RDF running time must compete with machine studies and required maintenance as well as other access requirements in the linac and booster.

The Target Test Station

The Target Test Station facility (TTS) will be arranged with the following: a 120 GeV proton beam of $\sigma_{x,y} = 0.15$ mm, 5×10^{12} ppp every three seconds on a 7 cm Ni target followed by a 15 cm Li lens, a 1.2 cm Be window and a PMAG dipole (1.56 T-m) with a studied sample at 218 cm from the target face. Steady-state beam intensity on the target is 1.67×10^{12} p/s. Fifty-four per cent (54%) of the proton beam reaches the sample, being spoiled (enlarged) by multiple Coulomb scattering and elastic or diffractive nuclear interactions in the target and lens as well as being swept by the dipole field. Details of the radiation field at TTS are shown in Figure 5. The strong radial gradient of the sample dose should be noted. Once in operation, TTS will provide possibilities for studying activation data, deep penetration in shielding, electronics and normal/superconducting materials irradiation.

Figure 5. Proton isofluxes [peak 3.4 × 10^{13} cm^{-2}s^{-1} (left)], radial distribution of absorbed dose [peak 0.031 MGy per pulse (centre)] and proton spectrum at sample axis (right). Flux and dose 10 times lower at 1.4 mm from the axis.

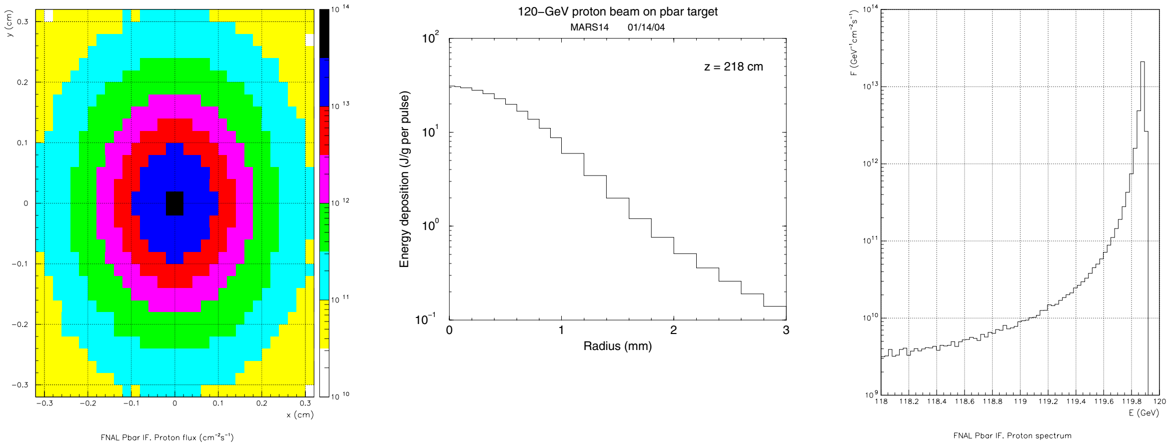

In the same area, possibilities exist for large-scale activation studies and deep penetration shielding benchmarking. Figure 6 shows the corresponding geometry for positioning of the activation samples, which are downstream of the antiproton target and above the thick iron shielding where neutron spectra are measured.

As shown in Figure 6 (right), residual dose rates on steel samples calculated with the MARS14 code agree very well with the measurements.

Figure 6. Configuration of the Target Test Station (left) and residual dose rates in steel samples (right) as calculated using MARS14 and measured at TTS

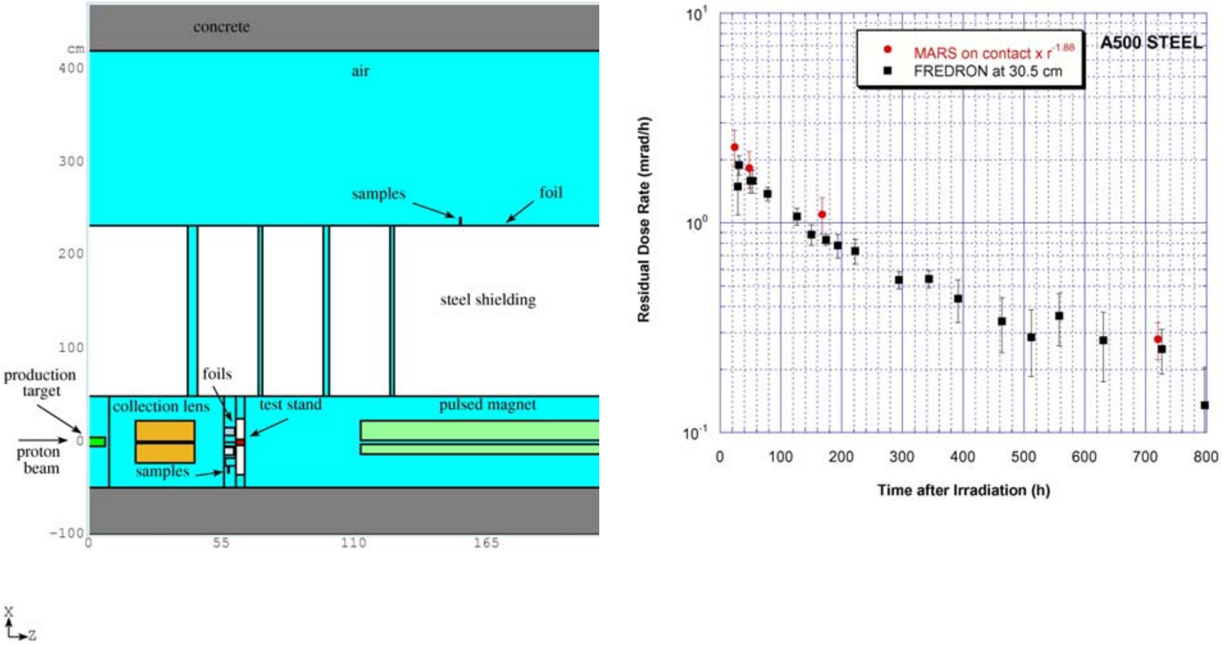

HANDBOOK ON SECONDARY PARTICLE PRODUCTION AND TRANSPORT BY HEAVY IONS OF ENERGIES ABOVE 100 MeV/NUCLEON – GENERAL VIEW AND CONTENTS

T. Nakamura
Cyclotron and Radioisotope Center, Tohoku University
Aoba, Aramaki, Sendai 980-8578, Japan

L. Heilbronn
Lawrence Berkeley National Laboratory
Berkeley, CA, 94720, USA

Abstract

In high-energy, heavy-ion particle facilities many secondary particles are created from nucleus-nucleus interactions. These particles, especially neutrons, can produce radioactivity induced in accelerator and structural materials (air, water and soil) and can penetrate through the facility building into the surrounding environment. Therefore, it is necessary to evaluate the emission of the secondary particles and the creation of the residual nuclei in various materials. To facilitate the evaluation, we created a handbook containing experimental data from heavy-ion reactions above 100 MeV/nucleon. The data contained in the handbook includes: thick-target (stopping-target) secondary neutron yields, thin-target secondary neutron production cross-sections, measurements of neutrons behind shielding, spallation product cross-sections and yields, and moving source parameterisations of neutron yields (thick and thin target). In addition, the handbook will contain PHITS calculations of selected data sets in order to explain issues that arise when comparing calculations with the data in the handbook. The following is an overview of the contents of the handbook.

Secondary neutron thick-target yields

Table 1 lists the secondary neutron thick-target data sets presented in the handbook. The first column contains the beam energy per nucleon and the second column shows the beam ion species. The third column lists the targets used with each beam. The fourth column lists the minimum neutron energy that was measured at each angle indicated in the fifth column. The fifth column contains the laboratory angles where spectra were measured. Details about the experiments, including diagrams, are included along with details about each individual analysis. Double-differential thick-target yields are presented, as are angular distributions and total neutron yields. Systematic trends in the angular distributions and total yields are parameterised.

Table 1. Information on the secondary-neutron thick-target yield experiments that are presented in the handbook

Energy (AMeV)	Ions	Targets	E min (MeV)	Angles
100	He, C, Ne	C, Al, Cu, Pb	3-10	0°-90°
155	He, C	Al	10	10°-160°
160	He	Pb	10	0°-150°
177.5	He	H_2O, C, Al, Cu, Pb	10	0°-150°
180	He, C, Ne	C, Al, Cu, Pb	3-10	0°-90°
272	Nb	Al, Nb	20	3°-80°
400	C, Ne, Ar, Fe, Kr, Xe	C, Al, Cu, Pb	3-10	0°-90°
435	Nb	Nb	20	3°-80°
800	Si	C, Cu	3-10	0°-90°

Secondary neutron production cross-sections

Table 2 contains a list of the secondary neutron cross-sections presented in the handbook. The first column contains the beam energy per nucleon and the second column shows the beam ion species. The third column lists the targets used with each beam. The fourth column indicates the minimum neutron energy that was measured at each angle shown in the fifth column. The fifth column contains the laboratory angles where spectra were measured. Details about the experiments, including diagrams, are included along with details about each individual analysis. Double-differential cross-sections are presented, as are angular distributions and total cross-sections. Systematic trends in the angular distributions are parameterised.

Neutron measurements behind shielding

Table 3 shows the basic details from shielding experiments, which are presented in the handbook. The first column gives the beam energy and ion, the second column shows the target used to produce neutrons before shielding, the third column shows the type of shielding used and the fourth column shows range of shielding thicknesses that were used. Experimental details are provided along with illustrations. The measured neutron fluences, dose, dose equivalents, attenuation lengths as well as MCNPX and LAHET calculations of the data are presented.

Table 2. Information on the secondary-neutron production cross-section experiments that are presented in the handbook

Energy (AMeV)	Ions	Targets	E min (MeV)	Angles
95	Ar	C, Al, Cu, Pb	10	0°-110°
135	He, C, Ne	C, Al, Cu, Pb	10	0°-110°
230	He	Al, Cu	5	5°-80°
290	C	Li, C, CH_2-, Al, Cu, Pb, Marsbar	5	5°-80°
400	C, N, Ne, Ar, Kr, Xe	Li, C, CH_2-, Al, Cu, Pb, ISS wall	5	5°-80°
500	Fe	Li, CH_2-, Al	5	5°-80°
560	Ar	C, Cu, Pb, Marsbar	5	5°-80°
600	Ne	Li, C, CH_2-, Al, Cu, Pb, Marsbar	5	5°-80°

Table 3. Experimental details from the neutrons-behind-shielding experiments presented in the handbook

Beam and energy (MeV/nucleon)	Target	Shielding	Thickness
C (400)	Cu	Concrete	0-250 cm
C (400)	Cu	Iron	0-100 cm
C (400)	Cu	Concrete Iron	0-400 cm 0-100 cm
He, C, O (155)	Hevimet	Concrete Iron	0-440 cm 0-25 cm

Spallation isotope production cross-sections

Table 4 lists the beams, energies and targets used in the spallation production cross-section experiments presented in the handbook. Other experimental details are provided along with illustrations. Production cross-sections, mass yields, excitation functions and dose-per-ion data are contained in the handbook.

Moving-source parameterisations

Moving-source parameterisations of the neutron thick-target yields and neutron production cross-sections are provided in the handbook. These parameterisations make for a useful and simple reproduction of the data. Details about the types of moving-source parameterisations are included along with some representative examples of the fits to the data.

Table 4. Listing of the beams, energies (MeV/nucleon), targets and facilities used to measure spallation product cross-sections

Beam	Energy	Target
^{14}N	278 AMeV	^{nat}Cu
^{12}C	2 083 AMeV	^{nat}Cu
^{40}Ar	2 000 AMeV	^{nat}Cu
^{12}C	2 100 AMeV	^{nat}Ag
^{20}Ne	211 AMeV	^{nat}Cu
^{20}Ne	377 AMeV	^{nat}Cu
^{12}C	135 AMeV	^{nat}Cu
^{4}He	100 AMeV	C, Al, Cr, Fe, Ni, Cu, Pb
^{12}C	100 AMeV	C, Al, Cr, Fe, Ni, Cu, Pb
^{20}Ne	100 AMeV	C, Al, Cr, Fe, Ni, Cu, Pb
^{4}He	230 AMeV	C, Al, Cr, Fe, Ni, Cu, Pb
^{12}C	230 AMeV	Al, Cr, Fe, Ni, Cu, Pb
^{20}Ne	230 AMeV	C, Al, Cr, Fe, Ni, Cu, Pb
^{40}Ar	230 AMeV	C, Al, Cr, Fe, Ni, Cu, Pb
^{12}C	400 AMeV	C, Al, Cr, Fe, Ni, Cu, Pb
^{20}Ne	400 AMeV	C, Al, Cr, Fe, Ni, Cu, Pb
^{40}Ar	400 AMeV	C, Al, Cr, Fe, Ni, Cu, Pb
^{40}Si	800 AMeV	C, Al, Cr, Fe, Ni, Cu, Pb

EXPERIMENTAL INVESTIGATION OF COLD NEUTRON SPECTRA AND COMPARISON WITH MONTE CARLO SIMULATIONS

K. Nünighoff, D. Filges, F. Goldenbaum, R-D. Neef, N. Paul, Ch. Pohl, H. Schaal
Institut für Kernphysik, Forschungszentrum Jülich GmbH, Germany

On behalf of the JESSICA collaboration

Abstract

In this contribution we present recent results of the JESSICA experiment located at the proton synchrotron COSY at Forschungszentrum Jülich. We measured the time-of-flight spectra and determined the energy spectra at T = 20 K for ice, liquid hydrogen, solid methane, mesitylene, methane hydrate and water at room temperature. These materials could/will be used in next generation high power spallation sources. We were able to normalise the measured spectra to the number of incident protons and thus our experiment is an ideal benchmark to validate source terms of moderators. We compared our measured spectra with MCNPX simulations thereby processing newly generated neutron scattering law data $S(\alpha,\beta,T)$. In the case of water, a comparison with the multi-group transport code MORSE will be presented. We will discuss the observed discrepancies, which will have an impact on the calculation of the neutron-induced radioactivity of specific components, e.g. neutron beam line shutters or the outer shielding in high power spallation sources.

Introduction

The main goal of the Jülich Experimental Spallation Target Set-up In COSY Area (JESSICA) experiment is the investigation of neutronic performance of particularly advanced cold moderators. Knowledge of the neutron spectra of cold moderators is needed for the design of neutron-scattering experiments and for the induced radioactivity in outer regions of a target station, which is dependent on the flux of thermal and cold neutrons. Most elements show an increasing absorption cross-section for thermal and cold neutrons, leading to higher activation levels the more intense and cold is the neutron flux. For such activation analysis, the source term from different moderator materials must be known.

Experimental set-up

The JESSICA experiment is a full-scale mock-up of the European Spallation Source (ESS) target-moderator-reflector assembly [1], which is installed with the Cooler Synchrotron (COSY) at Forschungszentrum Jülich. Due to the low proton beam intensity, COSY is particularly suitable for studying the neutronic performance of advanced moderators because radiolysis and activation levels are negligible. Not only can the proton beam energy be tuned from 0.8 GeV up to 2.5 GeV, the negligible activation rate permits one to easily modify the geometry, construction details and materials involved. Furthermore, the neutronic performance can be studied and the gathered data can be linearly scaled to higher beam intensities as they will be available in high power spallation neutron sources [1-4].

The experiment uses a proton beam with kinetic energy of 1.3 GeV, a pulse length of about 0.5 μs, a repetition rate of 0.05 Hz and intensity up to 10^9 protons per pulse. The proton beam hits the liquid-metal target containing 35 litres of mercury and thereby causes a hadronic cascade, which leads to the emission of neutrons. Most of the neutrons are released during the evaporation phase of the spallation reaction with a kinetic energy of 2-3 MeV. Theses neutrons are partially scattered back by the lead reflector with a height and a diameter of 1 m and 3 m, respectively. The reflector consists of lead rods that fill 80% of the volume. The remaining 20% of the volume is for D_2O cooling, which was not necessary in our experiment due to the low beam power. Inside the reflector, four moderators are positioned, two above and two below the target. All four moderators are rectangular in shape and have a width of 15 cm, a height of 12 cm and a depth of 5 cm. While three of the moderators are dummy moderators only, the bottom upstream moderator is used for our experiments. This moderator can be filled with different moderator materials and can be operated at any temperature between 10 K and 300 K. The latter property is mandatory for validating temperature-dependent neutron cross-section data sets. The set-up of the experiment is shown in Figure 1. The neutron flight path and the neutron detectors are shielded in order to reduce the background. This background is caused by high-energy neutrons leaving the reflector and being reflected at the concrete walls of the experiment hall. These high-energy neutrons are thermalised within a 22.5-cm thick polyethylene layer (42.5 cm in the case of detector housing), which surrounds the neutron flight path. The thermalised neutrons are kept from reaching the detector by being captured inside a boric acid layer with an average thickness of 2 cm.

Two different kinds of proton beam monitors are installed on the proton beam line. An integrating current transformer (ICT) and a wall current monitor (WCM) measure the number of protons per pulse, which are used to normalise the neutron spectra to absolute values. The start signal for the time-of-flight measurements is generated when the neutron pulse passes through the start counter, which is a commonly used plastic scintillator.

Figure 1. Schematic drawing of experimental set-up of the JESSICA experiment with proton beam monitors (ICT, WCM), start counter, neutron detectors, analyser crystal, and target-moderator-reflector assembly

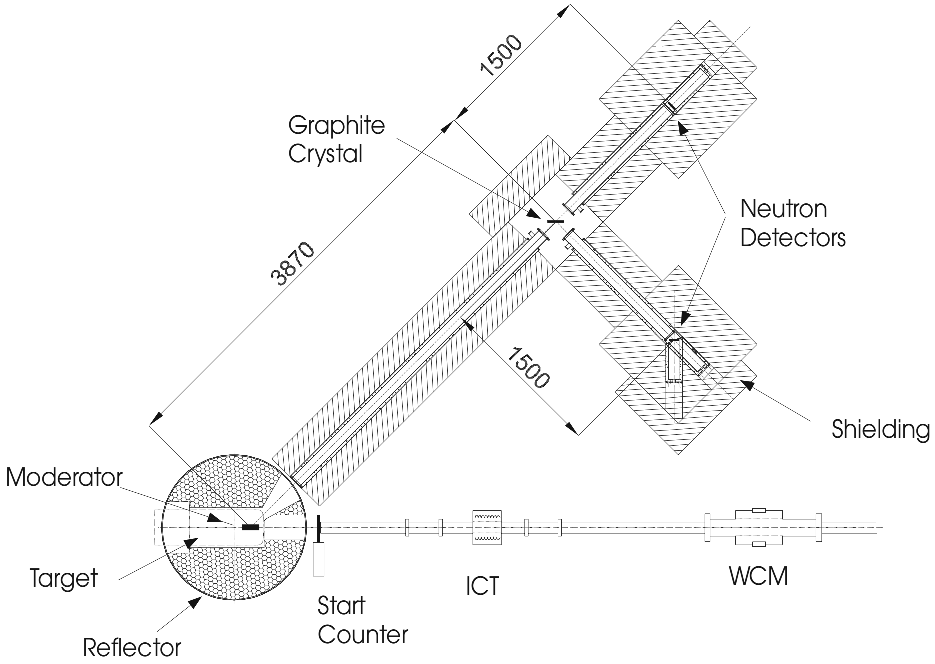

Time-of-flight spectrum and energy spectrum of a thermal water moderator

In this section, the time-of-flight spectrum and the energy spectrum of a thermal water moderator are discussed. Water around room temperature or up to 50-60° C is a commonly used material in research reactors and spallation neutron sources, and thus it is expected that the transport cross-sections for water are well understood. In Figure 2, the measured energy spectrum is shown and compared with a Monte Carlo simulation, which is performed with the HERMES [5] code package as well as MCNPX [6]. In contrast to MCNPX where the transport of neutrons below 20 MeV are simulated with MCNP (a transport code where the neutron cross-sections are as point data), the HERMES system uses the multi-group transport code MORSE. With the MORSE code, the neutron transport cross-sections are described as transition probabilities between the energy groups. As seen in Figure 2, both Monte Carlo simulations agree with the experimental data. However, the simulations result in 40% higher maximal values than the experimental data, which could be an effect of the inhomogeneous detector material, resulting in lower detector efficiency than theoretically expected.

The discrepancy in the thermal energy range can be clearly seen when comparing the measured and simulated time-of-flight spectra. The time-of-flight spectra for thermal neutrons are obtained from a different measurement. Data taken with a 1-mm thick Cd layer in front of the neutron beam line are subtracted from the data without the absorber. The left histograms show the comparison of the experimental and simulated data on an absolute scale. The maximum value is approximately 25% lower than the theoretical data. However, the histograms agree at the small peak of 800 μs. This peak is due to the decreasing absorption cross-section of cadmium. By normalising the simulated data to the peak value of the experimental data (shown in histograms on the right), the agreement of the shapes of both spectra can be seen. It can be concluded that the simulation codes describe well the neutron spectra of a thermal water moderator.

Figure 2. Energy spectrum for a water moderator at T = 293 K. Experimental data compared with Monte Carlo simulations performed with HERMES and MCNPX.

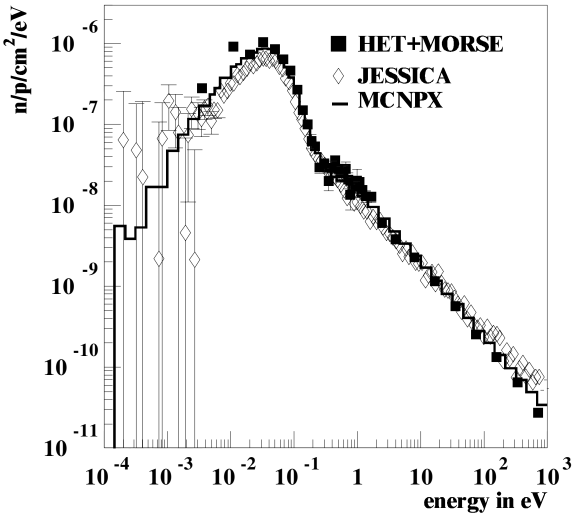

Figure 3. Time-of-flight spectrum for a water moderator at T = 293 K. Experimental data compared with MCNPX.

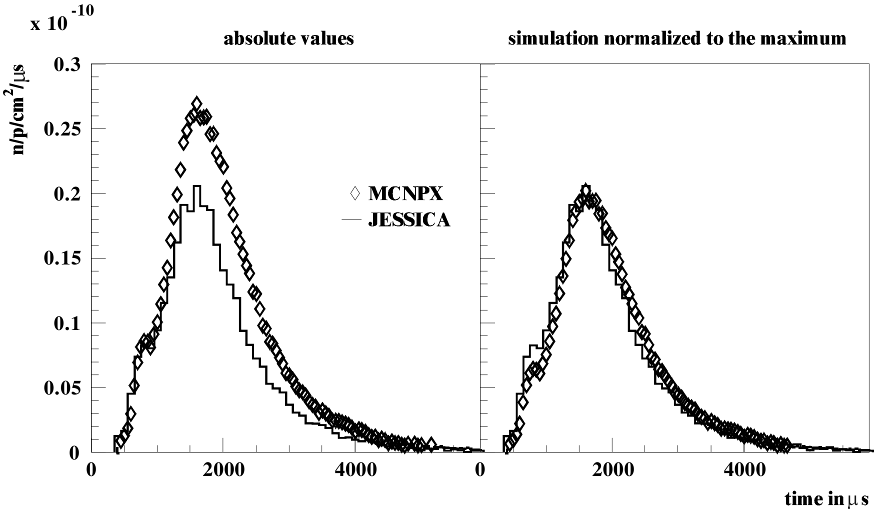

Energy and time-of-flight spectra of a cryogenic ice moderator

In the following section, the time-of-flight spectra and the energy spectra of an ice moderator operated at two cryogenic temperatures are discussed. MCNPX simulations we recently processed using S(α,β,T) data [7] were performed and compared with the experimental data. The shown spectra were measured at temperatures of T = 20 K and T = 70 K. Figure 4 illustrates the comparison of the experimental time-of-flight spectra and MCNPX simulations.

In contrast to the water spectrum, the shape of the ice spectra is not in line with theoretical predictions. Whereas the small peak at 800 μs is in agreement with the simulations, even on an absolute scale, large discrepancies in the shape of the time-of-flight spectra between 1 800 μs and 500 μs can

Figure 4. Time-of-flight spectra for an ice moderator at T = 20 K and T = 70 K. Experimental data compared with Monte Carlo simulations performed using MCNPX.

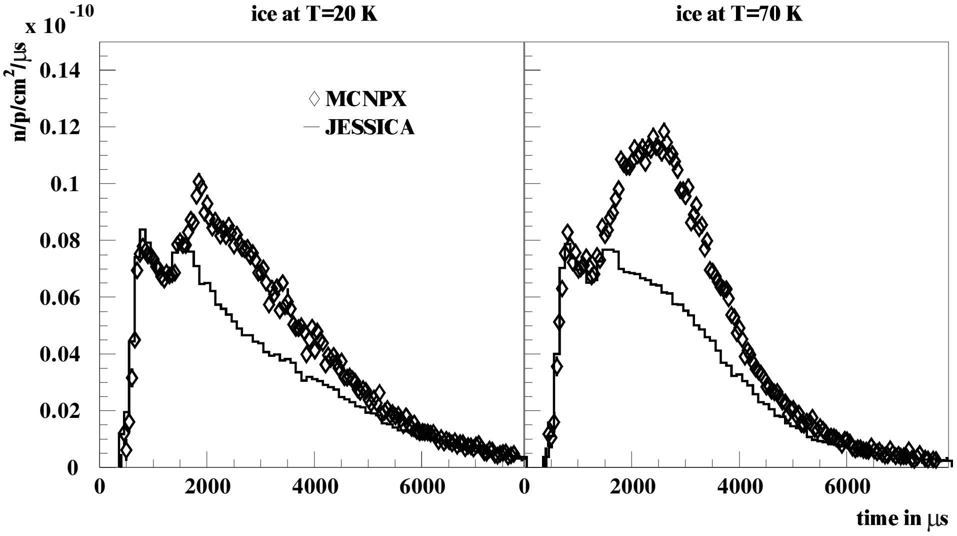

be observed. After transforming the time-of-flight spectra into energy spectra, the same effect can be observed as illustrated in Figure 5. The MCNPX simulations result in higher values in the energy range of 5×10^{-3} eV and 6×10^{-2} eV. However, the 1/E-slope is in agreement. In contrast to our experiment where the moderator material is filled in a rectangular box, a previous experiment at an electron accelerator was performed with a cylindrical moderator vessel with a re-entrant hole [8]. This experiment allowed for the observation of the neutron spectrum inside the moderator vessel. The disadvantage of this experiment is that the data are only given in arbitrary units, and thus are not applicable for validating Monte Carlo transport codes. But by normalising the spectra to the same value at 1 eV, a comparison is possible of the shape of the experimental and simulated spectrum. This comparison is shown in Figure 6. The perfect agreement of both spectra can be seen. From the comparison of our data and the data from Inoue, *et al.* (using MCNPX), we can conclude that the spectrum inside the moderator vessel can be described very well, but the leakage spectrum shows some deficiencies.

Figure 5. Energy spectra for an ice moderator at T = 20 K and T = 70 K. Experimental data compared with Monte Carlo simulations performed using MCNPX.

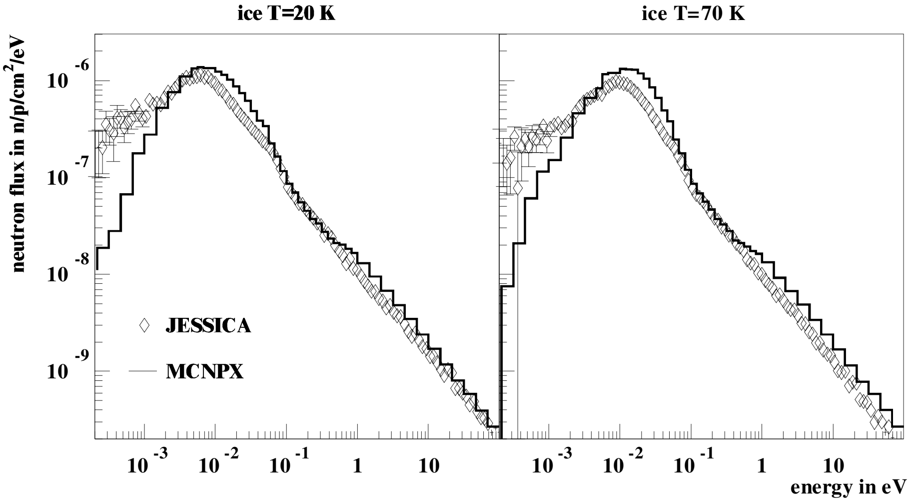

Figure 6. Energy spectra of an ice moderator at T = 20 K measured by Inoue, *et. al.* [8]. Experimental data compared with Monte Carlo simulations performed using MCNPX.

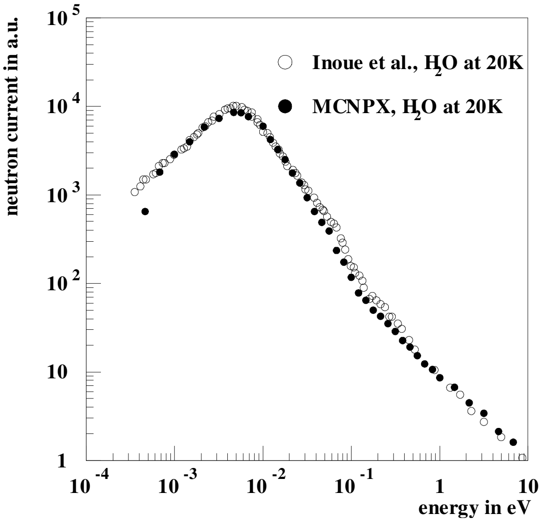

Energy spectra of solid methane, methane hydrate, liquid hydrogen and mesitylene

The neutron energy spectra were measured not only for water and ice, but also for commonly used moderator materials like solid methane and liquid hydrogen. A possible new moderator material is methane hydrate at T = 20 K, which is able to combine the moderation properties of ice and solid methane into a single material. The neutron energy spectrum (observed in experiments) is comparable to solid methane in the energy range below ~50 eV. But in the energy range between 7 meV and 100 meV, the neutron flux of a methane hydrate moderator is slightly lower than pure ice, which is thought to be due to the different crystal structure of ice in methane hydrate and pure ice. A comparison of the energy spectra of solid methane, methane hydrate and ice at T = 20 K is shown in Figure 7. The higher neutron intensity over a broader energy region is expected to yield in a higher activation of devices mounted in the neutron beam line of high intensity spallation neutron sources.

Figure 7. Measured energy spectra of a methane hydrate moderator compared with the energy spectra of an ice moderator and a solid methane moderator at T = 20 K

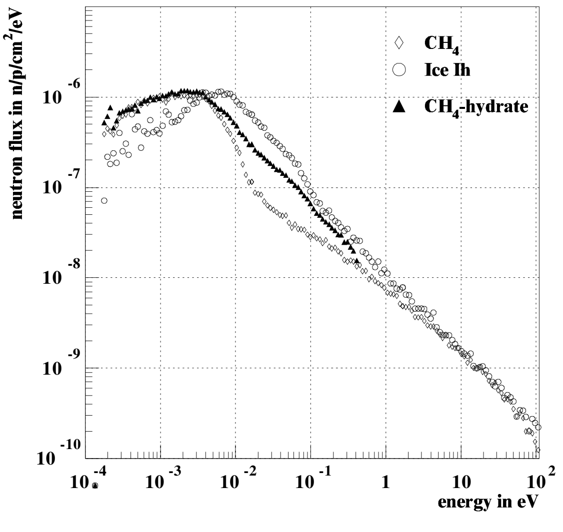

Discrepancies between experimental data and results of Monte Carlo simulations have been observed for cold moderator materials, i.e. solid methane and liquid hydrogen. In Figure 8, the energy spectra for solid methane and liquid hydrogen measured at the JESSICA facility are compared with simulations performed using MCNPX. In the case of solid methane, the experimental spectrum differs from the simulated one by up to a factor of five in the energy range below 1 eV. The results for liquid hydrogen (assuming a mixture of 85% ortho- and 15% para-H_2) were more in agreement with the Monte Carlo simulations.

Figure 8. Measured energy spectra of solid methane and liquid hydrogen moderators compared with Monte Carlo simulations performed using MCNPX

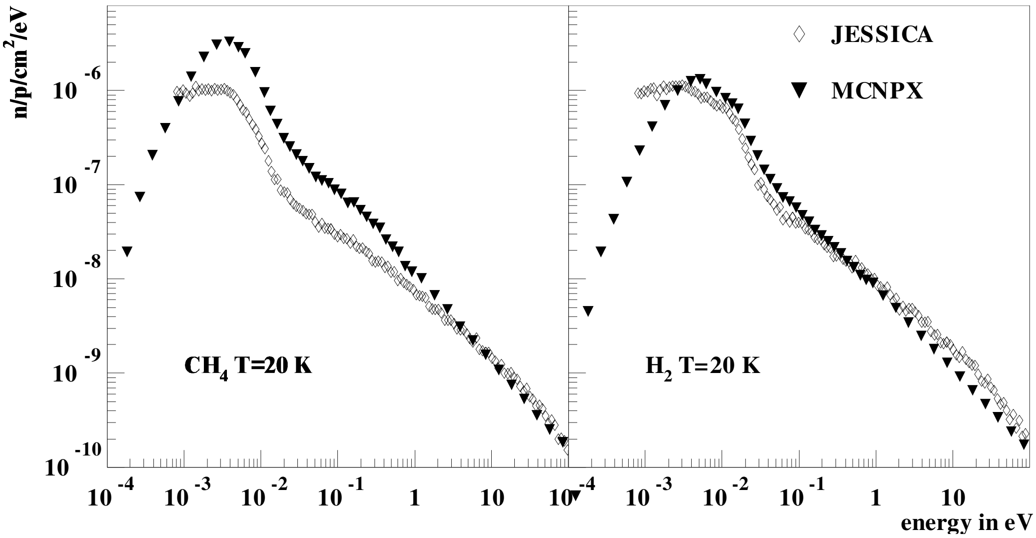

Conclusion and future needs

From the described results it can be concluded that the measured energy and time-of-flight spectra agree within 30% with the Monte Carlo simulation. In the case of water at room temperature, the agreement with experimental data can be demonstrated by applying the MCNPX code system as well as the HERMES code system. It was shown that with the new S(α,β,T) neutron-scattering cross-section data sets, the shape of the energy spectrum inside an ice moderator can be described very well. The exception was the leakage spectra from the moderator surface where differences, which are not yet understood, were observed. The most significant observed differences involved a solid methane moderator. However, the shape of the solid methane spectrum agreed with simulations when the data were normalised to 0.1 eV.

At the present time, the particle transport codes are unable to simulate the transport of neutrons through neutron guides, which are usually installed at spallation neutron sources. Whereas the intensity of the neutron beam is reduced by the solid angle when using the commonly applied transport codes, in the case of a neutron guide, the cold part of the neutron spectrum is reduced to a lesser extent. This must be taken into account for activation analysis. Possible simulated neutron guides would be helpful to simulate the neutron spectrum in larger distances from the moderator.

REFERENCES

[1] The European Spallation Neutron Source Study ESS, *The ESS Technical Study*, report ESS-96-53-M, ISBN 090 237 6659, Vol. III (1996).

[2] *The European Source Pro*ject, Technical Report, ISBN 3-89336-303-3, Vol. III (2002).

[3] *National Spallation Neutron Source*, Executive Summary, ORNL, May 1997.

[4] *High-intensity Proton Accelerator Facility Project*, J-PARC, http://j-parc.jp.

[5] Cloth, P., *et. al.*, *HERMES*, report JUEL 2203, ISSN 0366-0885, May 1988.

[6] Hughes, H.G., *et. al.*, *MCNPX – The LAHET/MCNP Code Merger*, X-Division Research Note XTM-RN (U) 97-012, LA-UR-97-4891, LANL (1997).

[7] Keinert, J., M. Mattes, W. Bernnat, *Thermal Cross-section Data for Light Water Ice, Liquid Hydrogen, and Solid Methane for the Temperature Range from 14 K Up to 273 K in MCNP(X) Format*, IKE 6-198 (2002).

[8] Inoue, K., N. Otomoe, *Journal of Nuclear Science and Technology*, 13, 865 (1976).

SESSION II

Measurements and Calculations of Induced Radioactivity and Activation Data

Chair: T. Nakamura

GADOLINIUM-148 PRODUCTION CROSS-SECTION MEASUREMENTS FOR 600 AND 800 MeV PROTONS

Karen Kelley[1,2], **Matt Devlin**[1], **Eric Pitcher**[1], **Stepan Mashnik**[1], **Nolan Hertel**[2]
[1]Los Alamos National Laboratory, Los Alamos, New Mexico 87544
[2]Georgia Institute of Technology, Atlanta, Georgia 30332-0425

Abstract

In a series of experiments at LANSCE's WNR facility, ^{148}Gd production was measured for 600 and 800 MeV protons on tungsten, tantalum and gold. These experiments used 3-μm thick W, Ta and Au foils and 10-μm thick Al activation foils. Gadolinium spallation yields were determined from these foils using alpha spectroscopy and compared with the LANL codes CEM2k+GEM2 and MCNPX.

Introduction

When heavy metal targets, such as tungsten, are bombarded with protons greater than a few hundred MeV many different nuclides are produced. These nuclides are both stable and radioactive and are created by spallation, proton activation, or secondary reactions with neutrons and other nuclear particles generated in the target. These products are distributed somewhat heterogeneously throughout a thick target because of the energy dependence of the cross-sections and the energy loss of the proton beam within the target. From this standpoint, it is difficult to measure nuclide production cross-sections for a given energy proton in a thick target.

At the Los Alamos Neutron Science Center (LANSCE) accelerator complex, protons are accelerated to 800 MeV and directed to two tungsten targets, Target 4 at the Weapons Neutron Research (WNR) facility and 1L Target at the Manuel Lujan Jr. Neutron Scattering Center. DOE requires hazard classification analyses to be performed on these targets and places limits on radionuclide inventories in the target as a means of determining the "nuclear facility" category level [1]. Presently, WNR's Target 4 is a non-nuclear facility while the Lujan 1L target is classified as a Category 3 nuclear facility. ^{148}Gd is a radionuclide created from the spallation of tungsten and other heavy elements. Allowable isotopic inventories are particularly low for this isotope because it is an alpha-particle emitter with a 75-year half-life. The activity level of ^{148}Gd is generally low, but it encompasses almost two-thirds of the total inhalation dose burden in an accident scenario for the two tungsten targets at LANSCE, based on present yield estimates [2,3]. From a hazard classification standpoint, this severely limits the irradiation lifetime of these tungsten targets.

As 800 MeV protons pass through the tungsten targets at WNR and the Lujan Center, the proton energy is degraded to 600 MeV upon exiting the target. Since the facility classification is partly driven by the inventory of ^{148}Gd, a better estimate of the true production rate in tungsten targets is needed.

From a basic nuclear physics standpoint, the ideal strategy would be to measure the ^{148}Gd production cross-sections for each tungsten isotope. However, obtaining isotopically pure tungsten foils was not feasible. An alternative was to perform measurements using a mono-isotopic element with an atomic number close to that of tungsten (Z = 74). Tantalum (Z = 73), which is 99.988% ^{181}Ta, provides a good alternative for testing physics models used to estimate spallation products at these energies. Further, tantalum is used as target cladding material at the KENS (Japan) and ISIS (United Kingdom) spallation neutron source facilities. These facilities operate at 500 MeV and 800 MeV, respectively. By measuring production from Ta, nuclear physics models can be used in conjunction with production cross-section measurements from elemental W to gain a better understanding of production rates for individual W isotopes, and to help evaluate dose burdens at other spallation neutron source facilities. Another mono-isotopic element of interest to the spallation target community is gold (Z = 79), which is next to mercury (Z = 80) on the periodic table. Mercury is the planned target material for the spallation neutron source being built at Oak Ridge National Laboratory.

The ^{148}Gd inventory in a thick target is difficult to deduce because ^{148}Gd decays only by alpha-particle emission with no associated gamma-ray emission. To date, only one measurement has been taken of the number of ^{148}Gd atoms produced in tungsten. A radiochemistry analysis, which was performed as part of the Accelerator Production of Tritium Project decay heat experiment, measured the number of ^{148}Gd atoms at the centre of three tungsten foils irradiated with 800 MeV protons [4,5]. Assuming that the isotope is only produced within the beam spot, a cumulative cross-section of 16.40 ± 0.41 mb can be inferred from this measurement. Cumulative yields include production from the decay of radioactive parents. A current theoretical estimate involving Mashnik, *et al.*'s CEM2k+GEM2 code [6] for cumulative production for tungsten, is 41.4 ± 0.4 mb at 800 MeV and 21.6 ± 0.3 mb at 600 MeV. The default physics models of code MCNPX (Bertini intra-nuclear cascade + MPM pre-equilibrium + Dresner evaporation with GCCI level density + RAL fission, hereafter referred to as "Bertini") [7] yields 20.9 ± 1.6 mb at 800 MeV and 10.9 ± 0.2 at 600 MeV for the cumulative production from elemental W. Since the accuracy of predicting the cumulative ^{148}Gd production cross-section via the Bertini model is unknown, the procedure approved by DOE regulators for calculating the ^{148}Gd inventory in the targets requires that the predicted value be multiplied by a factor of two. This uncertainty factor further limits the lifetime of the target. A comparison of independent and cumulative production yields from CEM2k+GEM2, Bertini and the APT measurement can be found in Figure 1. This figure illustrates that the independent ^{148}Gd production contribution using CEM2k+GEM2 is only 5-15% of the cumulative ^{148}Gd production, whereas Bertini indicates a contribution of 30-45%. The dominant factor among the cumulative ^{148}Gd production cross-sections is the difference in the ^{152}Er production (Table 1). Figure 2 shows the independent production cross-sections as a function of product mass and *Z*, for Z = 64 to 72. These rare-earth curves indicate that CEM2k+GEM2 typically predicts a higher cross-section for the lower masses than Bertini for a given *Z*, whereas Bertini predicts a higher cross-section for the higher masses for a given *Z*. These figures and tables demonstrate how different are the production yields for rare earth metals using these two intra-nuclear cascade models.

Figure 1. Calculated ^{148}Gd production cross-sections for W(p,x) ^{148}Gd using CEM2k+GEM2, Bertini in MCNPX and an inferred measurement from APT

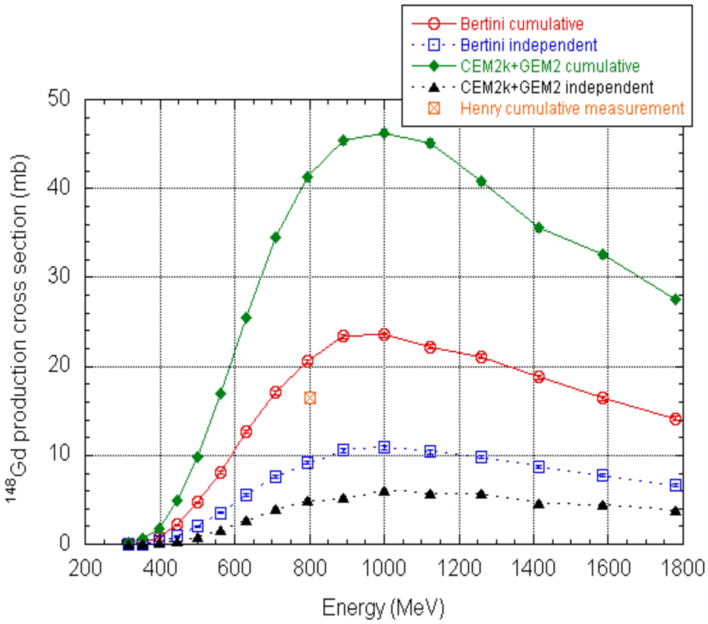

Methods

In order to accurately assess the production of ^{148}Gd in a thick target within the range of 600-800 MeV, a series of thin and thick target experiments within the energy range of interest must be performed. There are several methods by which ^{148}Gd production can be determined. One method is a thick target experiment where a cylindrical target (similar to the ones at LANSCE) is irradiated. The target would be cut into thin slices to determine production within small proton energy intervals since the initial proton energy is degraded as it passes through the target. The irradiated target would then be destructively assayed to determine quantities of isotopes produced. By measuring the production rate of ^{148}Gd as a function of depth in a target, the amount of the isotope created as a function of proton energy can be deduced. The primary drawback to this method is contamination by high-energy secondary protons.

Figure 2. Independent radionuclide production curves from 800 MeV proton incident on tungsten for Z = 64 to 72. Open blue squares represent CEM2k+GEM2 and red-filled circles represent Bertini.

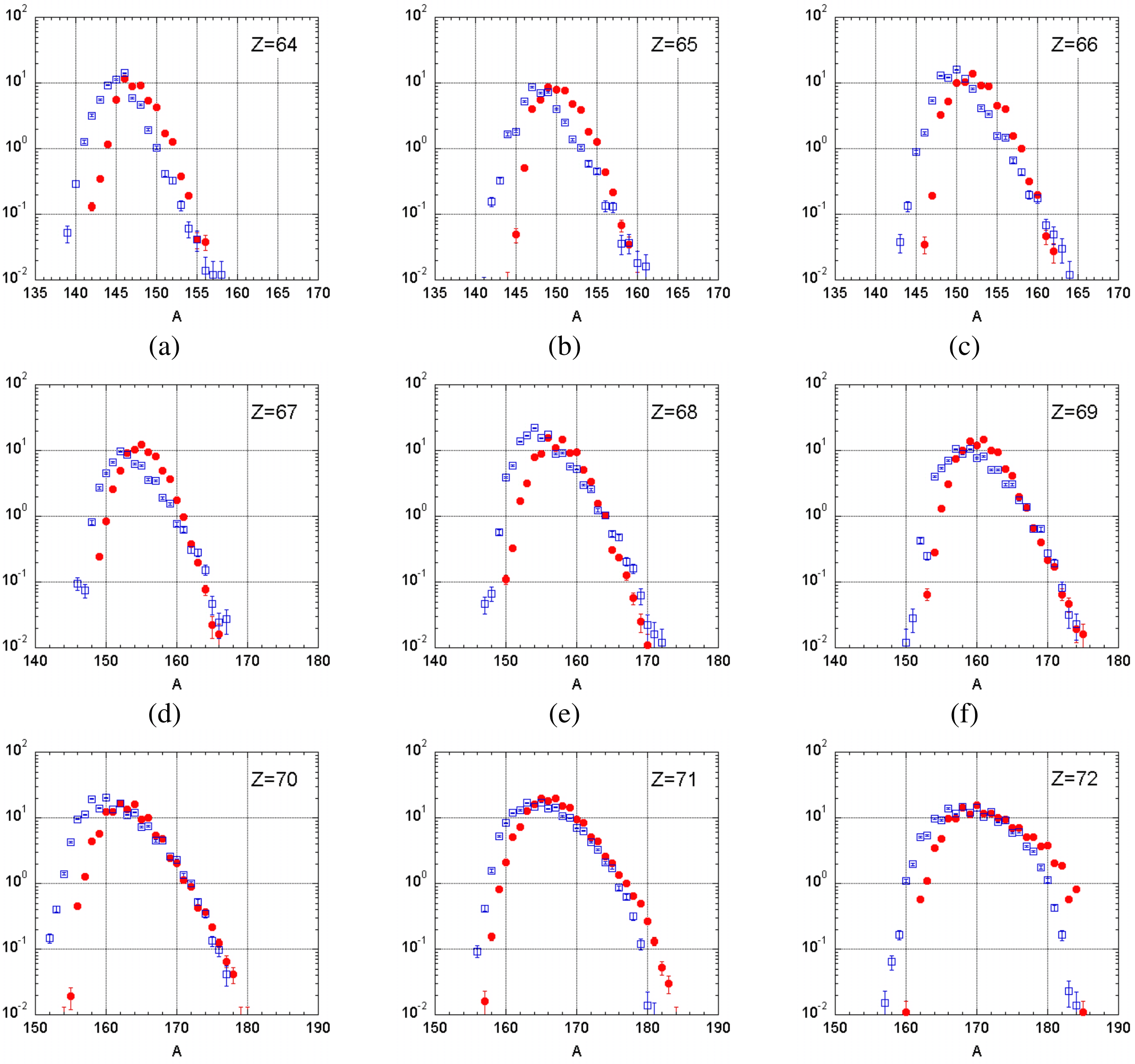

(a) (b) (c)

(d) (e) (f)

(g) (h) (i)

Another method is to irradiate thin foils at specific proton energies to obtain production cross-sections. Nuclear reaction models can then normalise the production cross-section from the threshold to 800 MeV for an array of heavy metals (tungsten, tantalum and gold). Thin foil experiments allow foils of different materials to be irradiated at the same time. Since the proton energy loss through each foil is negligible, all foils are essentially exposed to a single proton energy. Not only do the foils need to be thin enough to have negligible energy loss during irradiation, they also need to be thin enough for ^{148}Gd decay alphas to later escape and be detected. The foil thickness without permanent Mylar support backing was 3 µm for tungsten, tantalum and gold, and 10 µm for aluminium (based on ^{148}Gd's α range). It was decided to use the thin foil method for measuring the ^{148}Gd production cross-section because it could help evaluate dose burdens at spallation neutron source facilities and aid the nuclear physics model community.

Table 1. Comparison of independent radionuclide production cross-sections used in calculating the cumulative ^{148}Gd production cross-sections from an 800 MeV proton incident using tungsten for Bertini and CEM2k

	% Contribution to cumulative	Independent cross-section (mb) Bertini	Independent cross-section (mb) CEM2k	Bertini/CEM2k ratio
^{148}Gd	100	9.26 ± 1.58	4.65 ± 0.14	1.99
^{148}Tb	100	5.59 ± 0.13	6.98 ± 0.17	0.80
^{148}Dy	100	3.28 ± 0.10	12.9 ± 0.2	0.25
^{148}Ho	100	0.003 ± 0.003	0.812 ± 0.058	0.003
^{152}Dy	0.1	13.9 ± 0.19	8.17 ± 0.18	1.71
^{152}Ho	23.0	4.87 ± 0.12	9.56 ± 0.20	0.51
^{152}Er	91.2	1.72 ± 0.07	13.7 ± 0.2	0.13
^{152}Tm	91.2	0.003 ± 0.003	0.428 ± 0.042	0.006
^{156}Tm	0.007	3.08 ± 0.09	7.07 ± 0.17	0.44
^{156}Yb	9.13	0.455 ± 0.035	9.52 ± 0.20	0.048
^{156}Lu	86.6	0.000 ± 0.000	0.093 ± 0.019	0.00
^{160}Hf	0.064	0.011 ± 0.005	1.11 ± 0.07	0.010

A proposed foil stack to be irradiated would consist of one aluminium foil, three tungsten, tantalum or gold foils, followed by three aluminium foils. Aluminium foils are used to determine the proton flux via the well-known ^{27}Al(p,x)^{22}Na reaction. Eight measurements exist for 800 MeV protons, and two measurements for 600 MeV protons [8-16]. Our conclusion from a survey of available experimental data is that the recent measurement at 800 MeV [9] and the measurement from 1981 of 600 MeV [8] are most reliable. We used in our analysis the cross-section values of 14.3 ± 0.4 mb and 16.0 ± 1.1 mb at 800 and 600 MeV, respectively. Stacks of three foils are used to investigate a possible loss of ^{148}Gd and ^{22}Na recoils in the material of interest. When determining the proton flux and production cross-section, only the middle foils are counted where recoil from the first foil balances the loss by recoil to the third foil.

Another method is to irradiate only one foil, sandwiched between two aluminium foils. In this case, the sum of ^{148}Gd counted from the heavy metal foil and the two aluminium foils would be used to determine the production cross-section. This approach is viable because ^{148}Gd is not produced by spallation reactions in Al.

The proton flux for a known reaction cross-section σ of ^{27}Al(p,x)^{22}Na can be found by:

$$\phi_p = \frac{1}{N_{Al}\sigma_{Na}} \frac{C_{Na}\lambda_{Na}}{\varepsilon_{Na}(1-e^{-\lambda_{Na}t_i})(e^{-\lambda_{Na}t_1}-e^{-\lambda_{Na}t_2})} \tag{1}$$

where N is the number of atoms, λ is the decay constant, C is the integral number of counts, ε is the detection system efficiency, $t_i > 0$ is the total irradiation time and $t_2 - t_1$ is the detection counting time where $t_1 > t_i$. The proton flux can then be used to determine a production cross-section for W(p,x) ^{148}Gd.

$$\sigma_{Gd148} = \frac{1}{N_W\phi_p} \frac{C_{Gd}\lambda_{Gd}}{\varepsilon_{Gd}(1-e^{-\lambda_{Gd}t_i})(e^{-\lambda_{Gd}t_1}-e^{-\lambda_{Gd}t_2})} \tag{2}$$

Irradiations

A series of foil irradiations at 600 and 800 MeV have taken place in the Blue Room at WNR. Anticipated beam spot sizes were 1 cm in diameter, thus each foil had to be sufficiently large enough, (5 cm × 5 cm) to subtend the entire proton beam. Individual foils were sandwiched between aluminium frames for easy handling. Framed foils were then stacked together and mounted on a larger frame that centred the foils inside the vacuum chamber. Up to four foil stacks could be placed in the vacuum chamber in the Blue Room, upstream of the last steering magnet for Target 4. A phosphor was also placed in the vacuum box to aid in positioning and shaping of the beam spot on the foils.

The irradiations took place in two modes – sole use and parasitic. Behind the steering magnet is Target 4 at WNR, where neutrons are produced and scattered to different beam lines for experiments. When in the sole use mode, Target 4 was used as a beam stop but not for production of neutrons. In the parasitic mode, the proton beam passed through the foils and then on to Target 4 for neutron production. The energy loss through the foils was negligible (<0.11 MeV), thus all foils saw essentially the same energy with no proton energy loss to Target 4. It was determined that as much as 30 mg/cm^2 could be placed in the beam without significantly degrading the neutron production from Target 4.

After the irradiations, the aluminium foils were counted using an HPGe detector system to detect the 1 274 keV emission line of ^{22}Na (2.6-year half-life) to determine the integrated proton flux. These proton flux measurements compared well (within 10%) with the current monitors (3% uncertainty) upstream of the Blue Room (Table 2).

Table 2. Irradiations performed in the Blue Room at WNR during the 2002-2003 run cycle. Each irradiation measured the proton flux with Al foils for ^{22}Na activation and current monitors upstream of the Blue Room.

				Integrated φ_p (p/s)		
Metal foils	**Single or stacked foils**	**Mode of operation**	**E_p (MeV)**	**^{22}Na activation**	**Current monitor**	**Ratio of ^{22}Na to monitor**
				1.76×10^{13}	1.63×10^{13}	1.08 ± 0.09
Ta	stacks of 3	parasitic	800	1.42×10^{13}	1.32×10^{13}	1.08 ± 0.05
Au	stacks of 3	parasitic	800	2.38×10^{13}	2.32×10^{13}	1.03 ± 0.05
W	stacks of 3	parasitic	800	2.41×10^{13}	2.48×10^{13}	0.972 ± 0.049
W, Ta, Au	singles	sole use	800	1.83×10^{13}	1.72×10^{13}	1.06 ± 0.05

Results

Each foil was counted by a Si-charged particle semi-conductor detector in vacuum to measure ^{148}Gd production. Gadolinium-148 alpha emission occurs at 3.183 MeV and the α-particle loses up to 2.5 MeV of its energy, passing through as much as 3 μm of foil thickness before depositing its remaining energy in the detector [18]. Thus a broad, level α peak was expected in the range of about 1.0-3.2 MeV, assuming that ^{148}Gd is evenly created throughout the thickness of the foil.

A wide energy range of β and γ particles from various radio-nuclides were emitted from the foils and deposited a portion of their energy in the detector. This complicated the α counting since the lower energy portion of the α peak was superimposed on the β + γ background. One way to solve this problem was to place a sufficiently thick piece of aluminium foil in front of the irradiated foil to block all α's from reaching the detector so that only β + γ particles were detected. The β + γ spectrum could then be subtracted from the combined $\alpha + \beta + \gamma$ spectrum to produce a clean α peak. Representative charged-particle spectra of tungsten and tantalum foils irradiated at 800 MeV are shown in Figure 3 and Figure 4. The separation between the ^{148}Gd α peak and the $\beta + \gamma$ spectrum is distinct for tantalum, but not for tungsten and gold. In the case of tungsten and gold, two separate counts were used to produce the α spectra – one bare foil to measure the $\alpha + \beta + \gamma$ spectrum and one with a thin Al α absorber in front to measure the $\beta + \gamma$ spectrum. The number of counts in this $\beta + \gamma$ spectrum could then be subtracted from the combined $\alpha + \beta + \gamma$ spectrum to produce the α spectrum.

Table 3 summarises the cumulative ^{148}Gd production measurements as well as previous measurements using CEM2k+GEM2 and Bertini for W, Ta and Au. The production cross-sections measured at 600 MeV were 15.2±4.0, 8.31±0.92 and 0.591±0.155 for Ta, W and Au, respectively. The average production cross-sections measured at 800 MeV were 28.6 ± 3.5, 19.4 ± 1.8 and 3.69 ± 0.50 for Ta, W and Au, respectively. The average measurement for W at 800 MeV was 18% higher than the previous measurement by Henry and the average for Au at 800 MeV was 2% less than the previous measurement by Rejmund, *et al*. Theoretically, the Bertini model better predicted the ^{148}Gd production than the CEM2k+GEM2 model. Results using the Bertini model ranged from 2-25% of the Ta and W measurements and were 35-50% higher than the Au measurements. The CEM2k+GEM2 predictions were higher than the measurements by a factor of two to three. The comparison of Bertini and CEM2k+GEM2 was for Ta and worst for Au. This was possibly due in part to Ta being closer in nucleon number to Gd, compared with W and Au, and thus it being easier to predict ^{148}Gd from the spallation of Ta.

Figure 3. Charged particle spectrum of W7 from the 800 MeV stacked foil irradiation. Counting time was 3 days.

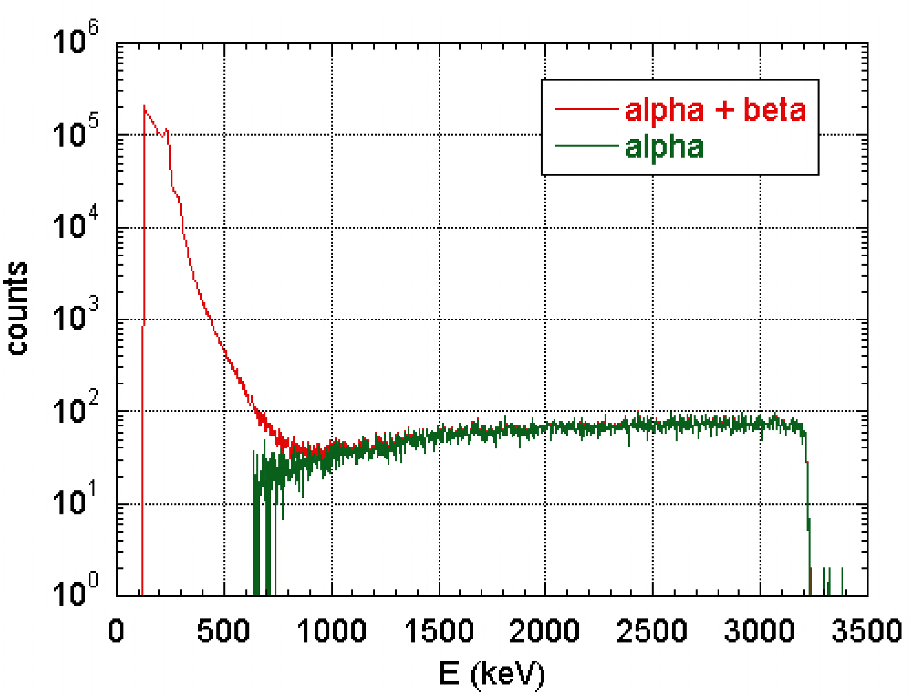

Figure 4. Charged particle spectrum of Ta5 from the 800 MeV stacked foil irradiation. Counting time was 2 days.

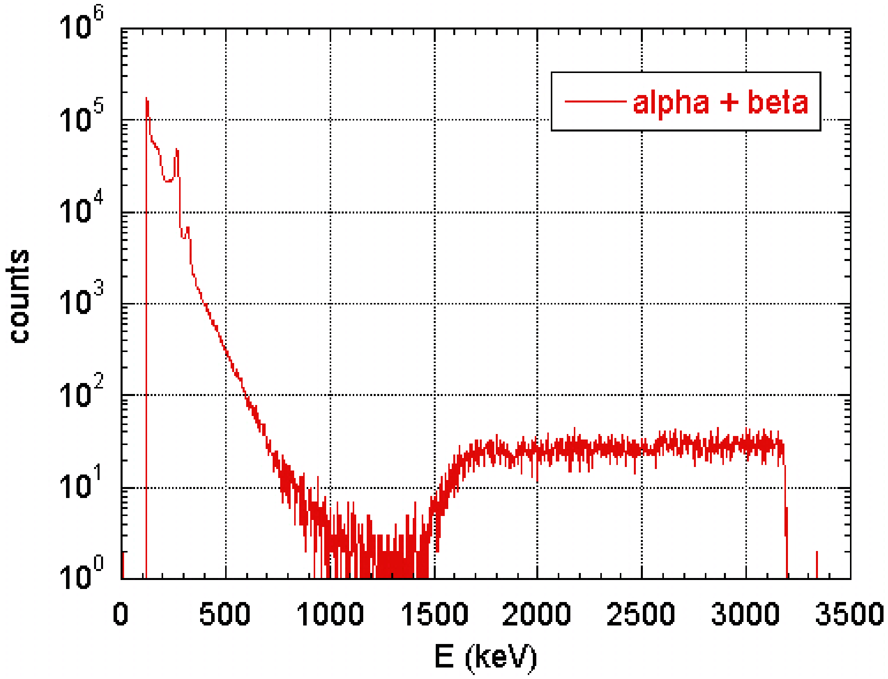

Table 3. Cumulative ^{148}Gd production cross-section measurements and comparisons to theoretical predictions and previous measurements

	Energy	Foil	^{148}Gd cumulative production cross-section (mb)			
			Current	Previous	Theoretical	
Target	(MeV)	set-up	measurement	measurement	CEM2k+GEM2	Bertini
Ta	600	stacked	15.2 ± 4.0		29.4 ± 0.2	15.5 ± 0.2
	800	stacked	29.7 ± 7.6		45.6 ± 0.3	24.4 ± 0.3
		single	27.6 ± 1.7			
		single	28.6 ± 7.3			
W	600	stacked	8.31 ± 0.92		21.6 ± 0.3	10.9 ± 0.2
	800	stacked	19.5 ± 1.2	16.4 ± 0.8[5]	41.4 ± 0.4	20.9 ± 1.6
		single	18.0 ± 1.1			
		single	20.7 ± 5.3			
Au	600	stacked	0.591 ± 0.155		1.41 ± 0.04	0.929 ± 0.049
	800	stacked	3.86 ± 0.98	3.74 ± 0.19[17]	12.9 ± 0.1	7.23 ± 0.14
		single	3.52 ± 0.22			

Conclusions

Measuring the ^{148}Gd production cross-section from protons on tungsten, tantalum and gold is of great benefit to the spallation neutron source community. A better estimate of the ^{148}Gd yield, and as a result, a better estimate of the dose burden, might extend the irradiation lifetime of spallation targets. A series of thin-foil irradiations were completed with 600 and 800 MeV protons on tungsten, tantalum, gold and aluminium. The ^{148}Gd production cross-section measurements for tungsten and gold agreed well with previous measurements. Theoretical predictions using the Bertini model agreed more than when using the CEM2k+GEM2 model, and all predictions came within a factor of two to three.

REFERENCES

[1] *DOE Technical Standard*, DOE-STD-1027-92 (1992).

[2] Bull, J.S., *et al.*, *LANL Report*, 53-BIO-004, Rev. 2 (2000).

[3] Bull, J.S., *LANL Internal Report*, CN-LANSCEFM-00-001 (2000).

[4] Quintana, D.L., *et al.*, *ANS Proc. 4th Intl. Top Mtg. Nucl. App. Acc. Tech.*, 405-414 (2000).

[5] Henry, E.A., K.J. Moody, *APT Internal Report*, LLNL (1999).

[6] Mashnik, S.G., *et al.*, *LANL Reports*, LA-UR-02-0608 (2002); LA-UR-03-2261 (2003).

[7] Waters, L.S., *et al.*, *LANL Report*, LA-CP-02-408 (2002).

[8] Tobailem, J., *Report*, CEA-N-1466 (5), 1981.

[9] Morgan, G.L., *et al.*, *Nucl. Inst. Meth.*, B211, 297-304 (2003).

[10] Michel, R., *et al.*, *Nucl. Inst. Methods*, B103, 183-222 (1995).

[11] Taddeucci, T.N., *et al.*, *Phys. Rev.*, C55, 1551-1554 (1997).

[12] Heydegger, H.R., *et al.*, *Phys. Rev.*, C14 (4), 1506-1514 (1976).

[13] Krupnyi, G.I., D.V. Snitko, A.A. Yanovich, *Atomic Energy*, 89 (5), 2 939-941.

[14] Vonach, H., *et al.*, *Phys. Rev.*, C55 (5), 2458-2467 (1997).

[15] Webber, W.R., J.C. Kish, D.A. Schrier, *Phys. Rev.*, C41 (2), 547-565 (1990).

[16] Raisbeck, G.M., F. Yiou, *Phys. Rev.*, C9 (4), 1385-1395 (1974).

[17] Rejmund, F., *et al.*, *Nucl. Phys.*, A683, 540-565 (2001).

[18] Ziegler, J.F., J.P. Biersack, *SRIM version 2000.40* (2000); http://www.srim.org.

THE PISA EXPERIMENT: SPALLATION PRODUCTS IDENTIFIED BY BRAGG CURVE SPECTROSCOPY

F. Goldenbaum[1], V. Bollini[1], A. Bubak[1,2], A. Budzanowski[3], J. Cugnon[4], D. Filges[1], S. Förtsch[5], A. Heczko[6], H. Hodde[7], L. Jarczyk[6], B. Kamys[6], M. Kistryn[3], St. Kistryn[6], St. Kliczewski[3], J. Kisiel[2], A. Kowalczyk[6], P. Kulessa[1], H. Machner[1], A. Magiera[6], W. Migdal[6], K. Nünighoff[1], H. Ohm[1], N. Paul[1], B. Piskor-Ignatowicz[6], K. Pysz[1,3], Z. Rudy[6], R. Siudak[1,7], E. Stephan[2], D. Steyn[5], M. Wojciechowski[6], W. Zipper[2]
[1]Institut für Kernphysik, Forschungszentrum Jülich GmbH, Germany
[2]University Silesia, Katowice, Poland
[3]Institute of Nuclear Physics, INP-PAN Krakow, Poland
[4]University de Liège, Belgium
[5]IThemba LABS Faure, South Africa
[6]Jagellonian Univ. Krakow, Poland
[7]University Bonn, Germany

The PISA collaboration

Abstract

In the framework of spallation neutron sources and accelerator-driven systems, the international PISA (Proton-induced Spallation) collaboration has initiated measurements of total- and double-differential cross-sections for products of spallation reactions in a wide range of target nuclei (C-U) at the COSY proton accelerator in Jülich (Germany). The purpose is to study secondary particle production created in structural, window and target materials via proton beams up to 2.5 GeV of incident kinetic energy. Residual nuclei [H, He up to intermediate mass fragment (IMF)] production cross-sections are of great importance for estimating the damage to target and structure materials involving the planned spallation neutron sources, given that the lifetime of window and target materials is directly associated to those cross-sections. The demand for reliable theoretical predictions on production cross-sections is by no means satisfied by the models and codes that are available today. In this context, it is essential that reliable and comprehensive experimental data exist (especially for p energies beyond 1 GeV), which can serve as benchmarks for code development and validation. Data taken via Bragg curve spectroscopy and silicon detector telescopes for the reaction 1.9 GeV p + Ni(Au) will be discussed. Rather small lower detection thresholds involving Bragg Curve Detectors (BCDs) at ~0.5 MeV/nucleon were realised. With cooled silicon detectors, an energy resolution of about 0.4% was achieved and using BCDs excellent mass identification was obtained for all measured fragments from helium to silicon (e.g. $2 \leq Z \leq 14$). Kinetic energy spectra and angular distributions of emitted light ions and intermediate mass fragments will be shown.

Objective of the experiment

The experimental programme of the PISA project strives to measure total- and double-differential cross-sections for products of spallation reactions in a wide range of target nuclei (C-U), which is induced by protons of energies between 100 MeV and 2 500 MeV. These cross-sections and the quantitative knowledge on the interaction of medium- and high-energy protons with atomic nuclei are important for the following:

- Providing an extensive set of benchmark data in the GeV incident *p* energy range where few and divergent data exist [1,2,3].
- Understanding the complex reaction mechanism [3,4] via a comprehensive and systematic description of all nuclear reactions and measurement of kinetic energies as well as angular distributions of the ejectiles.
- Testing and increasing the reliability of physical models [2], which describe both the fast intra-nuclear cascade (INC) phase and the subsequent statistical decay from an equilibrated or thermalised hot nucleus.
- Developing new models for the description of highly energetic composite particles (there exist no models capable of reliably predicting production cross-sections, energy spectra or angular distributions).
- Planning and construction of high-intensity neutron spallation sources [6-10], given that the production cross-sections are of particular interest for studying radiation damage in target, window and structural materials. For example, helium is known to destroy the mechanical strength of solids, which limits the lifetime of both window and target (if solid). The production of tritium, which is a radioactive gas of considerable toxicity, has bearing on radiation safety provisions.
- Providing the Li, Be and B data for proton-induced reactions on light targets (up to Fe), which are of crucial importance for understanding the anomalous abundance of light elements in the cosmic rays (compared to the solar system) and astrophysical questions of nucleo-synthesis of light nuclei [11,12].

Regarding the dynamics of nuclear reactions, the following issues are not yet fully understood:

1. The approach to thermal equilibrium [3].
2. Competition between the sequential and simultaneous emission of fragments [13,14].
3. The production mechanism of intermediate mass fragments (IMF) and its relation to possible liquid-gas phase transition [15].
4. Expansion of the nucleus during excitation and subsequent decay [16].

The mass dependence of production cross-sections (for a full range of targets from carbon to uranium) should shed light on the competition of various mechanisms of interaction for protons with nuclei. It should also fill the current void of systematic data on the evolution of the production process as a function of bombarding energy and decaying system mass. Therefore, a primary task of the PISA investigations is the determination of various IMF yields in their full kinetic energy range for several targets and incident proton energies. The PISA set-up, which allows for rather low (≤ 1 MeV/nucleon) energy thresholds, is an excellent experimental detection system.

Experimental set-up

Each of the eight detection arms (see Figure 1) in the PISA experiment consists of the following: two multi-channel plates (MCP) working as "start" and "stop" detectors for the time-of-flight measurement; a BCD [17] followed by three silicon detectors of 100, 300 and 4 900 μm thicknesses (for particle identification using ΔE-E techniques and kinetic energy measurement of intermediate-mass spallation products); and a set of double-layer scintillation detectors [fast and slow (phoswich)]. The purpose of the latter is to identify light-charged vaporation and spallation products such as *p*, *d*, *t* and He. [Currently, only the most forward detection arm (15°) and the most backward detection arm (120°) are mounted.) It will be shown that the TOF plus BCDs provide identification of light-heavy ions with masses up to 20-30 and kinetic energy starting from less than 1 MeV/amu.

Figure 1. Upper panel: Scattering chamber of PISA (October 2002) with the two full detector arms mounted at 15° and 120° and equipped with Bragg curve (BG), channel plate (inside chamber) and phoswich (PH) detectors. Lower panel: A detection arm in detail.

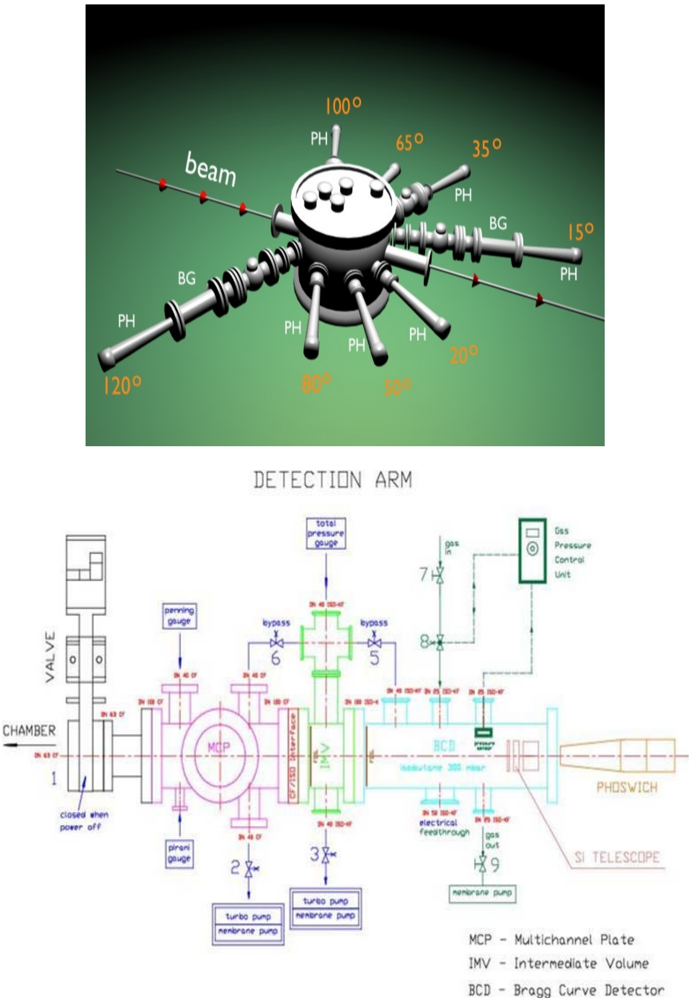

Channel-plate detectors

The telescope for the time-of-flight measurement is composed of two MCP detectors in the Chevron configuration. The channel plates were manufactured by the Galileo Corporation whereas we designed a suitable housing ourselves [18] (see the left panel of Figure 2).

The particles, which are to be registered, pass through the 20-µg/cm^2 thick carbon foil and knock out some δ electrons. These electrons are accelerated towards the MCP in the electric field between the foil, accelerating grid and second channel plate. The particular voltages are chosen to obtain the highest multiplication factor in the channel plates (10^7) and the best signal-to-noise ratio. Experiments showed that our MCPs performed best at voltages of 2 000 V (between the first and second channel plates) and ~400 V (between the carbon foil and accelerating grid).

The timing properties of MCPs were measured at the accelerator of the Heavy Ion Laboratory in Warsaw, Poland where a few low intensity beams of various ions passed through a telescope of two such assemblies (spaced by 27.4 cm). The measured time-of-flight resolution is smaller than 400 ps.

Figure 2. Left panel: Assembly for particle detection with the multi-channel plate detector. Right panel: BCD used for spallation studies of the COSY internal proton beam.

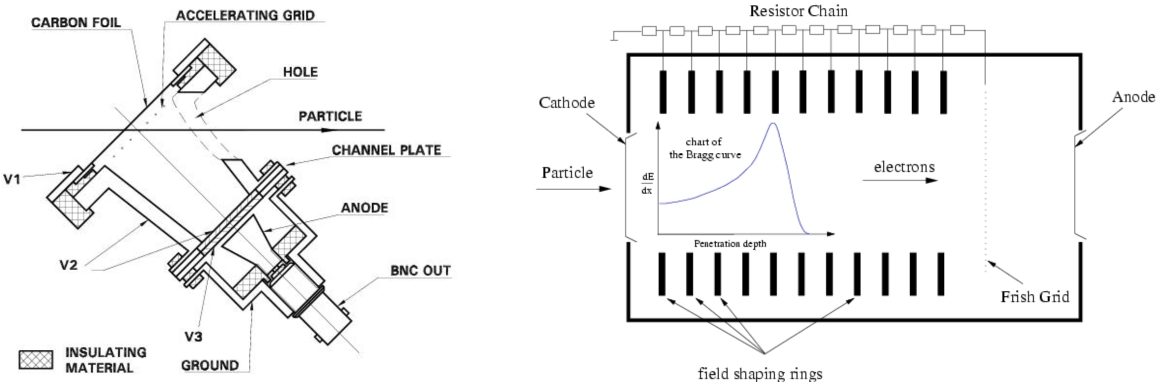

The Bragg curve detector

After successful utilisation of Bragg curve spectroscopy to identify highly-ionised particles [19,20], several detectors were built and used for various applications, which exploit Bragg curve characteristics. BCDs have allowed for the detection of fragments with high precision and over a broad range of nuclear charges with low registration thresholds [21-26]. This has been demonstrated in former experiments involving fragment production cross-sections for carbon with GeV proton beams [27,29].

Ref. [30] and a recently accepted paper [31] present the design of the BCD employed here and preliminary results of the first PISA test experiment. The design features of our BCD are very similar to those in Ref. [26] and references mentioned therein. Advantages (e.g. resistivity to radiation damage and insensitivity to minimally ionising particles) of BCDs compared to alternative detectors (e.g. gas-semiconductor ionisation chamber, solid state detectors, CsI(Tl) crystal scintillators) are outlined in Ref. [26]. The detector, as shown in the right panel of Figure 2, is an ionisation chamber with a gas volume of 22 cm in length and 5 cm in diameter. The detector is sealed off at its entrance by a 3-µm thick carbon-coated Mylar foil supported by a wire mesh, which will be operated by an anode (printed board) at ground potential and at the back end. The Frish grid, which defines the ionisation sampling section (2 cm from the anode), is made of 20 µm gold-plated tungsten wires with 1 mm spacing. The voltage (>1 800 V) between the Frish grid and the entrance window is divided by a resistor chain, which is connected to nine field-shaping rings in order to maintain a homogeneous electric field over the active-detector volume. The particles enter through the cathode and leave an ionisation track parallel to the electric field.

For charged, non-relativistic particles, the Bethe-Bloch formula and its specific energy losses in a given medium can be simplified to $-dE/dx \sim cZ^2/E$, where Z, E are the atomic number and kinetic energy of the detected particle and c contains all relevant constants together with the quantities characterising the detector medium.

Since the energy loss per single collision is small, dE/dx increases slowly along the particle path. Only when the remaining energy is small does dE/dx increase rapidly, forming the Bragg peak (BP). The electrons along the track drift through the grid and are viewed as an anode current. The output signal from the anode as a function of time is proportional to the energy-loss distribution of the detected particle along its path through the detector. The atomic number of the incident-detected particle is therefore related to the maximum pulse height (corresponds to the BP) and the total kinetic energy of the particle (obtained from the integration over the total output signal). The detector is filled with iso-butane and is operated at a pressure of about 300 mb. Since iso-butane is characterised by a 30% lower effective-ionisation potential compared to argon [32] or the P10 mixture (90% argon, 10% methane), the number of released primary electrons is increased. Bragg curve spectroscopy principals are illustrated in the right panel of Figure 2, which shows a typical output signal of a BCD.

In addition to the usual charge identification by Bragg spectroscopy in the PISA experiment, an isotope separation for detected particles was achieved for elements up to nitrogen. The basic experimental information regarding the BCD was received from a VME-flash ADC module (CAEN model V729A, 40 MHz, 12 bit), which allowed for the data processing of about 1 000 sample Bragg curves per second. When the particle was stopped in the active chamber, apart from the measured TOF, the certain values were calculated from the pulse shape. The values include: the integral of the specific ionisation over the track (total kinetic energy E of the particle); the maximum of the BP, which was derived from the maximum of the specific ionisation of the ion (BP proportional to Z); the duration R (corresponding to the range in the BCD gas volume); and a partial integral from the specific ionisation at the beginning of the track ($\sim\Delta E/dx$). Isotope identification was performed by using the correlations between the parameters R, E, ΔE and TOF. Details on the BCD design can be found in Ref. [31]. For energies of emitted particles as low as 0.5 MeV/nucleon, the BCD is capable of measuring elemental distributions for fragments ranging from $Z = 2$ up to Si.

Results of the PISA experiment

COSY internal beam experiments allowed for the investigation of reactions induced by protons in thin targets (50-200 µg/cm^2), thus enabling the generation of cross-sections without the uncertainties (e.g. absorption and energy loss) that result from the propagation of reaction products in the target material. The multiple circulation of the beam in the COSY ring is used to compensate for the small reaction rate of beam protons with the thin target and to allow for measurement with optimal counting rates (1 000-2 000 s^{-1}) for a total intensity in the ring of about 10^{10}. The constant reaction rate is achieved by a negative back-coupling between the counting rate and the degree of overlapping of the proton beam with the surface of the target, which occurs via the controlled shifting of the beam in respect to the axis of the COSY beam line. Therefore, such an internal beam experiment offers a unique possibility to efficiently and precisely measure the cross-sections in thin targets.

Figure 3. Identification spectrum of emitted fragments in forward- (15°) and backward-mounted (120°) detection arms following 1.9 GeV p + Ni collisions

The maximum of the BP versus energy deposited in the detector. The helium ions are not highly visible in this representation but Li, Be and C up to Si lines can be distinguished. In addition, there are visible points in the area where Al and Si ions are expected. The identified products are indicated.

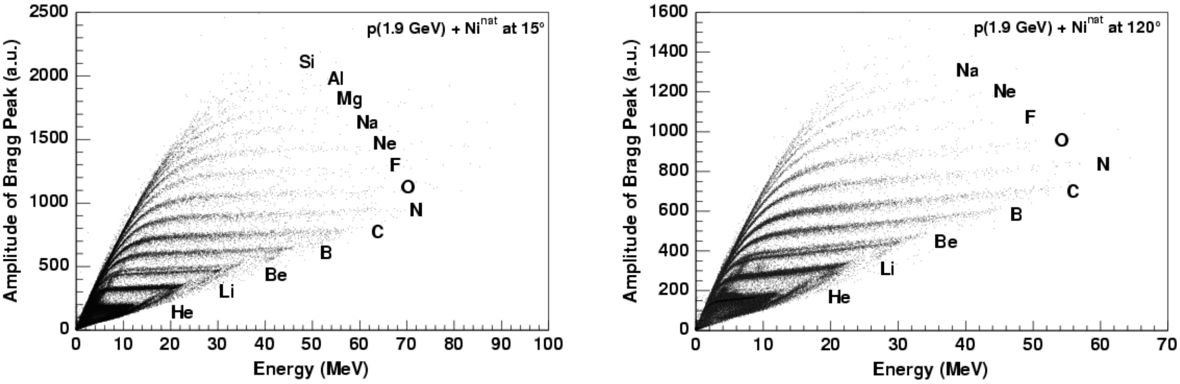

In a recently performed experiment (1.9 GeV p + Ni[Au]) involving BCDs, we observed an unambiguously identified charge of fragments from helium up to silicon (i.e. up to $2 \leq Z \leq 14$) and only a small amount of heavy fragments prevented us from finding the upper limit of the charge for emitted fragments. Figure 3 illustrates this phenomenon by showing the identification spectrum (BP versus energy E deposited in the gas volume) for the reaction 1.9 GeV p + Ni at the fragment emission angles of 15° (left panel) and 120° (right panel). Events with the same nuclear charge are located in branches parallel to the energy (range) axis and correspond to the particles stopped inside the BCD. The distinction of the charge is visible in the ranges of $2 \leq Z \leq 14$ and $2 \leq Z \leq 11$ at 15° and 120°, respectively. Most energetic particles with $Z \leq 6$ at 15° and $Z \leq 4$ at 120° have a range larger than the length of the BCD. This effect is quite visible in Figure 3, where the branch returns beyond the punch-through points (decreasing the energy deposited inside the BCD and the amplitude of BP). The slight slope in the BP amplitude, as a function of energy, was reported in earlier works and is caused by re-combination of the electrons and inefficiency of the Frish grid [27].

The rather good separation of elements (here shown for $3 \leq Z \leq 12$) is demonstrated in Figure 4, which is essentially a projection of the data in Figure 3 onto the axis denoting the Bragg peak. The resolution of charge distribution ΔZ was found to be between 10% and 12% per amu for peaks where isotopes were not distinguished, and 14% for Be where the isotopical structure was visible.

The measured range of kinetic energies is limited by lower- and upper-registration thresholds as demonstrated in the energy distributions shown for the reaction in Figure 5 (ejectiles emitted at 120° and 15° angles). The lower threshold is related to the energy losses of the emerging fragments in the target material and the BCD window foils to be penetrated. In Figure 3, the merging of the loci formed by the IMFs at the lowest energy (less than 1 MeV/nucleon) results from particles with energies that are too insufficient to form a BP in the counter. The upper registration threshold results from the finite active depth of the BCD, which mainly depends on the used gas and its pressure. The measured energy depends on the registered isotope and it is different for the forward and backward angles as Figure 5 illustrates for the reaction 1.9 GeV p + Ni. Note that the kinetic energy of particles emitted is larger in the case of forward angles than backward angles. Even for relatively heavy ejectiles (^{11,12,13,14}C and ^{13,14}N) emitted in a forward direction at 15° (shown in Figure 5, right panel), the kinetic energies were slightly higher than

Figure 4. Separation of elements by projection of Figure 3 (1.9 GeV p + Ni, 15°) onto the axis representing the BP. To effect the projection, a cut in the kinetic energy of particles was performed at 1.3 ≤ E_{kin} ≤ 3 MeV/N.

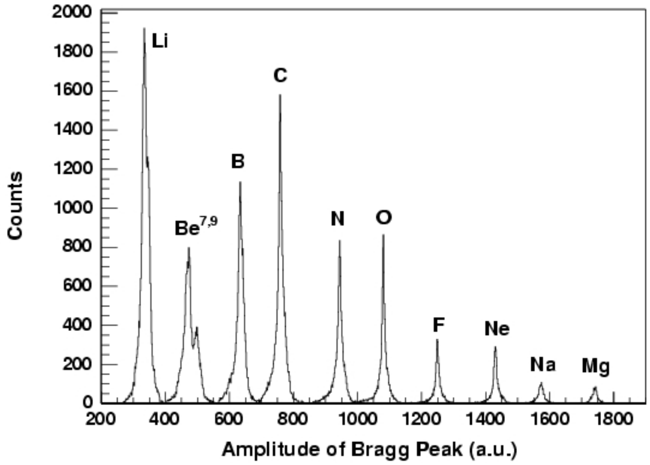

Figure 5. Left panel: Energy of different isotopes as identified by Figure 3 (1.9 GeV p + Ni, 120°) in combination with information from TOF. The spectra shown are neither corrected for detection efficiency nor normalised to absolute cross-sections. Right panel: Same as left but for 15°.

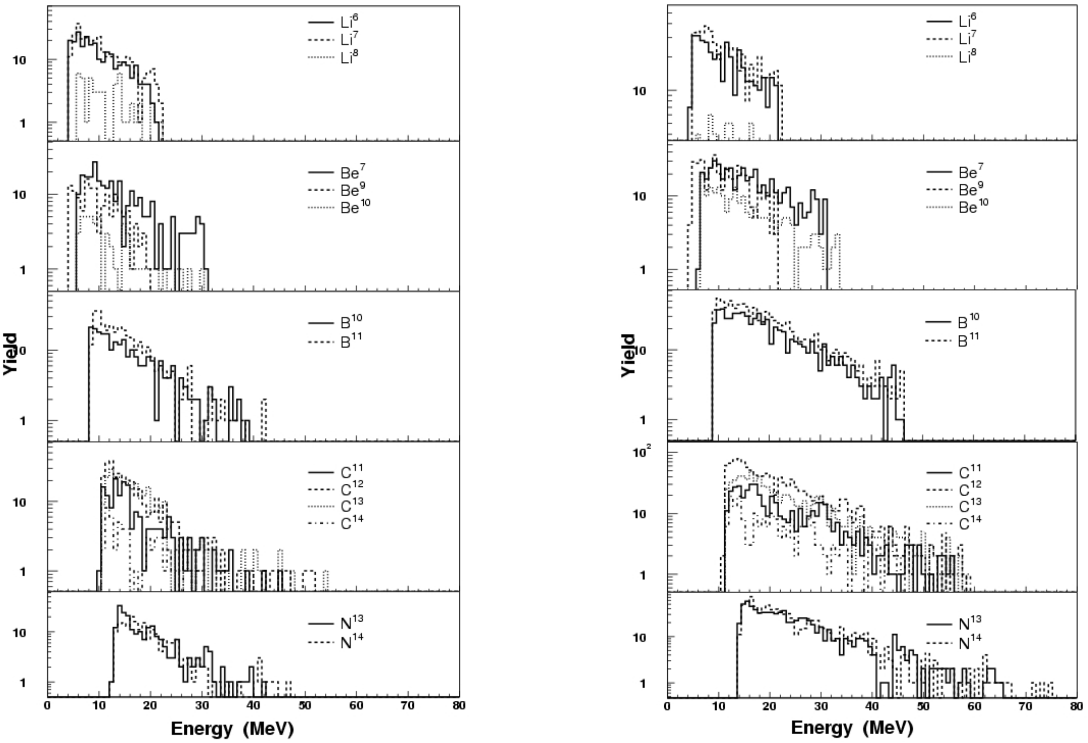

for particles emitted in a backward direction (Figure 5, left panel). The energy spectra shown are preliminary, since thus far no correction for detection efficiency has been considered and the absolute normalisation of the double differential cross-sections is still lacking. The Coulomb threshold within the energy spectra of fragments produced in p + Ni and p + Au collisions is expected at well above the registration threshold of the BCD presented in this work, $E_{kin} \approx$ 2-3 MeV/nucleon. Consequently, in using the BCD, the maximum of the kinetic energy spectra due to the Coulomb barrier was clearly identified.

The fragment energies were corrected for energy loss via foils in front of the BCDs and entrance windows. The low energy cut-off arises from detector thresholds (~0.5 MeV/u) and energy loss via the foils. The correction for the efficiency of MCPs as a function of mass and energy was taken into account.

It is observed in Figures 5 and 6 that the slope of the energy spectra at 120° is steeper than at 15°. This indicates that the temperature extracted from the slope of the energy spectra should decrease as the detection angle increases. The fragment energy spectra were therefore fitted using a moving-source fit [28], which allows for an estimate of the temperature *T*. Example energy spectra of ^{10}B, ^{11}B, ^{13}N and ^{14}N isotopes and moving-source fits are shown in Figure 6. Extracted *T* values are around 4-7 MeV for backward and forward angles [28].

Figure 6. Energy spectra of ^{10}B, ^{11}B, ^{13}N and ^{14}N isotopes from 1.9 GeV p + Ni reaction observed at 15° and 120°

The identification of the isotopes was done by means of BCD spectroscopy combined with the time-of-flight method. The spectra shown are corrected for MCP efficiency. The solid lines represent moving-source fits.

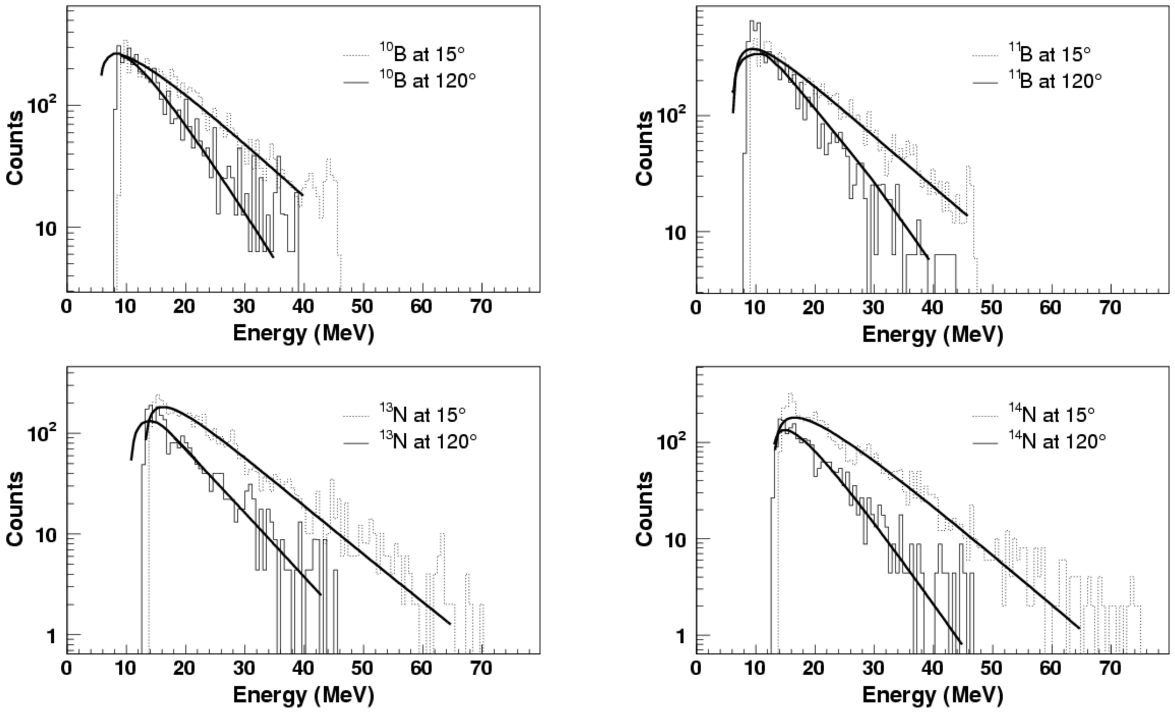

After selecting an element of given *Z* in the Bragg curve identification spectrum (Figure 3), an isotope separation or mass identification of the emitted fragments is possible due to different time-of-flights for different isotopes. The isotope separation was done by combining the information from MCPs (time-of-flight) and BCD (energy deposited inside the BCD), allowing for the separation of the following isotopes: ^{6}Li, ^{7}Li, ^{8}Li-^{7}Be, ^{9}Be, ^{10}Be-^{10}B, ^{11}B-^{11}C, ^{12}C, ^{13}C, ^{14}C, ^{13}N and ^{14}N. Note that due to the lack of ^{8}Be an isotopic separation is possible for ^{7,9}Be ions, even using the information provided in Figure 3 alone (i.e. without TOF knowledge).

Representatives of mass identification for isotopes up to ^{14}N are shown in Figure 7 for the 15° case.

Figure 7. The mass identification spectra for the 1.9 GeV p + Ni reaction products measured at 15°, which were obtained via the projection of mass distributions along the centres of gravity of ^{7}Li, ^{9}Be, ^{11}B, ^{11}C and ^{14}N

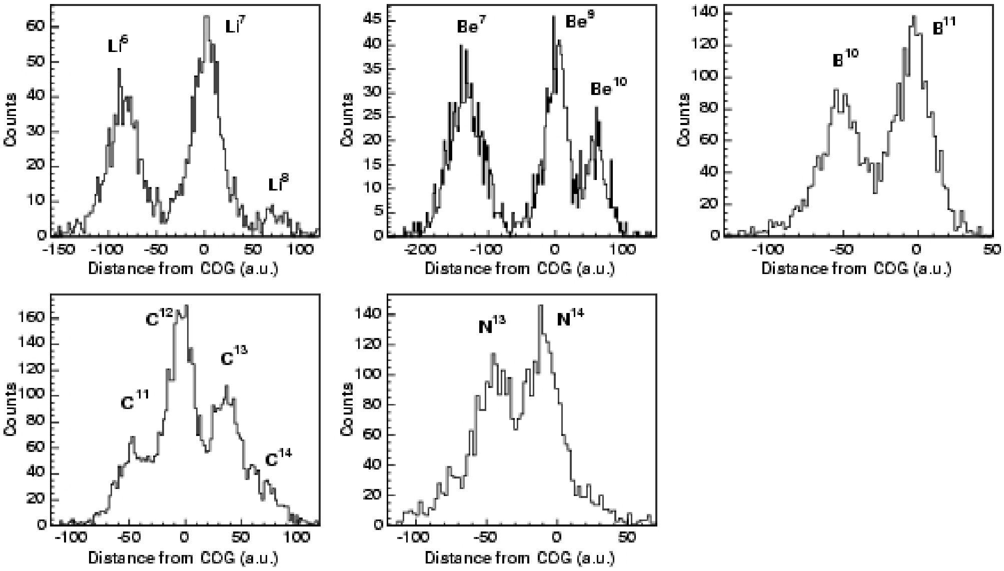

The second method of isotope identification consists of using Si-detector telescopes cooled down to -10°C. In fact, the telescope at 35° and 100° with respect to the proton beam consisted of the following four Si detectors: 50, 100, 400 and 3 000 µm and 20, 50, 100 and 400 µm, respectively. Excellent mass identification of all simultaneously measured fragments from helium to carbon was obtained as shown in Figure 8 for ejectiles emitted from p + Ni collisions at 1.9 GeV and 35°. The yield ratios of ^{7,9,10}Be and ^{8,10,11}B (see Figure 8) roughly reproduce the ones published in Ref. [29].

Figure 8. Mass identification spectrum of ejectiles emitted from p + Ni collisions at 1.9 GeV and 35° with respect to the proton beam

Energy loss of the ejectiles in the first silicon detector (50-µm thick) is plotted versus energy loss in the second silicon detector (100 µm) of the cooled Si telescope. The helium (^{4}He and ^{6}He), lithium (^{6}Li, ^{7}Li, ^{8}Li), beryllium (^{7}Be, ^{9}Be, ^{10}Be), boron (^{10}B, ^{11}B) and carbon (^{11}C, ^{12}C, ^{13}C) ions are well-separated. There are also visible individual points in this part of the figure where N ions are expected.

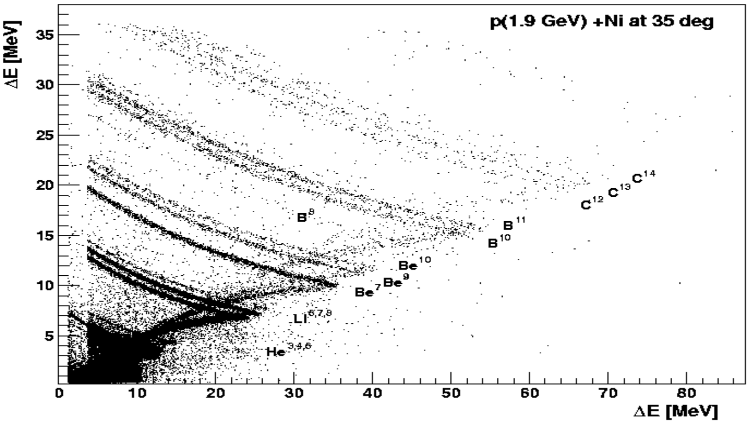

Conclusion

The aim of the current campaign is to check, revise and improve the predictive power of nuclear reaction models for spallation-source and astrophysics-relevant data and to identify existing INC/evaporation code deficiencies. The measurements on intermediate-mass fragments are considered as important experimental benchmark data for the development and testing of reliable new models. These models are capable of describing the emission of composite particles' high-energy component, which is produced in GeV reactions.

The PISA experiment at COSY-Jülich was consulted to validate models on reaction cross-sections, reaction probabilities, charged particle production cross-sections and angular and energy distributions following 1.9 GeV-proton induced reactions on thin C, Ni and Au targets. In summary, the experiment showed that in using the proposed technique, we are able to measure the products of proton-nucleus collisions with Z-identifications up to $Z = 16$ and to identify isotopes for masses up to 13-14 with particularly low energy thresholds of 0.5 MeV/A. The next beam time for PISA is requested for early 2004. Thinner films for the entrance windows are desired in order to reduce the energy loss. The most restrictive model tests are provided by data from exclusive experiments. Therefore, coincidence measurements (high-energy protons with other charged particles) are planned. A comprehensive comparison of the experimental data with the Monte Carlo predictions will be the subject of a forthcoming publication.

Acknowledgements

The excellent proton beam at COSY and the assistance provided by the COSY team were much appreciated. The project described in greater detail in Refs. [17,18,31,33] is supported by the EU-LIFE programme, the BMBF-Verbundforschung, the EU HINDAS project FIS5-1999-00150 and the EU TMR project ERB-FMRX-CT98-0244.

REFERENCES

[1] Enke, M., *et al.*, "Evolution of a Spallation Reaction: Experiment and Monte-Carlo Simulation", *Nucl. Phys.*, A657, 317 (1999).

[2] Filges, D., F. Goldenbaum, Y. Yariv, eds., "Models and Codes for Spallation Neutron Sources", *Proceedings of the 5th Workshop on Simulating Accelerator Radiation Environments (SARE-5)*, ISSN 1433-559X, ESS 112-01-T, OECD Headquarters, Paris, France, 17-18 July 2000 (2001).

[3] Herbach, C.M., *et al.*, "Light Particle Production in Spallation Reactions Induced by Protons of 0.8 to 2.5GeV Incident Kinetic Energy", *Proceedings of the International Conference on Nuclear Data for Science and Technology ND2001*, Tsukuba, Japan, Nuclear Data Center, JAERI, Tokai-mura, Naka-gun, Ibaraki-ken, 319-1195, Japan, 7-12 October 2001.

[4] Goldenbaum, F., *et al.*, "Decay Modes Induced by Light Particles", *International Workshop XXVII on Gross Properties of Nuclei and Nuclear Excitations*, Waldemar-Petersen-Haus, Hirschegg, Kleinwalsertal, Austria, 17-23 January 1999, GSI Darmstadt, ISSN 0720-8715, pp. 104-115 (1999).

[5] Pienkowski, L., *et al.*, "Vaporization and Multifragmentation in the Reaction 1.2GeV pbar + Cu and Ag.", *Phys. Lett.*, B472, 15 (2000).

[6] Appleton, B., *Proc. ICANS-XIII*, Report PSI 95-02, 814 (1995).

[7] Nagamiya, S., "JAERI-KEK Joint Project on High Intensity, Proton Accelerator", *9th Int. Conf. on Radiation Shielding*, Tsukuba, Int. Congress Center, Japan, 17-22 October 1999.

[8] *Spallation Neutron Source SNS*, Status Report, Oak Ridge National Laboratory, USA, See the web site http://www.ornl.gov/sns/.

[9] *The ESS Project*, Vol. III, Technical Report, ISBN 3-89336-303-3 (2002).

[10] Goldenbaum, F., D. Filges, "The ESS Future Project: Research with Neutrons, MESON2002", *7th International Workshop on Meson Production, Properties and Interaction of Mesons*, Cracow, Poland, 24-28 May 2002, World Scientific, L. Jarczyk, A. Magiera, C. Guaraldo, H. Machner, eds., ISBN 981-238-160-0, pp. 269-280 (2002).

[11] Reeves, H., *Rev. Mod. Phys.*, 66, 193 (1994).

[12] Silverberg, R., C.H. Tsao, *Phys. Rep.*, 191, 351 (1990).

[13] Botvina, A.S., D.H.E. Gross, "Sequential or Simultaneous Multifragmentation of Nuclei", *Phys. Lett.*, B344, 6 (1995).

[14] Moretto, L.G., *et al.*, "Are Multifragment Emission Probabilities Reducible to an Elementary Binary Emission Probability", *Phys. Rev.*, 74, 1530 (1995).

[15] Pochodzalla, J., *et al.*, "Probing the Nuclear Liquid-gas Phase Transition", *Phys. Rev. Lett.*, 75, 1040 (1995).

[16] Botvina, A.S., A.S. Iljinov, I.N. Mishustin, J.P. Bondorf, R. Donangelo, K. Sneppen, "Statistical Simulation of the Break-up of Highly Excited Nuclei", *Nucl. Phys.*, A475, 663 (1987); *Nucl. Phys.*, A448, 753 (1986); *Nucl .Phys.*, A444, 460 (1985); *Nucl. Phys.*, A443, 321 (1985).

[17] The PISA Coll., *IKP/COSY Annual Report 1999*, Jül-3744, ISSN0944-2952, p. 175ff (1999).

[18] The PISA Coll., *IKP/COSY Annual Report 2000*, Jül-3852, ISSN0944-2952, p. 172ff (2000).

[19] Schiessl, Ch., *et al.*, *Nucl. Instr. Meth.*, 192, 291 (1982).

[20] Gruhn, C.R., *et al.*, *Nucl. Instr. Meth.*, 196, 33 (1982).

[21] McDonald, R.J., *et al.*, *Nucl. Instr. Meth.*, 219, 508 (1984).

[22] Moroni, A., *et al.*, *Nucl. Instr. Meth.*, 225, 57 (1984).

[23] Westfall, G.D., *et al.*, *Nucl. Instr. Meth.*, A238, 347 (1985).

[24] Kotte, R., *et al.*, *Nucl. Instr. Meth.*, A257, 244 (1987).

[25] Kotov, A.A., *et al.*, *Exp. Technik der Phys.*, 36, 6, 513 (1988).

[26] Ochiishi, H., *et al.*, *Nucl. Instr. Meth.*, A369, 269 (1996).

[27] Andronenko, L.N., *et al.*, *Nucl. Inst. Meth.*, A312, 467 (1992).

[28] Bubak, Arek, PhD thesis, To be published (2003).

[29] Andronenko, L.N., *et al.*, *Nucl. Phys. Inst.*, Gatchina, Preprint 2217, NP-3-1998 (1998).

[30] Budzanowski, A., *et al.*, *IKP/COSY Annual Report 1999*, p. 176.

[31] Barna, *et al.*, *Nucl. Instr. Meth.*, A519, 610-622 (2003).

[32] Sauli, F., *Principles of Operation of Multiwire Proportional and Drift Chambers*, CERN 77-09 (1977).

[33] The PISA Coll., *IKP/COSY Annual Report 2001*, Jül-3978, ISSN0944-2952, p. 210ff (2001).

EXPERIMENTAL STUDY OF INDEPENDENT AND CUMULATIVE PRODUCT YIELDS IN ^{208,207,206,nat}Pb AND ^{209}Bi TARGETS IRRADIATED WITH 0.04-2.6 GeV PROTONS

Yu.E. Titarenko, V.F. Batyaev, V.M. Zhivun, R.D. Mulambetov,
S.V. Mulambetova, S.L. Zaitsev, K.A. Lipatov
Institute for Theoretical and Experimental Physics (ITEP)
B. Cheremushkinskaya 25, 117259 Moscow, Russia

S.G. Mashnik
Los Alamos National Laboratory, Los Alamos, NM 87545, USA

Abstract

More than 5 000 independent and cumulative yields of radioactive residual product nuclides with lifetimes ranging from 13.2 minutes (^{187}Re) to 31.55 years (^{207}Bi) were measured in ^{208,207,206,nat}Pb and ^{209}Bi thin targets and were irradiated by 0.04, 0.07, 0.10, 0.15, 0.25, 0.4, 0.6, 0.8, 1.2, 1.6 and 2.6 GeV external proton beams from the ITEP U10 accelerator. The ^{27}Al (p,x)^{22}Na reaction was used as a monitor. The experiments were made using the direct gamma spectrometry method based on a Ge detector with a 1.8 keV resolution at a 1 332 keV ^{60}Co gamma line. The measured gamma spectra were processed by the GENIE2000 code. The residual product nuclides were identified and their independent and cumulative yields determined, using the PCNUDAT database and the ITEP-designed SIGMA code.

Introduction

The cross-sections and yields of residual product nuclei are of great importance when estimating such basic radiation-technology characteristics of ADS hybrid facility targets as: total target activity, target “poisoning”, build-up of long-lived nuclides, product nuclide (Po) alpha activity, content of low-pressure evaporated nuclides (Hg), evolution of gaseous reaction products, and production of chemically active nuclides that spoil the corrosion resistance of the facility structure materials.

The present inaccuracy and/or absence of needed cross-sections has resulted in the need for experiments to measure the independent and cumulative yields of radioactive residual product nuclides in thin Pb and Bi samples under 0.04-2.6 GeV proton irradiation [1].

Experiment

The experimental techniques are described in detail in Refs. [2-4]. The actual experiments were performed using mono-isotopic target samples of the following composition: ^{208}Pb (^{206}Pb = 0.87%, ^{207}Pb = 1.93%, ^{208}Pb = 97.2%); ^{207}Pb (^{204}Pb = 0.03%, ^{206}Pb = 2.61%, ^{207}Pb = 88.3%, ^{208}Pb = 9.06%); ^{206}Pb (^{206}Pb = 94.0%, ^{207}Pb = 4.04%, ^{208}Pb = 1.96%); ^{nat}Pb (^{204}Pb = 1.4%, ^{206}Pb = 24.1%, ^{207}Pb = 22.1%, ^{208}Pb = 52.4%); and ^{209}Bi > 99.9%.

The thin ^{208,207,206,nat}Pb and ^{209}Bi targets of 10.5 mm diameter and $\frac{121}{350}$ mg/cm^2 thickness together with aluminium monitors of the same diameter and $\frac{127}{259}$ mg/cm^2 thickness were irradiated using an external beam of ITEP U10 proton synchrotron. The ^{27}Al(p,x)^{22}Na reaction was used as monitor. The proton fluencies ranged from 3.1×10^{13} to 1.4×10^{14} p/cm^2. The produced radionuclides were detected using the direct gamma spectrometry method based on a Ge detector with a 1.8 keV resolution at a 1 332 keV ^{60}Co gamma line. The distances of 40-900 mm between the irradiated target and the Ge detector’s cryostat enabled for the avoidance of spectrometer overload. The height-dependent efficiency of the spectrometer was obtained using analytical expressions of 100-2 600 keV absolute efficiencies, which were determined by measuring the standard gamma sources. The efficiencies discovered allowed us to obtain height factors that were used to normalise all the measured gamma-line intensities to a 40 mm bias height.

Each of the irradiated targets was measured over a period of 3-6 months. The gamma spectra were processed via an interactive mode of the GENIE2000 program, using preliminary results of automatic mode processing. For example, Figure 1 shows measured gamma spectra from two ^{nat}Pb targets, which were irradiated with 2.6 GeV (upper curve) and 0.04 GeV (lower curve) protons. Both spectra were measured after the irradiations at the same cooling time (~6 days). The windows demonstrate examples of resolving multiplets.

The results of processing the gamma spectra of a particular irradiation are compiled into one file, which is the input for the SIGMA code. The SIGMA code identifies the measured gamma lines using the PCNUDAT nuclear decay database and determines the yields (cross-sections) of the produced radionuclides using Eqs. (1-9), which were derived from the three-chain decay scheme (Figure 2).

Figure 1. Gamma spectra from ^{nat}Pb targets irradiated with 2.6 GeV (upper curve) and 0.04 GeV (lower curve)

The spectra were measured after the irradiations at the same cooling time (~140 hours). The lower spectra were multiplied by 0.1 for visual convenience.

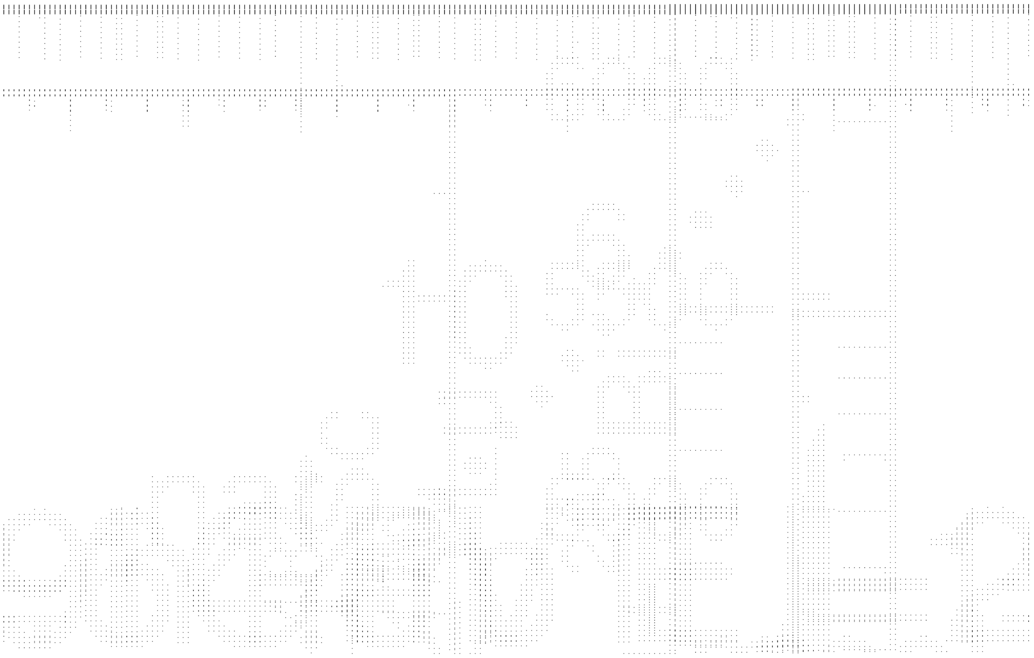

Figure 2. Three-chain decay scheme

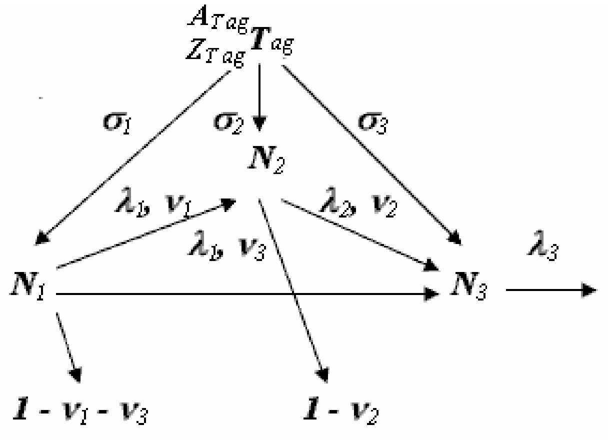

In total, 55 experiments were conducted. The resultant statistics for the measured products are presented in Table 1. The errors of the measured data range from 10-40%. Experimental error arose primarily from the uncertainty surrounding the monitor reaction cross-section, however there were some cases when the errors were dominated by the uncertainty surrounding nuclear decay data and spectra statistics. The data themselves and their graphical representation will be presented in the final technical report of the ISTC Project #2002 and will be uploaded to the EXFOR database.

$$\sigma_1^{cum} = \frac{1}{N_{Tag} \cdot \Phi} \cdot \frac{A_1}{F_1} \tag{1}$$

$$\sigma_1^{cum} = \frac{1}{N_{Tag} \cdot \Phi} \cdot \frac{B_1}{F_1} \cdot \frac{1}{\nu_{12}} \cdot \left(1 - \frac{\lambda_1}{\lambda_2}\right) \tag{2}$$

$$\sigma_2^{ind} = \frac{1}{N_{Tag} \cdot \Phi} \cdot \left(\frac{B_2}{F_2} + \frac{B_1}{F_1} \cdot \frac{\lambda_1}{\lambda_2}\right) \tag{3}$$

$$\sigma_2^{cum} = \sigma_2^{ind} + \nu_{12} \cdot \sigma_1^{cum} = \frac{1}{N_{Tag} \cdot \Phi}\left(\frac{B_1}{F_1} + \frac{B_2}{F_2}\right) \tag{4}$$

$$\sigma_1^{cum} = \frac{1}{N_{Tag} \cdot \Phi} \cdot \frac{C_1}{F_1} \frac{1}{\nu_{13} + \nu_{12} \cdot \nu_{23} \cdot \dfrac{\lambda_2}{\lambda_2 - \lambda_1}} \cdot \left(1 - \frac{\lambda_1}{\lambda_3}\right) \tag{5}$$

$$\sigma_2^{ind} = \frac{1}{N_{Tag} \cdot \Phi}\left[\frac{C_2}{F_2} \cdot \frac{1}{\nu_{23}} \cdot \left(1 - \frac{\lambda_2}{\lambda_3}\right) + \frac{C_1}{F_1} \cdot \nu_{12} \cdot \frac{\dfrac{\lambda_1}{\lambda_2 - \lambda_1}}{\dfrac{\lambda_2}{\lambda_2 - \lambda_1} \cdot \left(\nu_{13} + \nu_{12} \cdot \nu_{23} \cdot \dfrac{\lambda_2}{\lambda_2 - \lambda_1}\right)}\right] \tag{6}$$

$$\sigma_2^{cum} = \sigma_2^{ind} + \nu_{12} \cdot \sigma_1^{cum} = \frac{1}{N_{Tag}\Phi} \cdot \left[\frac{C_2}{F_2} \cdot \frac{1}{\nu_{23}} \cdot \left(1 - \frac{\lambda_2}{\lambda_3}\right) + \frac{C_1}{F_1} \cdot \nu_{12} \cdot \frac{\dfrac{\lambda_2}{\lambda_2 - \lambda_1}}{\dfrac{\lambda_2}{\lambda_2 - \lambda_1} \cdot \left(\nu_{13} + \nu_{12} \cdot \nu_{23} \cdot \dfrac{\lambda_2}{\lambda_2 - \lambda_1}\right)}\right] \tag{7}$$

$$\sigma_3^{ind} = \frac{1}{N_{Tag} \cdot \Phi} \cdot \left[\frac{C_3}{F_3} + \frac{C_2}{F_2} \cdot \frac{\lambda_2}{\lambda_3} + \frac{C_1}{F_1} \cdot \frac{\lambda_1}{\lambda \cdot_3}\right] \tag{8}$$

$$\sigma_3^{cum} = \sigma_3^{ind} + \nu_{13} \cdot \sigma_1^{cum} + \nu_{23} \cdot \sigma_2^{cum} + \nu_{12} \cdot \nu_{23} \cdot \sigma_1^{cum} = \frac{1}{N_{Tag} \cdot \Phi} \cdot \left[\frac{C_1}{F_1} + \frac{C_2}{F_2} + \frac{C_3}{F_3}\right] \tag{9}$$

where $\sigma_1^{cum}, \sigma_2^{cind}, \sigma_2^{cum}, \sigma_3^{ind}$ *and* σ_3^{cum} are independent and cumulative cross-sections; N_1, N_2, N_3 and N_{Tag} are the number of nuclei ${}^{A_{Tag}}_{Z_{ag}}Tag$ in the experimental target; Φ is the average flux of protons; A_1, B_1, B_2, C_1, C_2 and C_3 are the factors defined by experimental point fitting; F_1, F_2 and F_3 are saturation functions; ν_{12}, ν_{13} and ν_{23} are branching factors; and λ_1, λ_2 and λ_3 are decay constants.

Table 1. Total statistics of the measured products from ^{208,207,206,nat}Pb and ^{209}Bi

A dash indicates that the cross-section is still being determined

Energy (GeV)	Yield type	^{nat}Pb	^{208}Pb	^{207}Pb	^{206}Pb	^{209}Bi	Total
2.6	i	16	15	14	14	13	72
	$i_{\Sigma mj}$	16	16	16	16	20	84
	$i_{\Sigma mj+g}$	16	14	14	14	13	71
	c, c^*	123	120	120	120	133	616
1.6	i	17	17	15	15	13	77
	$i_{\Sigma mj}$	16	17	17	17	18	85
	$i_{\Sigma mj+g}$	15	15	15	15	13	73
	c, c^*	121	123	123	123	127	617
1.2	i	17	16	16	16	–	65
	$i_{\Sigma mj}$	16	16	16	16	–	64
	$i_{\Sigma mj+g}$	13	13	13	13	–	52
	c, c^*	116	116	116	116	–	464
0.8	i	16	16	15	15	14	76
	$i_{\Sigma mj}$	18	19	18	19	21	95
	$i_{\Sigma mj+g}$	12	12	12	13	12	61
	c, c^*	100	99	100	101	100	500
0.6	i	15	14	14	14	–	57
	$i_{\Sigma mj}$	18	18	18	18	–	72
	$i_{\Sigma mj+g}$	12	12	12	12	–	48
	c, c^*	85	86	85	84	–	340
0.4	i	13	13	13	12	16	51
	$i_{\Sigma mj}$	17	17	16	17	20	67
	$i_{\Sigma mj+g}$	13	13	12	12	9	50
	c, c^*	69	66	67	67	81	269
0.25	i	13	13	13	12	–	51
	$i_{\Sigma mj}$	14	14	14	14	–	56
	$i_{\Sigma mj+g}$	9	9	9	9	–	36
	c, c^*	52	51	51	52	–	206
0.15	i	10	10	11	10	12	41
	$i_{\Sigma mj}$	12	12	12	12	11	48
	$i_{\Sigma mj+g}$	8	8	7	8	7	31
	c, c^*	27	27	28	28	32	110
0.1	i	8	8	8	8	–	32
	$i_{\Sigma mj}$	4	3	5	7	–	19
	$i_{\Sigma mj+g}$	5	5	5	5	–	20
	c, c^*	20	16	19	20	–	75
0.07	i	7	7	7	6	8	27
	$i_{\Sigma mj}$	2	2	2	2	1	8
	$i_{\Sigma mj+g}$	3	3	3	3	4	12
	c, c^*	13	13	13	12	19	51
0.04	i	6	4	4	4	–	18
	$i_{\Sigma mj}$	1	0	0	2	–	3
	$i_{\Sigma mj+g}$	3	2	2	2	–	9
	c, c^*	6	2	3	4	–	15
TOTAL		**1 113**	**1 092**	**1 093**	**1 099**	**717**	**5 114**

Comparison with data obtained elsewhere

The obtained data were compared with data from other laboratories [5-11]. Most of the comparable data are from Refs. [5,11]. Other works provide a small amount of comparable data: ^{48}V, ^{48}Sc, and ^{46}Sc at 1, 2 and 3 GeV from Ref. [6]; ^{83}Rb, ^{84}Rb, ^{86}Rb, ^{106m}Ag, ^{110m}Ag, ^{110}In and ^{129}Cs at 0.6 GeV from Ref. [7], ^{7}Be and ^{24}Na from Ref. [8], ^{7}Be at 0.4 GeV from Ref. [9]; and ^{111}In at 0.45 GeV from Ref. [10].

Note that only Ref. [5] uses the same method as ours, using direct kinematics and gamma spectrometry, which allows for a direct comparison of the results. Ref. [11] uses the inverse kinematics method and thus the resultant data need to be recalculated using the decay branch factors from Ref. [12] in order to obtain the required cumulative cross-sections. Figures 3-6 present several examples from our comparison.

The preliminary comparison of 105 excitation functions from ^{nat}Pb measured at ITEP using other results, which were obtained via direct kinematics, shows a satisfactory agreement of most (> 90%) of the data. Nine products show deviations above experimental errors [^{198}Tl(c), ^{170}Hf(c), ^{173}Lu(c), ^{155}Dy(c*), ^{153}Tb(c*), ^{145}Eu(c), ^{131}Ba(c), ^{102}Rh(i), ^{101m}Rh(c)]; eight products show deviations above experimental errors at 2.6 GeV [^{193m}Hg(i), $^{194(m1+m2+g)}$Au(i), ^{183}Re(c), ^{181}Re(c), ^{178}W(c), ^{166}Er(c), ^{160}Er(c), ^{111}In(c)]; two products show deviations above experimental errors at 1.6 and 2.6 GeV [^{195}Au(c), $^{88(m+g)}$Y(i)]; and four products deviate above 0.6 GeV energy [^{206}Bi(i), ^{205}Bi(i), ^{121}Te(c), ^{114m1}In(i[m])]. The cause of such discrepancies involves the methods of processing gamma spectra and gamma line identification, the used decay databases and the monitor reaction cross-sections.

Despite some deviations between the data of ITEP and ZSR [5], these measurements can be used together to produce files of evaluated excitation functions. The data that deviate strongly from each other should be reviewed and, if needed, re-measured.

Our comparison between the ITEP measurements and the GSI data (obtained via inverse kinematics data at 0.5 and 1.0 GeV*A) points to systematical discrepancies or/and errors. The mentioned recalculation of the GSI independent cross-section, whose purpose is to produce the required cumulative cross-sections, may not affect the shape of excitation functions but may affect their normalisation. Our comparison of the GSI data for 143 products with respective ITEP data shows agreement in 119 cases (83%). The following twenty-four cases present discrepancies above experimental errors: ^{207}Bi(i), ^{199}Pb(c*), ^{200}Tl(i), $^{191(m+g)}$Au(i), $^{192(m1+g)}$Ir(i), $^{190(m+g)}$Ir(i), ^{188}Ir(i), ^{186}Ir(c), ^{181}Os(c), ^{172}Ta(c*), ^{170}Hf(c), ^{161}Er(c), ^{121}Te(c), ^{105}Rh(c), ^{102}Rh(i), ^{103}Ru(c), ^{99}Mo(c), ^{95}Nb(c), ^{95}Zr(c), $^{86(m+g)}$Rb(i), ^{83}Rb(c), $^{82(m+g)}$Br(i), ^{72}Ga(c) and ^{72}Zn(c). Details on the direct and inverse kinematics result comparison are presented in our previous work [14]. The cause of some observed discrepancies involved uncertainties surrounding the decay-chain branching factors and the monitor reaction cross-sections.

Our analysis of the excitation functions, which were measured by different groups, shows that the data obtained using similar methods agree more than the data obtained using different methods. The cause of the discrepancies will be studied further.

A comparison of ITEP data on ^{209}Bi with respective data from other laboratories is in progress and will be presented in future works.

Figure 3. Experimental and simulated excitation functions of ^{203}Pb, ^{199}Tl and ^{196}Au produced in ^{208}Pb (left) and ^{nat}Pb (right)

■ – *this work,* ╬ – *Ref. [11]*

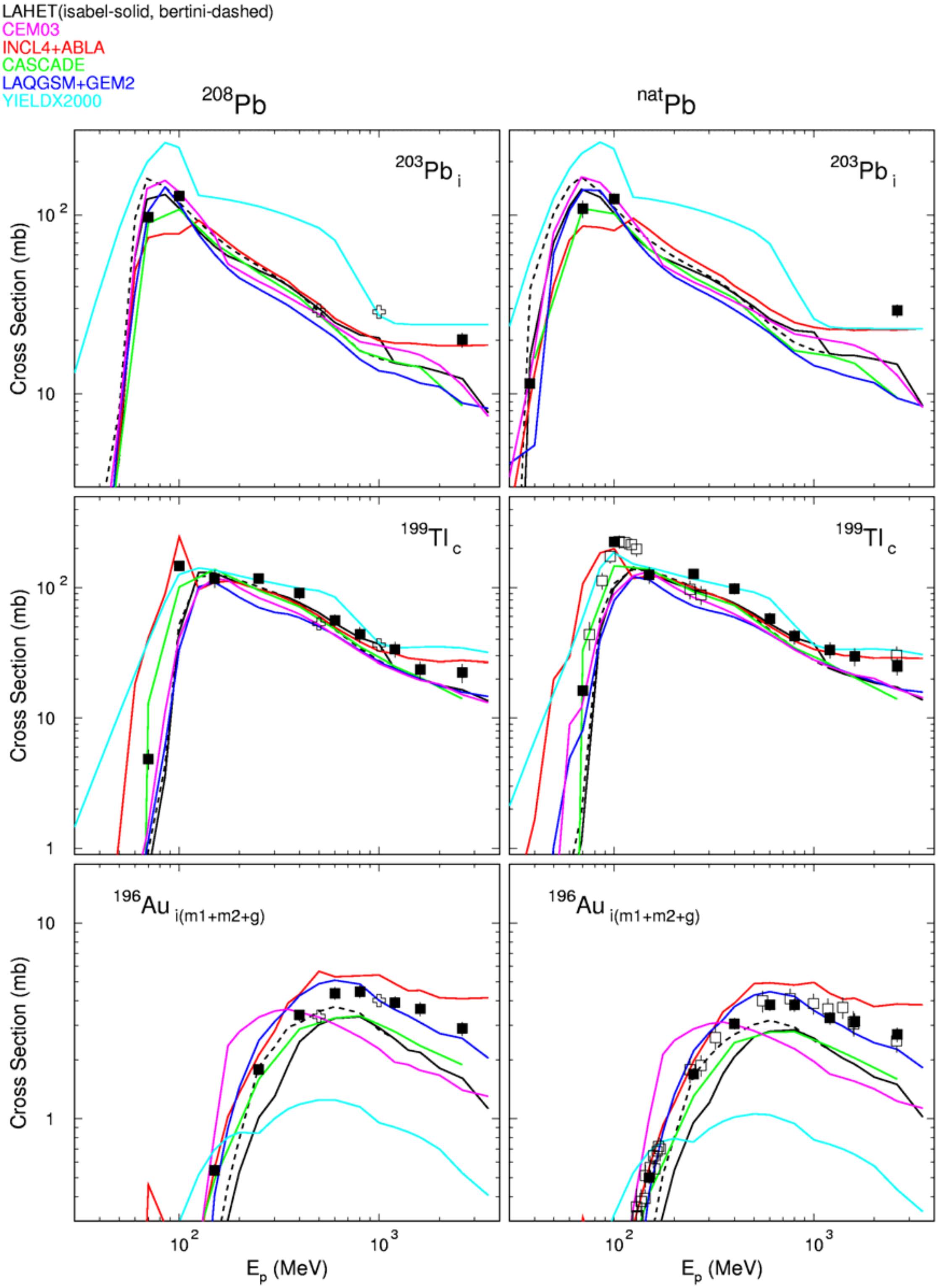

Figure 4. Experimental and simulated excitation functions of ^{86}Rb, ^{24}Na and ^{7}Be produced in ^{208}Pb (left) and ^{nat}Pb (right)

■ – *this work,* Δ – *[7],* ◊ – *[8],* ╬ – *Ref. [11]*

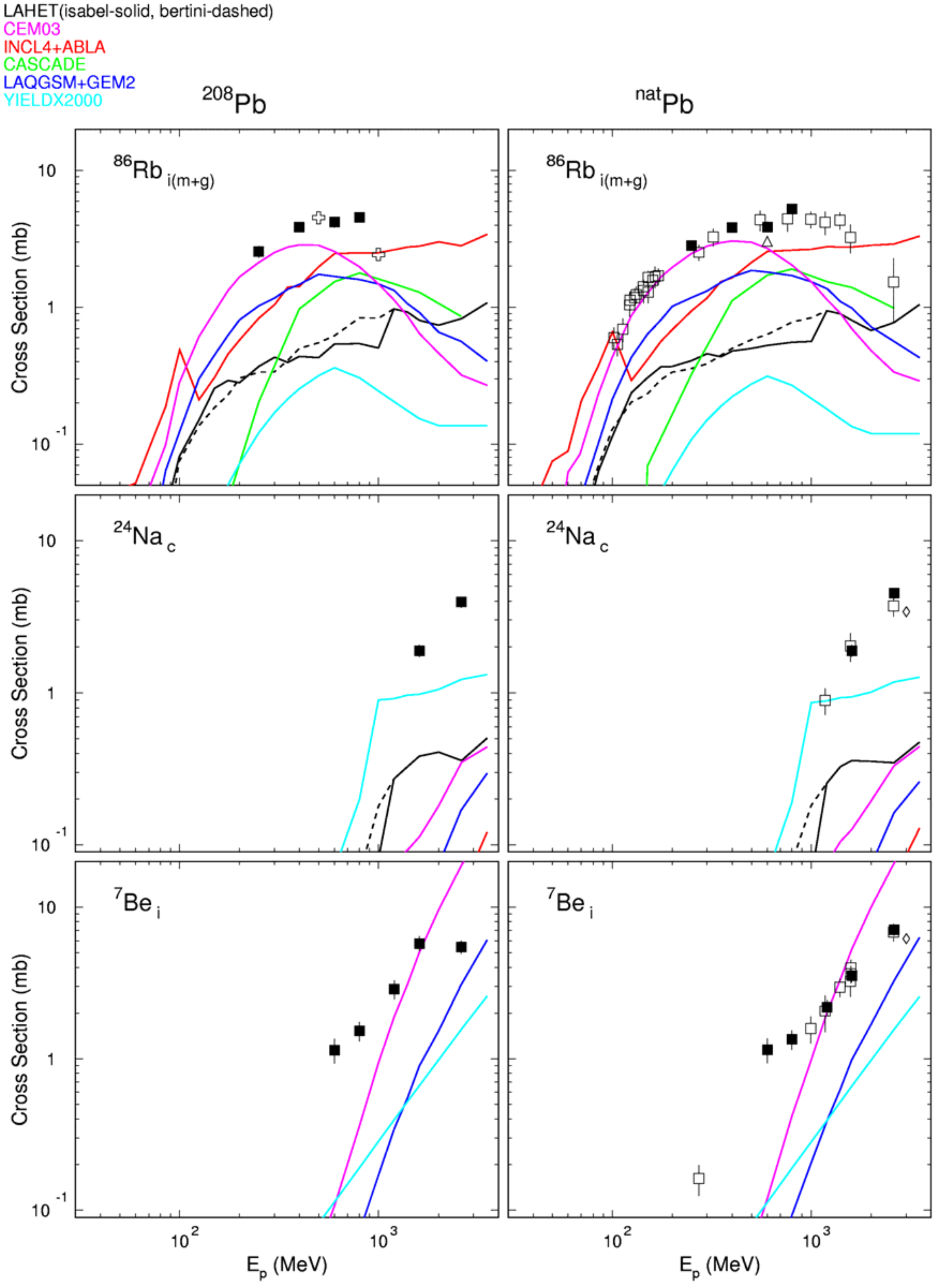

Figure 5. Experimental and simulated excitation functions of ^{190}Ir, ^{173}Lu and ^{101m}Rh produced in ^{208}Pb (left) and ^{nat}Pb (right)

■ – *this work*, ╬ – *Ref. [11]*

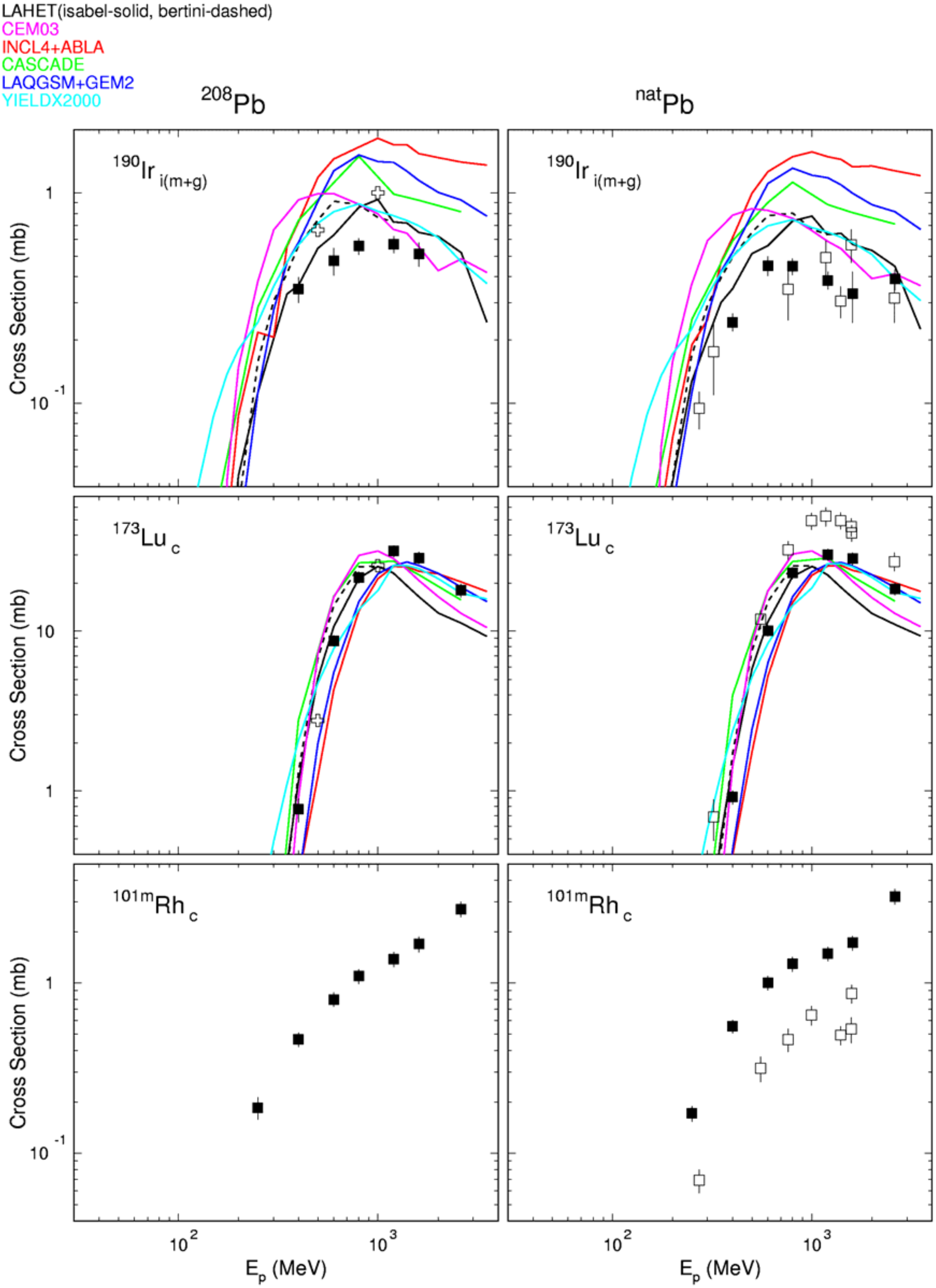

Figure 6. Experimental and simulated excitation functions ^{200}Tl, ^{192}Ir and ^{59}Fe produced in ^{208}Pb (left) and ^{nat}Pb (right)

■ – *this work*, ╬ – *Ref. [11]*

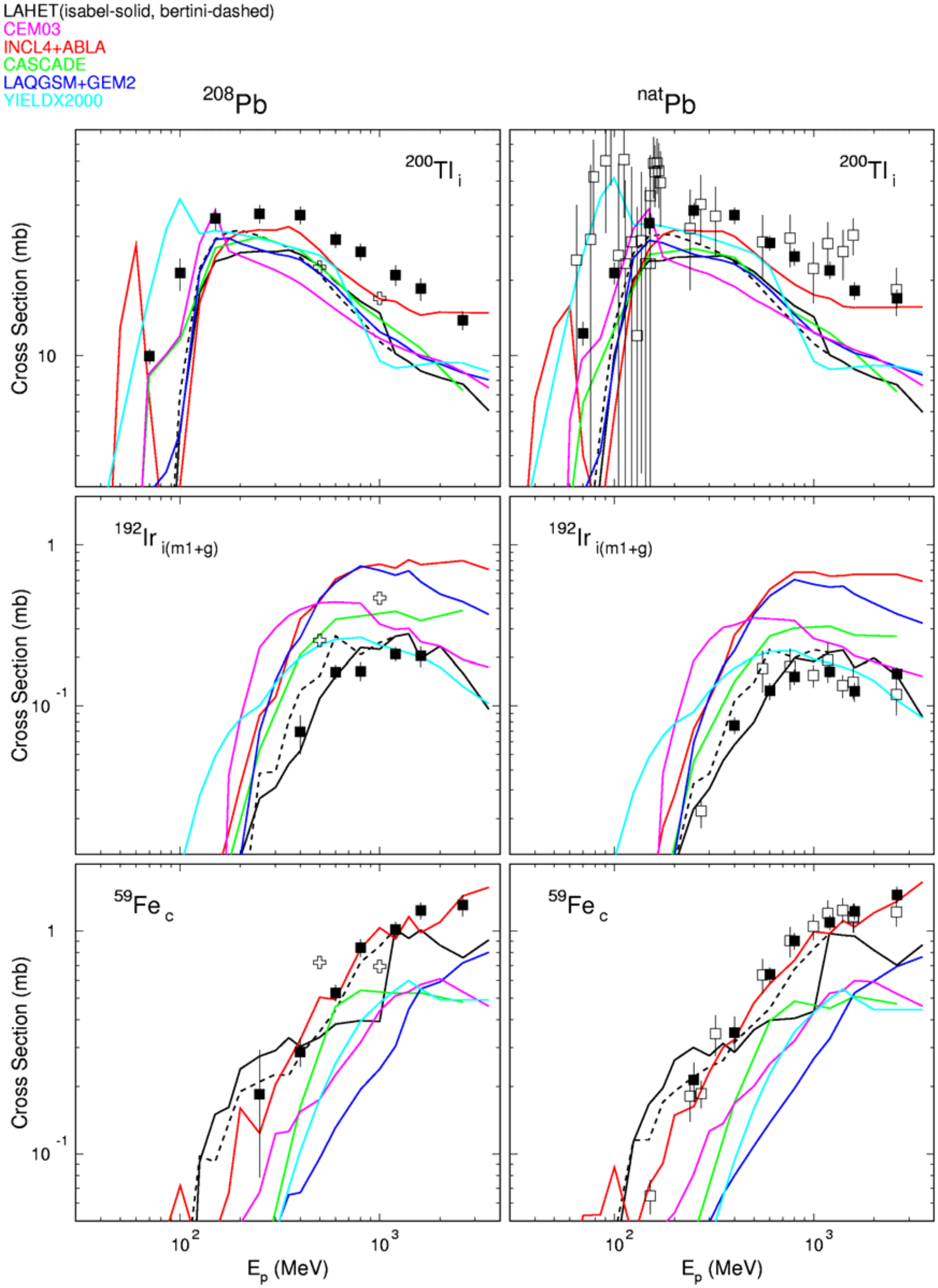

Theoretical simulation of the measured cross-sections

Figures 3-6 present experimental and simulated excitation functions for several products from ^{208}Pb and ^{nat}Pb. The simulations were made using LAHET (the ISABEL and BERTINI models), CEM03, INCL4+ABLA, CASCADE, LAQGSM+GEM2 and YIELDX2000 codes. A short description of these codes and their convergence with experimental data can be found in Ref. [13] and references contained therein.

The predictive power of the tested codes varied but was found to be satisfactory for most of the nuclides in the spallation region. However, none of the benchmarked codes agreed well with the data on the mass region of product nuclides. Moreover, all codes should be further improved.

Acknowledgements

This work was performed under the ISTC Project #2002, which was supported mainly by the European Community, and in part by the US Department of Energy and the NASA ATP01 grant, NRA-01-ATP-066.

REFERENCES

[1] Proton-Pb and Proton-Bi Reaction Yields, ISTC Project #2002, see the corresponding internet site http://tech-db.istc.ru/istc/db/projects.nsf/all-projects/2002.

[2] Titarenko, Yu.E., *et al.*, "Experimental and Theoretical Study of the Yields of Residual Product Nuclei in Thin Targets Irradiated by 100-2 600 MeV Protons", IAEA, Nuclear Data Section, INDC (CCP)-434, September (2002); http://www-nds.iaea.org/reports/indc-ccp-434.pdf.

[3] Titarenko, Yu.E., O.V. Shvedov, V.F. Batyaev, *et al.*, "Cross Sections for Nuclide Production in 1 GeV Proton-irradiated ^{208}Pb", *Phys. Rev.*, C65, 064610 (2002).

[4] Titarenko, Yu.E., O.V. Shvedov, M.M. Igumnov, *et al.*, "Experimental and Computer Simulation Study of the Radionuclides Produced in Thin ^{209}Bi Targets by 130 MeV and 1.5 GeV Proton Induced Reactions", N*ucl. Instr. and Meth.*, A414, 73 (1998).

[5] Gloris, M., R. Michel, F. Sudbrok, *et al.*, "Proton-induced Production of Residual Radionuclides in Lead at Intermediate Energies", *Nucl. Instr. and Meth.*, A463, 593 (2001); EXFOR file O0500.

[6] Chu, Y.Y., G. Friedlander, L. Husain, "Production of Nuclides with Atomic Mass 43<=A<=51 in the Interaction of 1-28.5 GeV Protons with V, Ag, in Pb and U Targets", *Phys. Rev.*, C15, 352 (1977); EXFOR file O0399.

[7] Hagebo, E., T. Lund, "Fission of Lead Induced by 600 MeV Protons", *Inorganic Nuclear Chemistry*, 37, 1569 (1975); EXFOR file O0327.

[8] Hudis, J., S. Tanaka, “Production of Be-7, Na-22, and Na-24 Fragments from Heavy Elements at 3, 10 and 30 GeV”,. *Phys. Rev*., 171, 1297 (1968); EXFOR file C0341.

[9] Korteling, R.G., A.A. Caretto, “Systematics of Na-24 and Na-22 Production with 400 MeV Protons”, *Inorganic Nuclear Chemistry*, 29, 2863 (1967); EXFOR file O0412.

[10] Panontin, J.A., N.T. Porile, “Recoil Properties and Charge Distribution in the Fission of Pb-208 by 450 MeV Protons”, *Inorganic Nuclear Chemistry*, 30, 2891 (1968); EXFOR file O0332.

[11] Enqvist, T., W. Wlazlo, P. Armbruster, *et al*., “Isotopic Yields and Kinetic Energies of Primary Residues in 1 A GeV 208Pb + p Reactions”, *Nucl. Phys*., A686, 481 (2001); “Primary Residue Production Cross Sections and Kinetic Energy in 1 A GeV ^{208}Pb on Deuteron Reactions”, *Nucl. Phys*., A703, 435 (2002); B. Fernandez, PhD Thesis, University de Caen, France, March 2003.

[12] Tuli, J.K., Nuclear Wallet Cards, *BNL*, 6th edition, January 2000.

[13] Titarenko, Yu.E., V. F. Batyaev, V.M. Zhivun, *et al*., “Theoretical Simulation of Residual Nuclide Products in $^{208, 207, 206}$Pb, ^{nat}Pb and ^{209}Bi (p,x) Reactions at Inter-medium and High Energies”, To be published in *Proc. of ICRS-10*, RPS 2004 Int. Conferences, Funchal, 9-14 May 2004.

[14] Titarenko, Yu.E., V.F. Batyaev, V.M. Zhivun, *et al*., “Nuclide Production in ^{197}Au, ^{208}Pb, and ^{nat}U Irradiated with 0.8-1 GeV Protons: Comparison with Other Experiments and with Theoretical Predictions”, *Proceedings of the Workshop on Nuclear Data for the Transmutation of Nuclear Waste*, ISBN 3-00-012276-1, GSI-Darmstadt, September 2003.

SESSION III.1

Benchmark Experiments and Calculations

Chair: B. Kirk

INTERCOMPARISON OF MEDIUM-ENERGY NEUTRON ATTENUATION IN IRON AND CONCRETE (5)

Hideo Hirayama
KEK, High Energy Accelerator Research Organization
1-1 Oho, Tsukuba, Ibaraki, 305-0801 Japan

Attenuation Length Sub-working Group
Japan

Abstract

Based on results presented at SATIF-6, problems were revised and sent by the Japanese Working Group to the participants of this action for re-calculation. To determine their energy dependence, 50 and 100 GeV neutrons were then added as the source neutrons. The secondary neutron spectrum for 90°, which was produced by 24 GeV protons on an Hg target, was added as the secondary neutron source. The purpose was to determine the dependence of the attenuation length of secondary neutrons on their spectra.

This paper presents a comparison of the neutron attenuation length of iron and concrete. Results reviewed include those recently (April 2004) sent by three groups to the organiser and those presented at previous SATIF meetings. The paper also discusses themes evoked from this comparison, which should be investigated in the future.

Introduction

Neutron attenuation at a high energy (above a few GeVs) is not supposed to depend on the energy. Its energy dependence below this energy, especially below 1 GeV, is not well understood. The desire is to reach a consensus on the behaviours of neutrons inside various materials. Such a consensus is necessary in order to agree on definitions of the attenuation length, which is very important for shielding calculations involving high-energy accelerators. One such attempt was made by Japanese attendants of SATIF-2, who proposed to compare various computer codes and data on the attenuation of medium-energy neutrons inside iron and concrete shields (cited as a suitable action for SATIF). From the results for neutrons below 400 MeV presented at SATIF-3 [1], it has become clear that neutrons above 20 MeV are important for understanding that the attenuation length and the geometry (planar or spherical) does not substantially affect the results. The attenuation length of neutrons above 20 MeV was compared with the planer geometry for secondary neutrons produced by medium-energy protons at SATIF-4 [2]. Although attenuation lengths varied, all of the results showed the same tendency for an attenuation length increase and neutron energy increase up to 10 GeV [2,3,4]. From the results presented at SATIF-4, SATIF-5 and SATIF-6, it is clear that the attenuation length of secondary neutrons depends strongly on their spectra.

Considering previous SATIF results, problems were revised for re-calculation by the Japanese Working Group and sent to the participants of this action. To determine their energy dependence, 50 and 100 GeV neutrons were then added as source neutrons. The secondary neutrons emitted at 90° from an Hg target [4] bombarded by 24 GeV protons, which were calculated by F. Maekawa [5] using NMTC/JAM [6], were also added as source neutrons.

Results from the three groups were sent to the organiser by the end of April 2004. This paper presents a comparison of the neutron attenuation lengths of iron and concrete, including the results presented at previous meetings and the future themes resulting from this comparison.

Problems involving the intercomparison (5)

Considering the results presented at SATIF-6 [4], the following revised problems were proposed for calculation using various codes and their databases. Secondary neutrons produced from an Hg target by 24 GeV protons at 90° were also added, which were calculated by F. Maekawa using NMTC/JAM [6].

Attenuation calculation

Source neutron energy

a) Source neutrons are uniformly distributed within the following energy regions: 40-50 MeV, 90-100 MeV, 180-200 MeV, 375-400 MeV, 1 GeV, 1.5 GeV, 3 GeV, 5 GeV, 10 GeV, 50 GeV and 100 GeV.

b) Secondary neutrons at 90° from an Fe target (5 cm diameter, 5 cm length) and the following: from 200 MeV protons, from 500 MeV protons, from 1 GeV protons, from 3 GeV protons and from 5 GeV protons (Figure 1).

c) Secondary neutrons in various directions from an Hg target with a Pb moderator (120 cm diameter, 120 cm length) are shown in Figure 2 with 3 GeV protons.

d) Secondary neutrons at 90° from an Hg target shown with 24 GeV protons in Figure 2.

Figure 1. Secondary neutrons at 90° from an iron target bombarded by protons (FLUKA calculations)

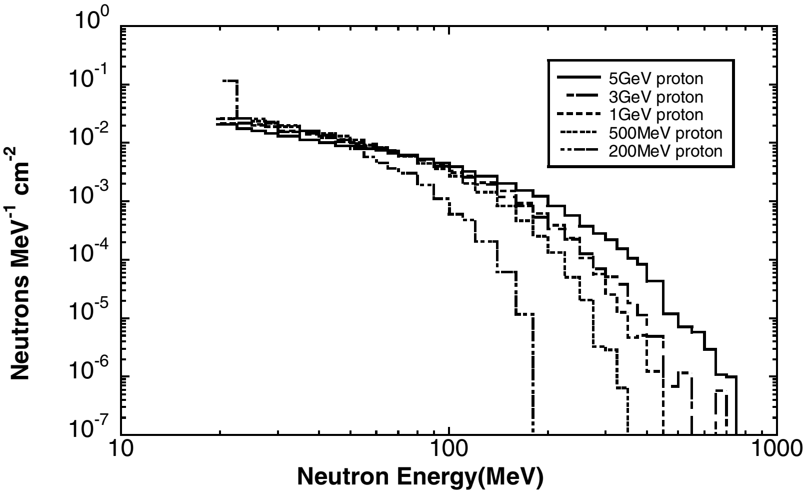

Figure 2. Secondary neutron spectrum from an Hg target bombarded by 3 GeV protons (by MCNPX) and 24 GeV protons (by NMTC/JAM)

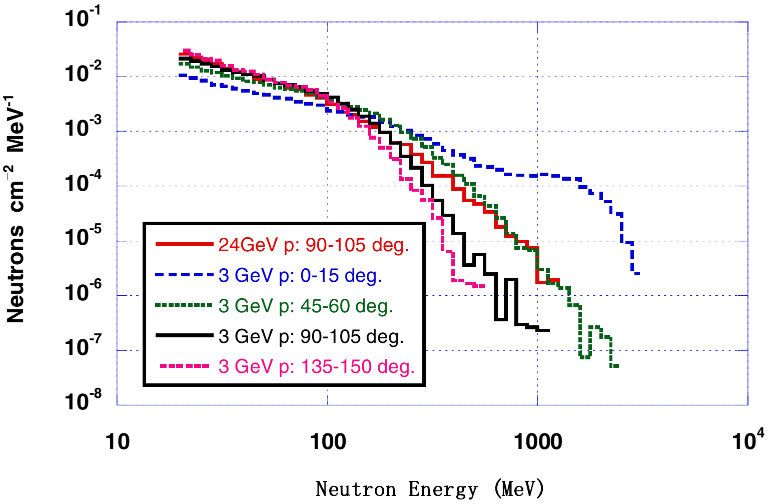

Geometry

The geometry used was plane (6 m thick) with normal incident parallel beams.

Shielding material

As typical shielding materials, iron and concrete were selected. The densities of the two materials were 7.87 g cm P^{-3P} (iron) and 2.27 g cm P^{-3P} (concrete) [Type 02-a, ANL-5800 and 660 (1963)]. The composition of concrete is given in Table 1.

Energy group and fluence-to-dose equivalent conversion factor

The energy group in Table 2 is presented as the standard. If possible, the neutron spectra should be presented in this energy group.

In dose calculations, use of the neutron flux-to-dose equivalent conversion factor (Table 3) is recommended, thus avoiding any ambiguity due to the conversion factor. The values given in Table 3 are conversion factors for the neutron energy corresponding to that given in Table 2.

Table 1. Composition of concrete

Element	Atomic number density (10P^{24P}/cmP^{3P})	Weight per cent	Element	Atomic number density (10P^{24P}/cmP^{3P})	Weight per cent
H	1.3851E-2	1.02	Si	1.6621E-2	34.21
C	1.1542E-4	1.00	K	4.6205E-4	1.32
O	4.5921E-2	53.85	Ca	1.5025E-3	4.41
Mg	1.2388E-4	0.22	Fe	3.4510E-4	1.41
Al	1.7409E-3	3.44	–	–	–

Table 2. Upper energy of 66 neutron energy groups (MeV)

1.00E+5	9.00E+4	8.00E+4	7.00E+4	6.00E+4	5.00E+4	4.00E+4	3.00E+4	2.00E+4
1.80E+4	1.60E+4	1.40E+4	1.20E+4	1.00E+4	9.00E+3	8.00E+3	7.00E+3	6.00E+3
5.00E+3	4.50E+3	4.00E+3	3.50E+3	3.00E+3	2.50E+3	2.00E+3	1.90E+3	1.80E+3
1.70E+3	1.60E+3	1.50E+3	1.40E+3	1.30E+3	1.20E+3	1.10E+3	1.00E+3	9.00E+2
8.00E+2	7.00E+2	6.00E+2	5.00E+2	4.00E+2	3.75E+2	3.50E+2	3.25E+2	3.00E+2
2.75E+2	2.50E+2	2.25E+2	2.00E+2	1.80E+2	1.60E+2	1.40E+2	1.20E+2	1.10E+2
1.00E+2	9.00E+1	8.00E+1	7.00E+1	6.50E+1	6.00E+1	5.50E+1	5.00E+1	4.50E+1
4.00E+1	3.50E+1	3.00E+1	2.75E+1	2.50E+1	2.25E+1	2.00E+1	–	–

Table 3. Neutron flux-to-dose conversion factor [(Sv/hr)/(n/sec/cmP^{2P})] [7]

1.98E–5	1.96E–5	1.93E–5	1.93E–5	1.90E–5	1.85E–5	1.78E–5	1.58E–5	1.40E–5
1.35E–5	1.30E–5	1.24E–5	1.17E–5	1.09E–5	1.05E–5	1.00E–5	9.55E–6	9.01E–6
8.42E–6	8.11E–6	6.77E–6	7.41E–6	7.02E–6	6.72E–6	6.32E–6	6.22E–6	6.11E–6
5.98E–6	5.84E–6	5.69E–6	5.52E–6	5.34E–6	5.14E–6	4.94E–6	4.72E–6	4.47E–6
4.18E–6	3.78E–6	3.26E–6	2.72E–6	2.25E–6	2.20E–6	2.15E–6	2.10E–6	2.05E–6
1.99E–6	1.93E–6	1.86E–6	1.82E–6	1.79E–6	1.77E–6	1.74E–6	1.72E–6	1.70E–6
1.68E–6	1.65E–6	1.64E–6	1.63E–6	1.62E–6	1.61E–6	1.60E–6	1.59E–6	1.58E–6
1.57E–6	1.56E–6	1.55E–6	1.54E–6	1.53E–6	1.52E–6	–	–	–

Quantities to be calculated

The following quantities must be calculated for the comparison: dose equivalent due to neutrons above 20 MeV at 50, 100, 150, 200, 250, 300, 350, 400, 450 and 500 cm; and neutron spectrum in *n* cm $^{-}$P^{2P}MeV^{-1} per source neutron at 100, 200, 300, 400 and 500 cm.

Summary of contributors

Neutron attenuation calculation

The three groups sent their results to Hideo Hirayama at KEK before the end of April 2004. Table 4 lists the participants as well as the computer codes used and their corresponding databases.

Table 4. Summary of contributors

Name of participant and the organisation	Computer code used	Database corresponding to the computer code
H. Nakashima (JAERI)	PHITS [8]	Library data in PHITS
N. Mokhov (FNAL)	MARS14 [9,10,11]	Library data in MARS14
A.M. Voloschenko (Keldysh Institute of Applied Mathematics)	ROZ-6.5 [12,13,14]	SADCO-2

Results and discussions

Attenuation length

The attenuation length (λ, g cm P^{-2P}) for each case was obtained by a least-squares fitting at the region where the dose decreased exponentially. The obtained neutron attenuation lengths for iron and concrete are shown in Figures 3 and 4, respectively.

In the case of iron, the results for PHITS were calculated for a 300 cm slab, and not a 600 cm slab. (In addition to these calculations, Figure 3 also shows the results presented at previous SATIF meetings.) The attenuation lengths for iron are scattered around each other below 500 MeV, but are relatively close above the 1 GeV level, except for the ROZ-6.5 results. Based on the results of MARS14, the attenuation lengths seem to be almost constant above a few GeV. On the other hand, the results of PHITS and NMTC/JAM increase as the source neutrons increase, even above 10 GeV. The attenuation lengths of these results were obtained for the 150 and 300 cm regions. It is assumed that at this depth the neutron spectrum for a high-energy source does not reach equilibrium. This assumption is confirmed by the attenuation lengths between 150 and 300 cm for MARS14 (Figure 4), which is similar to the results of PHITS and NMTC/JAM.

In the case of concrete, the differences in attenuation lengths for each code are relatively small, and do not depend on the source neutron energy, except for the results of ROZ-6.5 above 200 MeV. The attenuation length increases as the source neutrons increase, even at 100 GeV. This tendency can be explained using the same reason as that mentioned in the iron case for the results of NMTC/JAM and PHITS. The quantities related to the neutron interaction depend on the depth in g cm^{-2}, rather than in cm. If we consider the densities of concrete and iron, 600 cm of concrete corresponds to 173 cm of iron. The neutron spectrum in the 300-500 cm region for concrete is not supposed to reach equilibrium for high-energy neutrons above GeV.

The results for ROZ-6.5 are less than those produced by other codes when above several hundreds of MeV. Despite this fact, the results for ROZ-6.5 are very important in this intercomparison, considering that most of the results are based on Monte Carlo methods. We hope that A.M. Voloschenko, *et al.*, will improve their data and continue to contribute to this intercomparison.

Figure 3. Comparison of the attenuation length of iron

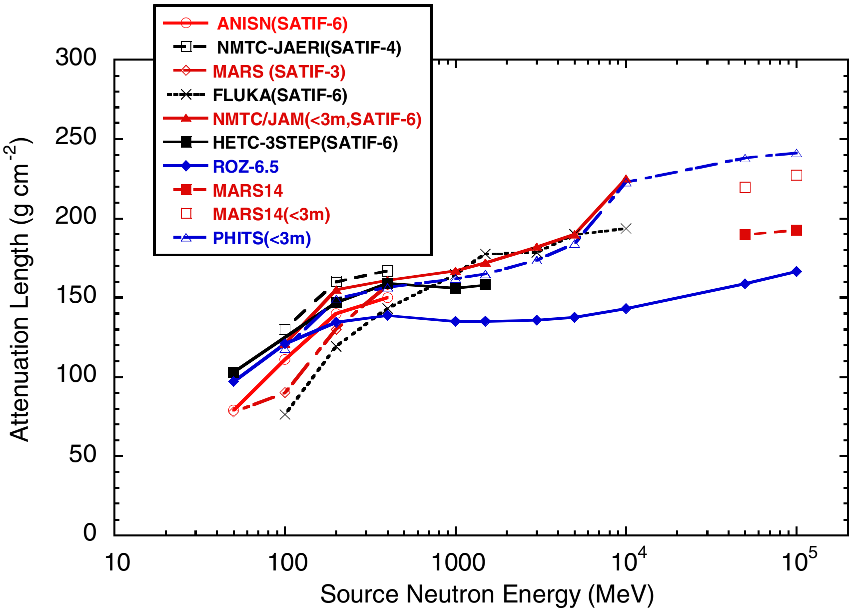

Figure 4. Comparison of the attenuation length of concrete

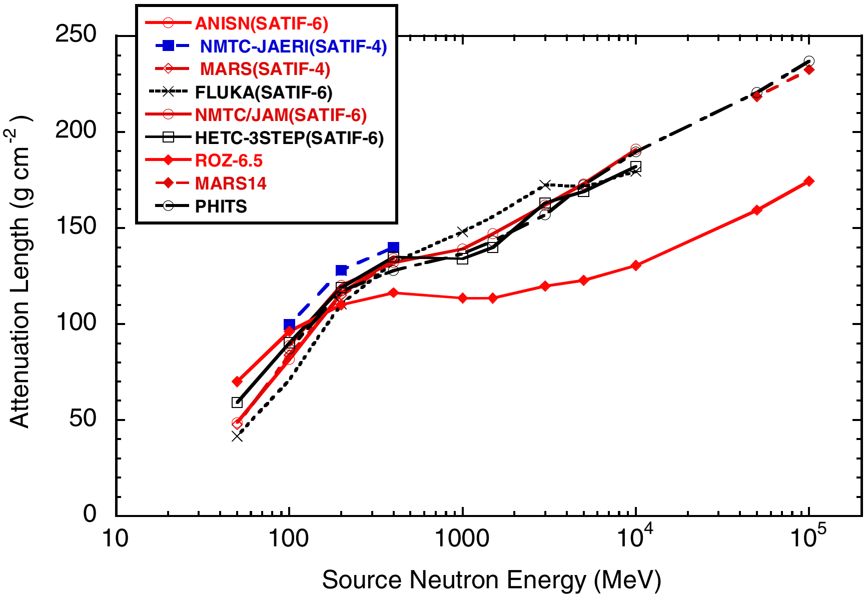

The attenuation lengths of iron and concrete for secondary neutrons from an Hg target with 3 and 24 GeV protons are shown as a function of the emission angle in Figures 5 and 6, respectively. The PHITS results show a similar tendency concerning the values of the attenuation length and their emission angle dependence with those presented at SATIF-6. The results of ROZ-6.5 are smaller than those of other codes, and show a weak dependence on the emission angle. The results for secondary neutrons from 24 GeV protons show a larger attenuation length than those from 3 GeV protons, reflecting the higher energy neutrons shown in Figure 3. The experimental results at ISIS [7] and LANSCE [8] for 800 MeV protons are shown in Figures 5 and 6.

Figure 5. Comparison of the neutron attenuation length of iron for secondary neutrons from an Hg target with 3 and 24 GeV protons

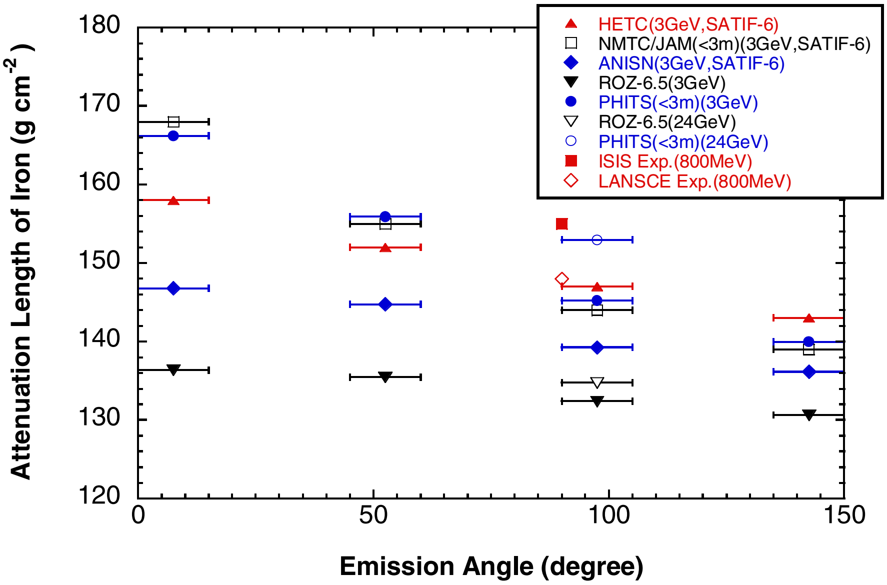

Figure 6. Comparison of the neutron attenuation length of concrete for secondary neutrons from an Hg target with 3 and 24 GeV protons

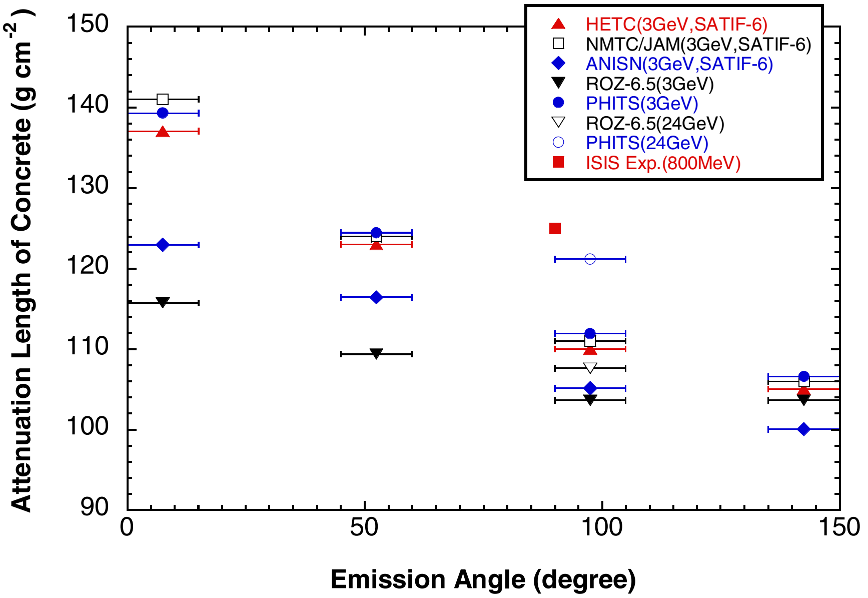

The attenuation lengths of iron and concrete for secondary neutrons from an iron target and from high-energy protons are shown in Figures 7 and 8, respectively. In these figures, the experimental results at ISIS [7] and LANSCE [8] for 800 MeV protons are plotted for comparison. Results of both ROZ-6.5 and PHITS show almost similar values to previous results, except for a slightly weak dependence on the proton energy in the case of ROZ-6.5.

Figure 7. Comparison of the neutron attenuation length of iron for secondary neutrons from an iron target with protons

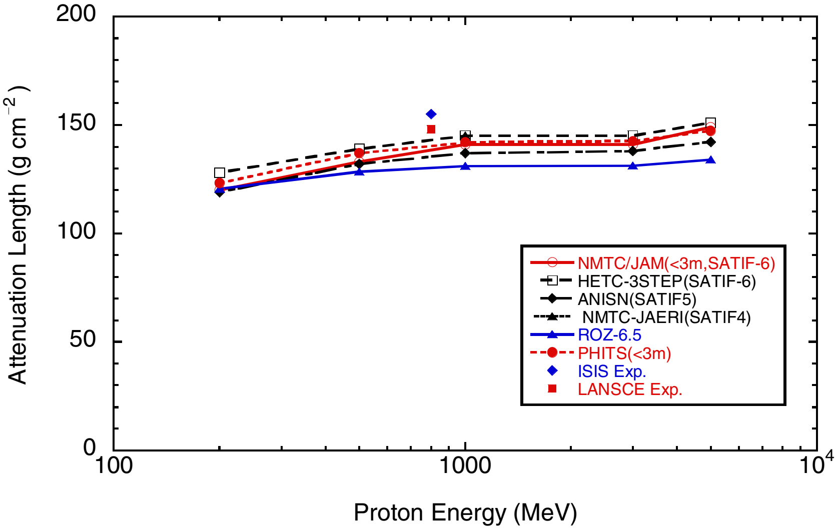

Figure 8. Comparison of the neutron attenuation length of concrete for secondary neutrons from an iron with protons

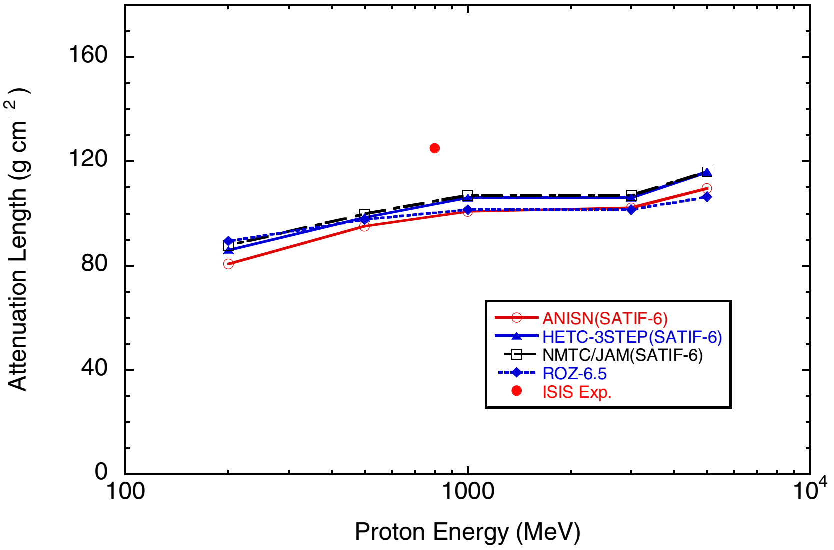

Future themes

From the above comparisons, the following activities should be discussed and performed as the next steps:

A. Compare with the results of other codes to confirm the tendency shown above. It would be desirable to receive results from other groups for comparison.

B. Neutron-dose equivalent attenuation deep inside shields (at 3-5 m for iron and 6-10 m for concrete) in order to confirm that the attenuation length reaches a constant value.

C. Select suitable experiments for comparison in order to understand the attenuation length of secondary neutrons from high-energy protons. The results of AGS shielding experiments presented by H. Nakashima, *et al.*, are suitable for this purpose.

D. Dose equivalents are different depending on the code used, which was seen in this intercomparison even for simple problems. Good benchmark experiments are desired to check the models used in each code system.

REFERENCES

[1] Hirayama, H., *et al.*, "Inter-comparison of the Medium-energy Neutron Attenuation in Iron and Concrete", *Proceedings of the SATIF-3, Shielding Aspects of Accelerators, Targets and Irradiation Facilities*, Tohoku University, pp. 185-195, 12-13 May 1997.

[2] Hirayama, H., *et al.*, "Inter-comparison of the Medium-energy Neutron Attenuation in Iron and Concrete (2)", *Proceedings of the Shielding Aspects of Accelerators, Targets and Irradiation Facilities – SATIF-4*, Knoxville, Tennessee, USA, pp. 143-154, 17-18 September 1998.

[3] Hirayama, H., *et al.*, "Inter-comparison of the Medium-energy Neutron Attenuation in Iron and Concrete (3)", *Proceedings of the Shielding Aspects of Accelerators, Targets and Irradiation Facilities – SATIF-5*, Paris, France, pp. 189-201, 18-21 July 2000.

[4] Hirayama, H., *et al.*, "Inter-comparison of the Medium-energy Neutron Attenuation in Iron and Concrete (4)", *Proceedings of the Shielding Aspects of Accelerators, Targets and Irradiation Facilities – SATIF-6*, SLAC, USA, 10-12 April 2002.

[5] Maekawa, private communication.

[6] Niita, K., *et al.*, *High Energy Particle Transport Code NMTC/JAM*, JAERI-Data/Code 2001-007 (2001).

[7] ICRP Publication 51, "Data for Use in Protection against External Radiation", *Annals of the ICRP*, 17 (2/3) 1987.

[8] Iwase, H., K. Niita, T. Nakamura, "Development of General-purpose Particle and Heavy Ion Transport Monte Carlo Code", *J. Nucl. Sci. Technol.*, 39, 1142-1151 (2002).

[9] Mokhov, N.V., *The MARS Code System User's Guide*, Fermilab-FN-628 (1995).

[10] Krivosheev, O.E., N.V. Mokhov, "MARS Code Status", *Proc. Monte Carlo 2000 Conf.*, Lisbon, p. 943, 23-26 October 2000; Fermilab-Conf-00/181 (2000).

[11] Mokhov, N.V. *Status of MARS Code*, Fermilab-Conf-03/053 (2003).

[12] Voloschenko, M., A.A. Dubinin, *ROZ-6.5 – One-dimensional Discrete-ordinates Neutron, Photon and Charged Particles Transport Code*, User's Guide, Report No. 7-6-98, Keldysh Institute of Applied Mathematics, Moscow (1998) [in Russian].

[13] Averin, V., A.M. Voloschenko, E.P. Kondratenko, A.A. Dubinin, "The ROZ-6.4 One-dimensional Discrete-ordinates Neutrons, Gamma-rays and Charged Particles Transport Code", *Proc. Int. Topical Meeting on Advances in Mathematics, Computations and Reactor Physics*, Pittsburgh, USA, Vol. 5, pp. 30.3 5-1, 28 April-2 May 1991.

[14] Voloschenko, M., S.V. Gukov, "Some New Algorithms for Solving the Coupled Electron-photon Transport Problems by the Discrete-ordinates Method", *Proc. Int. Conf. on the New Frontiers of Nuclear Technology: Reactor Physics, Safety and High-performance Computing – PHYSOR 2002*, Seoul, Korea, 7-10 October 2002.

[15] Nunomiya, T., *et al*., "Measurement of Deep Penetration of Neutrons Produced by 800 MeV Proton Beam through Concrete and Iron at ISIS", *Nucl. Instr. and Meth.*, B179, pp. 89-102 (2001).

[16] Bull, J.S., J.B. Donahue, R.L. Burman, "Measurement of Neutron Attenuation through Thick Shields and Comparison with Calculation", *Proc. of the 4th Workshop on Simulating Accelerator Radiation Environments – SARE4*, Knoxville, Tennessee, pp. 201-208, 14-16 September 1998.

Annex

PROPOSAL BY ANDREI M. VOLOSCHENKO

It is not a simple task to subdivide high-energy neutrons and protons (and maybe pions) transport when performing target/accelerator radiation shield calculations. The coupled hadron cascade problem should be solved.

Additionally, it is difficult to compare the calculation of problems using a high-energy neutron source only with experimental data, as a real target emits more than just neutrons.

Computers today are quite powerful. As a result, perhaps more realistic and thus more complicated intercomparison problems should be developed. I believe that the beam spill and full stop problems described by H. Handa, *et al.*, in "Deep Penetration Calculations of Neutrons up to 1.5 GeV" from the SATIF-5 proceedings are quite acceptable for intercomparison.

I sent you some results of the 2-D model for the liquid metal target shield calculations. Charged components of radiation cannot be neglected in this calculation, and sufficiently high order angular quadrature and PL approximation of scattering cross-sections should be used to achieve acceptable results.

SUMMARISED EXPERIMENTAL RESULTS OF NEUTRON SHIELDING AND ATTENUATION LENGTH

Takashi Nakamura
Cyclotron and Radioisotope Center, Tohoku University
Aoba, Aramaki, Aoba-ku, Sendai, 980-8578, Japan
Phone: +81 (22) 217-7792, Fax: +81 (22) 217-7809
E-mail: nakamura@cyric.tohoku.ac.jp

Abstract

Several experiments on the high-energy neutron shielding of energies above 100 MeV were recently performed using the following: 800 MeV protons at ISIS of the Rutherford Appleton Laboratory (RAL), England; 400 MeV/nucleon carbon ions at the Heavy Ion Medical Accelerator Facility (HIMAC) of the National Institute of Radiological Sciences (NIRS), Japan; 500 MeV protons at KENS, the spallation neutron source of the High Energy Accelerator Research Organization (KEK), Japan; 155 MeV/nucleon He, C and O ions at the National Superconducting Cyclotron Laboratory (NSCL), USA; 500 MeV protons at the accelerator facility, TRIUMF, Canada; 1.6-24 GeV protons at the Alternating Gradient Synchrotron (AGS) of Brookhaven National Laboratory (BNL), USA; 28.7 GeV electrons at the Stanford Linear Accelerator Center (SLAC), USA; 800 MeV protons at the Los Alamos Neutron Science Center (LANSCE), Los Alamos National Laboratory (LANL), USA; 120, 205 GeV/c protons and 160 GeV/nucleon lead ions at CERN, Switzerland; 230 MeV protons at the Loma Linda University Medical Center, USA; 200 MeV protons at the Orsay Proton Therapy Center, France; and 155 MeV/nucleon He, C, O ions at the National Superconducting Cyclotron Laboratory (NSCL), USA.

In this paper, the attenuation lengths obtained by these deep penetration experiments are summarised and the outlines for the ISIS, HIMAC and SLAC experiments are described, which provide the neutron energy spectra penetrated through the shield.

Introduction

The shielding experiments are important to investigate the accuracy of calculations, since the calculations are usually adjusted or corrected in the model as are the parameters/data used in the code to fit the experimental results. Accurate benchmark and mock-up experiments are strongly needed.

Several experiments on high-energy neutron shielding have recently (within the past 10 years) been performed using medium- to high-energy accelerators for energies above 20 MeV. Below 100 MeV, the benchmark experiments were performed using the following: 25 and 35 MeV p-Li quasi-monoenergetic neutrons at CYRIC (Cyclotron and Radioisotope Center) of the Tohoku University, Japan [1]; and 43 and 68 MeV p-Li quasi-monoenergetic neutrons at the proton cyclotron facility, TIARA, of the Japan Atomic Energy Research Institute (JAERI) [2-4]. Above 100 MeV, the neutron shielding experiments have been done only with the white (continuous spectrum) neutron sources using the following: 800 MeV protons at ISIS of the Rutherford Appleton laboratory (RAL), England [5]; 400 MeV/nucleon carbon ions at HIMAC of the National Institute of Radiological Sciences (NIRS), Japan [6-8]; 500 MeV protons at KENS of the High Energy Accelerator Research Organization (KEK), Japan [9]; 500 MeV protons at TRIUMF, Canada [10]; 1.6-24 GeV protons at AGS of Brookhaven National Laboratory, USA [11,12]; 28.7 GeV electrons at SLAC (Stanford Linear Accelerator Center) [13,14]; 800 MeV protons at LANSCE of the Los Alamos National Laboratory (LANL), USA [15]; 120, 205 GeV/c protons and 160 GeV/nucleon lead ions at CERN, Switzerland [16,17]; 230 MeV protons at Loma Linda University Medical Center, USA [18]; 200 MeV protons at Orsay Proton Therapy Center, France [19]; and 155 MeV/nucleon He, C and O ions at the National Superconducting Cyclotron Laboratory (NSCL), USA [20]. These experiments are summarised in Tables 1-3 on the physical properties of neutron sources, shielding materials and neutron detectors.

The outlines of these deep penetration experiments were summarised in our review paper, Ref. [21]. In this paper, the attenuation lengths obtained by these deep penetration experiments are summarised and the outlines for the ISIS, HIMAC and SLAC experiments are described, which give the neutron energy spectra penetrated through the shield. The new high-energy neutron spectrometers, the self-TOF detector, the C and Bi spallation detectors and the large organic liquid scintillator, which were used in these three experiments, are described in another review paper, Ref. [22].

Table 1. Physical properties of neutron sources, shielding materials and neutron detectors for projectile energies below 100 MeV

Site	Accelerating particle	Target (thickness)	Neutron source	Shield (thickness)	Detector
CYRIC	25, 35 MeV proton	Li (2 mm)	Quasi-monoenergetic collimated beam at 0 deg.	concrete (10-40 cm) iron (25-100 cm)	NE213 (5.08 cm diameter x 5.08 cm long) proton recoil proportional counter (7cm diameter, 4.5 atm H_2 gas and 0.5 atm CH_4 gas) Bonner Ball (5.08 cm diameter, 10 atm. ^{3}He counter)
TIARA	43 MeV proton	Li (3.6 mm)	Quasi-monoenergetic collimated beam at 0 deg.	concrete (25-200 cm) iron (10-130 cm) polyethylene (30.5 - 183.0 cm)	BC501A (12.7 cm diameter x 12.7 cm long) Bonner Ball (5.08 cm diameter, 10 atm. ^{3}He counter)
	68 MeV proton	Li (5.2 mm)			

Table 2. Physical properties of neutron sources, shielding materials and neutron detectors for projectile energies between 100 and 500 MeV

Site	Accelerating particle	Target (thickness)	Neutron source (measured angle)	Shield (thickness)	Detector
Loma Linda	230 MeV proton	Al, Fe, Pb (stopping length 10.2 cm diam.)	White spectrum (0, 22, 45, 90 deg.)	Concrete (39 - 515 g/cm^2 1.88 g/cm^3 density)	TEPC (1, 100, 1000 cm^3)
Orsay	200 MeV proton	Al (9 cm diam. x 15 cm long) Water (20 x 20 cm^2 x 32 cm)	White spectrum (0, 22.5, 45, 67.5, 90 deg.)	Concrete (0 - 300 cm)	Ion chamber (515 cm^3) TEPC (56.9 mm diam.) TEPC (NAUSICAA, 5 cm diam. x 5 cm long) Rem counter (2202D) Rem counter with lead (LINUS) LiF TLD with moderators
HIMAC	400 MeV/nucleon C	Cu (10 x 10 cm^2 x 5cm)	White spectrum (0 deg.)	Concrete (50 - 200 cm) Iron (20 - 100 cm)	TEPC (12.55 cm diam.) NE213 (12.7 cm diam. x 12.7 cm long) Activation detectors of Bi, C (8 cm diam. x 1 cm thick) Self - TOF
NSCL	155 MeV/nucleon He, C, O	Hevimet (5.08 cm x 5.093 cm)	White spectrum (44 to 94 deg.)	Concrete (308 - 1057 g/cm^2 2.4 g/cm^3 density)	Bonner Ball LiI(Eu) 2, 3, 5, 8, 10, 12 inch

Table 3. Physical properties of neutron sources, shielding materials and neutron detectors for projectile energies above 500 MeV

Site	Accelerating particle	Target (thickness)	Neutron source (measured angle)	Shield (thickness)	Detector
TRIUMF	500 MeV proton	-	White spectrum (-)	Concrete (-)	Bonner Ball loading ^{6}LiI(Eu) ^{11}C activation of NE102A (5cm diam. x 5cm long)
KENS	500 MeV proton	W (stopping length)	White spectrum (0 deg.)	Concrete (0 - 4 m)	Activation detectors of Bi, Al, Au
LANSCE	800 MeV proton	Cu (21 cm diam. x 60 cm length)	White spectrum (90 deg.)	Iron (4 - 5 m)	6 ton water Cherenkov detector
ISIS	800 MeV proton	Ta (9 cm diam. x 30 cm length)	White spectrum (90 deg.)	Concrete (20 - 120 cm) Iron (10 - 60 cm) After 284 cm thick iron and 97 cm thick concrete	Activation detectors of Bi, Al, Au Bonner Ball loading In Rem counter
AGS	1.6, 12,24 GeV proton	Hg (20 cm diam. x 130 cm length)	White spectrum (0 deg.)	Steel (0 - 3.7 m)	Activation detectors of Bi, In, Al, Au
			White spectrum (90 deg.)	Concrete (0 - 5 m) Steel (0 - 3.3 m)	
SLAC	28.7 GeV Electron	Al (38 cm diam. x 145 cm length)	White spectrum (90 deg.)	Concrete (274, 335, 396 cm)	NE213 (12.7 cm diam. x 12.7 cm long) Bonner Ball loading ^{6}LiI(Eu)
CERN	120, 205 GeV/c proton	Cu (7 cm diam. x 50 cm length)	White spectrum (90 deg.)	Iron (40 cm) Concrete (80 cm)	TEPC (HANDI) Bonner Ball loading ^{3}He counter Rem counter with lead (LINUS) ^{209}Bi and ^{232}Th fission chambers
	160 GeV/nucleon lead	Pb (-)	White spectrum (-)	Concrete (-)	

Experiments using 400 MeV/nucleon carbon ions at HIMAC [6-8]

Neutron energy spectra penetrated through concrete and iron shields were measured by our group [6-8] at the HIMAC facility of the National Institute of Radiological Sciences using four types of detectors: the self-TOF detector [23,24], a 12.7 cm diameter × 12.7 cm long NE213 organic liquid scintillator [25], Bi and C activation detectors [26] as high-energy neutron spectrometers and a 12.55 cm diameter spherical TEPC (Far West Technology) as a neutron dose meter.

Figure 1 shows the experimental arrangements of a concrete shield at the HIMAC PH-2 beam course using the self-TOF, NE213 and activation detectors, respectively. The neutrons were produced by bombarding 400 MeV/nucleon ^{12}C ion beams on thick (stopping-length) copper target. The target size was 10 cm × 10 cm and 5 cm thick. A transmission-type ionisation chamber was placed behind the end window of a beam line as a beam monitor. An NE102A plastic scintillator (100 mm × 100 mm and 3 mm thick) was also used as a relative monitor.

Figure 1. Experimental arrangement at HIMAC of (a) the self-TOF detector, (b) an NE213 detector and (c) the Bi and C activation detectors

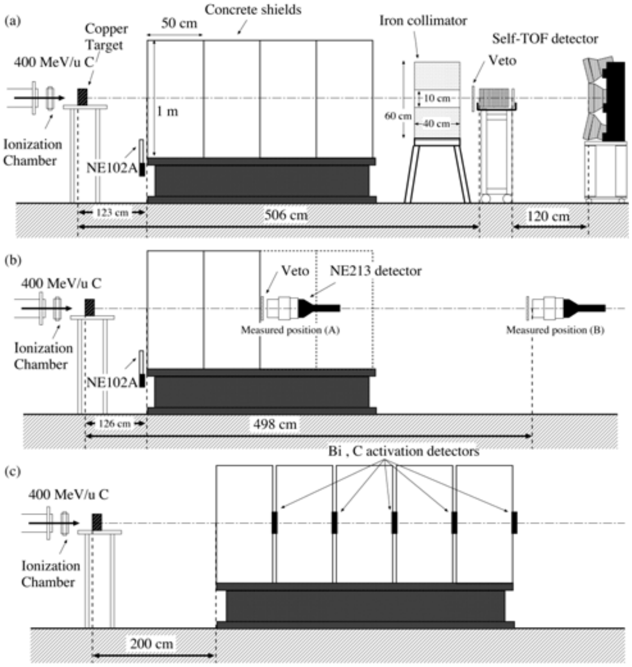

The self-TOF detector was placed 506 cm downstream from the target front face on the beam axis. This radiation field is known to have a lot of charged particles generated by fragmentation reactions, especially in the forward direction. An iron collimator of 60 cm × 60 cm and 40 cm thickness with a hole of 10 cm × 10 cm was set in front of the self-TOF detector to decrease the accidental signals that were induced by the incidence of fragment-charged particles on the stop counters, as well as to inject neutrons in a near normal fashion into the detector. The veto counter (a 150 mm × 150 mm and 5 mm thick NE102A plastic scintillator) was placed in front of the radiator to remove charged particles from the neutrons.

During the experiment, the self-TOF detector was fixed at the same position. On the other hand, the NE213 detector was placed in contact with the shielding surface [measured position (A)] and distant from the shielding surface [measured position (B), 5 m downstream of the copper target]. [See Figure 1(b) on the beam axis.] Measured position (B) is selected for comparison with the self-TOF results. The TEPC was placed at measured position (A). Five pairs of Bi and C activation detectors were inserted between each concrete shield of 50 cm thickness (50, 100, 150 and 200 cm thickness) and behind the most downstream shield of 250 cm thickness on the beam line, simultaneously [see Figure 1(c)]. After 10 hours of irradiation, measurements of the gamma-rays from the activation detectors were carried out with two high-purity germanium (HPGe) detectors.

The concrete shield slab (100 cm × 100 cm) was put onto the steel platform to fix the centre of the shield on the beam axis. The self-TOF detector and the NE213 detector were used to measure neutron energy spectra penetrating through shields up to 200-cm thick, the Bi and C detectors were used to measure neutron energy spectra penetrating through shields up to 250-cm thick and the TEPC was used to measure an absorbed-dose distribution (y-distribution) and dose equivalent behind the shield [8]. The assembly of iron shields (100 cm × 100 cm and 10 cm thickness) was put onto the steel platform to fix the centre of the shield on the beam axis. The thickness of iron shield assembly was changed to 20, 40, 60, 80 and 100 cm. The mass densities of the concrete and iron shields were 2.3 and 7.8 g cm^{-3}.

The neutron energy spectra measured by the self-TOF detector and the NE213 detector at measured position (B) are shown in Figure 2 and compared with the results of the MCNPX 2.1.5 calculation [27], since the measured position (B) of the NE213 detector is almost the same as the position where the self-TOF was set. The source neutron spectrum measured at 0° on the beam axis by Kurosawa, *et al.* [28], is also shown in the figure. In the energy ranges above 600 MeV and below 100 MeV, the self-TOF detector was unable to provide the neutron energy spectra. This may be caused by the insufficient number of neutrons above 600 MeV, and by the low-detection efficiency of 0.001-0.05% [24] for neutrons below 100 MeV. The spectra had a broad peak around 200 to 300 MeV and the shape of the spectra did not change much with the thickness of the concrete or iron shield.

The spectra measured by the self-TOF and NE213 were similar in their shape and absolute values. However, the broad peaks at around 200 to 300 MeV in the self-TOF spectra could not be clearly observed in the NE213 spectra since the window function parameters used in the FORIST unfolding process [29] were set up to 50% to obtain the continuous energy spectra without oscillative fluctuation. This broad peak component was distributed widely to the lower- and higher-energy region. It appears that the MCNPX results underestimated the experimental spectra in the energy region below 100 MeV and above 400 MeV, and overestimated in the energy region between 150 and 400 MeV. By increasing the concrete shield thickness, the calculated spectra showed similarities to the experimental results up to 150 cm, but large underestimation can be seen at 200 cm thickness as shown in Figure 2(a) in the energy range below 100 MeV.

As shown in Figure 2(b), the calculations overestimated the measurements when the iron thickness was increased in the energy range below 100 MeV. But the calculations agreed fairly well with the measurements in the energy range between 100 and 400 MeV, especially in the case of a whole energy range of 20-800 MeV for a 20-cm thick iron shield. The NE213 spectrum was much higher in the energy region below ~200 MeV for 100-cm thick iron than the self-TOF spectrum because the non-collimated NE213 detector detects a lot of neutron components scattered from the shield and the room floor.

Experiments using 800 MeV protons at ISIS/RAL [5]

The shielding experiment was performed as an international collaborative work of Tohoku University, KEK, RIKEN and RAL at the ISIS spallation neutron source facility of RAL [5,30,31] The ISIS facility consists of a 70 MeV H- linear accelerator, an 800 MeV proton synchrotron and a spallation neutron target station. The beam intensity is ~170 μA at the target with a 50 Hz repetition rate. A cross-sectional view around the target station along the 800 MeV proton beam axis is shown in Figure 3. The tantalum target is assembled using a 90-mm diameter tantalum disk of various thicknesses

Figure 2. Comparison of measured and calculated neutron energy spectra, penetrating through concrete (a) and iron (b) shields

Solid lines indicate the experimental results of the self-TOF detector, dashed lines are the experimental results of NE213, dotted lines are the calculations of MCNPX and broken lines indicate the source neutron spectrum measured with the TOF method by Kurosawa, et al. [28]

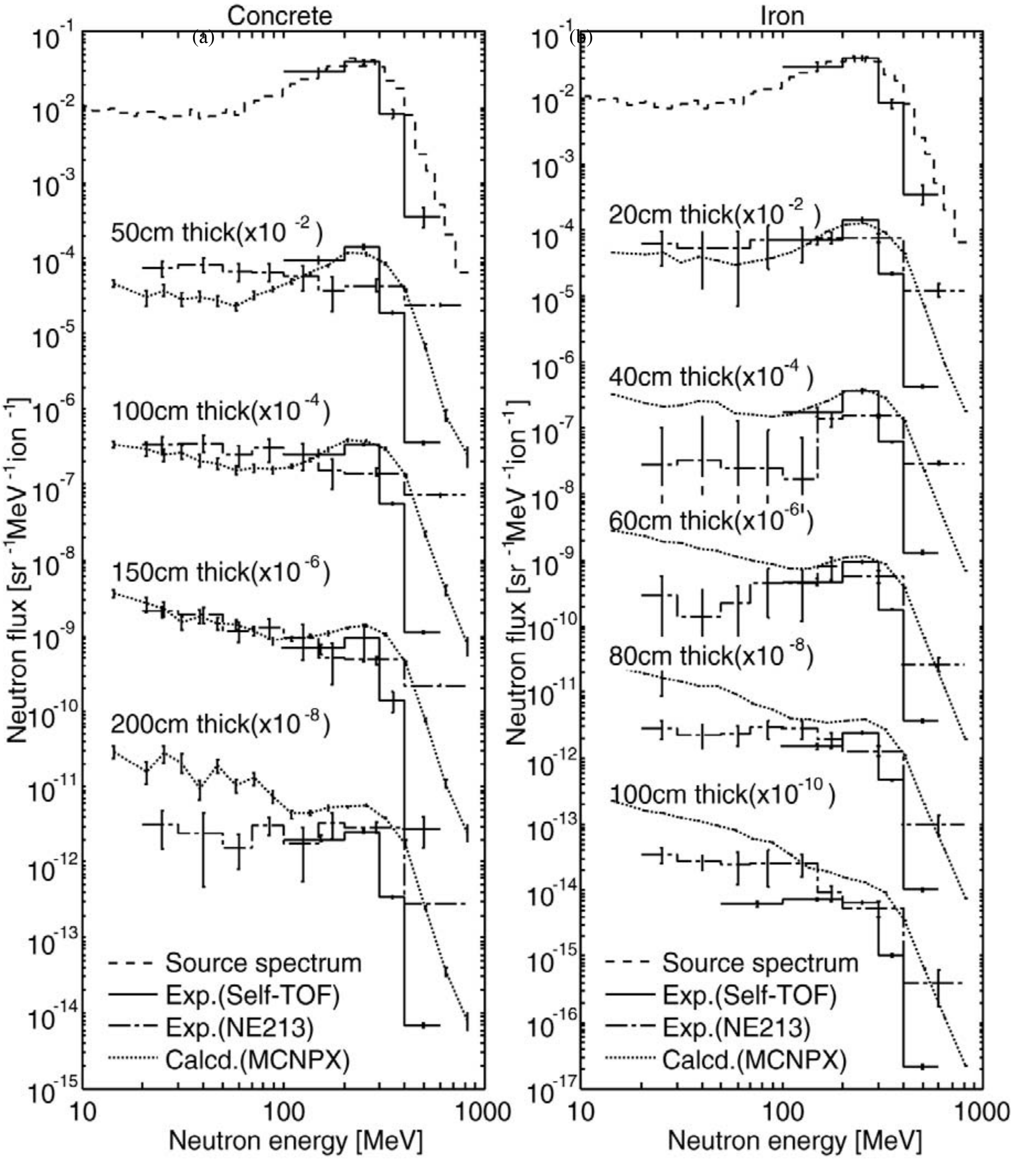

Figure 3. A cross-sectional view of the neutron spallation target station with an 800 MeV proton beam at ISIS and a vertical cross-sectional view of an iron igloo and an additional shield

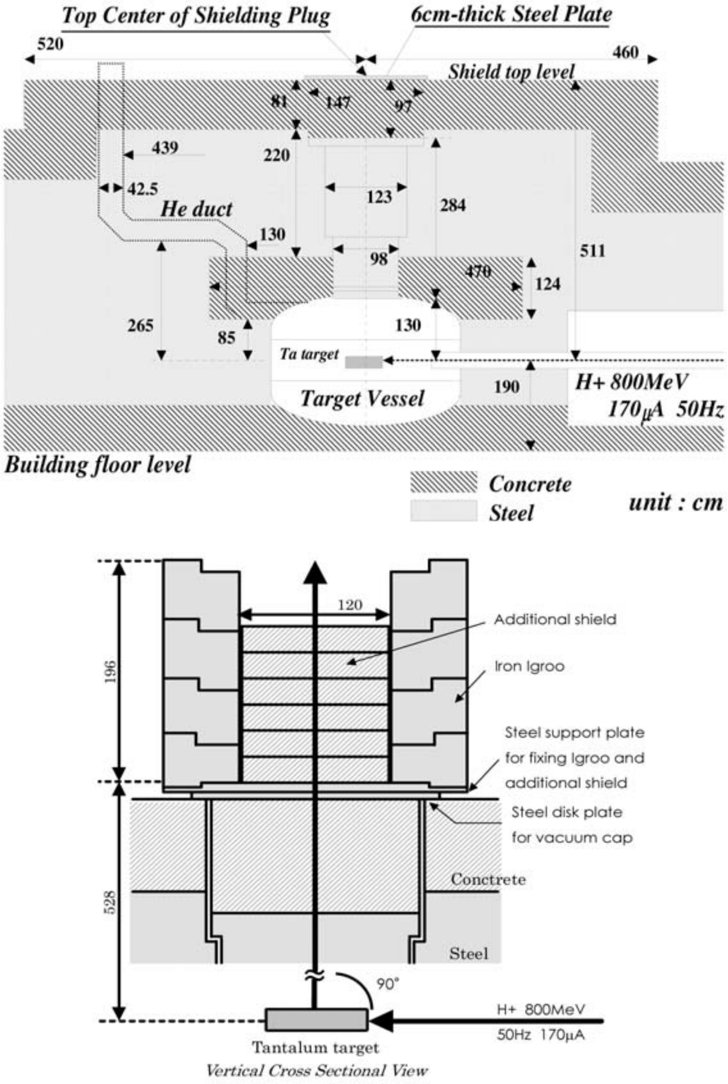

from 8.2 mm to 26.7 mm, and with a 1.75 mm gap between each disk for cooling water (D_2O) [32]. This stopping-length tantalum target (total length of 296.5 mm) is placed at the centre of the stainless steel vessel. The moderators of heavy water and beryllium reflectors are placed around the target.

The upward direction of the target station is shielded with a shielding plug of 284-cm thick steel and 97-cm thick ordinary concrete. This experiment was performed at the top of a shielding plug (shield top) just above the target station. As seen in Figure 3, a large curved duct with a ~42.5 cm × 42.5 cm cross-section, in which helium gas flows for filling the target vessel, reaches the shield top through the bulk shield downstream from the target. Neutrons that leaked from this duct became large background components in the measurement at the shield top. An iron igloo (60 cm thick, 120 cm inner diameter and 196 cm high) was set on the top centre of the target station to reduce the background neutrons. In addition, a shield of concrete or iron was piled up inside the igloo.

In this shielding experiment, the additional shielding blocks of ordinary concrete and iron were placed upon the top centre of the bulk shield just above the target, as shown in Figure 3. The additional concrete (20-120 cm thickness) and iron (10-60 cm thickness) blocks were assembled using blocks of 119 cm in diameter, 20 cm thick and 2.36 g/cm^3 in density and using blocks of 119 cm in diameter, 10 cm thick and 7.8 g/cm^3 in density, respectively. The concrete blocks contained an iron mesh for reinforcement.

Since the neutrons were produced from the target as burst pulses corresponding to 50 Hz synchrotron operation, the pulse counters could not be used. The reason was the pulse pile-up problem and the activation detectors of C, Al, Bi and the multi-moderator spectrometer inserted In were then used. The 2.875 g In_2O_3 powder is filled in a spherical cavity of 0.735 cm radius in a cylindrical acryl, which is placed in the spherical polyethylene moderator [33]. Five moderators of 9.8, 5.5, 3.2 and 2.0 cm radii, and a 0 cm radius without a moderator, were used to get the neutron energy spectrum through the unfolding technique. The response functions of these multi-moderator spectrometers were calculated using the MCNPX-2.1.5 code [27], the ENDF/B-VI data [34] and the LA-150 [35] data library. Large volume activation detectors of C, Al and Bi were adopted in order to obtain high-detection efficiencies. After neutron irradiations at the shield top, the gamma-rays from the activation detectors were measured with the high-purity germanium (HPGe) detectors.

The attenuation lengths of concrete and iron for high-energy neutrons above 20 MeV produced at 90° to the proton beam were obtained from the $^{12}C(n,2n)^{11}C$ reaction rates of graphite. The neutron spectra penetrated through concrete and iron were obtained from the reaction rates of $^{12}C(n,2n)^{11}C$, $^{27}Al(n,\alpha)^{24}Na$, $^{209}Bi(n,xn)^{210-x}Bi$ ($x = 4$–10) and $^{115}In(n,\gamma)^{116m}In$ in the energy range of thermal to 400 MeV through the unfolding by the SAND-II code [36].

The graphite activation detectors were set at various positions such as "centre", "up", "down", "left" and "right" on the additional shield surface of each thickness. Figure 4 shows the measured and calculated neutron energy spectra in lethargy unit on the shield top floor, behind the 60-cm thick additional concrete and behind the 30-cm thick additional iron at the centre position. The calculation of neutron penetration through a thick shield was performed with a three-dimensional multi-layer technique using the MARS14(02) Monte Carlo code [37] for comparison with the experimental results. The calculated energy spectrum behind the additional concrete shield agrees well with the experiment within ~40% for the energy region above 1 MeV. In general, the calculated energy spectra agree well with the measured ones within a factor of 2 over a broad energy range with the maximum differences reaching a factor of 3 (except at thermal energy).

Figure 5 shows the attenuation profiles of calculated $^{12}C(n,2n)$ reaction rates from the target vessel up to the shield top and the additional shields of iron and concrete. The measured reaction rates in the air and the iron and concrete shields above the shield top are also shown in the figure for comparison. Although the neutron flux attenuates more than a seventh order of magnitude (10^{-7}) from the source to the detection points, the agreement is surprisingly good between the calculated and measured results, especially in the iron and concrete shields.

This is the only shielding experiment performed at the high-energy electron accelerator facility as an international collaboration of Tohoku University, JASRI (Japan Synchrotron Radiation Research Institute) and SLAC [13,14]. Neutron energy and time-of-flight spectra were measured behind the lateral shield of a 28.7 GeV electron beam dump at the Final Focus Test Beam (FFTB) facility, where the electron beam was extracted from the SLAC accelerator at repetition rates of 10-30 Hz.

Figure 6 shows horizontal and vertical cross-sectional views of the FFTB dump together with the locations of the NE213 detector and the muon counter used in this study. The aluminium beam dump of

Figure 4. Comparison between the calculated and measured neutron energy spectra on the shield top floor, behind the additional concrete (60 cm thick) and iron (30 cm thick) shields at the "centre" position

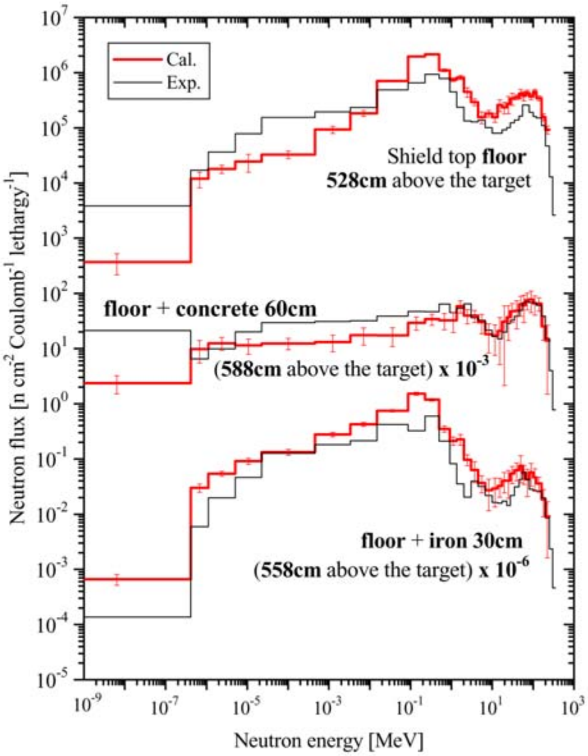

Figure 5. Comparison of the calculated and measured attenuation profiles of ^{12}C(n,2n) reaction rates through the bulk shield and the additional shield. Experiments using 28.7 GeV electrons at SLAC [13,14].

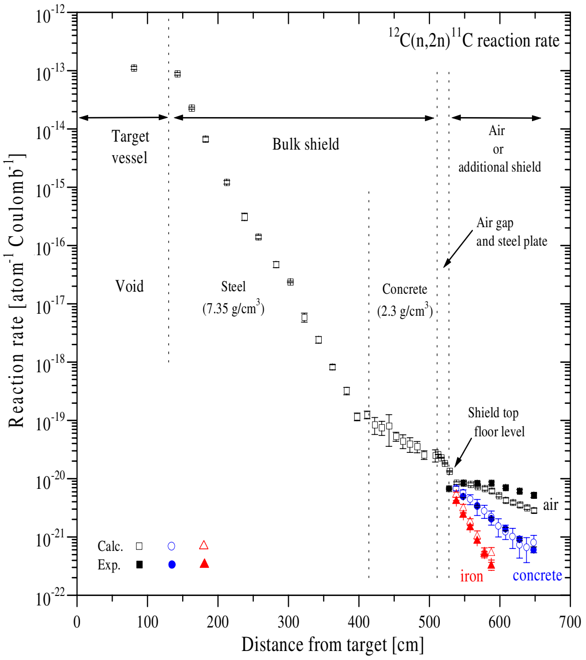

Figure 6. Horizontal and vertical cross-sectional views of the FFTB dump. The locations of the NE213 detector and the muon counter are also shown. The hatched zone indicates iron and the other zones are concrete blocks.

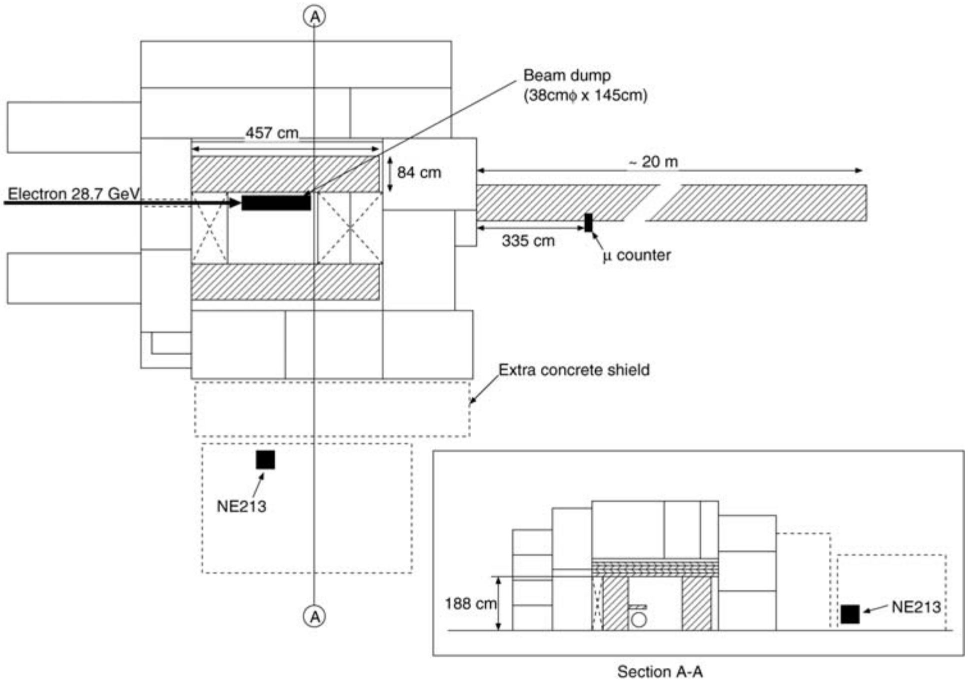

145 cm length and 38 cm diameter completely stops the electron beam. The dump is placed in a room that is shielded laterally by 84 cm of steel and is surrounded with a 183-cm thick concrete wall. Blocks of steel are placed outside the room in a forward direction to the beam line in order to attenuate muons generated in the dump.

The measurements were performed using a 12.7 cm diameter × 12.7 cm long NE213 organic liquid scintillator, which was placed ~36 cm from the concrete floor in a hutch at 90° with respect to the beam direction behind differing thicknesses of the concrete shield (274 cm, 335 cm and 396 cm). The neutron events were separated from the gamma-ray events by using two-dimensional graphical plots of total- and slow-pulse components. Pile-up events were eliminated using the two-dimensional graphical plots. The muon scintillator was set in the muon shield at a distance of 335 cm from the outer shield surface in order for it to be used as the event trigger and to generate start signals of the TOF measurements.

The neutron energy spectra per lethargy unit between 6 and 800 MeV were obtained with the unfolding technique using the FORIST code [29] and the detector response functions for 6 to 800 MeV [25]. In Figure 7, the measured neutron energy spectra in lethargy unit (points) are compared with the calculations using the FLUKA code [38] (histograms). The measured spectra generally agreed well with the calculations both in spectral shapes and in absolute values in the energy region from 6 to 200 MeV. In the energy region above 200 MeV, the measured energy spectra are lower than the calculations. This could be due in part to very poor statistics of detected counts and/or to the poor accuracy of the response function of the NE213 detector [25], which is caused by low-neutron detection efficiency in the high-energy region. For the 274 cm shield, the measured spectrum gives a somewhat smaller value than the calculated spectrum in the energy region around 20 MeV. This underestimation may arise partly from the larger contribution of the pile-up events, which could not be completely corrected because of higher counting rates.

Figure 7. Measured (points) neutron energy spectra penetrated through 274, 335 and 396-cm thick concrete shields compared with those calculated using the FLUKA code (histogram). The graph gives the measured results after a pile-up correction in units of cm^{-2}, lethargy^{-1} per one electron incident on the beam dump.

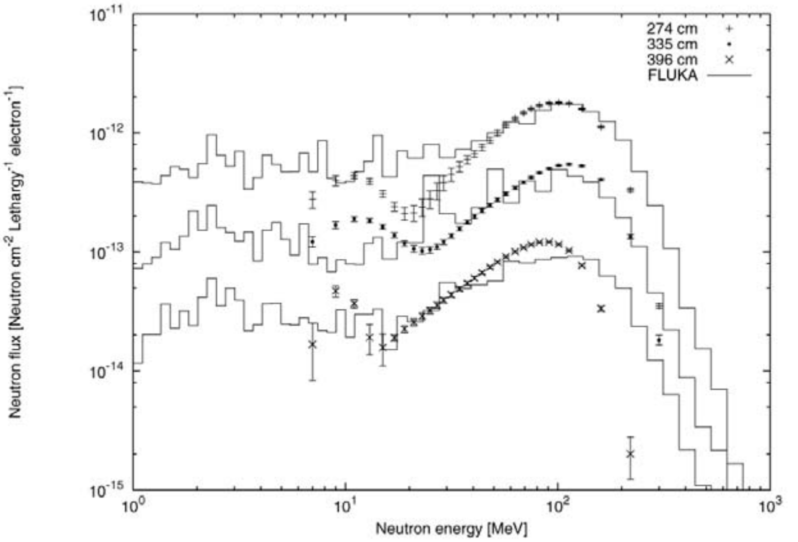

Attenuation lengths of neutron flux and dose equivalent

These experiments described in the previous sections give the attenuation lengths of neutron flux and dose equivalent/ambient dose, but the direct comparison of these attenuation lengths is not possible because the projectile types used in these experiments differ from each other. For direct comparison, we therefore estimated the source neutron energy spectra produced from the targets and aimed to express the attenuation length as a function of the effective maximum value, E_{max}, of the source neutron energy. The E_{max} value was approximated as follows: 1) a sharp-peak neutron energy for p-Li quasi-monoenergetic source neutrons at CYRIC and TIARA, 2) the neutron energy having 1/100 of the energy at the peak position in the neutron energy spectrum in lethargy unit when the neutron spectrum has a clear peak at the high-energy end as in the HIMAC experiment (Figure 2) and 3) the neutron energy at the position having 1/100 of the neutron flux in lethargy unit at 20 MeV when the neutron spectrum has no clear peak as typically seen in the white spectrum for all other experiments. For the last cases, the source neutron energy spectrum in lethargy unit was estimated by using each experimental condition of the projectile type and energy, as well as target type and thickness. In this estimation, the MARS Monte Carlo code [37] was used for the ISIS experiment in the section entitled *Experiments using 800 MeV protons at ISIS/RAL*, and the PHITS Monte Carlo code [39] was used for the other experiments.

Tables 4 and 5 summarise the attenuation lengths of neutron dose equivalent/ambient dose and neutron flux above 20 MeV for concrete and iron shields, respectively, which have been obtained in previous experiments and calculations. Figure 8 shows the dose attenuation length λ_D as a function of E_{max}. The λ_D values for concrete keep an almost constant value of ~30 g/cm^2 up to several tens of MeV, and gradually increase above 100 MeV, they then reach ~130 g/cm^2 beyond a few hundreds MeV, which may be the high-energy limit. While for iron the λ_D values increase slightly up to ~100 g/cm^2 at several tens of MeV, a big deviation can be seen between ~210 g/cm^2 for the HIMAC experiment and 340 g/cm^2 for the ISIS experiment in the energy region of several hundreds of MeV. This phenomenon may be influenced by the experimental conditions. Figure 9 shows the flux attenuation length λ_ϕ as a function of E_{max}. The λ_ϕ values for concrete increase from ~20 g/cm^2 at 20 MeV to ~120 g/cm^2 above 300 MeV, and

Table 4. Comparison of attenuation lengths for neutron dose rates obtained by various experiments and calculations

Shielding Material	Facility	Incident particle	Angle [deg]	Maximam neutron energy	lambda [g/cm2]	Density [g/cm3]	Detector	Ref
Concrete	SLAC	e28.7 GeV	90	400 MeV	129 ± 4	2.35	NE213	13
	HIMAC	C400 MeV/u	0	700 MeV	126 ± 9	2.25	TEPC	8
	HIMAC	C400 MeV/u	0	700 MeV	115.2 ± 0.8	2.25	Calculated	8
	ISIS	p800 MeV	90	370 MeV	120 ± 13	2.36	Rem counter	5,29,30
	ISIS	p800 MeV	90	370 MeV	116.7 ± 3.4	2.36	Calculated	5,29,30
	Loma Linda	p230 MeV	0	230 MeV	89.1 ± 1.8	1.88	TEPC	18
	Loma Linda	p230 MeV	22	230 MeV	86 ± 4	1.88	TEPC	18
	Loma Linda	p230 MeV	45	215 MeV	73 ± 6	1.88	TEPC	18
	Orsay	p200 MeV	0	200 MeV	90 ± 3	2.2	TEPC	19
	Orsay	p200 MeV	22.5	200 MeV	96 ± 3	2.2	TEPC	19
	Orsay	p200 MeV	45	190 MeV	100 ± 23	2.2	TEPC	19
	Orsay	p200 MeV	67.5	170 MeV	82 ± 13	2.2	TEPC	19
	Loma Linda	p230 MeV	90	130 MeV	51.9 ± 1.5	1.88	TEPC	18
	Orsay	p200 MeV	90	120 MeV	68 ± 6	2.2	TEPC	19
	TIARA	p68 MeV	0	65 MeV	37.9	2.31	NE213	2
	TIARA	p43 MeV	0	40 MeV	29.5	2.31	NE213	2
	CYRIC	p35 MeV	0	32.5 MeV	31.5	2.31	NE213	1
	CYRIC	p25 MeV	0	22 MeV	27.3	2.4	NE213	1
Iron	HIMAC	C400 MeV/u	0	700 MeV	211 ± 10	7.8	TEPC	8
	HIMAC	C400 MeV/u	0	700 MeV	209.2 ± 1.5	7.8	Calculated	8
	ISIS	p800 MeV	90	370 MeV	343 ± 11	7.8	Rem counter	5,29,30
	ISIS	p800 MeV	90	370 MeV	278 ± 13	7.8	Calculated	5,29,30
	TIARA	p68 MeV	0	65 MeV	102.3	7.87	NE213	2
	TIARA	p43 MeV	0	40 MeV	95.1	7.87	NE213	2
	CYRIC	p35 MeV	0	32.5 MeV	76.7	7.75	NE213	1
	CYRIC	p25 MeV	0	22 MeV	75.5	7.75	NE213	1

Table 5. Comparison of attenuation lengths of neutron fluxes above 20 MeV obtained by various experiments and calculations

Shielding material	Facility	Incident particle	Angle [deg]	Maximum neutron energy	Lambda [g/cm2]	Density [g/cm3]	Detector	Ref.
Concrete	SLAC	e28.7 GeV	90	400 MeV	124 ± 4	2.35	NE213	13
	HIMAC	C400 MeV / u	0	700 MeV	124.4	2.25	NE213	6
	HIMAC	C400 MeV / u	0	700 MeV	113.1 ± 0.9	2.25	Calculated	6
	KEK	p12 GeV	90	500 MeV	143	2.35	C, Al	39
	KEK	p500 MeV	0	500 MeV	123	2.35	C, Al	40
	CERN	p25 GeV	90	420 MeV	120	–	C, Al	41
	ISIS	p800 MeV	90	370 MeV	125.4 ± 5.1	2.36	C	5,29,30
	ISIS	p800 MeV	90	370 MeV	116.7 ± 3.4	2.36	Calculated	5,29,30
	ISIS	p800 MeV	90	370 MeV	116.1 ± 3.9	2.36	Calculated	5,29,30
	KEK	p500 MeV	90	230 MeV	90	2.35	C, Al	41
	TIARA	p68 MeV	0	65 MeV	39	2.31	NE213	2
	INS	p52 MeV	0	52 MeV	48.1	2.3	NE213	42
	TIARA	p43 MeV	0	40 MeV	29	2.31	NE213	4
	CYRIC	p35 MeV	0	32.5 MeV	31	2.4	NE213	1
	CYRIC	p25 MeV	0	22 MeV	27	2.4	NE213	1
Iron	HIMAC	C400 MeV / u	0	700 MeV	160.5	7.8	NE213	7
	HIMAC	C400 MeV / u	0	700 MeV	155.4 ± 1.9	7.8	Calculated	7
	KEK	p12 GeV	90	500 MeV	188 ± 12	7.01~7.15	C, Al	39
	CERN	p25 GeV	90	42 MeV	147 ± 10	–	C, Al	41
	ISIS	p800 MeV	90	370 MeV	161.1 ± 2.1	7.8	C	5,29,30
	ISIS	p800 MeV	90	370 MeV	150.3 ± 5.8	7.8	Calculated	5,29,30
	ISIS	p800 MeV	90	370 MeV	156.7 ± 5.5	7.8	Calculated	5,29,30
	LANSCE	p800 MeV	90	315 MeV	148 ± 2	7.18	Cherenkov	15
	KEK	p500 MeV	90	230 MeV	116	7.01~7.15	C, Al	40
	TIARA	p68 MeV	0	65 MeV	68	7.87	NE213	2
	INS	p52 MeV	0	52 MeV	68.1	7.14	NE213	42
	TIARA	p43 MeV	0	40 MeV	55	7.87	NE213	2
	CYRIC	p35 MeV	0	32.5 MeV	58	7.75	NE213	1
	CYRIC	p25 MeV	0	22 MeV	47	7.75	NE213	1

Figure 8. Comparison of attenuation lengths for neutron dose rates of concrete and iron as a function of the effective maximum energy of source neutrons

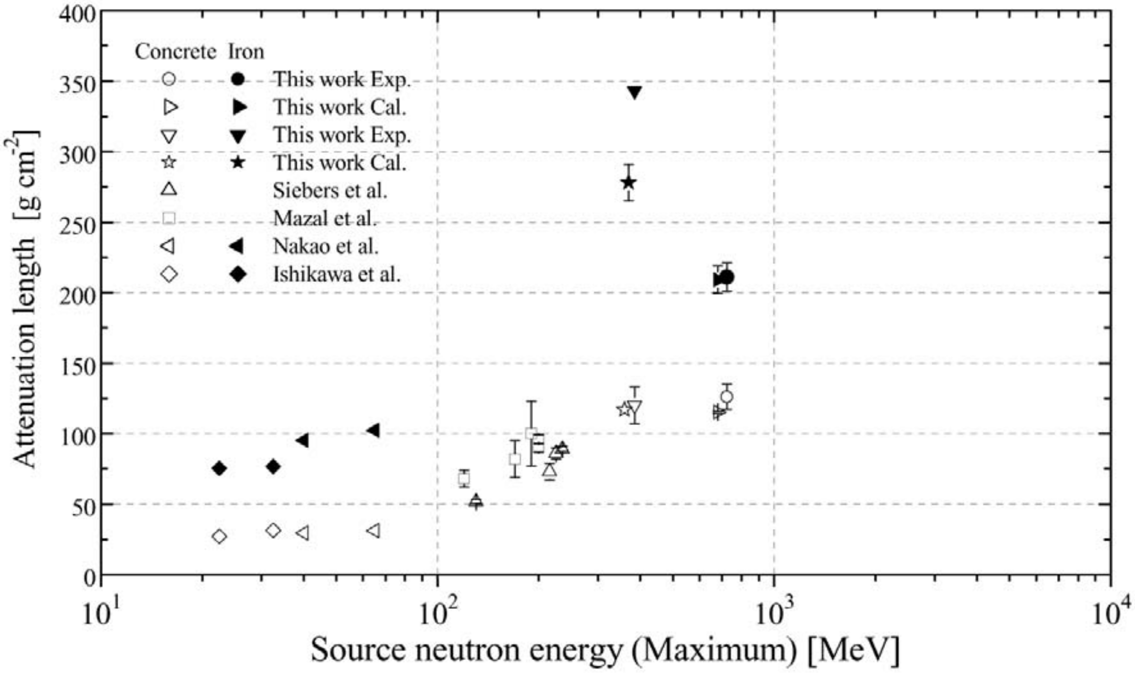

Figure 9. Comparison of attenuation lengths for neutron flux above 20 MeV for concrete and iron as a function of the effective maximum energy of source neutrons

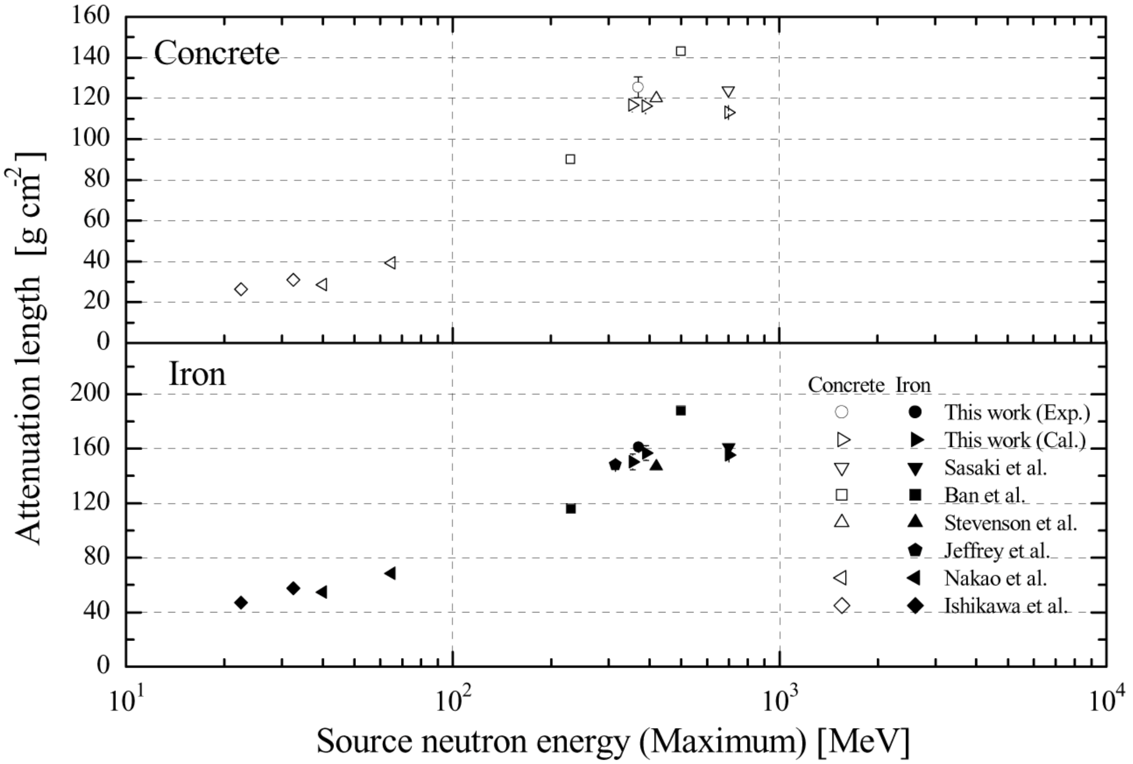

for iron from ~40 g/cm^2 at 20 MeV to ~160 g/cm^2 above 300 MeV, except for the 12 GeV proton experiment at the proton synchrotron facility (PS) of KEK [40]. In this experiment the shield thickness was not altered, but the detector position was transversely changed behind the constant shield thickness to increase the effective thickness. This may have had some effect on the attenuation profile.

The high-energy limits of λ_D and λ_ϕ values for concrete are very close together, but for iron λ_D values are much higher than λ_ϕ values. This is because the neutron spectrum transmitted through iron has a dominant peak around several hundreds of keV as clearly seen in Figure 4.

The summarised data of λ_D and λ_ϕ values will be quite useful for the shielding design study of a high-energy accelerator facility since attenuation length determines the shield thickness of the building.

Summary and future work

Below the 100 MeV energy region, shielding experiments have already been performed using p-Li quasi-monoenergetic neutron sources for 25, 35, 45 and 68 MeV protons at CYRIC [1] and TIARA [2-4]. However, above the 100 MeV energy region, shielding experiments have been performed only by using the white (continuous spectrum) neutron sources. Among these shielding experiments, the best benchmark experiments above a 100 MeV energy region that investigate the calculational accuracy of various transport codes are: the three experiments at HIMAC mentioned in the section *Experiments using 400 MeV/nucleon carbon ions at HIMAC*, the experiment at ISIS mentioned in the section *Experiments using 800 MeV protons at ISIS/RAL* and the experiment at SLAC mentioned in the section *Experiments using 28.7 GeV electrons at SLAC*. Only the HIMAC experiment gives both the source spectrum and the energy spectra behind the shield with various thicknesses under a simple experimental geometry, thus providing the best benchmark data (although the energy range is limited to 20 MeV). The ISIS and SLAC experiments were unable to give the source spectra, but did provide the energy spectra behind the shield with various thicknesses under a simple experimental geometry. The AGS experiments [11,12] may also generate good benchmark data, but at the present stage the experimental results are under analysis.

The plan of our group is to perform the shielding experiment using p-Li quasi-monoenergetic neutrons up to 400 MeV protons from the cyclotron at the Research Center of Nuclear Physics (RCNP) of Osaka University. In fact, a preliminary experiment has just begun. The unique deep penetration experiment at KENS/KEK continues in the forward direction to the incident proton beam [9]. These new results will be useful as benchmark shielding experiments for investigating the accuracy of transport calculation codes.

Acknowledgements

We wish to express our appreciation to Drs. N. Nakao, M. Sasaki and S. Taniguchi for providing their experimental results in electronic format, which are cited in this review paper. We are also grateful to Mr. H. Yamakawa for preparing this paper.

REFERENCES

[1] Ishikawa, T., Y. Miyama, T. Nakamura, "Neutron Penetration through Iron and Concrete Shields with Use of 22.0- and 32.5-MeV Quasi-Monoenergetic Sources", *Nucl. Sci. Eng*., 116, 278 (1994).

[2] Nakao, N., H. Nakashima, T. Nakamura, Sh. Tanaka, Su. Tanaka, K. Shin, M. Baba, Y. Sakamoto, Y. Nakane, "Transmission through Shields of Quasi-monoenergetic Neutrons Generated by 43- and 68-MeV Protons – I: Concrete Shielding Experiment and Calculation for Practical Application", *Nucl. Sci. Eng*., 124, 228 (1996).

[3] Nakashima, H., N. Nakao, Sh. Tanaka, T. Nakamura, K. Shin, Su. Tanaka, H. Takada, S. Meigo, Y. Nakane, Y. Sakamoto, M. Baba, "Transmission through Shields of Quasi-monoenergetic Neutrons Generated by 43- and 68-MeV Protons – II: Iron Shielding Experiment and Analysis for Investigating Calculational Method and Cross-section Data", *Nucl. Sci. Eng*., 124, 243 (1996).

[4] Nakao, N., M. Nakao, H. Nakashima, Su. Tanaka, Y. Sakamoto, Y. Nakane, Sh. Tanaka, T. Nakamura, "Measurements and Calculations of Neutron Energy Spectra Behind Polyethylene Shields Bombarded by 40- and 65-MeV Quasi-monoenergetic Neutron Sources", *J. Nucl. Sci. Technol*., 34 (4), 348 (1997).

[5] Nunomiya, T., N. Nakao, P. Wright, T. Nakamura, E. Kim, T. Krosawa, S. Taniguchi, M. Sasaki, H. Iwase, Y. Uwamino, T. Shibata, S. Ito, D.R. Perry, "Measurement of Deep Penetration of Neutrons Produced by 800-MeV Proton Beam through Concrete and Iron at ISIS", *Nucl. Instr. and Meth*., B179, 89 (2001).

[6] Sasaki, M., E. Kim, T. Nunomiya, T. Nakamura, N. Nakao, T. Shibata, Y. Uwamino, S. Ito, A. Fukumura, "Measurements of High Energy Neutrons Penetrated Through Concrete Shields Using Self-TOF, NE213, and Activation Detectors", *Nucl. Sci. Eng*., 141, 140 (2002).

[7] Sasaki, M., N. Nakao, T. Nunomiya, T. Nakamura, A. Fukumura, M. Takada, "Measurements of High-energy Neutrons Penetrated through Iron Shields Using Self-TOF Detector and NE213 Organic Liquid Scintillator", *Nucl. Instr. and Meth*., B196, 113 (2002).

[8] Nunomiya, T., S. Yonai, M. Takada, A. Fukumura, T. Nakamura, "Shielding Experiment of Heavy-ion Produced Neutrons Using a Tissue Equivalent Proportional Counter", *Radiat. Protec. Dosim*., 106, 207 (2003).

[9] Nakao, N., *et al*., "Shielding Experiment at the High-energy Neutron Beam Course of KENS", *Proceedings of the 16th Meeting of the International Collaboration on Advanced Neutron Sources (ICANS-16)*, Dusseldorf-Neuss, Germany, 12-15 May 2003, at press.

[10] Moritz, L.E., "Measurement of Neutron Leakage Spectra at a 500-MeV Proton Accelerator", *Health Phys*., 56 (3), 287 (1989).

[11] Nakashima, H., *et al.*, “Research Activities on Neutronics under ASTE Collaboration at AGS/BNL”, *J. Nucl. Sci. Technol.*, Suppl. 2, 1155 (2002).

[12] Nakashima, H., *et al.*, “Current Status of the AGS Spallation Target Experiment”, *Proceedings of the 6th Specialists Meeting on Accelerators, Targets and Irradiation Facilities (SATIF-6)*, April 2002, Stanford, USA.

[13] Taniguchi, S., T. Nakamura, T. Nunomiya, H. Iwase, S. Yonai, M. Sasaki, S.H. Rokni, J.C. Liu, K.R. Kase, S. Roesler, “Neutron Energy and Time-of-flight Spectra Behind the Lateral Shield of a High-energy Electron Accelerator Beam Dump, Part I: Measurements”, *Nucl. Instr. and Meth.*, A503, 595 (2003).

[14] Roesler, S., J.C. Liu, S.H. Rokni, S. Taniguchi, “Neutron Energy and Time-of-flight Spectra behind the Lateral Shield of a High-energy Electron Accelerator Beam Dump, Part II: Monte Carlo Simulations”, *Nucl. Instr. and Meth.*, A503, 606 (2003).

[15] Bull, J.S., J.B. Donahue, R.L. Bourman, “Measurement of Neutron Attenuation through Thick Shields and Comparison with Calculation”, *Proceedings of 4th Workshop Simulating Accelerator Radiation Environments (SARE-4)*, Knoxville (TN, USA), 14-16 September, p. 201 (1998).

[16] Birattari, C., A. Ferrari, M. Hoefert, T. Otto, T. Rancati, M. Silari, “Recent Results at the CERN-EC High-energy Reference Field Facility”, *Proceedings of the 3rd Specialists Meeting on Accelerators, Targets and Irradiation Facilities (SATIF-3)*, Sendai, Japan, May 1997, p. 219 (1998).

[17] Aroua, A., T. Buchillier, M. Grecescu, M. Hoefert, “Neutron Measurements around a High-energy Lead Ion Beam at CERN”, *Radiat. Protec. Dosim.*, 70, 437 (1997).

[18] Siebers, J.V., P.M DeLuca, Jr., D.W. Pearson, G. Coutrakon, “Shielding Measurements for 230-MeV Protons”, *Nucl. Sci. Eng.*, 115, 13 (1993).

[19] Mazal, A., K. Gall, J.F. Bottollier-Depois, S. Michaud, D. Delacroix, P. Fracas, F. Clapier, S. Delacroix, C. Nauraye, R. Ferrand, M. Louis, J.L. Habrand, “Shielding Measurements for a Protontherapy Beam of 200 MeV: Preliminary Results”, *Radiat. Protec. Dosim.*, 70, 429 (1997).

[20] Britvich, G.I., A.A. Chumakov, R.M. Ronningen, R.A. Blue, L.H. Heilbronn, “Measurements of Thick Target Neutron Yields and Shielding Studies Using Beams of 4He, 12C and 16O at 155 MeV/nucleon from the K1200 Cyclotron at the National Superconducting Cyclotron Laboratory”, *Rev. Sci. Instr.*, 70, 2314 (1999).

[21] Nakamura, T., T. Nunomiya, H. Yashima, S. Yonai, “Overview of Recent Experimental Works on High-energy Neutron Shielding”, *Prog. Nucl. Energy*, 44 (2), 85 (2004).

[22] Nakamura, T., “Recent Development of Advanced Neutron Detection Technology”, *J. Nucl. Radiochem. Sci.*, 4 (2), R15 (2003).

[23] Sasaki, M., M. Nakao, T. Shibata, N. Nakao, T. Nakamura, “Feasibility Studies of the Self-TOF Detector for High-energy Neutron Measurements in Shielding Experiments”, *Nucl. Instr. and Meth.*, A446, 545 (2000).

[24] Sasaki, M., N. Nakao, T. Nunomiya, T. Nakamura, T. Shibata, A. Fukumura, “Response Function Measurements of the Self-TOF Neutron Detector for Neutrons up to 800 MeV”, *J. Nucl. Sci. Technol.*, 38 (1), 8 (2001).

[25] Sasaki, M., N. Nakao, T. Nakamura, T. Shibata, A. Fukumura, "Measurements of the Response Functions of an NE213 Organic Liquid Scintillator to Neutrons up to 800 MeV", *Nucl. Instr. and Meth.*, A480, 440 (2002).

[26] Kim, E., T. Nakamura, A. Konno, Y. Uwamino, N. Nakanishi, M. Imamura, N. Nakao, T. Shibata, Su. Tanaka, "Measurements of Neutron Spallation Cross-sections of ^{12}C and ^{209}Bi in the 20- to 150-MeV Energy Range", *Nucl. Sci. Eng.*, 129, 209 (1998).

[27] *MCNPXTM User's Manual,* TPO-E83-G-UG-X-00001, Los Alamos National Laboratory, Waters, L.S., ed. (1999).

[28] Kurosawa, T., N. Nakao, T. Nakamura, Y. Uwamino, T. Shibata, A. Fukumura, K. Murakami, "Measurements of Secondary Neutrons Produced from Thick Targets Bombarded by High-energy Helium and Carbon Ions", *Nucl. Sci. Eng.*, 132, p. 30 (1999).

[29] Johnson, R.H., *FORIST: Neutron Spectrum Unfolding Code – Iterative Smoothing Technique*, PSR-92, ORNL/RSIC, Oak Ridge National Laboratory (1976).

[30] Nunomiya, T., N. Nakao, P. Wright, T. Nakamura, E. Kim, T. Krosawa, S. Taniguchi, M. Sasaki, H. Iwase, Y. Uwamino, T. Shibata, S. Ito, D.R. Perry, *Experimental Data of Deep-penetration Neutrons through a Concrete and Iron Shield at the ISIS Spallation Neutron Source Facility Using an 800-MeV Proton Beam*, KEK Report 2001-24 (2002).

[31] Nunomiya, T., N. Nakao, H. Iwase, T. Nakamura, *Deep-penetration Calculation for the ISIS Target Station Shielding Using the MARS Monte Carlo Code*, KEK Report 2002-12 (2003).

[32] Carne, A., G.H. Eaton, F. Atchison, T.A Broome, D.J. Clarke, B.R. Diplock, B.H. Poulten, K.H. Roberts, *SNS Target Station Safety Assessment*, Support Document to *SNS Target Station Hazard Survey*, SNS/ENV/N1/83 Rev. 1, SNSPC/P6/82 (1983).

[33] Uwamino, Y., T. Nakamura, A. Hara, "Two Types of Multi-moderator Neutron Spectrometers: Gamma-ray Insensitive Type and High-efficiency Type", *Nucl. Instr. Meth.*, A239, 299 (1985).

[34] *Evaluated Nuclear Data File ENDF/B-VI*, National Neutron Cross-section Center, Brookhaven National Laboratory (1990).

[35] Chadwick, M.B., L.J. Cox, P.G. Young, A.S. Meigooni, "Calculation and Evaluation of Cross-sections and Kerma Factors for Neutrons up to 100 MeV on Carbon", *Nucl. Sci. Eng.*, 123, 17 (1996).

[36] McElroy, W.N., S. Berg, T. Crockett, R.G. Hawkins, *A Computer Automated Interactive Method for Neutron Flux Spectra Determination by Foil Activation*, AFWL-TR-67-41, Air Force Weapons Laboratory (1967).

[37] Mokhov, N.V., *The MARS Code System User's Guide*, Fermilab-FN-628 (1995); N.V. Mokhov, O.E. Krivosheev, *MARS Code Status*, Fermilab-Conf-00/181 (2000). See details at the web page http://www-a/MARS.

[38] Fasso, A., A. Ferrari, J. Ranft, P.R. Sala, "FLUKA: Status and Perspectives for Hadronic Applications", *Proceedings of the International Conference on Advanced Monte Carlo for Radiation Physics – Particle Transport Simulation and Applications (MC2000)*, October 2000, Lisbon, Portugal, Springer-Verlag, p. 955, (2001).

[39] Iwase, H., K. Niita, T. Nakamura, "Development of General-purpose Particle and Heavy Ion Transport Monte Carlo Code", *J. Nucl. Sci. Technol.*, 39 (11), 1142 (2002).

[40] Ban, S., H. Hirayama, K. Kondo, S. Miura, K. Hozumi, M. Taino, A. Yamamoto, H. Hirabayashi, K. Katoh, "Measurement of Transverse Attenuation Length for Paraffin, Heavy Concrete and Iron around an External Target for 12 GeV Protons", *Nucl. Instr. Meth.*, 174, 271 (1980).

[41] Ban, S., H. Hirayama, K. Katoh, "Measurement of Secondary Neutron Fluxes around Beam Stop for 500 MeV Protons", *Nucl. Instrum. Meth.*, 184, 409 (1981).

[42] Stevenson, G.R., "Determination of Transverse Shielding for Proton Accelerators Using the Moyer Model", *Health Phys.*, 43, 13 (1982).

[43] Uwamino, Y., T. Nakamura, K. Shin, "Penetration through Shielding Materials of Secondary Neutrons and Photons Generated by 52-MeV Protons", *Nucl. Sci. Eng.*, 80, 360 (1982).

SESSION III.2

Benchmark Experiments and Calculations

Chair: A. Leuschner

BENCHMARK CALCULATIONS ON NEUTRON STREAMING THROUGH MAZES AT PROTON ACCELERATOR FACILITIES

H. Nakashima, N. Matsuda, H. Nakano, Y. Iwamoto
Japan Atomic Energy Research Institute
Tokai, Ibaraki 319-1195, Japan

T. Miura, M. Numajiri, N. Nakao
High Energy Accelerator Research Organization
Oho, Tsukuba, 305-0801, Japan

K. Niita
Research Organization for Information Science and Technology
Tokai, Ibaraki 319-1195, Japan

Abstract

In accelerator shielding designs one of the important issues is to estimate radiation streaming through mazes and ducts. In order to validate the accuracy of the calculation methods concerning such neutron streaming, benchmark analyses were carried out using two kinds of benchmark problems based on past experiments. The analyses showed that the design methods were applicable to neutron streaming calculations of proton accelerator facilities with an uncertainty within a factor of two. In the analyses, relative comparisons were conducted using a radiation source generated by GeV energy protons, and absolute comparisons were conducted using a low-energy neutron source of a few tens of MeV. A radiation streaming experiment was planned and carried out at KEK using a radiation source produced by a thin copper target irradiated by 12 GeV protons. The preliminary experimental analysis is presented below. In addition, the authors propose to compile benchmark problems on radiation streaming for accelerator facilities and to search for possible new streaming experiments at other facilities.

Introduction

High-energy proton accelerator facilities are being planned and constructed for various purposes around the world. In particular, shielding designs and radiation safety analyses are being advanced for the J-PARC (Japan Proton Accelerator Research Complex) project [1,2,3]. In the facilities, mazes and ducts connected with the accelerator and target rooms are kept wide enough for devices, RF tubes, etc. However, radiation generated in the accelerator and target rooms that penetrates through the mazes and ducts should be decreased as much as possible. The imprecise design of the mazes and ducts impairs the efficiency of the biological shield, which directly affects the construction cost of accelerator facilities. Therefore, it is essential to estimate radiation streaming through the mazes and ducts in order to design accelerator facilities in a reasonable manner.

Simplified methods using empirical formulas are convenient to estimate radiation streaming through numerous mazes and ducts in accelerator facilities and in the overall shielding design. Monte Carlo calculations are also effective for an exact estimation in a complicated geometry, although they require the preparation of a precise cross-section library and the consumption of much CPU time in order to obtain good statistical accuracy. As a result, both simplified and detailed design methods were used in the shielding design of the J-PARC project [4] in order to establish a reasonable shielding design. Because both methods were used, benchmarking was required to estimate the difference between them.

This report introduces the methodology used for the streaming calculation adopted by the J-PARC project and the related benchmarking, as well as new analysis on an experiment carried out at KEK (the High Energy Accelerator Research Organization). In addition, discussed below is the proposal to compile benchmark problems on radiation streaming for accelerator facilities and to search for possible new streaming experiments at other facilities.

Methodology for the streaming calculation adopted by the J-PARC project

A simple empirical formula has been prepared by Nakamura and Uwamino [5] and is applied during the early stage of design. Nakamura and Uwamino's formula assumes that the attenuation in the labyrinth obeys a simple $1/r^2$ law:

$$H(r) = H(a) \cdot a^2 / r^2 \tag{1}$$

where a is narrower by half in width and height of the cross-section of each leg (m), $H(a)$ is the neutron dose equivalent at the entrance of each leg, and r is the distance from the point where the distance of a is backward from the entrance of each leg (m).

A simplified duct streaming code, DUCT-III [6], is also applied in most cases of duct streaming calculations. DUCT-III was originally developed for duct streaming calculations at nuclear power reactors and/or nuclear fuel facilities, and was improved by introducing revised albedo data of neutron energy up to 3 GeV (obtained using the NMTC/JAM [7] and MCNP [8] codes).

Since applications of the code are restricted to straight and rectangular ducts, the calculations for other geometries, such as curved or bent ducts at any angle, are performed using the Monte Carlo calculations. The Monte Carlo codes (PHITS [9], MARS [10] and MCNPX [11]) are used for high-energy particle transport calculations above 20 MeV for neutrons and above 1 MeV for charged particles and mesons, depending on the shielding design and performance. The PHITS code is a multipurpose particle and heavy ion transport Monte Carlo code system based on the NMTC/JAM code, which was recently developed by RIST (Research Organization for Information Science and Technology), Tohoku University and JAERI (Japan Atomic Energy Research Institute). The MCNPX code is widely used for designs because of various kinds of estimators and variance reduction techniques. The MARS code provides calculation results on the radiation flux and dose in a rather short time as compared with other Monte Carlo codes. The MCNP-4 code with a nuclear data set, JENDL-3.3 [12], is applied for low-energy neutrons up to 20 MeV and photons in the case of the MARS code.

Benchmarking with past experiments

Two kinds of benchmarks based on past experiments were adopted. One was a streaming experiment using a radiation source produced by a thin copper target irradiated with 7 GeV protons accelerated by a synchrotron (NIMROD) at Rutherford Laboratory [13]. The other was a streaming experiment using a radiation source produced by a thick copper target irradiated with 68 MeV protons at TIARA (Takasaki Ion Accelerator Facility for Advanced Radiation Application) of JAERI [14]. Benchmark analyses were carried out mainly for the radiation shielding design codes: PHITS (NMTC/JAM), MCNPX and DUCT-III.

The NIMROD experiment

This experiment was carried out using two types of large concrete-lined tunnels at the synchrotron beam line of the NIMROD accelerator facility. The radiation sources for the experiments were produced by bombarding 7 GeV protons on a copper target of 10 mm in diameter and 50 mm in thickness. The protons were horizontally transported along the beam line to be bombarded on the copper target. As shown in Figure 1, tunnels were constructed as a part of the normal extracted beam blockhouse at right angles to the direction of the beam. The Phase I tunnel was straight and 18 m in length from its entrance. The Phase II tunnel contained a right-angled bend at 11 m from the entrance of the tunnel with a second leg of 8 m long. The cross-section of each tunnel was 2.3 m in width and 2.3 m in height. The extracted beam target was located on the centreline of the tunnel, which is 1.9 m from the entrance. The relative attenuations of the reaction rates along the centreline in the straight and bent tunnels were measured by using various activation detectors.

Figure 1. Cross-sectional views of the bend tunnel at NIMROD

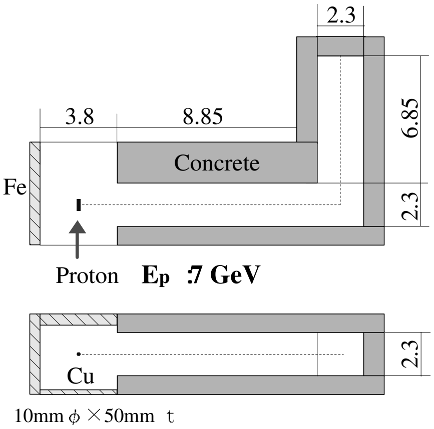

(Unit: m)

Figure 2 shows an example of the results of the experimental analysis. Attenuation curves of the calculated induced radioactivity of the $^{12}C(n,2n)^{11}C$ reaction are compared in the figure with measurements along the centreline in the straight and bent tunnels. For a comparison, the calculations were normalised by the measurements at the entrance of the tunnel. Calculations using the Monte Carlo codes reproduced the measurements within a factor of two at all regions in the tunnel. The calculations by DUCT-III were in good agreement with the Monte Carlo calculations and the measurements for the first leg, although they slightly overestimated (by a factor of two) for the second leg.

Figure 2. Attenuation curves of the induced radioactivity for the $^{12}C(n,2n)$ reaction in the bent tunnel at NIMROD

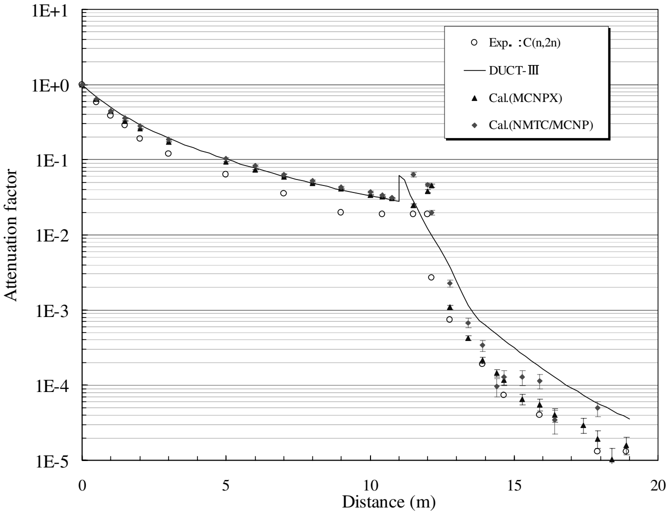

The TIARA experiment

This experiment was carried out in a labyrinth of three legs connected to the second light ion room (LIR2) of TIARA at JAERI. The source neutrons were generated in a thick copper target located in a Faraday cup and irradiated with 68 MeV protons in LIR2. The protons were accelerated using the AVF (azimuthally varying field) cyclotron, and were vertically transported along the beam transport line from the light ion room 1 (LIR1) and fully stopped at a copper target placed at a height of 108 cm above the floor. Figure 3 shows cross-sectional views of LIR2 and the labyrinth. Room LIR2 was 8.5 m.

Figure 3. Cross-sectional views of the labyrinth at TIARA

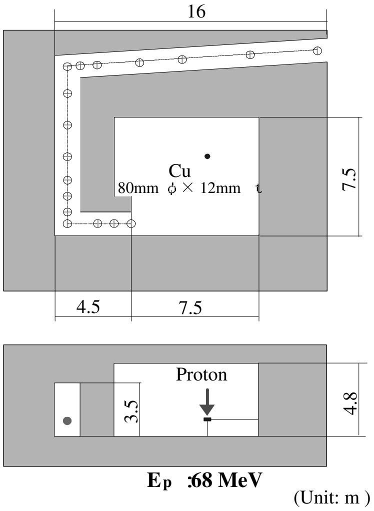

in length, 7.5 m in width, and 4.8 m in height. The labyrinth was composed of three legs: the first leg was 3.75 m in length, the second 10.0 m and the third 15.25 m, totalling ~29 m in length. LIR2 and the labyrinth were surrounded by walls and a floor made of ordinary concrete with a thickness greater than 2 m. The neutron energy spectra, the neutron dose equivalent rates and the thermal neutron flux were measured along the centreline in the labyrinth.

Figure 4 shows an example of the results. The calculated neutron dose equivalent rate distributions in the labyrinth were compared with the measured distribution, which was obtained using the Bonner ball counting rate and multiplied by the neutron flux-to-dose conversion factors based on the ICRP Publication 21 [15]. The Monte Carlo calculations are in excellent agreement with the measurements and the calculation by DUCT-III is in good agreement with the measurements within a factor of two.

Figure 4. Comparison of the calculated and measured neutron dose equivalent rates in the TIARA (LIR2) labyrinth

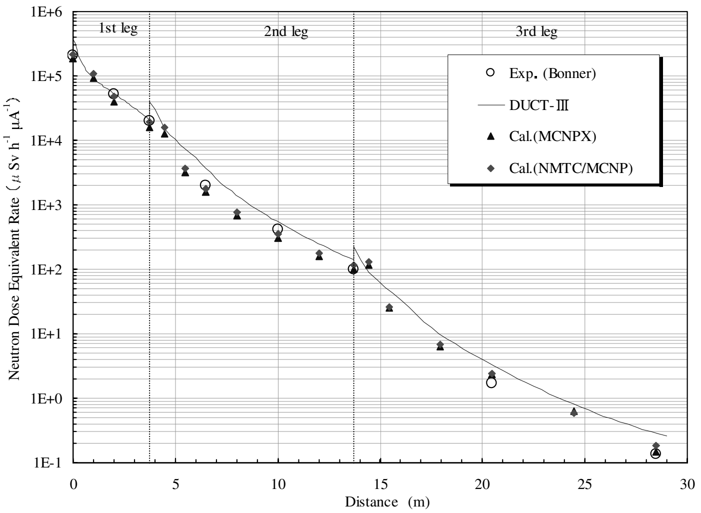

Summary of analyses on past experiments

Both experiment analyses indicate that the Monte Carlo methods are applicable to streaming calculations with high accuracy and that the DUCT-III code is also applicable with an uncertainty of a factor of two. However, such benchmarking methods have some defects. The NIMROD experiment generated relative experimental data and the TIARA experiment was carried out using low-energy source neutrons of a few tens of MeV. In order to estimate the accuracy of the streaming calculation methods for the shielding design of GeV energy proton accelerator facilities, absolute experimental data are required with a clear geometry and using source neutrons generated by GeV energy protons.

Preliminary analysis of a new experiment carried out at KEK

Experiment

An experiment was carried out in a tunnel called the neutrino beam line and in a labyrinth leading to the tunnel of KEK [16,17]. In the experiment, a 0.5-mm thick copper plate set in the tunnel was irradiated by a 12 GeV proton beam. The labyrinth was made of three legs, whose overall length equalled 19.15 m (shown in Figure 5). The height inside the labyrinth up to the length of 2 m equalled

6 m high and the other equalled 2.5 m high. The cross-section of the first leg was 2 × 6 m^2 up to 2 m from the entrance and 2 × 2.5 m^2 beyond 2 m from the entrance. The second and third legs had 2 × 2.5 m^2 and 2.5 × 2.5 m^2 cross-sections, respectively. The labyrinth was surrounded by ordinary concrete with a thickness of 0.6 m or more. A secondary emission chamber (SEC), which was located far upstream from the copper plate with an uncertainty of 10%, was used to measure the proton beam intensity. The reaction rate and dose rate distributions in the labyrinth were measured by using various kinds of activation detectors, such as bismuth, aluminium and indium, and TLDs.

Figure 5. Cross-sectional view of the experimental geometry comprised of a tunnel and a labyrinth leading to the tunnel

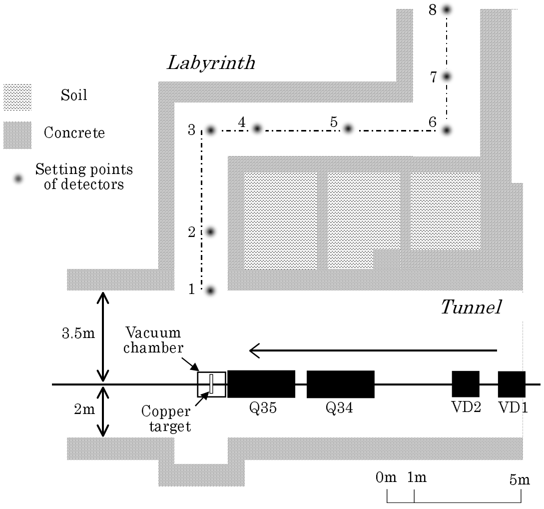

Analysis

Preliminary analysis comparing measurements and calculations using the PHITS and MCNPX codes on the ^{115m}In production reaction rate distribution along the labyrinth are shown in Figure 6. The MCNPX calculation agrees well with the measurement of the first leg and the PHITS calculation slightly underestimates the measurement by a factor of two. In the second leg, the MCNPX calculation slightly overestimates the measurement by a factor of two and the PHITS calculation agrees well with the measurement. It should be noted that the MCNPX calculation is systematically larger than the PHITS calculation by a factor of two.

In order to study the difference between the calculations, the calculated double-differential neutron emission cross-sections of copper at 12 GeV proton energy and in directions of 30°, 90° and 150° were compared (shown in Figure 7). At a forward angle of 30°, the cross-section composed of the first peak was due to direct interaction in the higher energy region and the second peak was due to the pre-equilibrium and evaporation reactions with a moving source of fragments in a lower energy region. At the other angles, only the latter peak is observed. The comparison shows that the cross-sections calculated by the MCNPX code are larger than the cross-sections using the PHITS code over almost all energy regions and by a factor of two or more. It seems that the reason for the difference between the streaming calculations is caused by the difference in the angular distribution of the cross-section at a direction of 90°. However, the comparison reveals that the lower peak component in the MCNPX calculation has an isotropic angular distribution, while the PHITS calculation has a forward angular distribution. The PHITS distribution is quite reasonable because the pre-equilibrium and evaporation reactions occur in the nucleus that is moving to the forward direction and not in the stopping nucleus.

Figure 6. Reaction rates measured using In activation detectors and calculations by the PHITS and MCNPX codes in the labyrinth

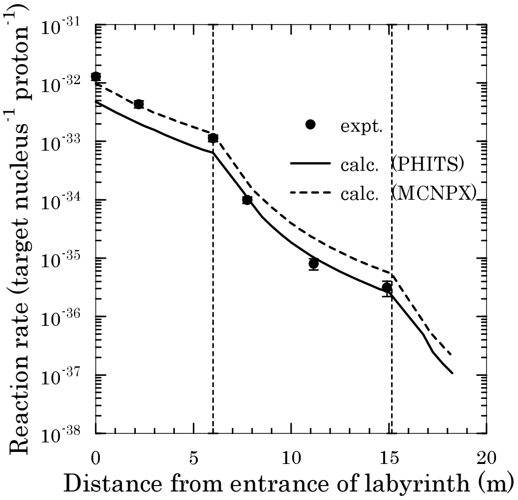

Figure 7. Double-differential cross-sections of Cu at an incident proton energy of 12 GeV, calculated by the PHITS and MCNPX codes

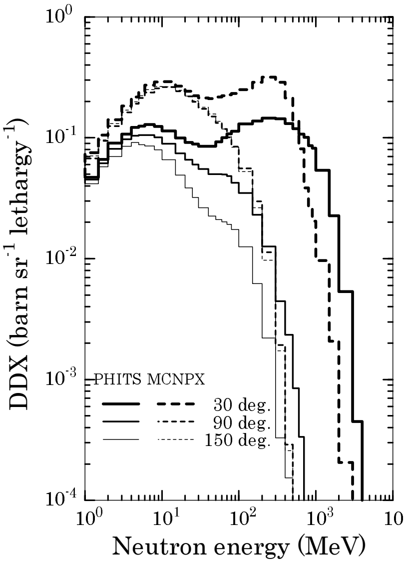

Regarding the double-differential particle emission cross-sections, some experiments exist on the invariant cross-section [18]. Figure 8 shows an example of a comparison between the AGS measurement and the calculation via JAM code involving the proton invariant transverse mass distribution for proton-induced reactions (p+Au at 14.6 GeV/c). The JAM code is the main part of the PHITS code in the high-energy region [19]. The calculation represents good agreement with the measurement of the proton-induced reaction in almost all energy regions. However, the difference in the streaming calculation was caused by a difference in the lower energy region from that in the measurement. The experiment confirms the accuracy of the code in an overall energy region; however, it does not validate the streaming calculation code. As a result, measurements in an energy region lower than a few tenths of MeV are essential for code validation involving streaming calculations.

Figure 8. Invariant cross-section of a proton from p+Au at 14.6 GeV/c. The calculations are compared with the E802 data from Ref. [18].

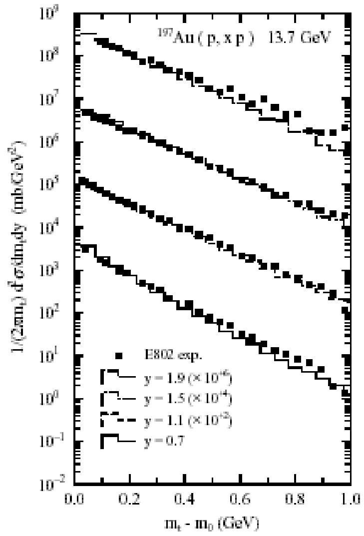

Summary

In order to validate the accuracy of calculation methods on neutron streaming through mazes and ducts, benchmark analyses were carried out using radiation shielding design methods. The analyses show that the shielding design methods are applicable to the shielding design on radiation streaming. However, previous streaming experiments have some defects for the benchmarking of design methods on GeV energy proton accelerator facilities. Although a new experiment was carried out at KEK, we have not yet obtained sufficient experimental data to estimate the accuracy of the design methods. As a conclusion of the analysis, we propose to compile benchmark problems on radiation streaming for accelerator facilities and to search for possible new streaming experiments and/or related basic data, such as double-differential cross-sections in a low-energy region.

REFERENCES

[1] Nagamiya, S., "JAERI-KEK Joint Project on High Intensity Proton Accelerators", *Proceedings of the Int. Conf. Radiation Shielding (ICRS-9)*, Tsukuba, 18-21 Oct. 1999; *Journal of Nuclear Science & Technology*, Supplement 1, 40-48 (2000).

[2] JAERI and KEK joint project team, High-intensity Proton Accelerator Facility Project, J-PARC, http://j-parc.jp.

[3] Tanaka, S., "High-intensity Proton Accelerator Project in JAPAN (J-PARC)", to be published in *Proceedings of the Int. Conf. Radiation Shielding (ICRS-10)*, Madeira, 9-14 May 2004.

[4] Nakashima, H., *et al.*, "Radiation Safety Design for the J-PARC Project", to be published in the *Proceedings of the Int. Conf. Radiation Shielding (ICRS-10)*, Madeira, 9-14 May 2004.

[5] Uwamino, Y., *et al.*, "Measurement and Calculation of Neutron Leakage from a Medical Electron Accelerator", *Med. Phys.*, 13(3), 374 (1986).

[6] Tayama, R., *et al.*, *DUCT-III, A Simple Design Code for Duct-streaming Radiations*, KEK Internal 2001-8 KEK (2001).

[7] Niita, K., *et al.*, "High Energy Particle Transport Code NMTC/JAM", JAERI-Data/Code 2001-007 (2001).

[8] Briesmeister, J.F., ed., *MCNP – A General Monte Carlo N-particle Transport Code Version 4A*, LA-12625 (1993).

[9] Iwase, H., *et al.*, "Development of General-purpose Particle and Heavy Ion Transport Monte Carlo Code", *Journal of Nuclear Science & Technology*, 39, 1142 (2002).

[10] Mokhov, N.V., *The MARS Code System User's Guide, Version 13(95)*, Reference Manual, Fermilab-FN-628 (1995).

[11] Waters, L.S., ed., *MCNPX^{TM} User's Manual*, TPO-E83-G-UG-X-00001, Los Alamos National Laboratory (1999).

[12] Shibata, K., *et al.*, "Japanese Evaluated Nuclear Data Library Version 3 Revision-3: JENDL-3.3", *Journal of Nuclear Science & Technology*, 39, 1125-1136 (2002).

[13] Stevenson, G.R., *et al.*, "An Experimental Study of Attenuation Radiation in Tunnels Penetrating the Shield of an Extracted Beam of the 7 GeV Proton Synchrotron NIMROD", *Health Physics*, 24, 87-93 (1973).

[14] Tanaka, S., *et al.*, "An Experimental Study on Radiation Streaming Through a Labyrinth in a Proton Accelerator Facility of Intermediate Energy", *Health Physics*, 81(4), 406-418 (2001).

[15] *Data for Protection Against Ionizing Radiation from External Sources: Supplement to ICRP Publication 15*, Publication 21, International Commission on Radiological Protection (1971).

[16] Matsuda, H., *et al.*, "Radiation Streaming Experiment through a Labyrinth of the 12 GeV Proton Accelerator Facility (1) – Activation Method", to be published in *Proceedings of the Int. Conf. Radiation Shielding (ICRS-10)*, Madeira, 9-14 May 2004.

[17] Nakamura, H., *et al.*, "Radiation Streaming Experiment through a Labyrinth of the 12 GeV Proton Accelerator Facility (2) – TLD Rem Counter Method", to be published in *Proceedings of the Int. Conf. Radiation Shielding (ICRS-10)*, Madeira, 9-14 May 2004.

[18] Abbott, T., *et al.* (E802 Collaboration), *Phys. Rev.*, D 45, 3906 (1992).

[19] Nara, Y., *et al.*, "Relativistic Nuclear Collisions at 10A GeV Energies from p+Be to Au+Au with the Hadronic Cascade Model", *Phys. Review*, C 61, 24901 (1999).

MEASUREMENT AND ANALYSIS ON RADIATION SHIELDING OF 18 MeV ELECTRON LINAC FOR MEDICAL USE

Koji Oishi, Kazuaki Kosako, Hiroshi Yamakawa, Takashi Nakamura
Institute of Technology, Shimizu Corporation, Japan

Yuki Kobayashi
Giken Kogyo Co., Ltd., Japan

Abstract

A large discrepancy of about two orders of magnitude was observed between measured and conventional calculated results on the dose rate outside of the shielding wall of an 18 MeV electron linac for medical use. Measurements of radiation fields inside and outside of the wall have been performed. It was discovered that the secondary neutrons produced from the iron, which is placed inside the concrete shielding wall, and their related secondary gamma-rays contributed to the dose rate outside of the wall. It can be concluded that consideration of the (γ,n) reaction in the shielding wall is very necessary for the design calculation of high-energy electron linac facilities.

Introduction

Neutrons were emitted from the target of the electron linac, whose acceleration energy is greater than 10 MeV. Since the dose rate of target neutrons was ~0.1-1% of that of photons, target neutrons were omitted from the shielding calculation in such electron linac facilities. However, much disagreement between measured and calculated results was observed outside the shielding wall of the 18 MeV electron linac (for medical use). ANISN [1] calculation include target neutrons was also performed, but the calculated results could not completely explain the measured results.

In this study, the dose rate distribution around the linac shielding wall was measured and characterised the radiation field. From these measurements, we determined the discrepancy of the calculated results and proposed a proper calculation method, which uses the MCNPX Monte Carlo calculation code system [2].

Measured values and calculated results via the conventional calculation method

Figure 1 shows the plain view and the estimated point for dose measurement and calculation. The accelerating electron energy of the linac was 18 MeV. The dose rate at the isocentre was 6 Gy/min. The total thickness of the shielding wall was 1 200 mm, where the thickness of concrete was 300 mm, sandwiched iron was 660 mm and concrete was 240 mm. The distance between the isocentre of the linac and the inner surface of the shielding wall was 3 100 mm.

Figure 1. Plain view of 18 MeV electron linac facility

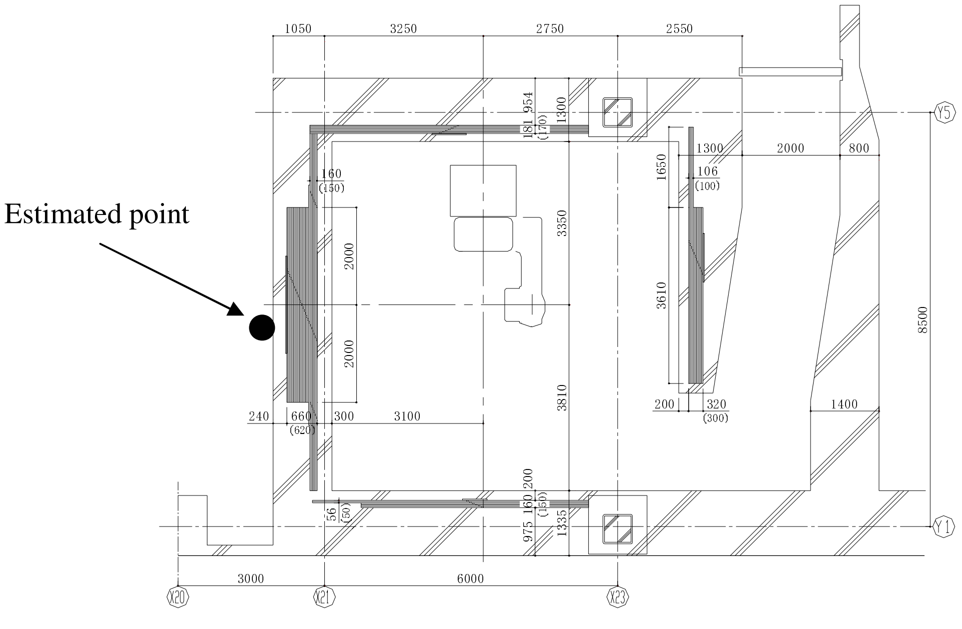

The calculated result of the dose rate (Dgc) of a gamma-ray at the estimated point by using Eq. (1) (below) was Dgc = 0.97 (μSv/h). However, the measured value (Dgm) when using an ionisation chamber (Victoreen 450-DE-SI) was Dgm = 98.8 (μSv/h).

$$ {}_{U}E_{(x)} = \frac{I_0 \times 60 \times 10^6}{L^2} \times D_t \times T \times U \times 1.0 \qquad (1) $$

where $_UE_{(X)}$ is the effective dose [μSv/(3 months)] at an evaluation position; I_0 is the X-ray dose rate (Gy/min) at 1 m of distance from the target; 60 is the conversion coefficient in minute to hour units; 10^6 is the conversion coefficient from Gy to μGy units; L is the distance (m) from the target to an evaluation position; D_t is the transmittance of shielding material with thickness t (cm); T is the operation time [hours/(3 months)], U is the directional useful rate; and 1.0 is the conversion coefficient from Gy to Sv units. The following equation should also be noted: $F_0 \times 10^{-t/x}$ where t is the effective thickness (cm) of the shielding material and x is the 1/10 thickness (cm) of the shielding material.

The measurement of the neutron dose rate by using an rem counter (Aloka TPS-451C) was also performed, and the neutron dose rate (Dnm) was observed [Dgm = 92 （μSv/h）].

The experiment-to-calculation ratio (E/C) for the dose rate of a gamma-ray was E/C = 101.9.

Calculations via S_N transport calculation code ANISN

Calculations including target neutrons have been performed by using ANISN S_N transport calculation code. The target gamma-rays and neutron spectra were calculated by using MCNPX calculation code and its related nuclear data library, which was produced by using nuclear data processing code, NJOY. Photonuclear reaction data were applied from an evaluated nuclear data file by KAERI. The calculated gamma-rays and neutron spectra are shown in Figures 2(a) and 2(b).

Figure 2. Calculated spectra from the target via MCNPX

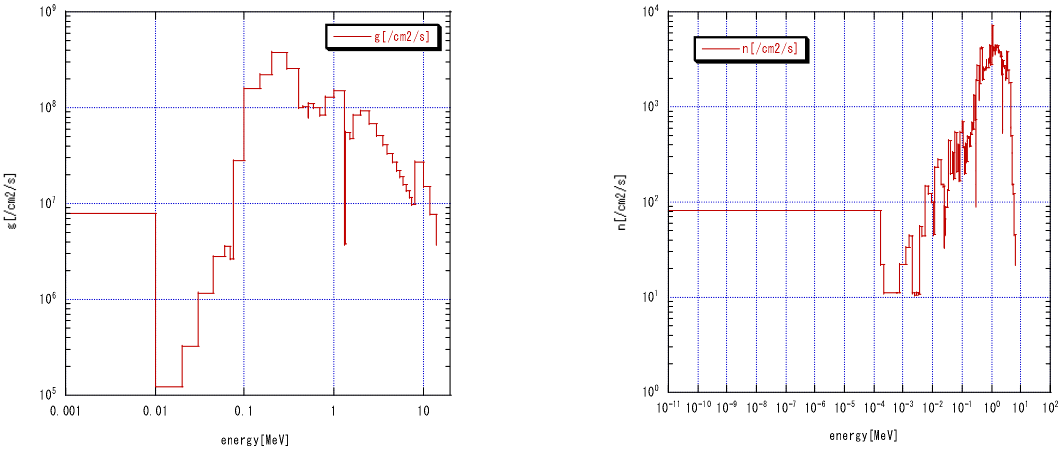

***(a)** Calculated gamma-ray spectra from the target via MCNPX* ***(b)** Calculated neutron spectra from the target via MCNPX*

Since the linac was operated by pulse (width was 4 μsec, peak current was 30 mA and repetition was 188 pps), we applied average beam current Ie calculated by the pulse condition (i.e. 22.6 μA). The calculated results were normalised using the average current.

The calculated results of the ANISN calculations are shown in Figure 3. The neutron dose rate neutron equalled 0.1-1% of the gamma-ray dose rate inside the linac room, which is indicated in the conventional calculation method. However, in the iron region of the shielding wall the decrease of the neutron was much slower than that of the gamma-ray. In the case of the dose rate in the iron region the order of magnitude was reversed. In the outer concrete region there emerged a secondary gamma-ray from neutrons. In addition, at the end surface of the shielding wall the dose rate of the gamma-ray and the neutron became almost of equal value. These calculated results indicate that in a qualitative manner the neutrons were measured as the same values as the gamma-rays at the estimated point.

However, the absolute values of the calculated results using ANISN on the dose rate of the gamma-ray Dganisn and the neutron Dnanisn were Dganisn = 0.28 (μSv/h) and Dnanisn = 0.30 (μSv/h).

The E/C values of the gamma-ray and the neutron were 352.9 and 306.7, respectively. The calculated results using ANISN could not explain the measured values.

Figure 3. Calculated results via ANISN, including target neutron

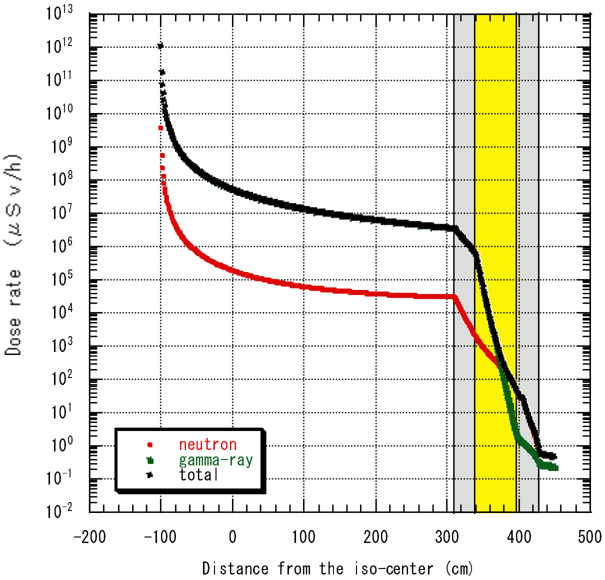

Measurement of the dose rate distribution around the linac room

Five types of experiments were performed in order to elucidate the cause of the discrepancies between measured and calculated results.

Shielding experiment of target neutrons [1]

Since a large amount of neutrons was observed at the estimated point, it is necessary to check the target neutron yield, even though the neutron yield produced by the (γ,n) reaction was well-known. If the target neutrons contribute to the dose rate at the estimated point, a shielding experiment by the water would dramatically reduce the dose rate outside of the wall. Since the neutron spectra from the target were similar to those of Cf-252 [shown in Figure 2(b)], the 1/10 thickness of the 2 MeV neutrons through water was ~200 mm.

The experimental layout is shown in Figure 4. In the experiment, the thickness of the water *t* varied from 200 mm to 800 mm.

The neutron dose rate was measured at the estimated point and the measured results are shown in Figure 5. From the results it is obvious that the observed neutrons did not came from the target, since the behaviour of attenuation is not related to the thickness of the water shield.

Figure 4. Experimental layout of water shielding near the target

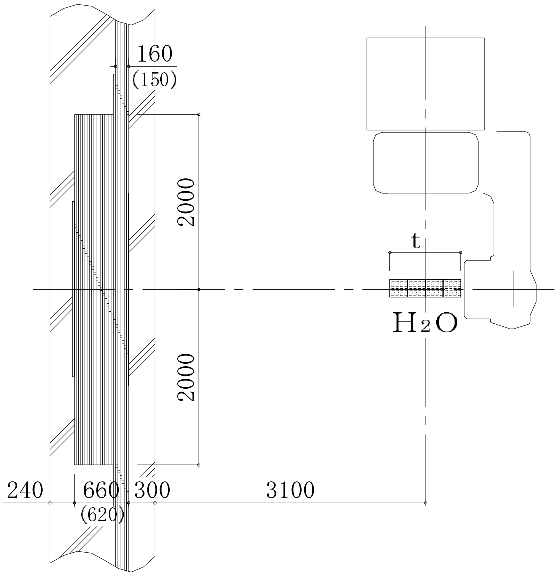

Figure 5. Dose rate change vs. depth of water

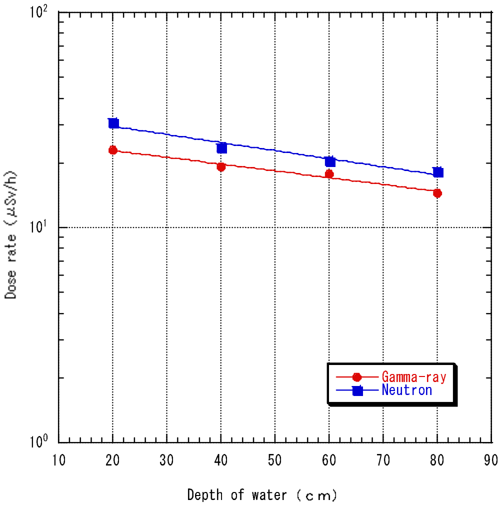

Shielding experiment of target neutrons [2]

A neutron shielding experiment was performed at the outer surface of the shielding wall. Since the shielding area is larger than that near the target, the dose rate at the estimated point was measured only for the case of 20 cm thickness of water. The measured value was Dn (20 cm) = 19.46 (μSv/h).

The dose rate without the water shield Dn (0 cm) was 92.0 (μSv/h), and the attenuation ratio with and without the 20 cm water shield was Dn (20 cm)/Dn (0 cm) = 0.2.

The attenuation of the neutron dose rate is almost one order of magnitude, i.e. 1/10 thickness. This means that the neutron source may exist between the target and the shielding wall.

Figure 6. Experimental layout of water shielding outside of the shielding wall

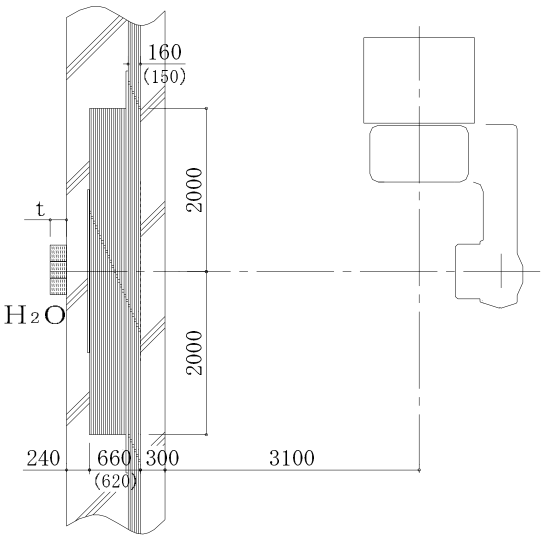

Dose distribution outside of the shielding wall

If the observed dose rate of the gamma-ray and the neutron originated from the target, the dose rate distribution outside of the shielding wall should behave in accordance with the formula, $1/r^2$. Dose rate measurement outside of the wall was performed for the gamma-ray and the neutron from the outer surface of the wall to 7 m from the surface.

The measured results are shown in Figure 7 with the curve of $1/r^2$ as a reference. The behaviour of the gamma-ray and the neutron dose rate did not follow the $1/r^2$ formula. However, the dose rate of the gamma-rays and the neutrons increased as the distance became closer between the detector position and the outer surface of the shielding wall. These results indicate that the shielding wall is the source of not only neutrons but gamma-rays.

Neutron attenuation by the shielding wall

To compare the calculated and measured attenuation values generated by the shielding wall, the dose rate distribution of neutrons in the linac room was measured using a CR-39 track etch detector. The measured results are shown in Figure 8. In order to compare the measured results of the dose rate in the linac room with those outside of the shielding wall, the attenuation rate of the shielding wall (for neutrons) was estimated via experimentation. The dose rate on the inner and outer surface of the wall obtained by the measurements [Dnm (in) and Dnm (out)] and those obtained by ANISN calculation [Dnc (in) and Dnc (out)] included the following: Dnm (in) = 100 (mSv/h) and Dnm (out) = 92 (μSv/h), and Dnc (in) = 29.84 (mSv/h) and Dnc (out) = 0.3 (μSv/h).

From these values the attenuation ratios of the shielding wall were obtained by measurement (Rattm) and calculation (Rattc). The resultant attenuation ratios were as follows: Rattm = 1.1E+3 and Rattc = 1.0E+5.

This discrepancy explains the large disagreement between the measured and calculated results of the dose rate for neutrons of about two orders of magnitude.

Figure 7. Dose rate distribution outside of the shielding wall

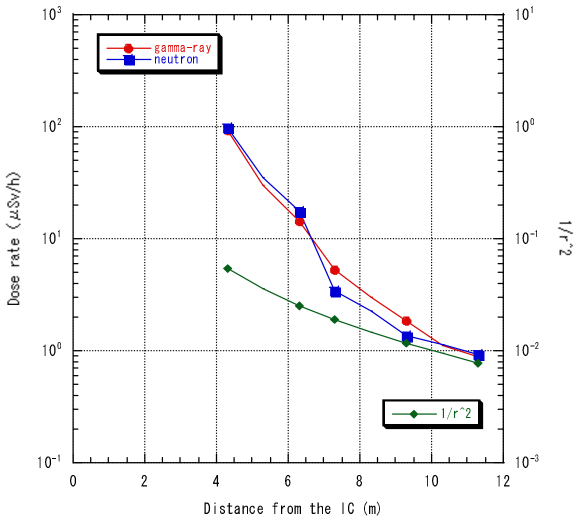

Figure 8. Dose rate distribution of neutrons in the room measured by CR-39

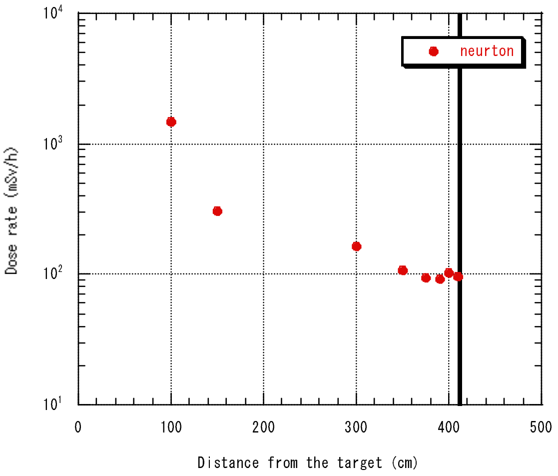

Shielding experiment by iron shield for target gamma-rays

From the results of former experiments it is presumed that neutrons were produced inside the shielding wall. The target gamma-rays (parents) were bombarded into concrete and iron shielding wall and produced secondary neutrons (daughters). These neutrons emitted gamma-rays (grand-daughters), especially in concrete as shown in Figure 9.

To verify these phenomena, a shielding experiment of the target gamma-rays in iron was performed. If secondary neutrons and the subsequently emitted gamma-rays indicate the same decreasing behaviour as that of target gamma-rays shielded by iron, it is proven that the produced neutrons in the wall were due to target gamma-rays.

An iron shield, whose thickness t varied from 4.5 to 18.0 cm, was set in front of the target to cover radiation corn perfectly. Figure 10 shows the experiment layout.

Figure 9. Neutron and gamma-ray production in the shielding wall

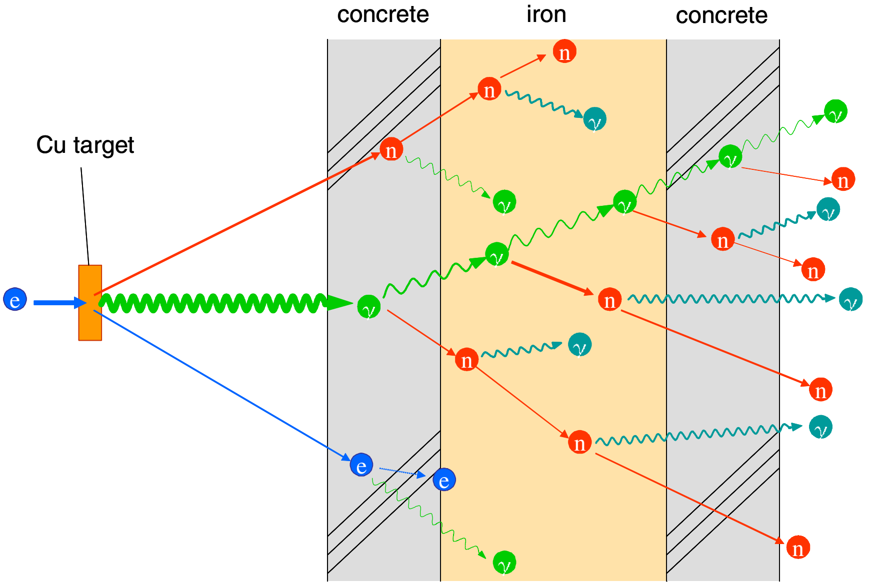

Figure 10. Experimental layout for the target gamma shielding experiment

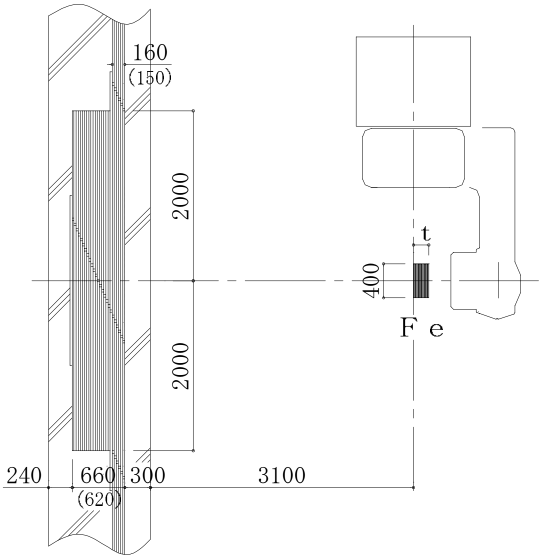

The experimental results of the dose rate measurement on neutrons and gamma-rays outside of the shielding wall (estimated point) are shown in Figure 11. The dose rate of neutrons and gamma-rays decreased exponentially. The 1/10 thickness of the secondary neutrons and the subsequently emitted gamma-rays equalled ~10 cm, which is the same as the 1/10 thickness for iron and the gamma-ray produced by 18 MeV electron bombardment onto the Cu target of an electron linac.

These results indicate that the observed neutrons outside of the wall (estimated point) were produced inside of the shielding wall by the target gamma-ray, which were bombarded into the concrete and the iron shield. The observed s-rays were produced by the secondary neutrons inside of the wall and not the gamma-rays produced on the target.

Figure 11. Dose rate measurements of gamma-rays and neutrons in the iron shielding experiment

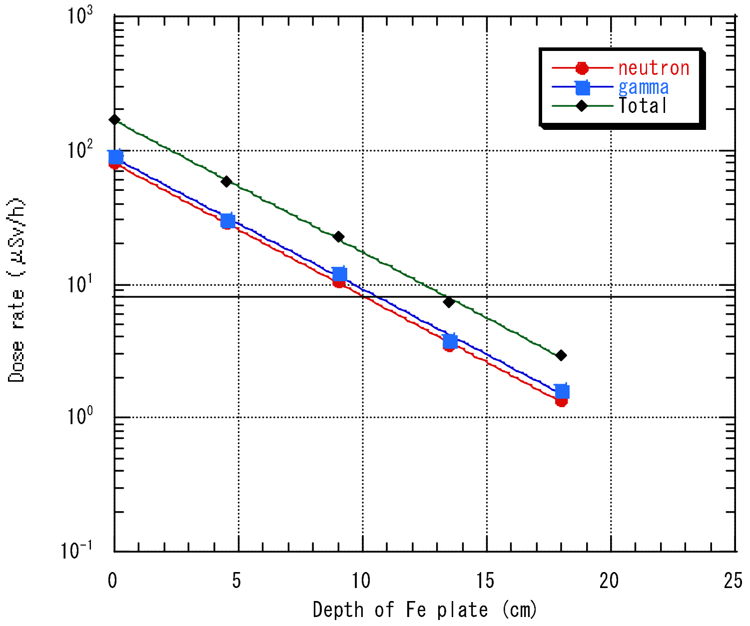

Analysis via the Monte Carlo calculation code system MCNPX

Neutron and gamma-ray dose rate calculations using MCNP were performed. The block diagram of the calculation code system is shown in Figure 12.

Figure 12. Block diagram of the calculation code system

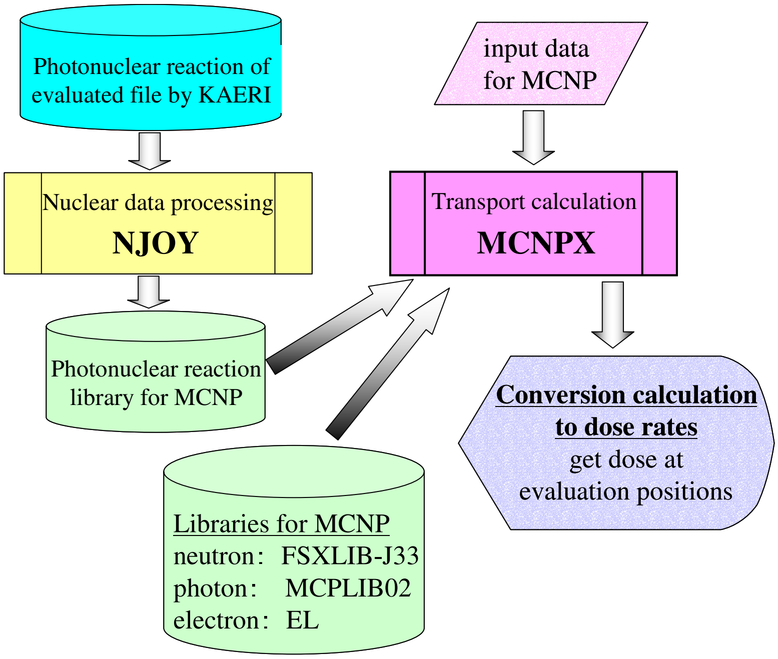

The calculation conditions are listed below.

- Transport code: MCNPX-2.4.
- Cross-section library:
  - Neutron [FSXLIB-J33 (JENDL-3.3)].
  - Photon and electron (MCNPDATA).
  - Photonuclear [LA150 (MCNPXDATA)].
- Particle: neutron, photon and electron.
- Target model:
  - Copper target [2 × 2 × 2 (cm^3) of cubic].
  - 18 MeV electron (pencil beam incident vertically to rear surface of target).
  - Tungsten collimator (cylinder with inner radius of 3 cm, outer radius of 4 cm, length of 5 cm; distance from target is 1 cm).
- Wall component:
  - Concrete [type 3, density 2.2 (g/cm^3)] – analytic density 2.29 (g/cm^3).
  - Iron [density 7.86 (g/cm^3)].
- Variance reduction: cell importance method.
- Cut-off energy: 0.3 MeV for electrons.
- Tally: surface crossing tally and cell tally (only outside the wall).
- Number of sources: 150 million for electrons.
- Calculation time: ~100 hours by 150 million electrons (CPU was Intel Pentium-4, 3 GHz).

The calculated results are shown in Figure 13. From this figure it is obvious that the target gamma-rays decreased quickly inside of the shielding wall, especially in the iron region. However, secondary neutrons emerged not only in the iron region but also in the front concrete region. The secondary neutrons produced inside the wall decreased quickly in the end concrete region, but the subsequently emitted gamma-rays emerged in the end concrete region of the shielding wall.

The calculated dose rate of neutrons at the front surface of the shielding wall in the linac room and the calculated dose rate of neutrons and gamma-rays outside of the wall agreed very well (0.8-1.6) with the measured dose rate. Figure 14 shows the calculation-to-experiment ratio (C/E) of the dose rate distribution. The calculated results in the linac room underestimated the experimental results, since the gantry of the electron linac was not included in the calculations.

Figure 13. Calculated results of the secondary neutrons and the subsequently emitted gamma-rays in the shielding wall using the MCNPX calculation code system

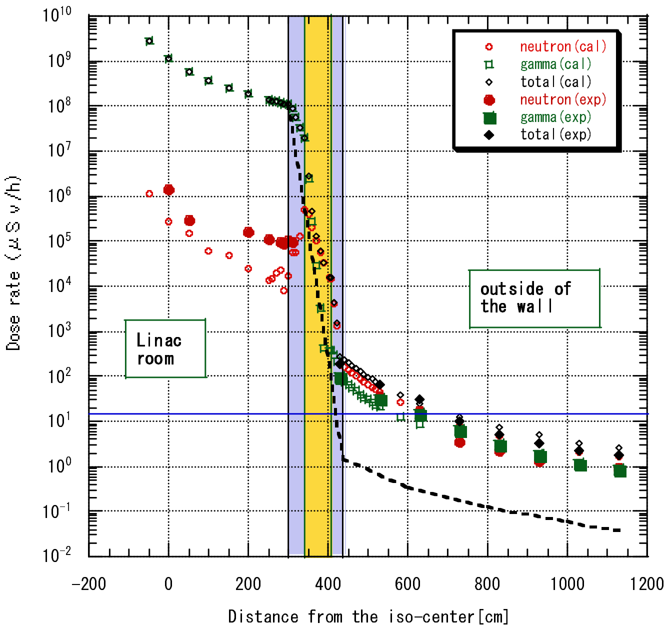

Figure 14. C/E value of the dose rate distribution

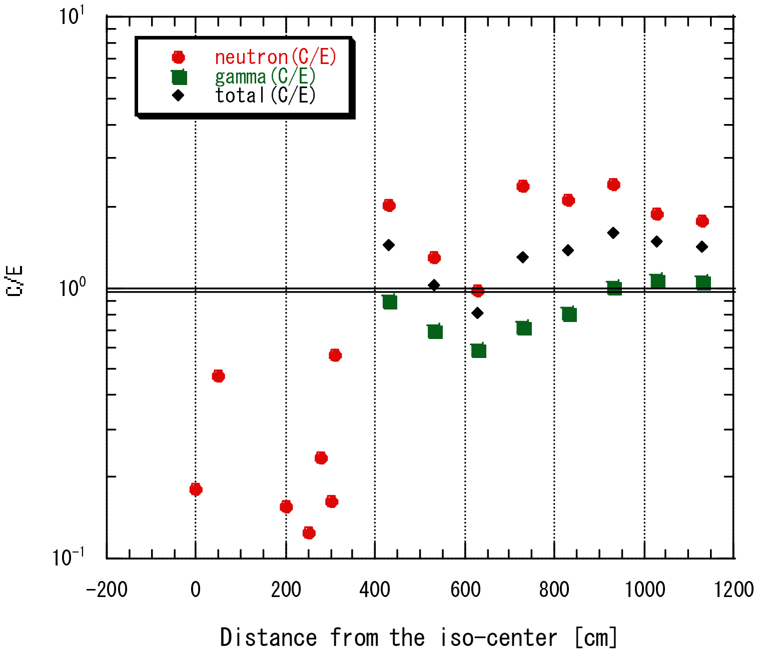

Conclusion

A very large discrepancy (greater than two orders of magnitude) was obtained for the shielding calculation of an 18 MeV electron linac facility. The discrepancy arose between the experimental results and the calculated results by the conventional calculation method and ANISN transport calculation code.

Dose rate measurements of neutrons and gamma-rays around the shielding wall have been performed. In the process it was discovered that the secondary neutrons produced by a (γ,n) reaction and the subsequently emitted gamma-rays produced by a (n,γ) reaction contributed to the dose rate outside of the shielding wall. Calculations using the MCNPX Monte Carlo calculation code were performed, including a (γ,n) reaction, and the results of the experiment and the calculations agreed quite well (within a factor of two). It was concluded that the MCNPX calculation code is necessary for the precise estimation of dose rate calculation for electron linac facilities, when electron energy is greater than 10 MeV.

REFERENCES

[1] Engel, Jr., W.W., *A Users Manual for ANISN, A One-dimensional Discrete Ordinates Code with Anisotropic Scattering*, K-1693, Union Carbide Corporation (1976).

[2] Hendricks, J.S., MCNPX team, *MCNPX™ User's Manual, Version 2.4.0.*, LA-CP-02-408 (2002).

MEASUREMENT OF NEUTRON ENERGY AND TIME-OF-FLIGHT SPECTRA BEHIND THE LATERAL SHIELD OF A HIGH-ENERGY ELECTRON BEAM DUMP

S. Taniguchi[1,2], **M. Sasaki**[2], **T. Nunomiya**[2], **H. Iwase**[2], **S. Yonai**[2],
T. Nakamura[2], **S.H. Rokni**[3], **J.C. Liu**[3], **S. Roesler**[4], **K. Kase**[3]
[1]Japan Synchrotron Radiation Research Institute
Koto 1-1-1, Mikazuki-cho, Sayo-gun, Hyogo, 679-5198, Japan
[2]Tohoku University, Sendai, Japan
[3]Stanford Linear Accelerator Center, Stanford, CA 94309, USA
[4]CERN, CH-1211 Geneva 23, Switzerland

Abstract

The experiment of neutron spectra behind the lateral shield of the 28.7 GeV electron beam dump has been done at the Final Focus Test Beam (FFTB) facility of the Stanford Linear Accelerator Center (SLAC) by using an NE213 organic liquid scintillator and the multi-moderator spectrometer (Bonner Sphere). Following the previous NE213 measurements performed with three additional concrete thicknesses of 91, 152 and 213 cm behind a fixed shield of iron (84 cm) and concrete (183 cm), the Bonner sphere measurement was conducted with additional 91-cm thick concrete and the NE213 measurement with additional 274-cm thick concrete. The neutron spectra were also calculated with the FLUKA Monte Carlo simulation code. The calculated and measured results agreed rather well.

Introduction

Electron accelerators have been widely used for high-energy physics, synchrotron radiation and various other purposes. They produce high-energy (> 20 MeV) neutrons through photonuclear reactions from the *bremsstrahlung* photons generated in targets, beam stops and other beam line components. The information on neutron spectra due to high-energy electron beams is indispensable for the radiation safety and shielding design at high-energy electron accelerator facilities. Since very few experiments have been conducted, we performed a series of Japan-US collaborative experiments on neutron spectra behind the lateral shield of the 28.7 GeV electron beam dump at the Final Focus Test Beam (FFTB) facility of the Stanford Linear Accelerator Center (SLAC) [1,2]. Following these experiments, we performed a similar measurement using a thicker concrete shield, which is discussed here.

Experiment

The measurements were performed using the 28.7 GeV electron beam at the FFTB facility, which was extracted from the SLAC linear accelerator at repetition rates of 10-30 Hz. The number of electrons in each beam pulse was monitored using the Toroid Charge Monitor (TCM) and the beam intensity was limited to 2×10^9 to 5×10^9 electrons/pulse in order to minimise the pulse pile-up in the detector.

Figure 1 is the schematic view of the experimental set-up. The aluminium beam dump (145 cm length, 38 cm diameter) completely stops the electron beam. The dump is placed in a room, which is laterally shielded by 84 cm of steel and surrounded with a 183-cm thick concrete wall. Blocks of steel are placed outside the room in a forward direction relative to the beam line in order to attenuate muons generated in the dump.

Figure 1. Schematic view of the experimental set-up at FFTB of SLAC

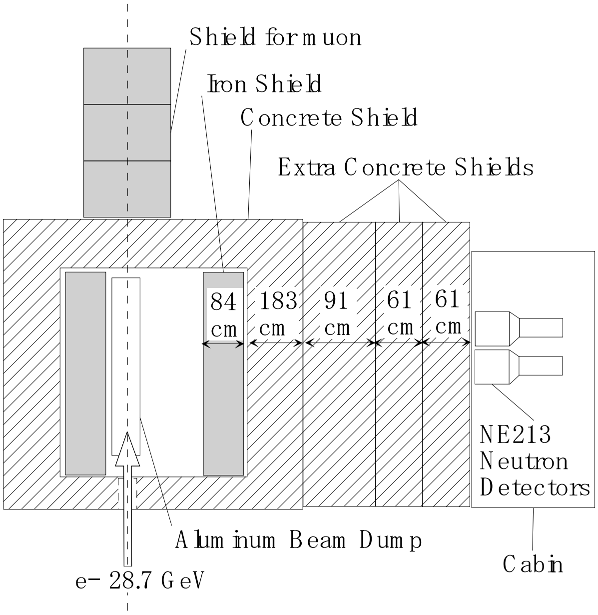

To measure the energy and the TOF spectra of neutrons generated in the beam dump, an NE213 detector (12.7 cm diameter, 12.7 cm length) was placed ~36 cm from the concrete floor in a hutch at 90° in relation to the beam direction behind the shield wall. The muon scintillator (0.625 cm thick by

10.16 × 30.48 cm^2 of plastic) was set in the muon shield at a distance of 335 cm to the outer shield surface in order for it to be used as the event trigger and for start signals of the TOF measurements. The measurements were performed with added concrete shielding of four different thicknesses (91, 152, 213 and 274 cm) between the fixed wall and the detector. Thus, the total thicknesses of the concrete shield are 274, 335, 396, and 457 cm, respectively. Only for a 274 cm concrete shield, the multi-moderator spectrometer (Bonner sphere, or BS) was used to measure the neutron spectrum down to thermal energy. The BS consists of a ^{6}Li glass scintillator (4 mm length, 4 mm diameter) surrounded by six polyethylene moderators of 5.08, 7.62, 12.7, 20.32, 25.4 and 30.48 cm thicknesses.

The output signal from the muon counter was adjusted in time with the programmable delay unit (PDU) signal from the accelerator, which was used as the event trigger. The integrated charges of the total component and the slow (decay) component of the signals from the NE213 detector were measured via the charge analog-to-digital converter (QDC) for particle identification between neutrons and gamma-rays (i.e. neutron-gamma discrimination using pulse-shape differentiation). The time difference between the pulses of the muon scintillator and the NE213 detector, which represents the difference between the beam-on-dump time and the particle detection time, was also measured as the TOF spectra. The neutron TOF spectra and energy spectra can then be compared with those calculated using the FLUKA Monte Carlo code [3].

Data analysis

The neutron events were separated from the gamma-ray events by using two-dimensional graphical plots of the total and slow pulse height components of the NE213 detectors, as shown in Figure 2. The pile-up events were also eliminated using Figure 2. The neutron events can be clearly discriminated from the gamma-ray events, though some fraction of pile-up is seen in the figure.

Figure 2. Two-dimensional plot of the total and slow components of pulse charges of the NE213 detector for neutron and gamma-ray discrimination

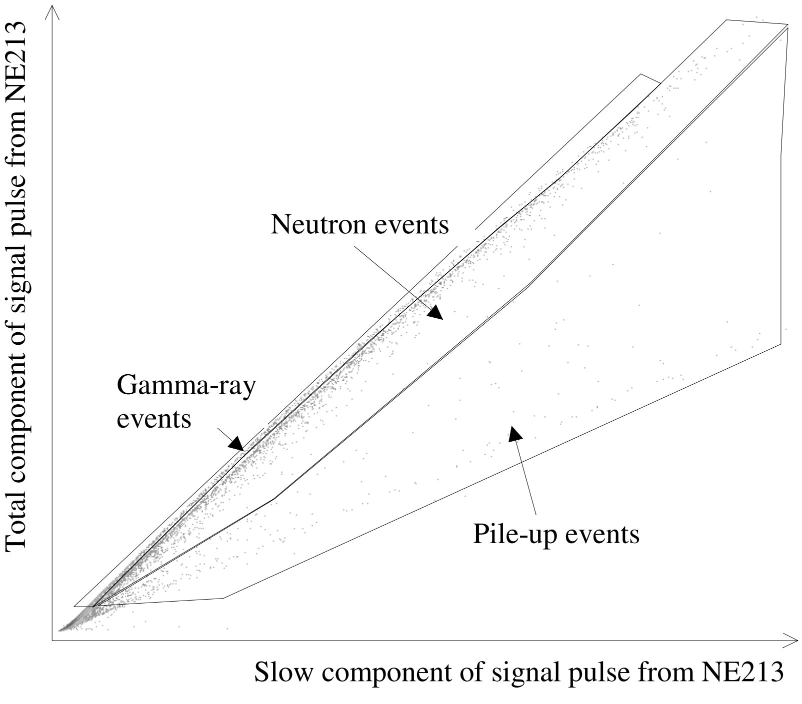

Table 1. Measurement conditions for each of shield thickness

Concrete thickness [cm]	Count/pulse (above 3 MeVee threshold)	Pile-up events [%]	Neutron events [%]	Correction factor F_1	Correction factor F_2
274	0.096	24	59	1.64	1.72
335	0.11	13	70	1.30	1.34
396	0.031	7	67	1.15	1.18
457	0.032	3	65	1.04	1.08

Table 1 provides the fractions of neutron events N_n/N_t and pile-up events N_p/N_t, while the rest represents the fraction of photon events N_g/N_t, where N_t is the total of events $N_g + N_n + N_p$. The fraction of pile-up events is larger for the thinner (91 cm thick) additional concrete shield, which is due to higher counting rates (shown in Table 1). The fraction of neutron events does not change much with the changing shield thickness as seen in Table 1. In an initial approximation, all the pile-up events were assumed to consist of two pulses (neutron-neutron, neutron-photon or photon-photon). Thus, the absolute values of neutron pulse counts were multiplied simply by the following pile-up correction factors. We considered two different factors *F* from our previous study [2]. One factor is simplified as follows:

$$F_1 = \frac{N_n + N_g + 2N_p}{N_n + N_g} \tag{1}$$

A second factor involves Poisson statistics as follows:

$$F_2 = \frac{N_n + N_p\left(1 + N_n/\left(N_n + N_g\right)\right)}{N_n} \tag{2}$$

The F_1 and F_2 values were obtained by using Eqs. (1) and (2), respectively, and are shown in Table 1. The *F* values estimated using these two methods are quite similar, with a difference of only a few percentage points. The F_2 values were estimated from Eq. (2). The pile-up correction factor was quite large at 1.72 for added concrete (91 cm thick).

The light output data in each channel of the NE213 detector are converted into a light output unit of MeVee (electron equivalent). This was done by using the Compton edges of 1.17 MeV and 1.33 MeV gamma-rays, and by using a 4.43 MeV gamma-ray in the spectra of a ^{60}Co gamma-ray source and a ^{241}Am-Be source, respectively. For the calibration of higher light output, Eq. (3) of Ref. [4] was used.

The neutron energy spectrum was obtained using the unfolding technique of the FORIST code [5] as well as the response functions of the NE213 detector for neutrons from 6-800 MeV [6]. In the analysis, the threshold of the light output pulses was set to 3 MeVee, which corresponded to the threshold (6 MeV) of the response function. In addition, the window function in the FORIST code was adjusted to obtain a reasonable convergence by varying the energy resolution values between 10-200%.

The total counts above the cut-off level obtained with the BS of seven different moderator thicknesses were unfolded using the SAND-2 code [7] with the response functions [8]. The neutron energy spectrum down to thermal energy was obtained using the initial guess spectrum, which was calculated with the FLUKA code [3].

Results and discussions

TOF spectra

Figure 3 shows the pile-up corrected experimental neutron TOF spectra (points) in cps units behind the four different total shield thicknesses of 274, 335, 396 and 457 cm. These are compared with the results calculated using the FLUKA code [3] (histograms). When FLUKA-calculated neutron currents above 6 MeV (3 MeVee) were folded with the detection efficiency of the NE213 detector as a function of neutron energy, the calculated TOF spectra were directly compared with the measured count rates as a function of time-of-flight (in nano-seconds). The detection efficiency, having a light output threshold of 3 MeVee, is given by the Cecil code [9], which was accurate to within 10-15% up to the neutron energy of several hundreds of MeV [10]. It should be noted that in this experiment the absolute time reference for TOF was obtained only for a 457-cm thick concrete measurement. Therefore, the other three measured TOF spectra were arbitrarily shifted to match the peaks of the calculated TOF spectra. The agreement in the shapes of the TOF spectra for the experiment and calculations was acceptable, especially for the 274 cm thickness. The longer tails of the larger TOFs in the measured distributions could be due to the time resolution of the measuring circuit. The absolute time-spectrum comparison for the 457 cm thickness showed that the experiment and calculations agreed rather well. The measured TOF spectrum for the 335 cm shield shows a small peak at very low TOF, which was not seen in the calculations. This spurious peak may have arisen from a small contribution to the neutron events that are produced by beam loss on a collimator, which is located upstream of the FFTB beam dump.

Energy spectra

In Figure 4, the neutron energy spectra unfolded using the FORIST code (points) were compared with the spectra calculated using the FLUKA code [3] (histograms). The graphs give the measured spectra per lethargy after pile-up correction was normalised for one electron incident on the beam dump measured with the TCM. Measured spectra after the pile-up correction generally agreed rather well with the calculated spectra both in spectral shapes and in absolute values for the energy region of 6-200 MeV and for 274, 335 and 396 cm thicknesses. In the energy region above 200 MeV, the measured energy spectra were lower than the calculated spectra. However, for the 457-cm thick shield, the measured spectrum was shifted to a lower energy region (~40 MeV lower) and compared to the FLUKA calculation. These results could be due in part to very poor statistics on detected counts and to poor accuracy of the NE213 detector's response function [6], which is caused by low neutron detection efficiency in the high-energy region. For the 274-cm thick shield, the pile-up corrected measured spectrum gave a somewhat smaller value than the calculated spectrum in the energy region around 20 MeV. This underestimation may arise partly from the larger contribution of the pile-up events, which could not be completely corrected as previously described.

Figure 5 compares both the neutron energy spectra measured with the NE213 and the BS, together with the FLUKA calculation [3] for the 274-cm thick concrete shield. The NE213 and the BS spectra agreed well both in the spectral shapes and the absolute values for the energy region above ~30 MeV, excluding a large dip around 20 MeV in the NE213 spectrum that is not seen in the BS and FLUKA spectra. The BS spectrum agreed well with the FLUKA spectrum. However, the FLUKA spectrum underestimated the BS spectrum in the energy region below ~100 keV.

Figure 3. Measured TOF spectra (points) penetrated through 274, 335, 396, 457-cm thick concrete shields compared with calculations using the FLUKA code (histograms). Measured results are given after a pile-up correction.

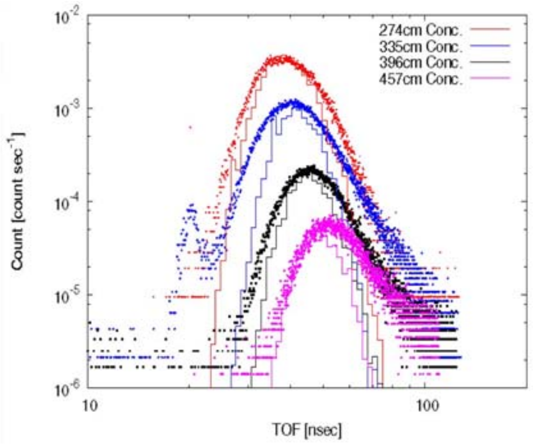

Figure 4. Measured (points) neutron energy spectra penetrated through 274, 335, 396, 457-cm thick concrete shields compared with FLUKA-calculated spectra (histograms). Measured results after pile-up correction are given in units of cm^{-2} lethargy^{-1} per 1 electron incident on beam dump.

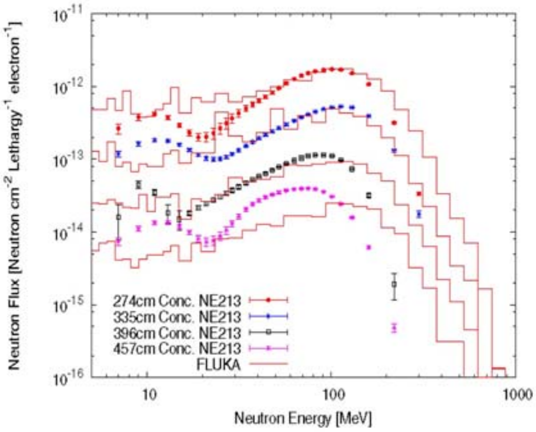

Figure 5. Comparison of two energy spectra measured with NE213 and BS, together with the FLUKA calculation behind a 274-cm thick concrete shield

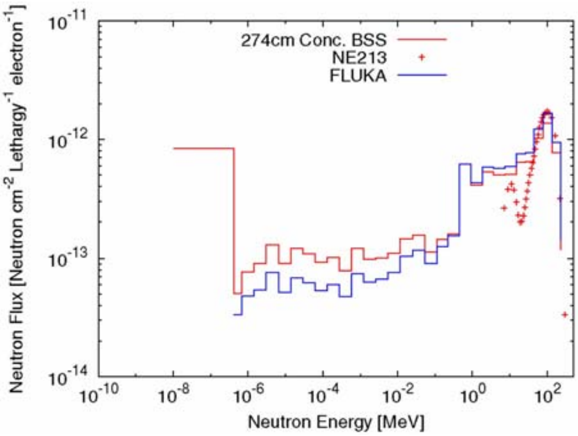

Conclusions

Neutron energy and time-of-flight spectra behind thick concrete shielding at 90° to the 28.7 GeV electron beam dump of the FFTB facility at SLAC were measured using an NE213 organic liquid scintillator and a multi-moderator spectrometer. The spectra were compared with simulations performed using the FLUKA Monte Carlo particle transport code. The measured neutron spectra agreed well with the calculated spectra. These experimental data will act as a good benchmark for deep penetration of high-energy neutrons through a concrete shield at high-energy electron accelerator facilities as well as for checking the accuracy of transport codes and analytical formulas used in shielding design.

Acknowledgements

The authors are grateful to Clive Field, Ronald Seefred and the staff of the Accelerator Operation and the Experimental Facility departments at SLAC for their support and assistance in setting up the experiment, and operation of the electron beam. This work was supported in part by the US Department of Energy under contract DE-AC03-76SF00515.

REFERENCES

[1] Taniguchi, S., M. Sasaki, T. Nunomiya, H. Iwase, S. Yonai, T. Nakamura, K. Kase, J.C. Liu, S.H. Rokni, S. Roesler, "Measurements of Neutron Energy Spectra behind the Lateral Shield of a High-energy Electron Beam Dump", *Shielding Aspects of Accelerators, Targets and Irradiation Facilities (SATIF-6)*, Stanford Linear Accelerator Center, Menlo Park, CA, USA, 221-225, 10-12 April 2002.

[2] Taniguchi, S., T. Nakamura, T. Nunomiya, H. Iwase, S. Yonai, M. Sasaki, S.H. Rokni, J.C. Liu, K. Kase, S. Roesler, "Neutron Energy and Time-of-flight Spectra behind the Lateral Shield of a High-energy Electron Accelerator Beam Dump. Part I: Measurements", *Nucl. Instr. and Meth.*, A503, 595 (2003).

[3] Roesler, S., J.C. Liu, S.H. Rokni, S. Taniguchi, "Neutron Energy and Time-of-flight Spectra Behind the Lateral Shield of a High-energy Electron Accelerator Beam Dump. Part II. Monte Carlo Simulations", *Nucl. Instr. and Meth.*, A503, 606 (2003).

[4] Nakao, N., T. Nakamura, M. Baba, Y. Uwamino, N. Nakanishi, H. Nakashima, S. Tanaka, "Measurements of Response Function of Organic Liquid Scintillator for Neutron Energy Range Up to 135 MeV", *Nucl. Instr. and Meth.*, A362, 454 (1995).

[5] Johnson, R.H., B.W. Wehring, ORNL/RSIC-40, Oak Ridge National Laboratory (1976).

[6] Sasaki, M., N. Nakao, T. Nakamura, T. Shibata, A. Fukumura, "Measurements of the Response Functions of an NE213 Organic Liquid Scintillator to Neutrons Up to 800 MeV", *Nucl. Instr. and Meth.*, A480, 2-3, 188 (2002).

[7] McElroy, W.N., S. Berg, T. Crockett, R.G. Hawkins, AFWL-TR-67-41, Vol. 1-4, Air Force Weapons Laboratory (1967).

[8] Sanna, R.S., "Thirty-one Group Response Matrices for the Multisphere Neutron Spectrometer over the Energy Ranges Thermal to 400 MeV", Health and Safety Laboratory, US Atomic Energy Commission, New York, HASL-767 (1973); see also V. Vylet, J.C. Liu, S.H. Rokni, L.H. Thai, "Measurements of Neutron Spectra at the Stanford Linear Accelerator Center", *Radiat. Protec. Dosim.*, 70, 425 (1997).

[9] Cecil, R.A., B.D. Anderson, R. Madey, *Nucl. Instr. and Meth.*, 161, 439 (1979).

[10] Nakao, N., T. Kurosawa, T. Nakamura, Y. Uwamino, "Development of a Quasi-monoenergetic Neutron Field and Measurements of the Response Function of an Organic Liquid Scintillator for the Neutron Energy Range from 66 to 206 MeV", *Nucl. Instr. and Meth.*, A476, 176 (2002).

SESSION IV

Dose and Related Issues

Chair: S. Rokni

USE OF ISODOSE RATE PICTURES FOR THE SHIELDING DESIGN OF A PROTON THERAPY CENTRE

Werner Hofmann, Wolfgang Dittrich
Framatome ANP GmbH, Radiation Protection, Erlangen, Germany
E-mails: werner.hofmann@framatome-anp.com, wolfgang.dittrich@framatome-anp.com

Abstract

The advantage of calculated dose rate field visualisation is demonstrated by a shielding example taken from the Rinecker Proton Therapy Center (RPTC), which is being constructed in Munich, Germany. The example consists of the representation of various shielding alternatives. This paper will discuss the following: basic conditions, the resulting isodose rate pictures and the principle method for their creation.

General

The RPTC is located in an urban area of Munich, which is close to the river Isar, resulting in subsoil of gravel and sand with significant ground water. At a very early stage, the decision was made not to construct an underground bunker. Consequently, the building walls must shield the radiation fields at the site boundary so as to maintain legal limits for public exposure. Special boundary conditions included the limitation of the outer wall thicknesses to a maximum of 2.4 m and the avoidance of additional concrete slabs on the exterior wall sides.

The owner of the centre is ProHealth AG of Munich, Germany (udo.peter@prohealth-ag.de) and the turnkey contractor is the M+W Zander Facility Engineering GmbH of Stuttgart, Germany (peter.gruebling@mw-zander.com). ACCEL Instruments GmbH of Bergisch-Gladbach, Germany (krischel@accel.de) supplies the proton cyclotron with 250 MeV proton energy and 500 nA net, the degrader with horizontal driven graphite wedges (the same type as at the PSI in Switzerland) and all other components of the beam line. The therapy units will consist of four gantries and one fixed beam installation.

Major problems regarding the shielding design of the ESS area consisted of the varying proton currents based on therapies and the different energies of the protons leaving the degrader (vary between ~70 and ~250 MeV) and the requirement for variable treatment plans based on patients' future needs. These result in varying intensities of the major radiation sources for primary protons, secondary neutrons, etc.

Strategy for improvement of shielding design with the degrader as the radiation source

All calculations for the ESS area were performed using a 500 nA net proton cyclotron current. For the calculations, the minimum post-degrader energy equalled 70 MeV, which corresponds to the maximum source intensity for secondary neutrons in this region. Using the calculated dose rate values, the annual shielded dose were estimated in accordance with a reference treatment programme (defined by the owner, ProHealth) and the corresponding proton data (provided by the supplier of the proton beam installations, ACCEL). The estimated shielded dose was then compared with the dose target for the specific shielding situation.

The dose targets (effective exposure) for the RPTC equalled < 5 mSv/yr individual exposure of the proton beam operational staff in the treatment and system rooms and < 1 mSv/yr individual exposure in rooms outside the proton beam areas and outside the building. At the site boundary the target was 1 mSv/yr, assuming the continual presence of a member of the public.

Alternatives for the shielding design

Figure 1 shows the isodose rate lines for the secondary neutrons caused by the degrader when adjusted to 70 MeV protons in the initial geometry case with heavy concrete in the walls. It is clear that additional methods for the reduction of the dose rate outside the wall should be considered.

Figure 2 illustrates the isodose rate lines for the same radiation source with the proposed mobile shielding elements in the form of a complex arrangement of blocks of heavy concrete. The reduction in exterior dose rate is clearly seen, however, there is a streaming effect of the neutron dose rate through thin layers and gaps as well as propagation through the access.

Figure 1. Degrader 70 MeV horizontal section through beam line

Isodose rate plot of neutron dose rate – without mobile shields

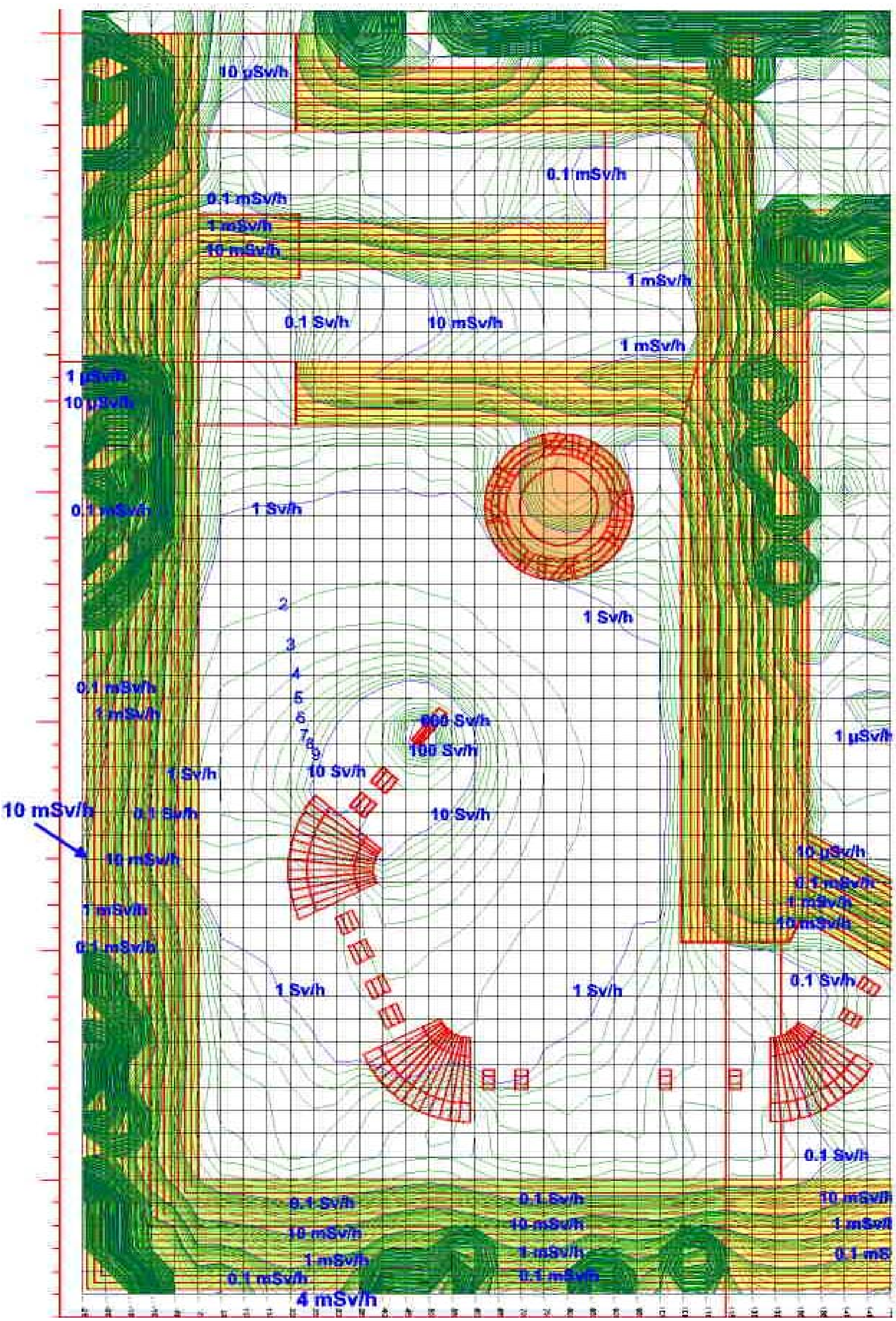

Figure 2. Degrader 70 MeV horizontal section through beam line

Isodose rate plot of neutron dose rate – first draft of mobile shields

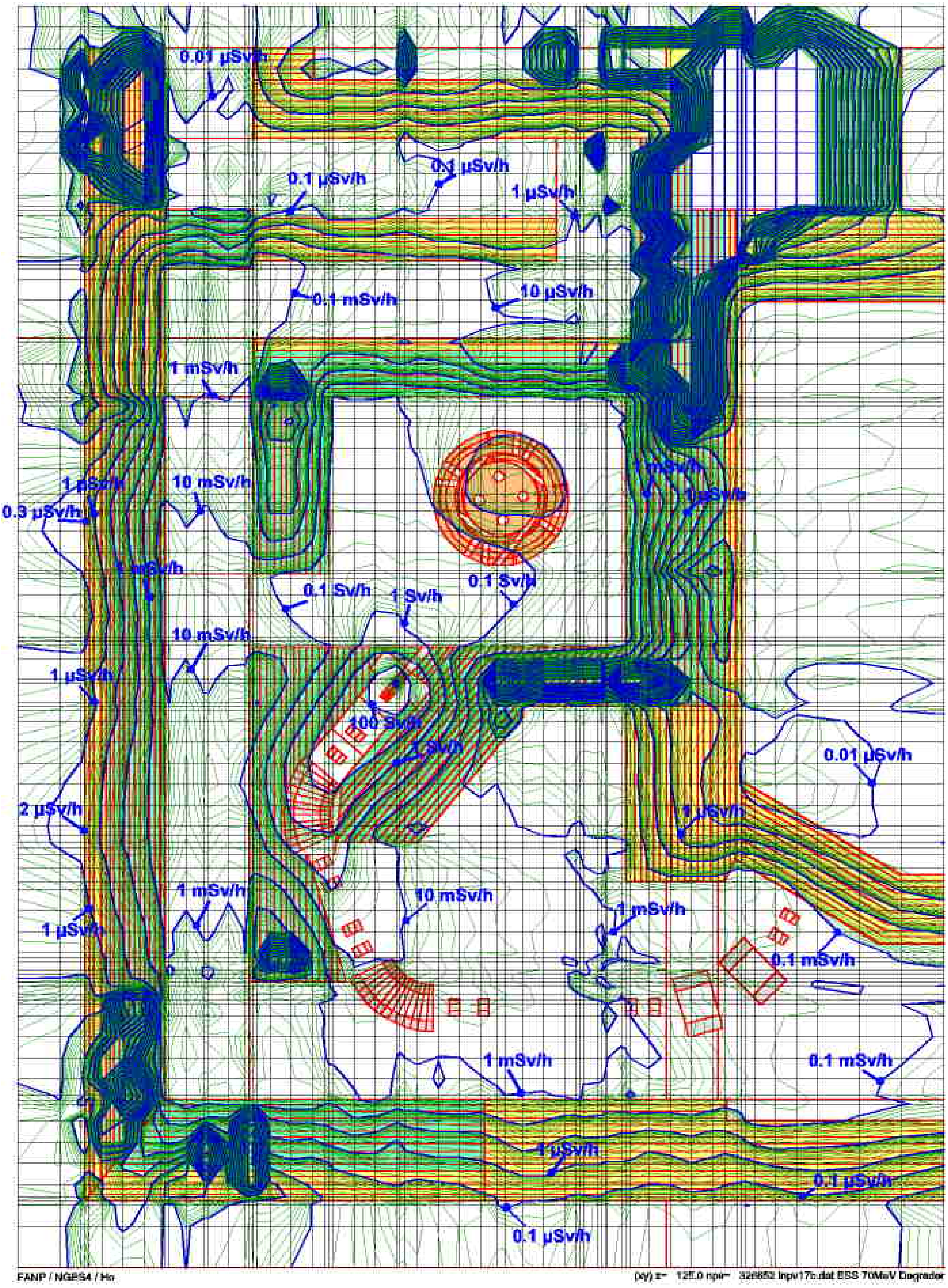

Figure 3 shows the results of the final approach using additional shielding in the form of mobile elements. During the calculation phase, a representation of the dose rate levels by means of colours was constructed (Figure 4). In our view, the main advantage is the very clear demonstration of radiation streaming effects.

Calculation method for the isodose rate pictures

The Monte Carlo code MCNPX was used. The particle source was a proton beam impinging on the regarded specific volume surface. The neutron dose rate was obtained by means of a mesh tally. As a uniform distribution in statistical error on the calculation results was needed, the variance reduction was performed by setting importances. Therefore, spatial partitioning was needed in the numerous slabs forming the walls, as can be seen in the figures. The results of the mesh tally were interpolated in a separate routine from MCNPX in order to get the isodose rate lines. To obtain the final picture, the figure with the isodose rate lines was imported into a graphic tool together with a picture of the corresponding section through the geometry model of the calculation (included in Figures 1-4). Lastly, attributes were added manually.

Conclusion

The representation of the radiation field as isodose rate contours provides a clear visualisation of the calculated radiation field. It enables the recognition of streaming effects through shielding gaps, ducts or labyrinths as well as the recognition of weak points in shields. Therefore, it is not only a very useful tool for the shielding design, but also for the visualisation of radiation heating in materials. Usage of this tool has increased at Framatome ANP over the past two years.

Figure 3. Degrader 70 MeV horizontal section through beam line

Isodose rate plot of neutron dose rate – final version of mobile shields

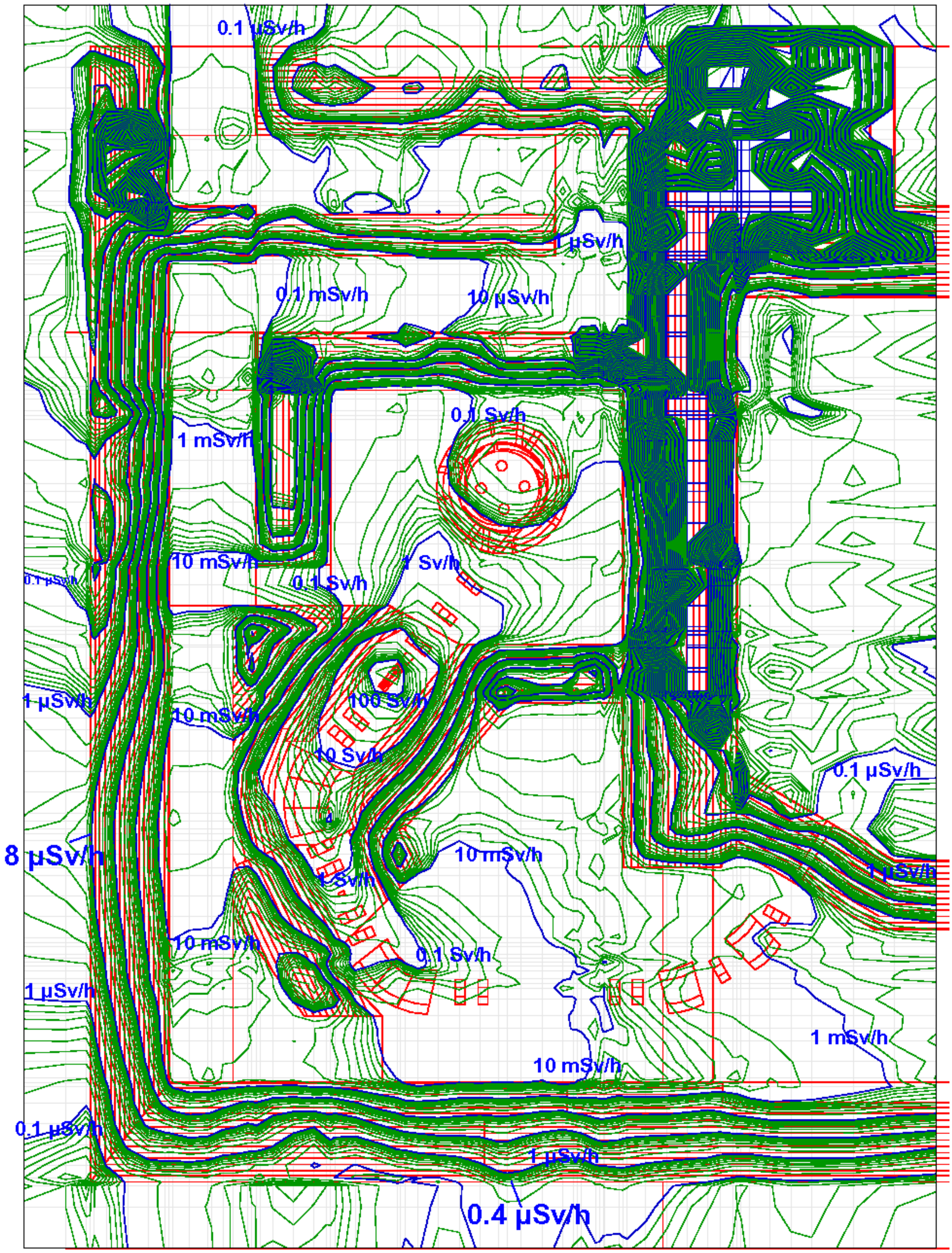

Figure 4. Degrader 70 MeV horizontal section through beam line

Representation of neutron dose rate – final version of mobile shields

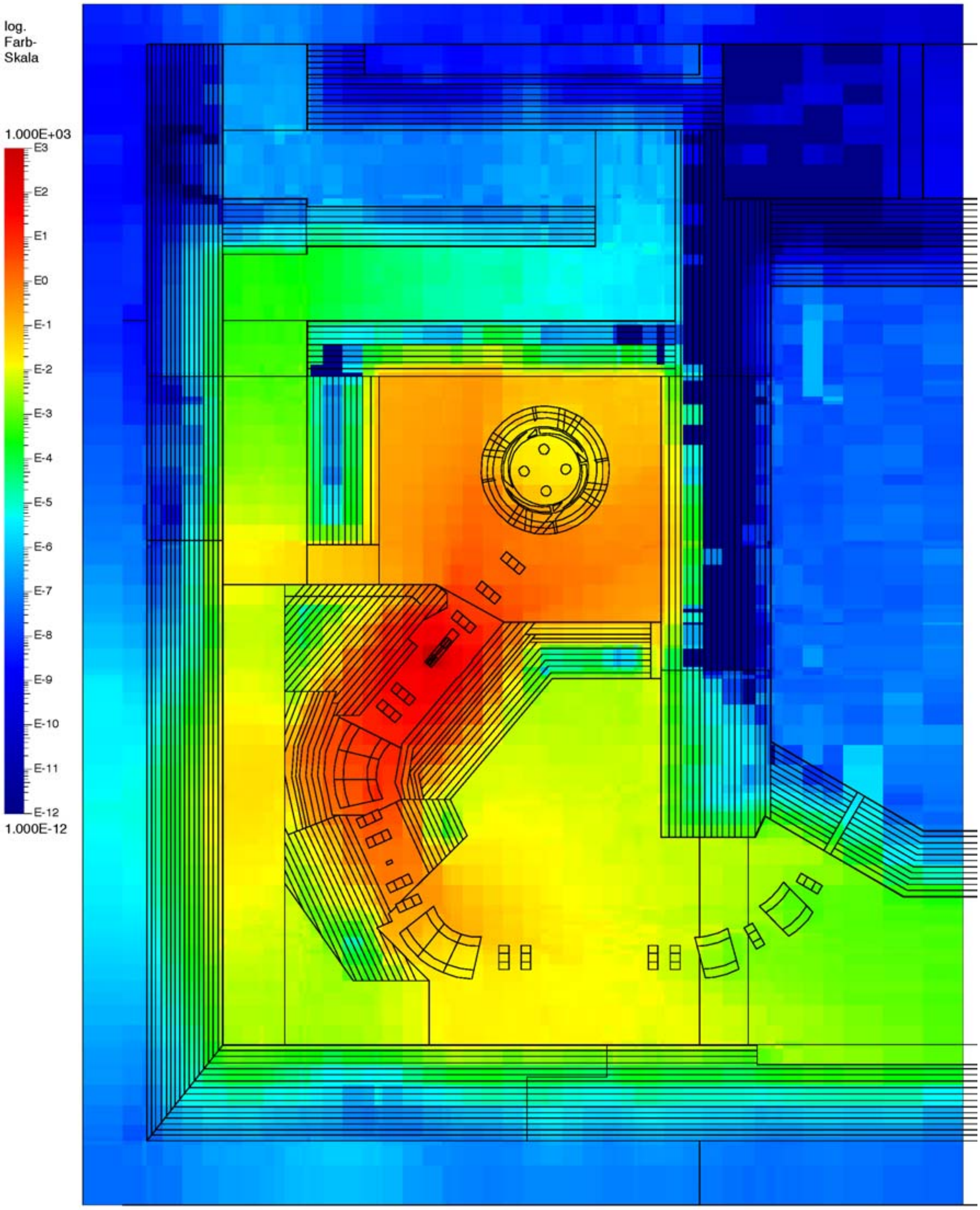

BENCHMARK STUDIES OF INDUCED RADIOACTIVITY AND REMANENT DOSE RATES PRODUCED IN LHC MATERIALS

M. Brugger, S. Mayer, S. Roesler, L. Ulrici
CERN SC-RP
1211 Geneva 23, Switzerland
E-mail: Markus.Brugger@cern.ch

H. Khater, A. Prinz, H. Vincke
SLAC, M.S. 48
2575 Sand Hill Road
Menlo Park, CA 94025, USA

Abstract

Samples of materials that will be used for elements of the LHC machine as well as for shielding and construction components were irradiated in the stray radiation field of the CERN-EU high-energy Reference Field facility. The materials included various types of steel, copper, titanium, concrete and marble as well as light materials such as carbon composites and boron nitride. Emphasis was put on an accurate recording of the irradiation conditions, such as irradiation profile and intensity, and on a detailed determination of the elemental composition of the samples. After the irradiation, the specific activity induced in the samples as well as the remanent dose rate were measured at different cooling times ranging from about 20 minutes to two months. Furthermore, the irradiation experiment was simulated using the FLUKA Monte Carlo code and specific activities. In addition, dose rates were calculated. The latter was based on a new method simulating the production of various isotopes and the electromagnetic cascade induced by radioactive decay at a certain cooling time. In general, solid agreement was found, which engenders confidence in the predictive power of the applied codes and tools for the estimation of the radioactive nuclide inventory of the LHC machine as well as the calculation of remanent doses to personnel during interventions.

Introduction

Radiation safety is a concern regarding the activation of the beam line components at high-energy accelerators such as the Large Hadron Collider (LHC). This is the case not only during the operation and maintenance of the machine but also later in decommissioning and final disposal of the activated materials. In all cases, accurate calculations of the radionuclide inventory are required, which are typically performed with modern particle interaction and transport codes. In the case of the LHC, mainly the Monte Carlo code FLUKA [1,2] is used.

In contrast to integral quantities such as the dose equivalent of personnel by prompt radiation or the dose to components, predictions for the production of individual isotopes can be much less reliable as they depend strongly on details of the models implemented in the Monte Carlo (MC) code. Thus, benchmark experiments are of the utmost importance in order to verify the accuracy and limits of applicability of these models. Unfortunately, activation experiments are not trivial and are prone to uncertainties of various natures.

Several experiments have already been performed for both electron [3,4] and hadron [5-11] accelerators. However, most of these studies concentrate either on induced activity or on remanent dose rates although both are closely linked to each other. Due to the complexity of the involved physical processes and analysis methods, it is often difficult to attribute disagreements between calculated and measured results to their respective source of uncertainty.

In addition, previous attempts to estimate the remanent dose rates from activated LHC components were typically performed using the so-called omega factors [12] by relating the dose rates measured on contact with the respective object to the density of inelastic interactions. However, this approach has several significant limitations that strongly restrict its range of application. As a result, a method (to be used with FLUKA) has been developed [13] that is based on an explicit simulation of the production of radioactive isotopes as well as their decay for a certain cooling time. Decay photons are sampled according to their emission intensities, and electrons and positrons are sampled according to the decay energy spectra. These particles are then transported and dose equivalent rates can be calculated at any point of interest in the respective geometry.

This work is a continuation of the studies reported in Refs. [13,14], addressing a larger variety of materials. Furthermore, the present study combines activation and dose rate measurements, and attempts to reduce uncertainties found in previous benchmark experiments as well as in performed simulations. The following aspects are covered: careful monitoring of the irradiation parameters, low-level gamma spectrometry measurements, proper treatment of decay chains of isotopes, detailed elemental analysis of the irradiated material and simulations of isotope production with high statistical significance.

Description of the experiment

All samples were irradiated at the CERN-EU high-energy Reference Field (CERF) facility [15]. At CERF, a pulsed 120 GeV/c mixed hadron beam (1/3 protons, 2/3 positively charged pions) from the Super Proton Synchrotron (SPS) accelerator is aimed at a 50-cm long copper target, which creates a stray radiation field around the target that is similar to beam loss regions at high-energy accelerators (collimators, dumps, etc.). The samples were either laterally attached to the target or placed on a sample holder, located immediately downstream of the target and centred with its axis. Figure 1 shows a schematic view of the experimental area as well as a picture of the copper target together with the samples and sample holder.

Figure 1. Axonometric view of the CERF facility

In the graphical representation, the side shield is removed to show the inside of the irradiation cave with the copper target set-up

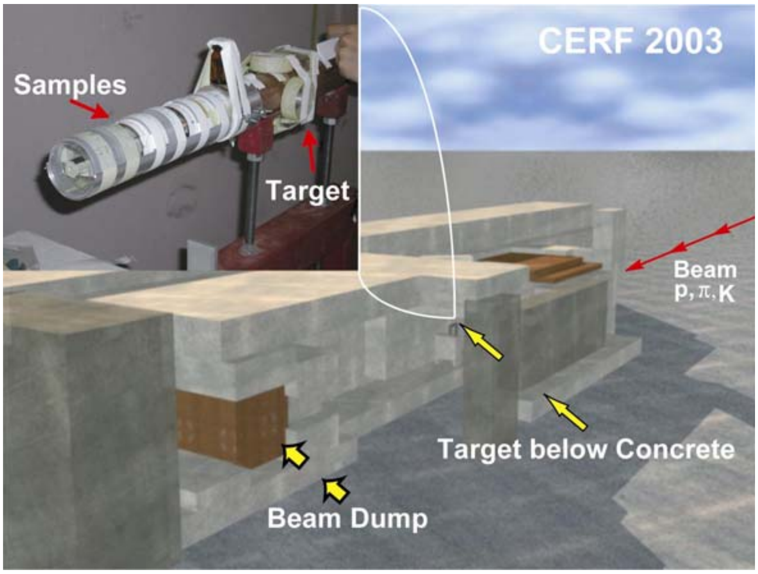

The alignment of the target with respect to the beam axis was measured at the upstream and downstream faces of the target using Polaroid film and was then taken into account for the simulations. The samples were irradiated with exposure times ranging from a few hours to several days and a total number of accumulated beam particles ranging from 1.6×10^{11} to 1.5×10^{12}. The lateral beam profile and the number of particles in each beam spill (cycle length of 16.8 s) were recorded for later use in the simulation as well as during the post-processing of the FLUKA results (see Figures 2, 3).

Figure 2. Beam profile as measured during one of the irradiations

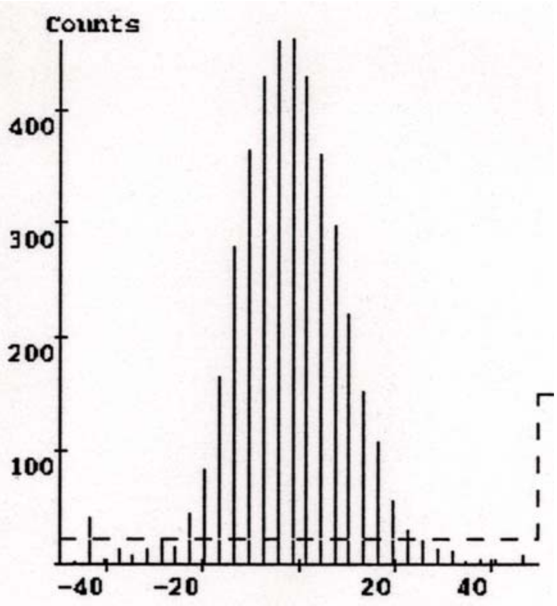

Figure 3. Beam intensity profile as a function of the irradiation time (given in the number of spill, or 16.8 s each) for the longest irradiation period (~1 week)

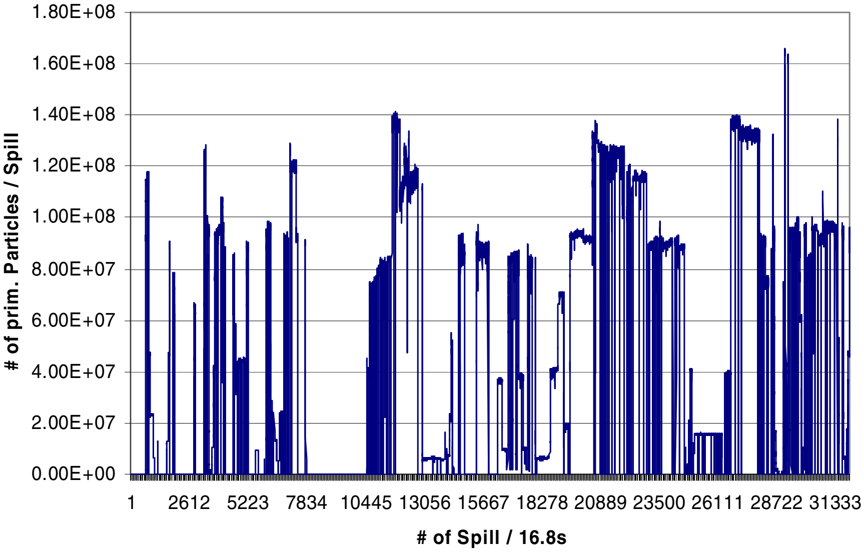

Samples

A total of 14 different materials used in the construction of the LHC were selected, ranging from various types of steel, copper, titanium, concrete and marble to light materials, such as carbon composites and boron nitride. Of these materials, 40 samples were machined to a size of about $2 \times 2 \times 2$ cm^3 except for the concrete and marble samples, which were powdered and filled into boxes of ~4 cm in length and diameter. The elemental compositions of the materials were analysed by a number of different outside companies and institutes (EMPA Dübendorf, Überlandstrasse 129, CH-8600 Dübendorf, Switzerland; EIG, Ecole d'Ingenieurs – hes Geneve, 4 rue de la Prairie, CH-1202 Geneva, Switzerland; EA Elemental Analysis, Inc., Lexington, KY 40511, USA) using a variety of techniques. The materials discussed in this paper, their elemental composition as well as their densities, are summarised in Table 1.

Gamma spectrometry

The specific activities of the irradiated samples were measured at different cooling times ranging from about 20 minutes to two months. The gamma spectrometry measurements were performed with a high-sensitivity, low-background High-Purity Germanium (HPGe) detector by Canberra [(245 cm^3 sensitive volume, 60% efficiency at 1.33 MeV); CANBERRA EURISYS SA, 4 avenue des Frênes, 78067 Saint-Quentin-en-Yvelines, France]. The data acquisition and analysis were carried out using the software GENIE2000 (version 2.1) by Canberra and the PROcount-2000 counting procedure software. This system was complemented with LABSOCS (Laboratory Sourceless Calibration Software, version 4.1.1), mathematical efficiency calibration software by Canberra, which takes into account geometrical effects and corrects for self-absorption in the samples.

The samples were positioned on a custom-made sample holder at different reproducible distances from the detector. The distance for each sample was chosen on the basis of its remanent dose rate and on the respective dead time of the measuring system. For each distance the efficiency of the detector was calculated using LABSOCS.

Table 1. Density ρ and elemental composition (in per cent by weight) of the samples discussed in this paper. Note that the density of concrete corresponds to powdered concrete.

Elemental composition in per cent by weight											
Steel **ρ = 7.25 g/cm^3**		**Copper** **ρ = 8.89 g/cm^3**		**Aluminium** **ρ = 2.72 g/cm^3**		**Concrete** **ρ = 1.70 g/cm^3**		**Titanium** **ρ = 4.42 g/cm^3**		**Resin** **ρ = 1.24 g/cm^3**	
Fe	63.088	Cu	99.328	Al	96.4589	O	47.87	Ti	88.036	C	66.77
Cr	17.79	Al	0.4745	Si	1.08	Ca	35.4	Al	6.5	O	27.64
Mn	11.43	Si	0.13	Mg	0.83	C	9.24	V	5.28	H	5.59
Ni	6.5	Fe	0.0261	Mn	0.696	Si	4.0	Fe	0.093		
Si	0.38	S	0.0137	Fe	0.5	Al	0.97	Cr	0.05		
N	0.31	Cd	0.004	Cu	0.115	Fe	0.69	Ni	0.0116		
Co	0.11	Sb	0.004	Zn	0.1044	Mg	0.64	Cl	0.0102		
P	0.019	Cr	0.0021	Cr	0.033	H	0.6	Mn	0.0071		
C	0.095	Te	0.002	Ti	0.0302	K	0.26	Cu	0.0043		
Mo	0.09	Pb	0.002	Pb	0.0287	S	0.15	Zn	0.004		
Cu	0.085	Sn	0.002	Sn	0.0278	Ti	0.06	P	0.0038		
V	0.07	As	0.002	Ca	0.0201	Sr	0.05				
Ti	0.01	Ag	0.002	Bi	0.0161	P	0.03				
Nb	0.01	Zn	0.002	Ni	0.0128	Na	0.03				
W	0.01	Mn	0.0016	P	0.0126	Mn	0.01				
O	0.002	Se	0.0011	Ga	0.0102						
S	0.001	Bi	0.001	Cl	0.0087						
		Ni	0.001	S	0.0076						
		P	0.0004	V	0.0041						
		Co	0.0002	Zr	0.0024						
				Am	0.0014						

The analysis performed by the GENIE2000 software includes advanced analysis algorithms for nuclide identification, interference correction (resolution of overlapping peaks into individual components), calculation of specific activities, background subtraction and efficiency correction. The nuclide identification within GENIE2000 is based on standard or user-specific libraries. The latter were created for each sample material taking into account the chemical composition, the possible activation reaction channels and the cooling time. All results of the analyses have since been revised manually for some radionuclides (e.g. in the case of interference in the gamma energies of different nuclides), the semi-manual calculation of the specific activity having turned out to be the most accurate method.

Dose rate measurements

Following the irradiation of each sample, remanent dose rates were measured with two different instruments, a portable spectrometer and a dose meter, at various cooling times and distances to the surface of the samples (see Figure 4).

The first instrument is a Microspec portable spectrometer by Bubble Technology Industries [(BTI); Bubble Technology Industries Inc., HWY. 17, Chalk River, Ontario, Canada K0J 1J0]. It is based on a NaI crystal of cylindrical shape with a diameter and height of about 5 cm. The scintillation light is detected by a photomultiplier tube, which converts the scintillation light into an electronic signal and amplifies the signal. Dose rates can be measured up to 100 μSv/h in a range of 60 keV to 3 MeV. Before each use the spectrometer was calibrated with a ^{22}Na source according to the manufacturer's recommendation. To determine dose rates the device measures energy spectra, which are then internally folded with the detector response as calculated by the manufacturer.

Figure 4. Instruments used to measure remanent dose rates: Microspec (left) and Eberline (right)

The second instrument is a Thermo Eberline dose meter of type FHZ 672 (Thermo Electron ESM Eberline Instruments GmbH, Frauenauracherstr. 96, D-91056 Erlangen, Germany). This instrument is based on a combination of an organic scintillator material and a NaI(Tl) crystal with a cylindrical shape of 9 cm in height and diameter. It achieves the energy characteristic of an ambient dose equivalent H*(10) covering a range of 48 keV to 6 MeV. Dose rates can be measured in a range from a few nSv/h up to 100 μSv/h. In contrast to the Microspec spectrometer, here dose rates are not obtained via gamma energy. Instead, an average detector response value is assumed.

Since an absolute comparison of measured and calculated dose rates (especially on contact) requires knowledge of the effective centre of the detector it was determined in the CERN calibration laboratory. The dose rates from three different calibration sources (^{60}Co, ^{137}Cs and ^{22}Na) were measured at distances R between the source and the surface of the detector, varying between contact ($R = 0$) and 30 cm. The results for each source were fitted using the following $1/R^2$ behaviour:

$$\frac{dD}{dt}\left[\frac{\mu Sv}{h}\right] = \frac{K_0}{(R + R_0)^2}$$

Here R_0 (in cm) denotes distance from the surface (contact) to the effective centre of the detector and K_0 is a free fit parameter. The resulting parameter R_0 varies slightly for the different sources with an average value of 2.4 cm and 7.3 cm for the Microspec and Eberline instruments, respectively.

For the dose rate measurements, the irradiated samples were placed on a holder to allow for distances of 12.4 cm, 22.4 cm and 32.4 cm between the surface of the sample (the surface that was facing the CERF target during the irradiation) and the centre of the detector. The dose rate at the latter distance of 32.4 cm was only measured using the Microspec instrument. In addition, the samples were placed in direct contact with the detectors. All measurements were carried out in a laboratory with a low background radiation dose rate of 55 nSv/h.

FLUKA simulations

Both the specific activities of different radionuclides in the samples and the remanent dose rates at various distances were calculated using FLUKA. For the isotope production, the simulations were based on a detailed description of the experimental set-up containing the copper target, the holder with the samples, as well as the concrete enclosure of the beam line shielding. According to the beam profile measurements, the beam was assumed to be rectangular with a Gaussian profile of 2.1 cm and 2.6 cm full widths at half maximum (FWHM) in lateral directions. The small offset of the beam axis with respect to the axis of the copper target was also included in the simulation. Furthermore, the elemental compositions of the samples were considered as given in Table 1.

The full hadronic cascade was simulated in the target, samples and beam line enclosure. Neutrons were transported down to thermal energies; for all other hadrons a threshold of 1 keV was applied. For the simulation of isotope production, the electromagnetic cascade was not simulated as activation by photonuclear interactions can be neglected in hadron-induced cascades. Separate simulations were performed for proton and pion beam particles and their results were combined in a post-processing step in accordance with actual beam composition. The total yield of all produced radionuclides was scored separately for all samples and the results were written into output files. These data files were then post processed [16] and specific activities were calculated taking into account the decay chains and build-up of isotopes as well as the correct intensity profile of the respective irradiation experiment.

Additionally, remanent dose rates were calculated following the two-step approach as introduced in Refs. [13,17]. In the first step (i.e. the calculation of isotopes), FLUKA implementation of the geometry of the CERF experimental area includes all details as described above. In order to increase the statistical significance of the results for the relatively small samples, particle transport into the sample regions was biased using region importance factors. Isotope information was written into files for a total of 12 cooling times [ranging from six minutes to 1 000 hours (~42 days)] and for the exact profile of the respective irradiation (each beam pulse and the actual number of particles were considered).

In the second step of the simulation (i.e. the calculation of remanent dose rates), the FLUKA geometry consisted only of the respective sample surrounded by air, which roughly represents the situation during laboratory dose rate measurements. Backscattering of photons from the walls of the laboratory (concrete) was found by MC simulation to have only a minor influence on the dose rate results. Therefore, the laboratory walls were neglected in the simulations as was the sample holder, which provided only a small volume for scattering. A dedicated simulation of the electromagnetic cascade caused by gamma and positron emitters was performed for each cooling time and the dose equivalent was calculated by folding the particle fluence with appropriate fluence-to-dose equivalent conversion factors [18]. The emission of electrons was neglected as it was found to give a negligible contribution to the total dose rate. Results of these calculations were compared to experimental values. In addition, the CERF copper target, being a relatively large object as compared to the samples, was used to benchmark the FLUKA simulation approach.

Results for specific activities

In the text that follows the calculated and measured specific activities are compared for each material. All cooling times refer to the beginning of the respective gamma spectrometry measurement. As previously mentioned, the first gamma spectrometry measurement was typically performed after a cooling time of between 20 minutes and one hour. This allowed for the identification of isotopes with half-lives of less than one hour. Tables 2-8 show the simulated and experimentally measured specific activities in Becquerel together with their corresponding errors in percent. In addition to the ratios of calculated-to-measured specific activities, the ratios of measured specific activities to the so-called Minimal Detectable Activity (MDA) of the gamma spectrometry measurement are listed in the tables below. Except for some isotopes in the resin sample, only those isotopes are given that were identified by both the experiment and the simulation. Except for this particular case where the chemical composition was not sufficiently well-known, more isotopes are usually predicted by the simulation than can be detected in the measurement for various reasons: an insufficient yield of gamma lines in the detectable range, the inability to separate their contribution to the 511 keV peak from the contributions of other isotopes or an activity level below the MDA.

Many isotopes were detected at different cooling times and their specific activities were determined. However, for the final comparison with FLUKA predictions only one measurement result was selected for each nuclide based on the following criteria: smallest experimental uncertainty, largest ratio between the measured specific activity and the respective MDA and the appropriate cooling time as compared to the half-life of the respective isotope. The experimental errors contain both statistical and systematic uncertainties of the spectrometry analysis. For the calculated values the errors represent statistical uncertainties only. Isotopes predicted with an uncertainty larger than 20% are not listed. Uncertainties in the half-lives used to follow the radioactive decay chains were found to have a negligible influence on the results. The errors of the ratios for calculated-to-measured specific activities were obtained by summing up the relative errors of the latter.

Aluminium

Table 2 shows results for the isotopes detected in the aluminium sample. Many isotopes are relatively well-reproduced by FLUKA. The light nuclide ^{7}Be is underestimated by FLUKA due to the fact that multi-fragmentation processes are not implemented in the code. Furthermore, ^{44}Sc and ^{46}Sc are overestimated by the simulation, possibly due to uncertainties in the assumed elemental composition (calcium content) or due to an overestimation of the respective production channels [17]. Finally, in the case of ^{58}Co the reaction (n,p) on nickel most likely contributes a significant fraction and, thus, the higher FLUKA value might indicate an overestimation in the nickel content of the sample. Furthermore, the more elevated activity of ^{52}Mn may be explained by the fact that individual meta-stable states cannot be predicted by FLUKA and, thus, equal sharing of the calculated activity among the different states is assumed.

Table 2. Comparison of calculated and measured specific activities of isotopes in the aluminium sample for the cooling times: (1) 1 d, 16 h, 55 m, (2) 16 d, 8 h, 56 m and (3) 51 d, 9 h, 47 m

Ratios of the experimental results-to-MDA (Exp/MDA) and of the calculated-to-measured specific activities (FLUKA/Exp) are given. Note that the errors of the specific activities are quoted in %, whereas those of the ratios are given as absolute values.

Cooling time	Isotope	$t_{1/2}$	FLUKA (Bq/g) ± (%)	Experiment (Bq/g) ± (%)	Exp/MDA	FLUKA/Exp
3	^{7}Be	53.29 d	0.287 ± 3.6	0.789 ± 12.6	20.4	0.36 ± 0.06
3	^{22}Na	2.60 y	0.307 ± 1.2	0.365 ± 9.6	94.8	0.84 ± 0.09
1	^{24}Na	14.96 h	33.0 ± 0.4	38.6 ± 3.6	821.3	0.85 ± 0.03
1	^{44}Sc	3.93 h	0.508 ± 3.3	0.229 ± 23.6	2.1	2.22 ± 0.60
2	^{46}Sc	83.79 d	0.039 ± 3.3	0.025 ± 15.7	5.2	1.57 ± 0.30
1	^{47}Sc	80.28 h	0.161 ± 16.5	0.163 ± 10.6	6.0	0.99 ± 0.27
1	^{48}V	15.97 d	0.185 ± 10.9	0.199 ± 7.4	5.0	0.93 ± 0.17
2	^{51}Cr	27.70 d	0.224 ± 6.3	0.257 ± 16.8	4.8	0.87 ± 0.20
1	^{52}Mn	5.59 d	0.531 ± 4.0	0.224 ± 5.6	8.3	2.37 ± 0.23
3	^{54}Mn	312.12 d	0.078 ± 3.5	0.080 ± 11.4	17.7	0.97 ± 0.14
3	^{57}Co	271.79 d	0.004 ± 17.6	0.004 ± 32.3	1.3	0.83 ± 0.42
2	^{58}Co	70.82 d	0.035 ± 5.0	0.019 ± 21.6	3.7	1.82 ± 0.48

Stainless steel

The results for stainless steel are given in Table 3. The specific activities of most of the heavier isotopes (A > 43) are remarkably well-reproduced by FLUKA. Except for a few cases, the agreement of calculated and measured values is within the given uncertainties. The activities of light isotopes are underestimated as already observed for the aluminium sample. The nuclide ^{56}Mn, which is mainly produced by neutron capture on ^{55}Mn, is slightly overestimated, possibly due to uncertainties in the elemental composition.

Further explanations, related to the gamma spectrometry analysis and the simulation set-up, are under investigation. Finally, the two isotopes, ^{56}Co and ^{57}Ni, are products of spallation reactions on nickel. As the nickel content was determined with rather high accuracy and the uncertainties of both the calculated and measured activities are rather small, inaccuracies in the simulation of the respective production channels remain the only reason for the slight overestimation of measured value by FLUKA.

Table 3. As in Table 2, stainless steel sample.
Cooling times: (1) 22 m, (2) 31 m, (3) 59 m, (4) 1 d, 6 h, 28 m and (5) 17 d, 10 h, 39 m.

Cooling time	Isotope	$t_{1/2}$	FLUKA (Bq/g) ± (%)	Experiment (Bq/g) ± (%)	Exp/MDA	FLUKA/Exp
5	^{7}Be	53.29 d	0.02 ± 9.3	0.205 ± 24.3	1.9	0.10 ± 0.03
4	^{24}Na	14.96 h	0.142 ± 4.3	0.513 ± 4.3	65.2	0.28 ± 0.02
3	^{41}Ar	1.82 h	1.06 ± 15.4	2.87 ± 8.7	21.9	0.37 ± 0.09
1	^{42}K	12.36 h	4.73 ± 4.3	5.98 ± 23.9	3.4	0.79 ± 0.22
4	^{43}K	22.30 h	0.678 ± 4.1	1.08 ± 4.6	19.0	0.63 ± 0.05
1	^{38}Cl	37.24 m	3.5 ± 5.3	6.9 ± 11.5	11.6	0.51 ± 0.09
1	^{39}Cl	55.60 m	1.39 ± 13.3	2.24 ± 14.4	3.5	0.62 ± 0.17
1	^{m34}Cl	32.00 m	3.34 ± 5.4	2.67 ± 17.3	6.7	1.25 ± 0.28
4	^{47}Ca	4.54 d	0.042 ± 18.9	0.098 ± 25.1	2.5	0.42 ± 0.19
1	^{43}Sc	3.89 h	15.3 ± 3.1	12.9 ± 17.9	6.5	1.19 ± 0.25
4	^{44}Sc	3.93 h	9.54 ± 1.0	13.8 ± 4.8	131.4	0.69 ± 0.04
4	^{m44}Sc	58.60 h	8.93 ± 1.0	6.51 ± 7.1	126.4	1.37 ± 0.11
5	^{46}Sc	83.79 d	0.734 ± 0.8	0.873 ± 8.3	63.3	0.84 ± 0.08
4	^{47}Sc	80.28 h	6.37 ± 1.5	6.57 ± 8.2	128.1	0.97 ± 0.09
4	^{48}Sc	43.67 h	1.98 ± 3.2	1.57 ± 5.2	68.9	1.27 ± 0.11
4	^{48}V	15.97 d	13.1 ± 0.7	8.97 ± 3.1	411.5	1.46 ± 0.06
4	^{48}Cr	21.56 h	0.633 ± 4.8	0.584 ± 6.7	10.8	1.08 ± 0.12
2	^{49}Cr	42.30 m	14.8 ± 2.7	13.3 ± 9.0	6.0	1.11 ± 0.13
5	^{51}Cr	27.70 d	19.1 ± 0.4	15.1 ± 12.5	102.0	1.26 ± 0.16
1	^{52}Mn	5.59 d	1.5 ± 1.5	1.4 ± 13.0	5.1	1.10 ± 0.16
2	^{m52}Mn	21.10 m	18.8 ± 1.5	17.9 ± 7.3	39.8	1.05 ± 0.09
5	^{54}Mn	312.12 d	3.02 ± 0.3	2.85 ± 10.1	195.2	1.06 ± 0.11
1	^{56}Mn	2.58 h	74.3 ± 6.4	53.8 ± 6.8	98.5	1.38 ± 0.18
1	^{52}Fe	8.28 h	0.79 ± 7.3	0.72 ± 39.1	1.1	1.10 ± 0.51
4	^{55}Co	17.53 h	1.16 ± 3.1	1.04 ± 4.6	19.3	1.11 ± 0.09
5	^{56}Co	77.27 d	0.69 ± 1.4	0.49 ± 7.6	48.8	1.42 ± 0.13
5	^{57}Co	271.79 d	0.546 ± 0.9	0.463 ± 10.7	24.6	1.18 ± 0.14
4	^{58}Co	70.82 d	2.06 ± 0.4	2.21 ± 5.9	45.8	0.93 ± 0.06
4	^{57}Ni	35.60 h	5.2 ± 2.0	3.5 ± 4.5	103.5	1.48 ± 0.10

Copper

The specific activities of the copper sample together with the ratios of calculated and measured values are given in Table 4. For many isotopes the simulated and measured activities agree within ~30%. The underestimation by FLUKA of the production of low-mass isotopes, which was observed for most metallic samples, is due at least in part to deficiencies in the description of fragmentation in FLUKA. Furthermore, activities of individual meta-stable states cannot be predicted by FLUKA and, thus, equal sharing of the calculated activity among the different states is assumed. This might lead to discrepancies between calculated and measured activities as in the cases of ^{m44}Sc/^{44}Sc and ^{m52}Mn/^{52}Mn. For some isotopes an error in the treatment of the parent-daughter correction in the gamma spectrometry analysis has led so far to unresolved problems and could explain the significant overestimation by the gamma spectrometry measurement [as with ^{28}Mg (parent of ^{28}Al)]. Regarding ^{65}Ni and ^{64}Cu, careful investigation of production cross-sections calculated with FLUKA (also available in the literature) may give further insight into the reasons for the disagreement. Overestimation of ^{65}Zn could be caused by the gamma spectrometry analysis and is presently under study.

Table 4. As in Table 2, copper sample. Cooling times: (1) 34 m, (2) 1 h, 7 m and (3) 48 d, 3 h, 21 m.

Cooling time	Isotope	$t_{1/2}$	FLUKA (Bq/g) ± (%)	Experiment (Bq/g) ± (%)	Exp/MDA	FLUKA/Exp
3	^{7}Be	53.29 d	0.06 ± 4.5	1.29 ± 12.6	11.9	0.05 ± 0.01
3	^{22}Na	2.60 y	0.02 ± 2.5	0.029 ± 14.3	5.6	0.66 ± 0.11
2	^{24}Na	14.96 h	3.94 ± 2	14.8 ± 8.5	121.3	0.27 ± 0.03
2	^{28}Mg	20.91 h	0.16 ± 13.9	1.89 ± 14.6	5.5	0.09 ± 0.03
1	^{38}K	7.64 m	0.21 ± 2.7	4.59 ± 34.5	4.0	0.05 ± 0.02
1	^{42}K	12.36 h	12.7 ± 1.7	21.6 ± 15.3	6.8	0.59 ± 0.10
2	^{43}K	22.30 h	4.19 ± 2.5	6.38 ± 11.1	11.4	0.66 ± 0.09
2	^{43}Sc	3.89 h	15.9 ± 1.4	24.6 ± 24.1	9.2	0.65 ± 0.17
2	^{44}Sc	3.93 h	52.7 ± 0.7	45.4 ± 9.5	88.0	1.16 ± 0.12
3	^{46}Sc	83.79 d	0.77 ± 0.7	0.865 ± 8.3	128.0	0.89 ± 0.08
2	^{47}Sc	80.28 h	10.2 ± 1.4	11.0 ± 14.2	6.1	0.93 ± 0.14
2	^{48}Sc	43.67 h	3.64 ± 2.9	3.16 ± 12.8	18.2	1.15 ± 0.18
2	^{m44}Sc	58.60 h	23.6 ± 0.7	18.4 ± 13.2	27.8	1.28 ± 0.18
3	^{48}V	15.97 d	1.84 ± 0.6	1.12 ± 7.8	186.0	1.65 ± 0.14
1	^{49}Cr	42.30 m	20.4 ± 1.2	15.0 ± 24.9	1.2	1.36 ± 0.35
3	^{51}Cr	27.70 d	4.64 ± 0.5	3.55 ± 12.7	38.7	1.31 ± 0.17
1	^{52}Mn	5.59 d	14.5 ± 0.8	18.3 ± 5.5	24.9	0.79 ± 0.05
1	^{m52}Mn	21.10 m	17.8 ± 0.8	9.2 ± 33.3	7.9	1.94 ± 0.66
3	^{54}Mn	312.12 d	1.33 ± 0.5	1.13 ± 10.2	97.4	1.18 ± 0.13
1	^{56}Mn	2.58 h	21.7 ± 1.3	27.7 ± 5.8	20.1	0.78 ± 0.05
3	^{59}Fe	44.50 d	0.39 ± 1.8	0.558 ± 10.4	42.9	0.70 ± 0.08
2	^{55}Co	17.53 h	6.34 ± 2.3	7.41 ± 10.2	16.1	0.86 ± 0.11
3	^{56}Co	77.27 d	1.4 ± 0.9	1.2 ± 7.2	127.0	1.16 ± 0.09
3	^{57}Co	271.79 d	1.6 ± 0.5	1.8 ± 9.9	92.6	0.92 ± 0.10
3	^{58}Co	70.82 d	5.79 ± 0.3	6.51 ± 10.2	533.6	0.89 ± 0.09
3	^{60}Co	5.27 y	0.14 ± 0.4	0.172 ± 8.5	9.1	0.80 ± 0.07
1	^{61}Co	99.00 m	44.0 ± 0.9	52.7 ± 12.3	4.2	0.84 ± 0.11
2	^{57}Ni	35.60 h	4.14 ± 2.7	4.78 ± 12.1	15.8	0.86 ± 0.13
2	^{65}Ni	2.52 h	5.38 ± 2.4	3.46 ± 19.3	3.5	1.55 ± 0.34
1	^{60}Cu	23.70 m	13.9 ± 1.2	16.4 ± 8.7	12.2	0.85 ± 0.08
1	^{61}Cu	3.33 h	173.0 ± 0.4	165.0 ± 27.2	13.2	1.05 ± 0.29
2	^{64}Cu	12.70 h	336.0 ± 0.7	595.0 ± 13.2	15.1	0.56 ± 0.08
2	^{62}Zn	9.19 h	6.86 ± 2.4	5.66 ± 19.9	4.4	1.21 ± 0.27
3	^{65}Zn	244.26 d	0.071 ± 2.5	0.117 ± 12.0	8.6	0.64 ± 0.09

Titanium

The results for the specific activities of the titanium sample are summarised in Table 5. Again relatively solid agreement is found for most isotopes. The activity of ^{43}Sc seems to be overestimated by FLUKA. The experimental uncertainty is rather large but the calculated value is still within the calculated and measured uncertainty. As in the case of copper, the assumption of equal sharing of the activity between the different states of an isotope might explain the discrepancies with ^{m44}Sc/^{44}Sc. Finally, the unresolved problem in the parent-daughter correction most probably led to the significant overestimation of the specific activity of ^{28}Mg by the gamma spectrometry measurement.

Table 5. As in Table 2, titanium sample.
Cooling times: (1) 2 h, 49 m, (2) 4 d, 1 h, 30 m and (3) 20 d, 4 h, 3 m.

Cooling time	Isotope	$t_{1/2}$	FLUKA (Bq/g) ± (%)	Experiment (Bq/g) ± (%)	Exp/MDA	FLUKA/Exp
2	^{22}Na	2.60 y	0.061 ± 6.8	0.056 ± 10.7	3.9	1.08 ± 0.19
1	^{24}Na	14.96 h	15.1 ± 2.6	25.1 ± 3.6	546.8	0.60 ± 0.04
1	^{28}Mg	20.91 h	0.524 ± 13.6	2.35 ± 5.5	13.0	0.22 ± 0.04
1	^{42}K	12.36 h	41.5 ± 1.8	46.9 ± 5.2	134.0	0.89 ± 0.06
1	^{43}K	22.30 h	16.2 ± 2.6	20.4 ± 3.7	124.4	0.79 ± 0.05
2	^{47}Ca	4.54 d	0.42 ± 9.7	0.58 ± 15.7	43.3	0.73 ± 0.18
1	^{43}Sc	3.89 h	31.5 ± 1.9	19.6 ± 56.7	21.3	1.61 ± 0.94
1	^{44}Sc	3.93 h	118 ± 1	97.6 ± 4.2	503.1	1.21 ± 0.06
2	^{m44}Sc	58.60 h	16.8 ± 1.1	7.61 ± 5.5	272.8	2.20 ± 0.14
3	^{46}Sc	83.79 d	4.86 ± 0.7	5.82 ± 8.2	559.6	0.84 ± 0.07
2	^{47}Sc	80.28 h	52.7 ± 1	61.6 ± 8.2	1422.6	0.86 ± 0.08
2	^{48}Sc	43.67 h	5.23 ± 2.1	4.79 ± 3.7	281.8	1.09 ± 0.06
2	^{48}V	15.97 d	2.73 ± 2.3	2.16 ± 6.1	213.9	1.27 ± 0.11
3	^{51}Cr	27.70 d	0.078 ± 9	0.094 ± 36.3	1.4	0.82 ± 0.37

Concrete

Table 6 shows results for the isotopes detected in the concrete sample. Once again, solid agreement exists between calculated and measured activities of many isotopes. Uncertainties in the elemental composition are thought to be the main reason for the discrepancies such as ^{47}Ca (sensitive to the calcium content of the concrete) or ^{48}V and ^{52}Mn (produced in reactions with trace elements).

Resin

In the case of the resin sample, the only gamma emitter that could be reproduced by the simulation with a significant yield was ^{7}Be. However, heavier isotopes were also detected in the gamma spectrometry measurements (see Table 7) that could not be reproduced by the simulation. This can most likely be explained by trace elements that were not resolved in the elemental analysis and thus not included in the simulation.

Carbon composite and boron nitride

Table 8 shows results for the carbon composite and the boron nitride sample. In both samples ^{7}Be was well-reproduced. In the case of the boron nitride sample, observed deficiencies for the two sodium isotopes are presumably due to trace elements and have their origin in different production channels.

Table 6. As in Table 2, concrete sample.
Cooling times: (1) 11 h, 41 m, (2) 12 d, 6 h, 40 m and (3) 55 d, 2 h, 31 m.

Cooling time	Isotope	$t_{1/2}$	FLUKA (Bq/g) ± (%)	Experiment (Bq/g) ± (%)	Exp/MDA	FLUKA/Exp
3	^{7}Be	53.29 d	2.63 ± 1.0	2.95 ± 11.9	263.4	0.89 ± 0.11
3	^{22}Na	2.60 y	0.060 ± 1.4	0.061 ± 9.9	101.5	0.98 ± 0.11
1	^{42}K	12.36 h	1.34 ± 8.8	1.03 ± 6.1	20.3	1.30 ± 0.19
1	^{43}K	22.30 h	1.58 ± 3.7	1.52 ± 3.4	157.7	1.04 ± 0.07
1	^{47}Ca	4.54 d	0.239 ± 6.8	0.343 ± 14.5	29.6	0.70 ± 0.15
1	^{44}Sc	3.93 h	0.304 ± 5.2	0.315 ± 6.3	12.0	0.97 ± 0.11
1	^{m44}Sc	58.60 h	0.242 ± 5.7	0.127 ± 9.1	15.5	1.91 ± 0.28
1	^{47}Sc	80.28 h	0.296 ± 6.4	0.325 ± 8.3	35.0	0.91 ± 0.13
2	^{48}V	15.97 d	0.086 ± 7.7	0.045 ± 8.8	36.4	1.90 ± 0.31
2	^{51}Cr	27.70 d	0.111 ± 5.0	0.085 ± 15.8	4.8	1.30 ± 0.27
1	^{52}Mn	5.59 d	0.19 ± 7.2	0.11 ± 4.1	15.1	1.74 ± 0.20
3	^{54}Mn	312.12 d	0.016 ± 5.5	0.015 ±11.9	9.5	1.06 ± 0.18
2	^{56}Co	77.27 d	0.0024 ± 19.8	0.003 ± 21.8	2.2	0.80 ± 0.33

Table 7. As in Table 2, resin sample. Cooling times: (1) 5 d, 3 h, 10 m and (2) 23 d, 9 h, 44 m.

Cooling time	Isotope	$t_{1/2}$	FLUKA (Bq/g) ± (%)	Experiment (Bq/g) ± (%)	Exp/MDA	FLUKA/Exp
1	^{7}Be	53.29 d	21.7 ± 1.3	21.1 ± 7.7	299.3	1.03 ± 0.09
1	^{22}Na	2.60 y	–	0.018 ± 19.5	2.9	–
2	^{46}Sc	83.79 d	–	0.006 ± 40.8	1.0	–
1	^{47}Sc	80.28 h	–	0.044 ± 13.0	3.7	–

Table 8. As in Table 2, boron nitride and carbon composite samples.
Cooling times: (1) 24 d, 7 h, 35 m, (2) 55 d, 8 h, 45 m, (3) 1 h, 22 m and (4) 26 d, 5 h, 58 m.

Boron nitride

Cooling time	Isotope	$t_{1/2}$	FLUKA (Bq/g) ± (%)	Experiment (Bq/g) ± (%)	Exp/MDA	FLUKA/Exp
1	^{7}Be	53.29 d	9.2 ± 1.7	9.2 ± 10.0	170	1.00
2	^{22}Na	2.60 y	0.0047 ± 18.1	0.0062 ± 29.8	2	0.76
3	^{24}Na	14.96 h	0.3 ± 11.9	0.142 ± 12.7	9	2.13

Carbon composite

Cooling time	Isotope	$t_{1/2}$	FLUKA (Bq/g) ± (%)	Experiment (Bq/g) ± (%)	Exp/MDA	FLUKA/Exp
4	^{7}Be	53.29 d	1.46 ± 6.0	1.61 ± 1.8	230	0.91

Results for remanent dose rates

Calculated and measured dose rates are compared in the following discussion for one sample of each material category (aluminium, copper, iron/stainless steel and concrete/marble). As mentioned above, values are compared for each instrument over four distances between the sample surface and the centre of the detector: contact, 12.4 cm, 22.4 cm and 32.4 cm (except for the Eberline dose meter). Note that due to the different sizes of the detectors, "contact" refers to a different effective distance for each instrument (2.4 cm for Microspec and 7.3 cm for Eberline).

All measured data points in the graphs carry error bars that include the following uncertainties: a 2 mm uncertainty for the determination of the effective centre of the detector, a 2 mm uncertainty for the positioning of the sample with the holder (i.e. distance to the detector), a statistical error obtained from repetitive measurements (only the Eberline dose meter) and a systematic instrument uncertainty of 1 nSv/h corresponding to the last significant figure on the display of the respective devices. Except for the aluminium sample measured, data below 10 nSv/h were systematically excluded from the comparison due to their proximity to the background value and the lower measurement threshold as indicated in the user manuals of the instruments. In the case of aluminium, they were kept in order to indicate the behaviour of the dose rate at long cooling times.

Aluminium

Figure 5 shows the remanent dose rates as measured and simulated for one of the aluminium samples at different distances. In general, agreement was observed between the values simulated with FLUKA and the values measured using the Microspec instrument. However, the Eberline instrument measured systematically higher values that may be due to differences in the responses of the two instruments to the gamma energies of ^{24}Na, which dominates the dose rate below $t_c = 100$ h. The latter is under investigation. Uncertainties of the measured data for the Microspec instrument are highest at contact due to the uncertainty in determining the effective centre of the detector (2 mm), which is most pronounced at small distances. Furthermore, fluctuations in the Microspec data at the longest distance indicate statistical uncertainties that are not included in the error bars as no repetitive measurements were performed using this instrument. Cooling time dependence is very well-reproduced, especially after ~200 hours when ^{22}Na becomes a major contributor to the remanent dose rate.

Figure 5. Dose equivalent rate as a function of cooling time for the aluminium sample

Measurements were taken with the Microspec and Eberline instruments and calculated using FLUKA at different distances between the surface of the sample and the effective centre of the detector

A DATABASE ON HEALTH PHYSICS AND RADIOLOGICAL SAFETY OF CYCLOTRONS 10-250 MeV

B. Mukherjee
Radiation Protection Group (D3), Deutsches Elektronen-Synchrotron (DESY)
Notkestrasse 85, D-22607 Hamburg, Germany
E-mail: mukherjee@ieee.org

E. Sartori
OECD NEA Data Bank
12 Boulevard des Iles, 92130 Issy-les-Moulineaux, France
E-mail: sartori@nea.fr

Abstract

Radiological safety is imperative for public acceptance and the safe and economic operation of cyclotrons. Early cyclotron pioneers dating from the late 1930s were aware of this fact. Consequently, numerous experimental and theoretical works on cyclotron health physics were carried out and published in various professional journals and reports. Many contemporary professionals are still involved with the radiation safety of cyclotrons. In order to avoid reinventing the wheel and to disseminate the valuable work of various past and present researchers, a hyperlinked database has been created (NEA-1694 SATIF/CYCLO-RADSAFE). The key words used in this database are the following: (1) low-energy cyclotron ($E < 20$ MeV), (2) medium-energy cyclotron ($20 < E < 100$ MeV), (3) high-energy cyclotron ($E > 100$ MeV), (4) shielding material, (5) source term, (6) Monte Carlo (shielding) calculation, (7) deterministic (shielding) calculation, (8) duct and mazes, (9) optimisation technique, (10) skyshine, (11) dosimetry-spectrometry, (12) radioactive effluent, (13) components and shielding activation and (14) waste management.

Introduction

In 1929, Dr. Ernest Orlando Lawrence of the University of California in Berkeley, California, invented the cyclotron. From its early years until the 1950s, cyclotrons were basically the essential instrument of nuclear physics; they are the predecessors of modern high-energy particle accelerators [1]. The early cyclotron pioneers were aware of the importance of the radiological safety aspects of cyclotrons and carried out a series of important research in the relevant fields. This work later gave birth to a new vocation – accelerator health physics [2].

Modern cyclotrons, which are capable of accelerating various types of ions to a wide range of beam currents and energy levels, are vital to applied science and environmental and medical research. At present, there are more than 230 cyclotrons in operation in various countries of the world [3] and ~30 new units are planned (Figure 1). Evidently, the largest number of cyclotrons belongs to the category of low-energy (E < 20 MeV) machines, which are primarily used in producing high activities of short-lived medical radioisotopes. These special purpose cyclotrons, which accelerate intense beams of protons (H^-) and deuterons (d^-), are known as "medical cyclotrons". Most medical cyclotrons are installed in urban hospitals and nuclear medical clinics and are usually frequented by members of the public (including children). During routine radioisotope production operation, the medical cyclotrons produce strong fields of gamma-rays and high-energy neutrons as well as high levels of gaseous radioactive effluent. As a result, sound operational health physics and efficient radiological protection measures are imperative for the safe operation and public acceptance of medical cyclotrons [4]. Of course the same operational safety aspects are mandatory for cyclotrons operating at higher energies (Figure 1).

Figure 1. The number of cyclotrons at different energy levels presently in operation or in the planning stage

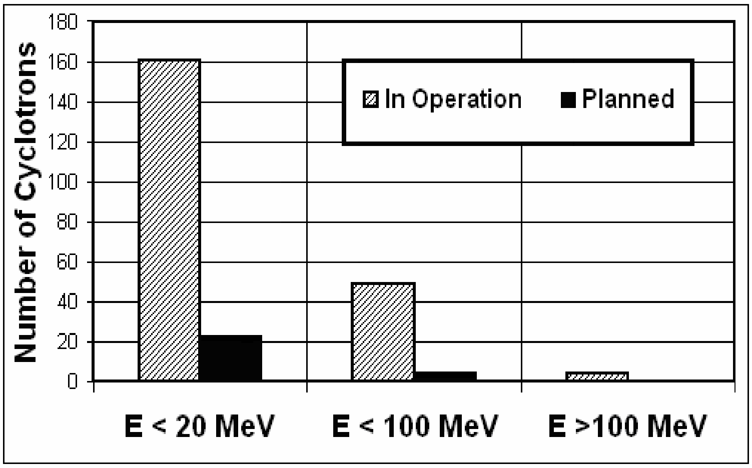

Modern industrial and medical cyclotron establishments have to cope with a changing work environment and operational conditions, such as frequent installation of new cyclotron components, dismantling radioactive parts, modification or custom design of radiological shielding and calculation of accidental radiation exposure. Specialist knowledge of accelerator health physics and dosimetry is required to tackle the above tasks. Often times the responsible officer must undertake extensive and time-consuming information research. As a result, a hyperlinked information database [5] encompassing all major radiological safety aspects of industrial and medical cyclotrons has been developed as an essential aid to concerned cyclotron physicists/engineers. The other major objective of this database is to introduce valuable early work on the radiological safety of cyclotrons to today's radiation protection fraternity [6].

The radiation environment of cyclotrons

High levels of prompt neutron and gamma-rays are generated during routine cyclotron operation (i.e. target bombardment) or during an unexpected beam loss when the defocused ion beam accidentally hits the internal wall of the beam tube. The prompt fast neutrons slow down via multiple scattering with the vault (containment) wall, and then bounce back to the centre of the vault thereby activating the cyclotron parts. These parts include: beam tubes, focusing magnets, target (irradiation) chambers, ducts/pipes and other ancillaries. Radioactive contamination of skin and whole-body (external) exposure to persons working in the vault may occur. In addition, the radioactive noble gas ^{41}Ar (half-life = 1.8 h) produced by the neutron capture (n,γ) reaction with the ^{40}Ar present in the vault air may cause whole-body (external) and inhalation (internal) radiation exposure.

The prompt gamma and neutron radiation may leak out to the external environment through an inadequately shielded lateral wall of the cyclotron vault, thus producing direct radiation exposure. In particular, neutrons penetrated through the roof are able to reach long distances via multiple scattering, with nitrogen and oxygen molecules in the air causing low-level radiation exposure. This phenomenon is known as skyshine. Figure 2 contains a generic flow chart elucidating various radiation production and corresponding exposure pathways of cyclotrons. The exposure modalities and the associated radiological safety aspects of cyclotrons as described above constitute the main search criteria of a recently published database [5], which deals with the health physics and the radiological safety of cyclotrons.

Figure 2. Radiation production pathways of cyclotrons and the nature of associated radiological exposure

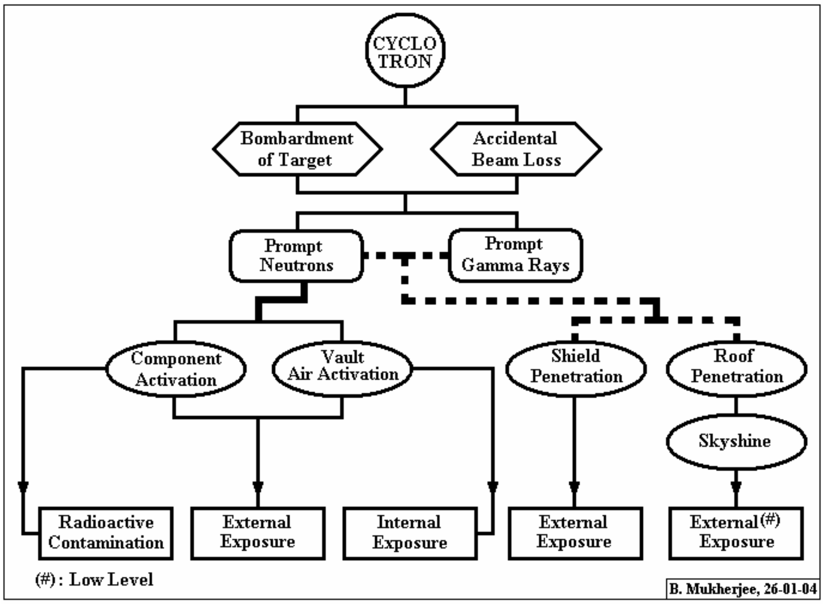

The Cyclotron Radiation Safety database

The Cyclotron Radiation Safety database described in this paper is based on 14 hyperlinked key words (Table 1), dealing with various radiological safety-related issues involving a wide range of modern medical and industrial cyclotrons. The key words used in this database are explained below.

Table 1. Keyword IDs used in the SATIF/CYCLO-RADSAFE database and the number of literature entries for each keyword

Key word ID	Key word description	Number of entries
1	Low-energy cyclotron (E < 20 MeV)	17
2	Medium-energy cyclotron (E < 100 MeV)	59
3	High-energy cyclotron (E > 100 MeV)	38
4	Shielding material	68
5	Source term	100
6	Monte Carlo (shielding) calculation	34
7	Deterministic (shielding) calculation	37
8	Duct and mazes	19
9	Optimisation technique	5
10	Skyshine	15
11	Dosimetry-spectrometry	105
12	Radioactive effluent	13
13	Components and shielding activation	21
14	Waste management	8

Cyclotron classification (keywords 1, 2, 3)

The cyclotrons are classified into three categories by energy level: a) low-energy cyclotron (E < 20 MeV) for short-lived positron emission tomography (PET) radioisotope production, b) medium-energy cyclotron (20 < E < 100 MeV) for longer-lived single photon emission computer tomography (SPECT) radioisotope production and industrial applications and c) high-energy cyclotron (E > 100 MeV) for radiotherapy of deep-seated tumours.

The energy and intensity of the secondary neutron and gamma radiation field produced by a cyclotron depend primarily on the energy of the accelerated ion beam and the atomic weight of the target (beam interaction) material.

Shielding materials and source terms (keywords 4, 5)

The intensity and energy distribution (spectrum) of a radiation field (generated by beam interaction) at unit distance (1 m) from its production point is defined as a source term. For the purpose of the cyclotron shielding calculation, the source term and attenuation characteristics of the shielding material are required. Evidently, for sound shielding design the mechanical and structural properties of shielding material should also be taken into account.

Shielding calculation techniques (keywords 6, 7, 8, 9, 10)

Monte Carlo (stochastic) simulation and various deterministic (analytical) shielding calculation techniques have been reported. These calculation methods are used to estimate the shielding wall thickness, the dimension of various types of mazes and ducts of cyclotron facilities and the skyshine radiation, as well as to optimise shielding parameters.

Dose assessment methods (keyword 11)

Various methods for the assessment of neutron and gamma dose distribution and the energy spectra of cyclotron-produced radiation fields have been documented in the database. The relevant data is imperative to determine the efficacy of cyclotron shielding and various radiation safety and exposure analysis-related issues.

Radioactive effluent and waste management (keywords 12, 13, 14)

The assessment of gaseous radioactive effluent and solid/liquid radioactive waste produced by cyclotrons (radioisotope production facilities in particular) plays a vital role in compliance with radiation safety regulations imposed by statutory bodies and in public acceptance of cyclotron laboratories.

Summary

A database has been created on health physics and radiological safety-related information relevant to a broad range of industrial and medical cyclotrons. SATIF/CYCLO-RADSAFE is a hyperlinked database that includes a significant collection of scientific literature published by various researchers and technologists over the past 40 years [6]. The main goal of this database is to provide cyclotron health physicists and engineers with valuable information to solve a myriad of scientific, technical and decision-making problems. A CD-ROM containing the latest version of the database is available from the OECD/NEA/Data Bank.

REFERENCES

[1] Livingston, M.S., ed., *The Development of High-energy Accelerators*, Dover Publications, Inc. (1966).

[2] Patterson, W., R.H. Thomas, *Accelerator Health Physics*, Academic Press, New York (1973).

[3] *Directory of Cyclotrons Used for Radionuclide Production in Member States*, International Atomic Energy Agency, IAEA-DCRP/CD, ISBM 92-0-133302-1 (2002).

[4] Mukherjee, B., "Radiological Safety and Operational Health Physics of Medical Cyclotrons", *Proceedings of the 3rd International Conference on Isotopes (3ICI)*, Vancouver, Canada, 6-10 September 1999.

[5] Mukherjee, B., *A Database on Health Physics and Radiological Safety of Cyclotrons 10-250 MeV*, NEA-1694 SATIF/CYCLO-RADSAFE (2004); http://www.nea.fr/abs/html/nea-1694.html.

[6] Thomas, R.H., "The History and Future of Accelerator Radiation Protection", *Radiat. Prot. Dosim.*, 96(4), 441-457 (2001).

SESSION V

Status of Computer Codes, Cross-sections and Data Libraries

Chair: N. Mokhov

ACQUISITION OF COMPUTER CODES, CROSS-SECTION LIBRARIES AND ACCELERATOR SHIELDING EXPERIMENTS – STATUS 2004

E. Sartori[1], **I. Kodeli**[1,2], **J.M. Galán**[1], **B.L. Kirk**[3]
[1]OECD/NEA Data Bank, Issy les Moulineaux, France
[2]IAEA, Vienna, Austria
[3]Radiation Safety Information Computational Center (RSICC)
Oak Ridge National Laboratory (ORNL), Oak Ridge, USA

Abstract

The OECD Nuclear Energy Agency Data Bank (NEA DB) and the ORNL Radiation Safety Information Computational Center (RSICC) acquire sets of computer codes, basic nuclear data and integral experiment data relevant to accelerator shielding and dosimetry applications. The following paper summarises such tools released over the past several years, representing the latest developments in this area.

Introduction

A full list of computer codes and associated data for radiation transport relevant to accelerator shielding and dosimetry applications were presented in the previous SATIF workshops [1-6]. This paper provides an update of the comprehensive set, as reported in Ref. [7].

The three main components relative to computer codes and acquired data, which have been reviewed and disseminated for use in accelerator application, include:

1. Basic nuclear data, derived application data libraries, group constants, continuous energy data.
2. Computer codes for different accelerator shielding and dosimetry modelling aspects.
3. Integral experiment database for validation of the combined use of components 1,2.

Updated codes and data libraries released since SATIF-6

The tools available at NEA DB and RSICC relevant to accelerator shielding and dosimetry analysis accelerator analytical tools released since the last SATF-6 meeting are briefly described below. Some of these tools are not specific to accelerator applications but could be useful in lower-energy transport analysis of particles generated from primary and secondary reactions within the accelerator target or shield. See the RSICC and NEA DB Web pages [8,9] for more details.

- Nuclear model, resonance treatment and decay process codes: CALENDF-2002, ECIS-2003, EMPIRE-II 2.18, GEM, NMTC/JAM and ERRORJ.
- Electron-photon transport: EDMULT-6.4, FOTELP-2K3, PENELOPE2003, MUTIL, NESKA and ELAST2.
- General radiation transport codes: MCNPX-2.4.0, MCNP5, TART-2002, TRISTAN, TRIPOS, TRIPOLI-4.3.3, MCNP4B-GN (γ,n) production and transport, BOT3P4.1, DOORS3.2a, PARTISN (parallel, time-dependent S_N) and GRTUNCL3D (uncollided flux and first collision source distributions).
- Activation analysis, decay build-up, burn-up, transmutation chain codes: CHAINFINDER 2.16, CHAINSOLVER 2.20, DCHAIN-SP 2001, EASY-99 (PC version), EASY-2001, MOCUP, NAAPRO, PLUTON, SWAT and PGAA (prompt γ neutron activation analysis).
- Shielding and irradiation codes: BULK-I (shielding for proton accelerators), DUCT-III, PVIS-4, C-SHIELDER, SRNA-2KG(proton transport) and SRIM-2003 (stopping power).
- General experimental data unfolding codes: HEPROW, UMG 3.3 and NAISAP.
- Databases of documents and data covering radiation protection/shielding: CYCLO-RADSAFE.
- Nuclide, chemical properties explorer and display utilities: CHIMISTE/CHEMENGL, NKE-2.16 and NUCLEUS-CHART.
- Continuous energy Monte Carlo and group-averaged cross-section libraries for specific applications and codes: DROSG-2000, FSXLIBJ33, MATXSLIBJ33, RRDF-98 and HILO-2K (83 neutron, 22 photon group cross-sections for neutron energies up to 2 GeV).

Library of FORTRAN modules for nuclear model code development

A working group of the OECD/NEA is fostering the development of a set of modern computer modules to be used in existing and future nuclear reaction codes. Such modules will eventually constitute a library of well-tested and well-documented pieces of code, which can be used safely and efficiently in all future programming efforts for nuclear reaction calculations. This effort will help to avoid any duplication of work, and will most certainly facilitate the very important intercomparison of existing codes. The first set of modules has been released (MODLIB-0.1) and covers:

- Calculation of gamma-ray strength functions.
- Calculation of width fluctuation correction factors.
- Calculation of level density parameters.
- Provision of nuclear structure properties.

EXFOR data for intermediate high-energy interactions

In a collaboration between the National Nuclear Data Center of BNL, the Nuclear Data Section of the IAEA, the Center for Nuclear Data of the Russian Federation and the OECD/NEA Data Bank, a large number of experimental cross-section data were compiled and entered into the EXFOR database, which is accessible on-line. The number of data sets included for the period 2001-2004 and for incident particle energies higher than 20 MeV, involved ~2 000 reactions. These data cover ~125 materials and isotopes: ^{1}H, ^{2}H, ^{3}H, ^{4}He, ^{9}Be, ^{10}B, ^{11}B, ^{0}C, ^{12}C, ^{13}C, ^{14}C, ^{0}N, ^{14}N, ^{15}N, ^{0}O, ^{16}O, ^{170}O, ^{18}O, ^{19}F, ^{22}Ne, ^{23}Na, ^{24}Mg, ^{25}Mg, ^{26}Mg, ^{27}Al, ^{0}Si, ^{28}Si, ^{29}Si, ^{30}Si, ^{32}S, ^{34}S, ^{40}Ar, ^{40}Ca, ^{42}Ca, ^{44}Ca, ^{48}Ca, ^{0}Ti, ^{46}Ti, ^{48}Ti, ^{0}V, ^{51}V, ^{52}Cr, ^{0}Fe, ^{56}Fe, ^{59}Co, ^{58}Ni, ^{60}Ni, ^{64}Ni, ^{0}Cu, ^{63}Cu, ^{65}Cu, ^{0}Zn, ^{64}Zn, ^{65}Zn, ^{66}Zn, ^{68}Zn, ^{75}As, ^{0}Se, ^{76}Se, ^{77}Se, ^{0}Br, ^{79}Br, ^{81}Br, ^{85}Rb, ^{87}Rb, ^{89}Y, ^{90}Zr, ^{91}Zr, ^{92}Zr, ^{94}Zr, ^{93}Nb, ^{0}Mo, ^{92}Mo, ^{96}Ru, ^{98}Ru, ^{103}Rh, ^{0}Pd, ^{110}Pd, ^{110}Cd, ^{111}Cd, ^{112}Cd, ^{113}Cd, ^{114}Cd, ^{116}Cd, ^{115}In, ^{112}Sn, ^{117}Sn, ^{118}Sn, ^{120}Sn, ^{124}Sn, ^{124}Sn, ^{125}Te, ^{128}Te, ^{130}Te, ^{127}I, ^{133}Cs, ^{142}Nd, ^{153}Eu, ^{160}Gd, ^{159}Tb, ^{0}Dy, ^{164}Dy, ^{165}Ho, ^{0}Ta, ^{181}Ta, ^{0}W, ^{182}W, ^{183}W, ^{184}W, ^{188}Os, ^{192}Os, ^{197}Au, ^{203}Tl, ^{205}Tl, ^{0}Pb, ^{204}Pb, ^{208}Pb, ^{209}Bi, ^{232}Th, ^{0}U, ^{232}U, ^{233}U, ^{235}U, ^{238}U and ^{237}Np. The elements for which the largest amount of data was gathered are: Pb, W, Cu, Si, Zr and Sn. The percentages of data by incident particle are shown below in Figure 1.

Figure 1. EXFOR compilations (~2 000); E > 20 MeV, 2001-2004, by incident particle

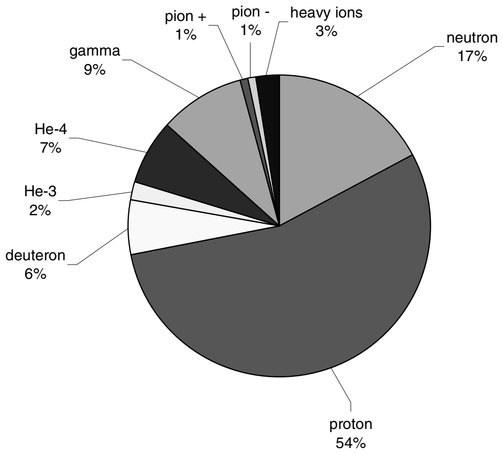

These data sets were measured in ~50 laboratories around the world. Major contributors include: Catholic University of Louvain (Belgium); University of Hannover, Forschungszentrum Jülich, Forschungszentrum Karlsruhe, University of Köln (Germany); Institute for Atomic Research of Debrecen (Hungary); Institute for Theoretical and Experimental Physics of Moscow, Nuclear Physics Institute of Moscow State University (Russian Federation); and Tohoku University of Sendai (Japan).

The EXFOR database has accumulated a set of experimental data for 34 534 reactions in the energy range of 20 to 2 000 MeV out of a total of 81 945 reactions for the period 1964-2004 and covering the full energy range (42%). More detailed information can be found by accessing the following website: http://www.nea.fr/html/dbdata/x4/.

SINBAD integral accelerator benchmark experiments

SINBAD, the benchmark experiments database for shielding and dosimetry applications, covers nuclear reactor shielding, fusion neutronics and accelerator shielding. In addition to the characterisation of the radiation source, it describes shielding materials and instrumentation as well as relevant detectors. The experimental results, be it dose, reaction rates or unfolded spectra, are presented in a tabular form that can easily be exported for further use. Most sets in SINBAD also contain computer models used for the interpretation of the experiment and, where available, results from uncertainty analysis. Since the last edition, several new experiments were added and some are in the process of compilation and evaluation. Table 1 contains the present status. The regularly updated list can be found at the following Internet site: http://www.nea.fr/html/science/shielding/sinbad/sinbadis.htm [10].

Table 1. SINBAD accelerator shielding benchmarks

Accelerator applications (compiled)	Facility
Transmission through shielding materials of neutrons and photons generated by 52 MeV protons	FM cyclotron, U-Tokyo
Transmission through shielding materials of neutrons and photons generated by 65 MeV protons	AVF cyclotron, U-Osaka
TIARA 40, 65 MeV neutron transmission through iron, concrete, polyethylene	Tiara JAERI
ROSTI I, II, III data and target yield series	CERN
RIKEN (quasi-monoenergetic neutron field using the ^{7}Li(p,n)^{7}Be reaction 70-210 MeV	RIKEN
HIMAC He, C, Ne, Ar, Fe, Xe and Si ions on C, Al, Cu and Pb targets	HIMAC NIRS Chiba
HIMAC/NIRS high-energy neutron (<800 MeV) measurements in iron	HIMAC NIRS Chiba
HIMAC/NIRS high-energy neutron (<800 MeV) measurements in concrete	HIMAC NIRS Chiba
BEVALAC experiment with Nb ions on Nb and Al targets	BEVELAC LBL
MSU experiment with He and C ions on Al target	NCSL MSU Michigan
High-energy neutron spectra generated by 590 MeV protons on thick lead target	PSI SIN
ISIS deep penetration of neutrons through concrete and iron	RAL ISIS
TEPC-FLUKA comparison for aircraft dose	ARCS
Accelerator applications (in progress)	**Facility**
Neutron production from thick targets of C, Fe, Cu, Pb by 30, 52 MeV protons	INS U-Tokyo
Shielding experiments through concrete and iron using 400 MeV/nucleon C ions on Cu target	HIMAC NIRS Chiba
Yields of residual product nuclei produced in thin targets irradiated by 100-2 600 MeV protons	ITEP Moscow
Neutron angular and energy distributions from 710 MeV alphas stopping in water, carbon, steel and lead	SREL
Neutron yields from stopping-length C, Al, Fe and depleted U targets for 256 MeV protons	LAMPF LANL

Other radiation shielding and dosimetry activities

Other radiation shielding and dosimetry activities include participation in the QUADOS activity and co-sponsoring of workshop as well as the paper, "Analysis of QUADOS Problem on TLD-Albedo Personal Dosimeter Responses Using Discrete Ordinates and Monte Carlo Methods" [11]. Through these activities the following problems were examined:

- Brachytherapy: ^{192}Ir gamma-ray source.
- Endovascular radiotherapy: ^{32}P $\beta-$ source.
- Proton therapy on the eye: 50 MeV proton beam source.
- TLD-albedo dosimeter response: neutron and/or photon sources.
- Phantom backscatter: X-ray ISO reference beams.
- Environmental scatter: ^{252}Cf neutron source.
- Germanium detector: photon sources 15 keV < E < 1 MeV.
- Consistency check device: ^{241}Am-Be neutron source.

Additional radiation shielding and dosimetry activities involved the acquisition of experimental data from the NIKIET skyshine experiment and the proposal of a benchmark. The experimental studies concerned the levels of neutron and gamma radiation scattered by the atmosphere (air) and were carried out using a specialised research reactor (RR). The RR was located in Kazakhstan on a test ground near Semipalatinsk (up to 1 000 m).

REFERENCES

[1] *Proceedings of the Shielding Aspects of Accelerators, Targets and Irradiation Facilities (SATIF-1)*, Arlington, Texas, USA, 28-29 April 1994, ISBN 92-64-14327-0.

[2] *Proceedings of the Shielding Aspects of Accelerators, Targets and Irradiation Facilities (SATIF-2)*, Geneva, Switzerland, 12-13 October 1995, ISBN 92-64-15287-3.

[3] *Proceedings of the Shielding Aspects of Accelerators, Targets and Irradiation Facilities (SATIF-3)*, Sendai, Japan, 12-13 May 1997, ISBN 92-64-16071-X.

[4] *Proceedings of the Shielding Aspects of Accelerators, Targets and Irradiation Facilities (SATIF-4)*, Knoxville, Tennessee, USA, 17-18 September 1998, ISBN 92-64-17044-8.

[5] *Proceedings of the Shielding Aspects of Accelerators, Targets and Irradiation Facilities (SATIF-5)*, OECD, Paris, France, 18-21 July 2000, ISBN 92-64-18691-3.

[6] *Proceedings of the Shielding Aspects of Accelerators, Targets and Irradiation Facilities (SATIF-6)*, SLAC, Stanford, California, USA, 10-12 April 2002, ISBN 92-64-01733-X.

[7] Hunter, H.T., J.B. Manneschmidt, B.L. Kirk, M. Greene, E. Sartori, T. Suzuki, P. Vaz, "Progress Report on the Available Analytical Tools for Accelerator Shielding Analysis", *Proceedings of the Shielding Aspects of Accelerators, Targets and Irradiation Facilities (SATIF-6)*, 10-12 April 2002, ISBN 92-64-01733-X, pp. 307-336.

[8] Nuclear Energy Agency Data Bank (NEA DB) of the Organisation for Economic Co-operation and Development (OECD), Paris, France, http://www.nea.fr/, or for detailed searches on codes and data: http://www.nea.fr/html/dbprog/search.htm.

[9] Radiation Safety Information Computational Center (RSICC) of the Oak Ridge National Laboratory (ORNL), Oak Ridge, TN, USA, http://rsicc.ornl.gov/.

[10] Kodeli, I., H. Hunter, E. Sartori, "Radiation Shielding and Dosimetry Experiments Updates in the SINBAD Database", *Proceedings of the 10th International Conference on Radiation Shielding (ICRS-10)* and *Radiation Protection and Shielding Topical 2005 (RPS-2004)*, Funchal, Madeira, 9-14 May 2004 (in print).

[11] *Proceedings of the International QUADOS Workshop "Intercomparison on the Usage of Computational Codes in Radiation Dosimetry"*, G. Gualdrini, P. Ferrari, eds., 14-16 July 2003, ENEA 2004, ISBN 88-8286-114-7, pp. 193-198.

DEVELOPMENT OF A RADIATION SHIELDING TOOL FOR PROTON ACCELERATOR FACILITIES (BULK-I)

Ryuichi Tayama, Katsumi Hayashi
Hitachi Ltd., Nuclear Plant Engineering Department, Japan

Hideo Hirayama
High Energy Accelerator Research Organization, Radiation Science Center, Japan

Nobuo Ohtani
Wakasawan Energy Research Center, Japan

Abstract

BULK-I was developed as a tool for the radiation shielding design of proton accelerator facilities using medium energy (50-500 MeV). This tool utilises a new formula that accounts for thin and thick concrete walls. The radiation shielding calculation parameters, which were calculated with the MCNPX code, for one layer of concrete and for two layers (one iron, one concrete) were utilised. BULK-I was confirmed as a valid radiation shielding design tool based on comparison with a radiation shielding experiment using 200 MeV protons at WERC.

Introduction

Accelerators using protons in an energy range from 50-500MeV are being used in such fields as medicine (e.g. cancer therapy) and biology (e.g. improvement of breed). When the protons strike an accelerator component and a target in a proton accelerator facility, secondary neutrons are produced by (p,xn) reactions and are a main source term for radiation shielding designs. The angular and energy distributions of the neutrons are very important for calculating facility wall thickness.

Exponential curve fit as a function of shield thickness (e.g. Moyer model [1]) is generally used in radiation shielding calculations for proton accelerator facilities. Parameters used in curve fit, such as source term and attenuation length, have been numerically and experimentally obtained by many researchers [2-7]. Curve fit is adopted only for deep penetration of the shield where the neutron spectrum is unchanged (equilibrium region). However, curve fit cannot be used when the shield is thin and where the neutron energy spectrum is changed (build-up region). It is also difficult to calculate dose rates accurately via curve fit when the radiation shield is made of two layers (iron and concrete).

In this work, a simple formula adopted for the equilibrium and build-up regions is proposed and the parameters for one- and two-layer radiation shields are numerically obtained with the Monte Carlo code, MCNPX. These are summarised as a tool for the radiation shielding design of a proton accelerator facility. The comparison with a radiation shielding experiment using 200 MeV protons at WERC (Wakasawan Energy Research Center) was performed, which validates the tool.

Characteristics

BULK-I is a tool for calculating neutron and photon effective dose rates after penetrating through concrete and iron/concrete shields in a medium-energy range proton accelerator facility.

A geometry used in the tool is shown in Figure 1. A target (radiation source) is set at the origin in the rectangular room surrounded by six concrete walls. The target is assumed to be thick iron, a typical component of proton accelerators. Protons with various energies and directions are taken into account in the dose rate calculation, which is based on the rotating gantry employed in a proton beam treatment facility. Dose rates at estimator points are calculated considering the emission angle θ_e relative to each

Figure 1. Geometry defined in BULK-I

θ_e is the emission angle relative to beam direction, θ_i is the incident angle into the concrete wall; and iron (1) is the beam direction dependent iron shield, iron (2) is the fixed iron shield

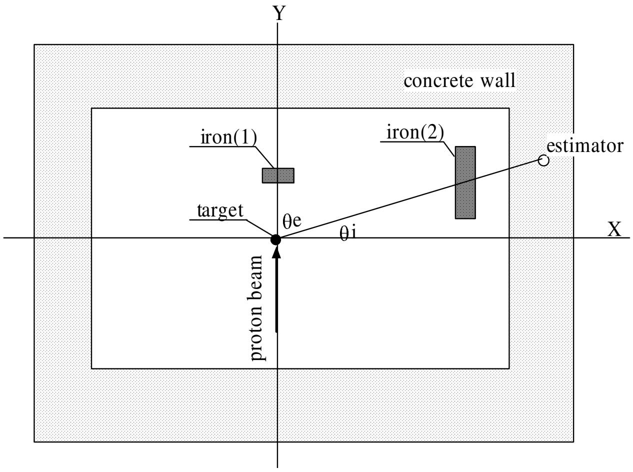

proton beam direction, and the incident angle θ_i relative to the X, Y or Z axis (automatically calculated by BULK-I). The distance from the target to the inner surface and the thickness of each concrete wall are given by users. The fixed type and the beam direction dependent type of iron shields are handled. For the former, the barrier thickness in iron as a measured radiation path through the shield is given for each estimator. For the latter, the thickness and solid angle relative to the beam direction are given. Estimators are set at any position inside and outside of the concrete walls. The attenuation in the air is not taken into account.

The application limits of BULK-I are as follows:

- Proton energy: 50-500 MeV.
- Emission angle relative to beam direction: 0°-180° (12 bins).
- Barrier thickness in concrete: 100-735 g/cm^2 (including build-up region).
- Barrier thickness in iron: 0, 25, 50 and 70 cm (density 7.83 g/cm^3).

The tool is not applicable for radiation streaming problems such as mazes and ducts, or for skyshine problems. However, the tool is recommended for the codes, DUCT-III [8] and SHINE-III [9].

Formula

The effective dose rate in an equilibrium region, where the radiation energy spectrum is unchanged, is expressed as follows:

$$H(r,t) = \frac{H_0 e^{-\frac{t}{\cos\theta_i \lambda}}}{r^2} \tag{1}$$

where $H(r,t)$ is the effective dose per unit proton (pSv), H_0 is the source term per unit proton（pSv cm^2）, λ is the attenuation length (g/cm^2), r is the distance from target to estimator (cm), t is the shield thickness (g/cm^2), θ_i is the incident angle（degrees）and H_0 and λ are given as a function of proton energy, emission angle of radiations, target material and shielding material. The bigger is the emission angle of radiation, the thicker is the build-up region in the shield. This tendency is remarkable with decreasing proton energy. In addition, the backward shield relative to the proton beam direction is thinner than the forward shield. This phenomenon is due to the radiation production rate, which decreases as the emission angle increases. If the required thickness of the backward shield is within the build-up region, the dose rate calculated with Eq. (1) may be underestimated. As a result, another formula is necessary by which the dose rate in the build-up region can be calculated. The next formula proposed in this work considers radiation production due to the slow down process and absorption.

$$H(r,t) = \frac{H_0}{r^2} e^{-\frac{t}{\cos\theta_i \lambda}} \left\{ \alpha - \left[1 - e^{-\frac{\beta}{\cos\theta_i} t} \right] \times (\alpha - 1) \right\} \tag{2}$$

where α is $H(r,0)\, r^2/H_0$ and β is the fitting parameter, and these are given as a function of proton energy, emission angle of radiations and shielding material. This formula extends the application range for the emission angle and proton energy as compared to Eq. (1), and can be adopted in the build-up region.

Estimation of parameters

MCNPX calculations

We calculated secondary neutron and photon yields emitted from a thick iron target for 50 to 500 MeV protons, and effective dose distributions in concrete and iron/concrete shields. The Monte Carlo code MCNPX2.1.5 [10] was used for the calculations in order to obtain radiation shielding parameters dependent on emission angles.

A geometry used in the radiation shielding calculations is shown in Figure 2. A cylindrical iron target with enough thickness to stop primary protons is mounted at the centre of a spherical shielding shell. The protons are assumed to be pencil beams and are incident to the centre axis of the target. The concrete shell is set outside of a 0, 25, 50 or 70-cm thick iron shell. The concrete shell is divided by a 24 in thickness and a 12 in solid angle relative to the beam direction. The concrete thickness equals 4 m; the angular dependent effective dose distributions in concrete up to 3.5 m are calculated (the remainder is a reflection area). Cross-sections used in the calculations are from the LA150 library [11], which is based on a pre-equilibrium model for particles up to 150 MeV, and the IntraNuclear Cascade (INC) model, Bertini [12], for particles above 150 MeV, which was implemented in MCNPX2.1.5. The MCPLIB02 library [13] is used for photons.

Figure 2. MCNPX model for calculating effective dose distribution in concrete

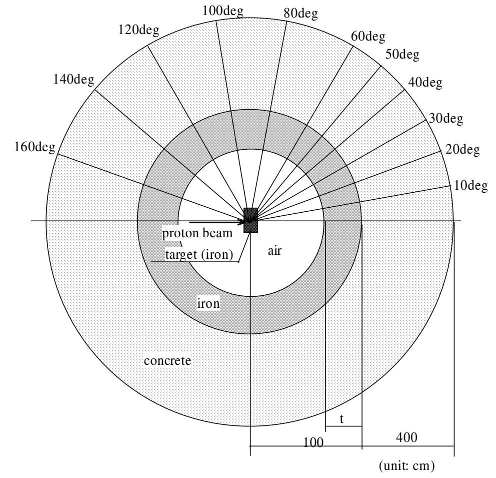

Proton energy (MeV)	Target thickness (cm)
50	4.32E-01
100	1.44E+00
150	2.90E+00
200	4.78E+00
250	7.00E+00
300	9.70E+00
400	1.60E+01
500	2.36E+01

iron thickness t (cm)
0.0
25.0
50.0
70.0

The concrete density is assumed to be 2.1 g/cm^3. The composition of concrete is based on ANL-5800 Type02-a [14]. The densities of the iron target and the iron shield are assumed to be 7.86 g/cm^3 (pure) and 7.83 g/cm^3, respectively. The impurities in the iron shield are not taken into account because concrete walls may be required with enough thickness to attenuate neutrons below 1 MeV. Flux-to-effective dose conversion factors with AP geometry are based on ICRP Publication 74 for photons and neutrons up to 200 MeV. Data were evaluated by Iwai, *et al.* [15], for neutrons above 200 MeV.

Parameters

Parameters in Eq. (2) have been estimated with the calculated neutron and photon dose rates as mentioned above. The parameters for neutrons have been estimated for three energy bins (500-5 MeV, 5 MeV-0.414 eV and 0.414-0.001 eV) because neutron attenuation curves in the build-up region are different for each bin. The parameters for photon were also estimated. The parameters have been tabulated for 12 emission angle bins (six bins in a range from 0°-60° and six bins in a range from 60°-180°). In the estimation of the parameters, we were careful to avoid the underestimation of the calculated dose rate with Eq. (2). These parameters are well-related to proton energy in the range from 50-500 MeV. Lastly, the parameters were approximated using the sixth order polynomial curve fit as a function of proton energy. For example, Figures 3 and 4 show the effective dose distribution in concrete calculated using Eq. (2) together with MCNPX results. The deviation of total dose rate due to this approximation is –18% to 30%, which corresponds to a few percentage points of concrete thickness. In some cases, Eq. (2) is not adopted for concrete thickness below 100 g/cm^2, which is the lower limit of BULK-I.

Figure 3. Effective dose distributions in concrete after penetrating through a 50-cm thick iron shield (250 MeV proton energy)

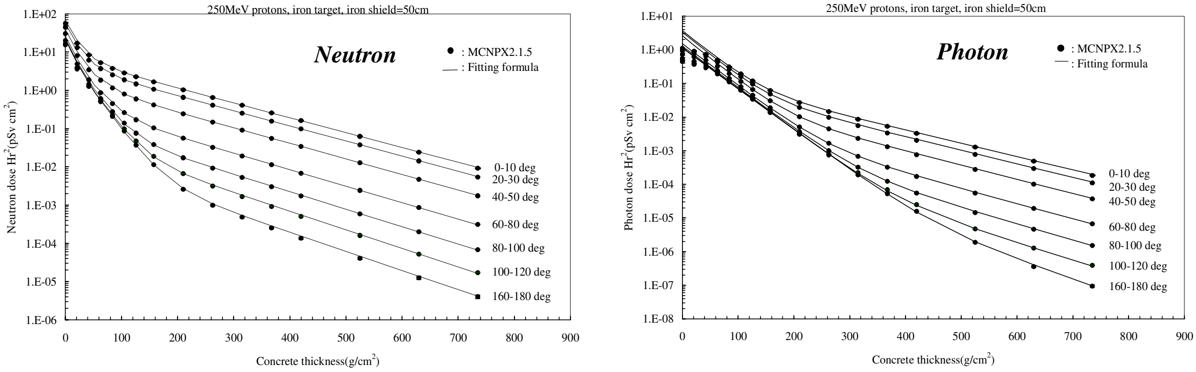

Figure 4. Effective dose distributions in concrete after penetrating through a 70-cm thick iron shield (500 MeV proton energy)

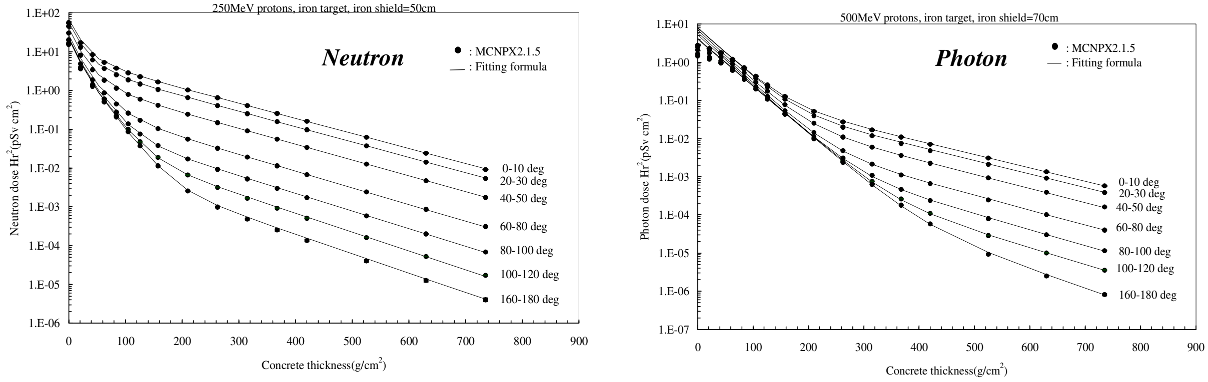

Validation of BULK-I

Experiment

A radiation shielding experiment was performed at WERC. The experimental layout is shown in Figure 5. Neutrons were produced with a 5-cm thick iron target for 200 MeV protons in radiation room No. 3. The incident angle of protons relative to the vertical direction against the 2-m thick concrete wall (density of 2.15 g/cm^3) was 37.7°. Neutron dose rates were measured with a rem counter (MSN10014) along the outer surface of the wall in the radiation control room.

Figure 5. Layout of the radiation shielding experiment at WERC

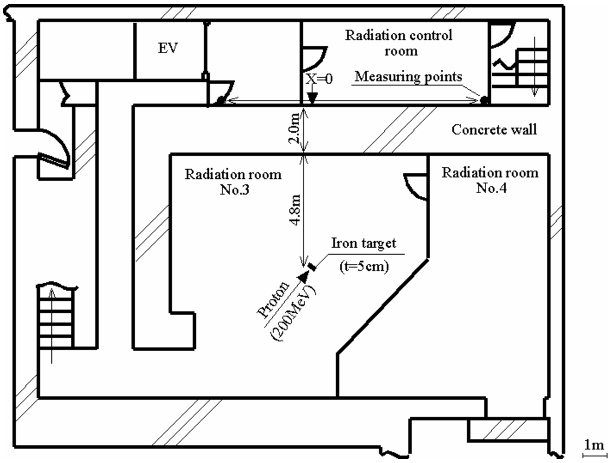

Results

Neutron dose rates corresponding to the experiment were calculated with MCNPX2.1.5 and BULK-I. For the MCNPX calculations, the effective dose conversion factors with AP geometry and the rem counter response calculated by Saegusa, *et al.* [16], were used.

Figure 6 shows the measured and calculated neutron dose rates along the outer surface of the wall. The MCNPX results with the rem counter response agree well with the experimental data within a factor of three. This discrepancy for low emission angle may be due to the overestimation of calculated neutron yields at high neutron energy [17]. These are three times lower than those with the effective dose conversion factor due to the discrepancy between the effective dose conversion factor and the rem counter response at neutron energy above 10 MeV. The effective dose rates using BULK-I agree well with those using MCNPX (within 25%). The dose distribution with BULK-I is not smooth because the width of emission angle bins is 10° or 20°. In this case, BULK-I has the same uncertainty as MCNPX2.1.5, and consequently is a valid tool for the radiation shielding design of proton accelerator facilities.

Figure 6. Comparison between measured and calculated dose distributions along the concrete wall

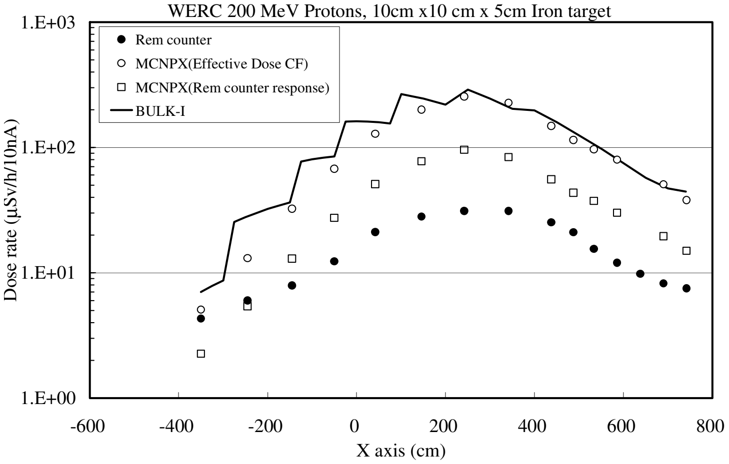

Conclusion

BULK-I was developed as a tool for radiation shielding design of proton accelerator facilities using medium energy (50-500 MeV). This tool utilises a new formula that accounts for thin and thick concrete walls. In addition, radiation shielding calculation parameters for one layer of concrete and for two layers (one iron, one concrete) are utilised. It was confirmed that BULK-I is a valid radiation shielding design through the comparison with the radiation shielding experiment using 200 MeV protons at WERC.

REFERENCES

[1] Moyer, B.J., *Evaluation of Shielding Required for the Improved Bevatron*, Rep. UCRL-9796, Lawrence Berkeley Lab., Berkeley, CA (1961).

[2] Hagan, N.K., L.L. Colborn, T.W. Armstrong Allen, *Nucl. Sci. Eng*., 98, 272 (1988).

[3] Siebers, J.V., P.M. DeLuca, Jr., D.W. Pearson, G. Coutrakon, *Nucl. Sci. Eng*., 115, 13 (1993).

[4] Aweschalom, M., FNAL-TM-1354 (1987).

[5] Knowles, H.B., *et al*., *Proceedings of the 1993 Particle Accelerator Conference*, Washington, DC, 17-20 May 1993, IEEE 1762 (1993).

[6] Braid, T.H., *et al*., *IEEE Trans. Nucl. Sci.*, NS-18, 821 (1971).

[7] Tesch, K., *Radiat. Protec. Dosim*., 11, 165 (1985).

[8] Tsukiyama, T., *et al*., *Nucl. Sci. Technol*., *Proc. of ICRS9*, Supplement 1, 640 (2000).

[9] Tayama, R., *et al*., *KEK Internal 2001-8*, November 2001.

[10] MCNPX version 2.1.5, CCC-705, *RSICC Computer Code Collection*, ORNL (1999).

[11] Chadwick, M.B., *et al*., *Nucl. Sci. Eng*., 131, 293 (1999).

[12] Bertini, H.W., *Phys. Rev*., 188, 1711 (1969).

[13] MCNPXS, DLC-189, RSICC Data Library (1997)

[14] *Reactor Physics Constants*, ANL-5800, Argonne National Laboratory, p. 660 (1963).

[15] Iwai, S., *et al*., *Proceedings of SATIF-3* (1997).

[16] Saegusa, J., *et al*., *Nucl. Instr. and Meth*., A 516, 193 (2004).

[17] Tayama, R., *et al*., *Nucl. Eng. Des*., 213, 119 (2002).

ANALYSIS OF THE JINR p(660 MeV) + ^{129}I, ^{237}Np AND ^{241}Am MEASUREMENTS WITH ELEVEN DIFFERENT MODELS

S.G. Mashnik[1], V.S. Pronskikh[2], J. Adam[2,3], A. Balabekyan[2,4], V.S. Barashenkov[2], V.P. Filinova[2], A.A. Solnyshkin[2], V.M. Tsoupko-Sitnikov[2], R. Brandt[5], R. Odoj[6], A.J. Sierk[1], R.E. Prael[1], K.K. Gudima[7], M.I. Baznat[7]
[1]Los Alamos National Laboratory, Los Alamos, New Mexico, 87544 USA
[2]Joint Institute for Nuclear Research, Dubna, 141980 Russia
[3]Institute for Nuclear Physics, Academy of Science of the Czech Republic, Rez, Czech Republic
[4]Yerevan State University, Republic of Armenia
[5]Institute of Nuclear Chemistry, Philipps University, Marburg, Germany
[6]Forschungszentrum Jülich, Germany
[7]Institute of Applied Physics, Academy of Science of Moldova, Chisinau, Moldova

Abstract

Isotopically enriched ^{129}I (85% ^{129}I and 15% ^{127}I), ^{237}Np and ^{241}Am targets were irradiated with a beam of 660 MeV protons at the JINR DLNP Phasotron and cross-sections of the formations of 207 residual products (74 from ^{129}I, 53 from ^{237}Np and 80 from ^{241}Am) were generated. In this paper, we analyse the resultant data using 11 different models, realised in eight codes: LAHET (Bertini, ISABEL, INCL+ABLA and INCL+RAL), CASCADE, CEM95, CEM2k, LAQGSM+GEM2, CEM2k+GEM2, LAQGSM+GEMINI and CEM2k+GEMINI. The purpose was to validate the tested models against the experimental data and to better understand the mechanisms for production of residual nuclei. The agreement of different models with the data varied quite a bit. We found that most of the codes were fairly reliable in predicting cross-sections for nuclides that were not too far away in mass from the targets, but that the codes differed greatly in the deep spallation, fission and fragmentation regions. None of the codes tested here except GEMINI allowed fission of nuclei as light as iodine. Thus, the ^{129}I data, especially in the $A = 40$-90 region, agreed best when the codes CEM2k and LAQGSM were merged with GEMINI. At the same time, GEMINI is not yet very reliable for an accurate description of actinides and the ^{237}Np and ^{241}Am data were better reproduced by LAHET (Bertini, ISABEL or INCL+RAL/ABLA), and by CEM2k or LAQGSM merged with GEM2. The ^{237}Np and ^{241}Am data were not so well-reproduced when using GEMINI. We conclude that none of the codes tested here were able to well-reproduce all the data and that improvements are needed. To this end, development of a better universal evaporation/fission model should be high priority.

Introduction

Interest in the physics of transmutation (i.e. conversion into stable isotopes as a result of nuclear reaction) of actinides and fission products produced at nuclear power stations has increased significantly during the last decade. Estimations made by different groups [1,2] show that the radiation risk associated with the possible leakage of spent nuclear fuel from deep underground storage systems after transmutation is about the same as uranium ore after 1 000 years of storage. This time period is significantly shorter than the 5×10^6 years necessary to store the same spent fuel, which has not undergone transmutation, in order to bring the radiation risk down to a similar level.

Analysis of spent fuel's radiation hazard indicated that after extraction of the uranium-plutonium group of elements and such fission products as ^{90}Sr, ^{137}Cs and ^{129}I, the greatest hazard comes from ^{237}Np and ^{241}Am [3]. Americium 241 ($T_{1/2}$ = 432.2 years) contributes the most to the radioactivity, while ^{237}Np ($T_{1/2} = 2.144 \times 10^6$ years) is dangerous due to its high concentration in the spent fuel as well as its high migration ability in the biosphere. This migration ability increases the probability of its penetration into the human body through the food chain [4].

Investigation of ^{237}Np and ^{241}Am transmutation dynamics in the flow of thermal neutrons with different densities shows that the higher the density of neutrons, the smaller the number of different actinides noticeably contributing to the radioactivity of wastes [4]. To solve the problem of transmutation, high-current proton accelerators can be used to produce neutron fluxes of $\sim 10^{17}$ $cm^{-2}c^{-1}$ for transmutation purposes. In some recent publications, both transmutation of actinides by thermal neutron irradiation and their spallation and fission with the proton and ion beams are investigated [5].

Hadron nucleus event generators are the basis for calculations on accelerator driven system (ADS) set-ups, their targets and the blanket effect. Such calculations are done using models of varying accuracy. The best test for models and codes used in such applications is to compare calculated and experimental yields of residual nuclei from reactions of interest. From an experimental viewpoint, determination of the independent cross-section for yields of short-lived nuclear products derived from mono-isotope targets is the most important element for such comparisons [6]. The experimental cross-sections for the residual nuclei in radioactive ^{129}I, ^{237}Np and ^{241}Am targets are undeniably important in the transmutation of nuclear waste in a direct proton beam. Measurements of the yield of residual nuclei from ^{237}Np, ^{241}Am and ^{129}I (85% ^{129}I and 15% ^{127}I) targets were recently performed at the JINR Phasotron with proton beams of 660 MeV [7,8]. In the present work, we analyse these measurements using 11 models, which have been implemented in several event generators and transport codes used in different nuclear applications, in order to test these models against the experimental data. The hope is to discover better mechanisms of nuclear reaction and ways to improve the models and codes.

Results

The ^{237}Np and ^{241}Am experimental data are published in tabulated form in Ref. [7], while the ^{129}I data are tabulated in Ref. [8]. Details on the measurements may be found in Refs. [7,8] thus we do not discuss them here.

We analysed all the measured data using 11 models, which are contained in eight transport codes and event generators. Specifically, we calculated the reactions with the LAHET3 version [9] of the transport code LAHET [10], which uses the Bertini [11] and ISABEL [12] IntraNuclear Cascade (INC) models merged with the Dresner evaporation model [13] and the Atchison fission model (RAL) [14]. Other codes utilised include the Liege INC code by Cugnon, *et al.*, INCL [15] merged in LAHET3 with ABLA [16] and Dresner [13] (+ Atchison [14]) evaporation (+ fission) models, with the Dubna transport code CASCADE [17], and with versions of the Cascade-Exciton Model (CEM) [18] as realised in certain codes. These codes include CEM95 [19] and CEM2k [20], and involve the merging of CEM2k [21-23] with the Generalized Evaporation/Fission Model code GEM2 by Furihata [24], with the Los Alamos version of the Quark-Gluon String Model code LAQGSM [25] merged [21-23] with GEM2 [24]. In addition, the CEM2k and LAQGSM codes were both [21] merged with the sequential binary decay code GEMINI by Charity [26]. The limited size of the present work does not allow us to discuss these models here. Descriptions of the models may be found in the original publications [9-26] and the references contained therein.

Let us start with a discussion of results for the ^{129}I target. As we have done previously (Refs. [6,27]), one qualitative and one quantitative criterion were chosen to judge how well our data are described by different models. The chosen criterion include the ratio of a calculated cross-section for the production of a given isotope to its measured value ($\sigma^{cal}/\sigma^{exp}$) as a function of the mass number of products (Figure 1) and the mean simulated-to-experimental data ratio (Table 1).

$$\langle F \rangle = 10^{\sqrt{\left\langle \left(\log\left[\sigma^{cal}/\sigma^{exp}\right]\right)^2 \right\rangle}} \tag{1}$$

with its standard deviation:

$$S(\langle F \rangle) = 10^{\sqrt{\left\langle \left(\left|\log\left(\sigma^{cal}/\sigma^{exp}\right)\right| - \log(\langle F \rangle)\right)^2 \right\rangle}} \tag{2}$$

Table 1. Comparison of experimental and calculated results for 42 selected product isotopes from ^{129}I (left panels) and for 22 spallation products with $A \geq 95$ (right panels)

Model	42 selected isotopes			22 spallation products with $A \geq 95$		
	$N/N_{30\%}/N_{2.0}$	$\langle F \rangle$	$S(\langle F \rangle)$	$N/N_{30\%}/N_{2.0}$	$\langle F \rangle$	$S(\langle F \rangle)$
Bertini+Dresner	36/6/22	3.72	3.00	22/6/19	1.67	1.34
ISABEL+Dresner	34/5/18	5.18	4.45	22/5/16	1.72	1.37
INCL+Dresner	33/14/21	3.86	3.16	22/14/21	1.42	1.28
INCL+ABLA	32/9/21	9.32	7.01	22/9/21	1.57	1.34
CASCADE	42/9/15	11.05	5.19	22/9/14	3.32	2.75
CEM95	40/10/20	5.40	3.52	22/9/18	1.78	1.44
CEM2k	33/13/26	2.89	2.74	22/11/20	1.48	1.27
LAQGSM+GEM2	33/13/22	3.16	2.68	22/13/21	1.50	1.34
CEM2k+GEM2	35/10/28	5.03	5.04	22/8/20	1.60	1.35
LAQGSM+GEMINI	42/12/29	4.28	3.58	22/17/21	1.31	1.21
CEM2k+GEMINI	42/12/27	2.74	2.15	22/9/20	1.46	1.25

For the comparison, out of the 74 measured cross-sections [8], only 42 were selected that satisfied rules based on appreciation of the physical principles realised in the models. For example, if only a long-lived isomer or the ground state of a nuclide was measured, such nuclides were excluded from quantitative comparison, but if both were measured separately, then their sums were compared with the calculations. Such rules are similar to those used by Titarenko, *et al.* [6,27].

To understand how different models describe nuclides produced in the spallation and fission/fragmentation regions, we divided all 42 measured nuclides included in our quantitative comparison into two groups, spallation ($A \geq 95$) and fission/fragmentation ($A < 95$). The panels on the

SESSION VI

Follow-up of Past SATIF Agreements and Actions

PRESENT STATUS OF THE DATA COLLECTION ON THE DOSE CONVERSION COEFFICIENTS FOR HIGH-ENERGY RADIATION

Yukio Sakamoto
Japan Atomic Energy Research Institute
Japan Nuclear Cycle Development Institute
Tokai-mura, Naka-gun, Ibaraki-ken, 319-1184 Japan
E-mail: sakamoto.yukio@jnc.go.jp

The SATIF Dosimetry Group

Abstract

The dose conversion coefficients for high-energy radiation were reviewed at several SATIF meetings. At the SATIF-6 meeting, the collection of different data sets on dose conversion coefficients was agreed upon and copies of relevant papers and numerical data were gathered. This paper contains summaries of data on: 1) dose conversion coefficients for high-energy radiation, including evaluation using various codes and researchers; and 2) effective dose conversion coefficients for high-energy photons, electrons, positrons, pions, muons, kaons, neutrons, protons and heavy charged particles (up to ^{56}Fe ions).

The dose conversion coefficients for high-energy radiation were reviewed at several SATIF meetings. At the SATIF-6 meeting, the collection of different data sets on dose conversion coefficients was agreed and copies of relevant papers and numerical data were gathered. Table Set 1 is the summary of dose conversion coefficients for high-energy radiation, including evaluation using various codes and researchers. This summary contains the type of radiation, irradiation geometries of effective dose and other dose quantities, and energy ranges of the data set for dose conversion coefficients as calculated by various code systems. These codes include FLUKA [1,2], MCNPX [3,4], PHITS [5,6] and HERMES [7,8]. Table Set 2 is the summary of effective dose conversion coefficients for high-energy photons, electrons, positrons, pions, muons, kaons, neutrons, protons and heavy charged particles (up to ^{56}Fe ions). Table Set 2 also includes ICRP Publication 74 data [11].

Figures 1-5 show the effective dose conversion coefficients at the AP and ISO irradiation geometries for high-energy photons, electrons, neutrons, protons and alpha particles.

In the case of photons, there are some discrepancies among the data at the AP irradiation geometry but the data nearly agreed with each other at the ISO irradiation geometry. The effective dose conversion coefficients for high-energy photons at the ISO irradiation geometry are a few times larger than those at the AP irradiation geometry. Since the secondary charged particles produced by high-energy photon bombardment can reach deep inside the human body, the important tissues and organs having larger tissue weighting factors in the front side of the human body receive a smaller amount of energy deposition with the AP irradiation geometry as compared to ISO irradiation geometry.

In the case of electrons, the data nearly agreed with each other at both irradiation geometries. The effective dose conversion coefficients for high-energy electrons at the ISO irradiation geometry are a few times larger than those at the AP irradiation geometry. The effective dose conversion coefficients for high-energy electrons at each irradiation geometry are a few times larger than those for high-energy photons at each irradiation geometry. This is due to the efficiency for energy deposition of primary electrons being superior to that of incident photons.

In the case of neutrons, there are some discrepancies among the data with the energy range from a few hundred MeV to 100 GeV at both irradiation geometries. The discrepancies are caused by the differences of the transport models and the library data in the hadron transport codes. The effective dose conversion coefficients for high-energy neutrons at the ISO irradiation geometry are a few times larger than those at the AP irradiation geometry.

In the case of protons, there are some discrepancies among the data with the energy range from a few hundred MeV to 100 GeV, with both irradiation geometries being similar for neutrons as well. The effective dose conversion coefficients for lower energy protons at each irradiation geometry are a few times bigger than those for lower energy neutrons at each irradiation geometry. This is because the efficiency for energy deposition of primary protons is superior to that of incident neutrons and there are bumps at ~100 MeV as shown in Figure 4. Protons with energy of ~100 MeV correspond to ~10 cm. The magnitudes of the effective dose conversion coefficients for high-energy protons at each irradiation geometry are similar to those for high-energy neutrons at each irradiation geometry.

In the case of alpha particles, there are only two calculations and some discrepancies in the compared data above 1 GeV/A. Profiles of effective dose conversion coefficients for high-energy alpha particles are similar to those for high-energy protons. The systematic formula of effective dose conversion coefficients for high-energy heavy ions is proposed for the function of the type of charged particle and its energy [7].

In the near future, the numerical data of the dose conversion coefficients for high-energy radiation will be summarised and stored in comparative tables and figures. Since the tissue weighting factors and radiation weighting factors will be changed in the new ICRP recommendation, the dose conversion coefficients data will then be re-evaluated.

Table Set 1. The summary of the dose conversion coefficients for high-energy radiation evaluated with various codes and by various researchers

Table 1(a). FLUKA/Pelliccioni [1,2]

Type of radiation	w_R	E: Effective dose						Other quantity	Energy range
		AP	PA	LAT	ROT	ISO	Other geometry		
Photons	1	●	●	●		●	BOTTOM Semi-ISO TOP	H*(d)	50 keV-100 GeV
Electrons	1	●	●	●		●	Semi-ISO TOP	H*(d)	5 MeV-100 GeV
Positrons	1					●		H*(d)	10 MeV-100 GeV
Neutrons		●	●	●		●	BOTTOM Semi-ISO TOP	H*(d)	0.025 eV-10 TeV
Protons	5	●	●	●		●	Semi-ISO TOP	H*(d)	5 MeV-10 TeV
Positive muons	1	●	●	●		●	Semi-ISO TOP	H*(d)	1 MeV-10 TeV
Negative muons	1	●	●	●		●		H*(d)	1 MeV-10 TeV
Positive pions		●	●	●		●		H*(d)	1 MeV-10 TeV
Negative pions		●	●	●		●		H*(d)	1 MeV-10 TeV
Positive kaons		●				●		H*(d)	1 MeV-10 TeV
Negative kaons		●				●		H*(d)	1 MeV-10 TeV

w_R: Radiation weighting factors, H(d): Ambient dose equivalent*

Table 1(b). MCNPX/Mares [3,4]

Type of radiation	w_R	E: Effective dose						Other quantity	Energy range
		AP	PA	LAT	ROT	ISO	Other geometry		
Photons	1					●			20 keV-10 GeV
Electrons	1					●			100 keV-10 GeV
Positive pions						●			10 MeV-100 GeV
Muons	1					●			10 MeV-100 GeV
Neutrons		●				●			10 MeV-5 GeV
Protons	5	●				●			10 MeV-50 GeV

Table 1(c). MCNPX/Sutton [5,6]

Type of radiation	w_R	E: Effective dose						Other quantity	Energy range
		AP	PA	LAT	ROT	ISO	Other geometry		
Photons	1	●	●	●					50 keV-2 GeV
Neutrons		●	●	●					10 MeV-2 GeV

Table 1(d). PHITS/Sato [7,8]

Type of radiation	w_R	E: Effective dose						Other quantity	Energy range
		AP	PA	LAT	ROT	ISO	Other geometry		
Neutrons		●				●			100 MeV-200 GeV
Protons	5	●				●			
Positive pions		●				●			
Negative pions		●				●			
Protons	5	●				●			5 MeV/A-2 GeV/A
Deutrons		●				●			
Tritons		●				●			
^{3}He		●				●			
α	20	●				●			
^{12}C	20	●				●			
^{20}Ne	20	●				●			
^{40}Ar	20	●				●			
^{40}Ca	20	●				●			
^{56}Fe	20	●				●			

Table 1(e). HERMES (EGS4)/Sato O. (photons) [10], HERMES (EGS4)/Tsuda (electrons) [10], HERMES (HETC-3STEP)/Yoshizawa (neutrons, protons, alpha particles) [9,10]

Type of radiation	w_R	E: Effective dose						Other quantity	Energy range
		AP	PA	LAT	ROT	ISO	Other geometry		
Photons	1	●	●	●	●	●		H*(d)	1 MeV-10 GeV
Electrons	1	●	●	●	●	●		H_E	1 MeV-100 GeV
Neutrons		●	●			●		H_E	20 MeV-10 GeV
Protons	5	●	●			●		H_E	
α	20	●	●			●		H_E	20 MeV/A-10 GeV/A

H(d): Ambient dose equivalent, H_E: Effective dose equivalent*

Table 1(f). ICRP Publication 74 [11]

Type of radiation	w_R	E: Effective dose						Other quantity	Energy range
		AP	PA	LAT	ROT	ISO	Other geometry		
Photons	1	●	●	●	●	●		H*(10)	10 keV-10 MeV
Electrons	1	●						H′(10, 0°)	0.1 MeV-10 MeV
Neutrons		●	●	●	●	●		H*(10)	1 MeV-180 MeV

H(10): Ambient dose equivalent, H′(10, 0°): Directional dose equivalent*

Table Set 2. Summary of the dose conversion coefficients for high-energy radiations

Table 2(a). Photons ($w_R = 1$)

Code	E: Effective dose						Energy range
	AP	PA	LAT	ROT	ISO	Other geometry	
FLUKA	●	●	●		●	BOTTOM Semi-ISO TOP	5×10^{-2} to 1×10^{5} MeV
MCNPX/Mares					●		2×10^{-2} to 1×10^{4} MeV
MCNPX/Sutton	●	●	●				5×10^{-2} to 2×10^{3} MeV
EGS4	●	●	●	●	●		1×10^{0} to 1×10^{4} MeV
ICRP 74	●	●	●	●	●		1×10^{-2} to 1×10^{1} MeV

Table 2(b). Electrons and positrons ($w_R = 1$)

Code	E: Effective dose						Energy range
	AP	PA	LAT	ROT	ISO	Other geometry	
FLUKA	●	●	●		●	Semi-ISO TOP	5×10^{0} to 1×10^{5} MeV
FLUKA (positron)					●		1×10^{1} to 1×10^{5} MeV
MCNPX/Mares					●		1×10^{-1} to 1×10^{4} MeV
EGS4	●	●	●	●	●		1×10^{0} to 1×10^{5} MeV
ICRP 74	●						1×10^{-2} to 1×10^{1} MeV

Table 2(c). Pions, muons and kaons

Code	E: Effective dose						Energy range
	AP	PA	LAT	ROT	ISO	Other geometry	
π^+: FLUKA	●	●	●		●		1×10^0 to 1×10^7 MeV
π^+: MCNPX					●		1×10^1 to 1×10^5 MeV
π^+: PHITS	●				●		1×10^2 to 2×10^5 MeV
π^-: FLUKA	●	●	●		●		1×10^0 to 1×10^7 MeV
π^-: PHITS	●				●		1×10^2 to 2×10^5 MeV
μ^+: FLUKA	●	●	●		●	Semi-ISO TOP	1×10^0 to 1×10^7 MeV
μ^-: FLUKA	●	●	●		●		1×10^0 to 1×10^7 MeV
μ: MCNPX					●		1×10^1 to 1×10^8 MeV
K^+: FLUKA	●				●		1×10^0 to 1×10^7 MeV
K^-: FLUKA	●				●		1×10^0 to 1×10^7 MeV

Table 2(d). Neutrons

Code	E: Effective dose						Energy range
	AP	PA	LAT	ROT	ISO	Other geometry	
FLUKA	●	●	●		●	BOTTOM Semi-ISO TOP	2.5×10^{-8} to 1×10^7 MeV
MCNPX/Mares	●				●		1×10^1 to 5×10^3 MeV
MCNPX/Sutton	●	●	●				2×10^1 to 2×10^3 MeV
PHITS	●				●		1×10^2 to 2×10^5 MeV
HETC-3STEP	●	●			●		2×10^1 to 1×10^4 MeV
ICRP 74	●	●	●	●	●		1×10^{-9} to 1.8×10^2 MeV

Table 2(e). Protons ($w_R = 5$)

Code	E: Effective dose						Energy range
	AP	PA	LAT	ROT	ISO	Other geometry	
FLUKA	●	●	●		●	Semi-ISO TOP	5×10^0 to 1×10^7 MeV
MCNPX/Mares	●				●		1×10^1 to 5×10^4 MeV
PHITS	●				●		1×10^2 to 2×10^5 MeV
HETC-3STEP	●	●			●		2×10^1 to 1×10^4 MeV

Table 2(f). Heavy charged particles ($w_R = 20$)

Type of radiation	E: Effective dose						Energy range
	AP	PA	LAT	ROT	ISO	Other geometry	
d: PHITS	●				●		5×10^0 to 2×10^3 MeV/A
t: PHITS	●				●		
^{3}He: PHITS	●				●		
α: PHITS	●				●		
α: HETC-3STEP	●	●			●		2×10^1 to 1×10^4 MeV/A
^{12}C: PHITS	●				●		5×10^0 to 2×10^3 MeV/A
^{20}Ne: PHITS	●				●		
^{40}Ar: PHITS	●				●		
^{40}Ca: PHITS	●				●		
^{56}Fe: PHITS	●				●		

Figure 1. The effective dose conversion coefficients for high-energy photons at the AP and ISO irradiation geometries

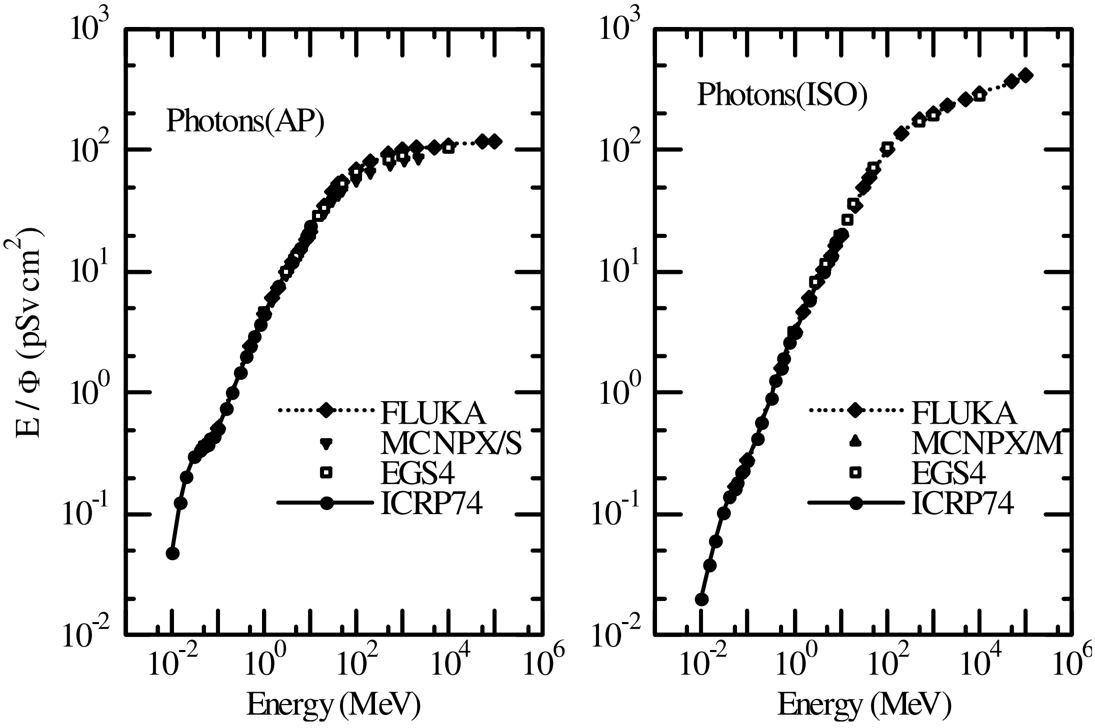

Figure 2. The effective dose conversion coefficients for high-energy electrons at the AP and ISO irradiation geometries

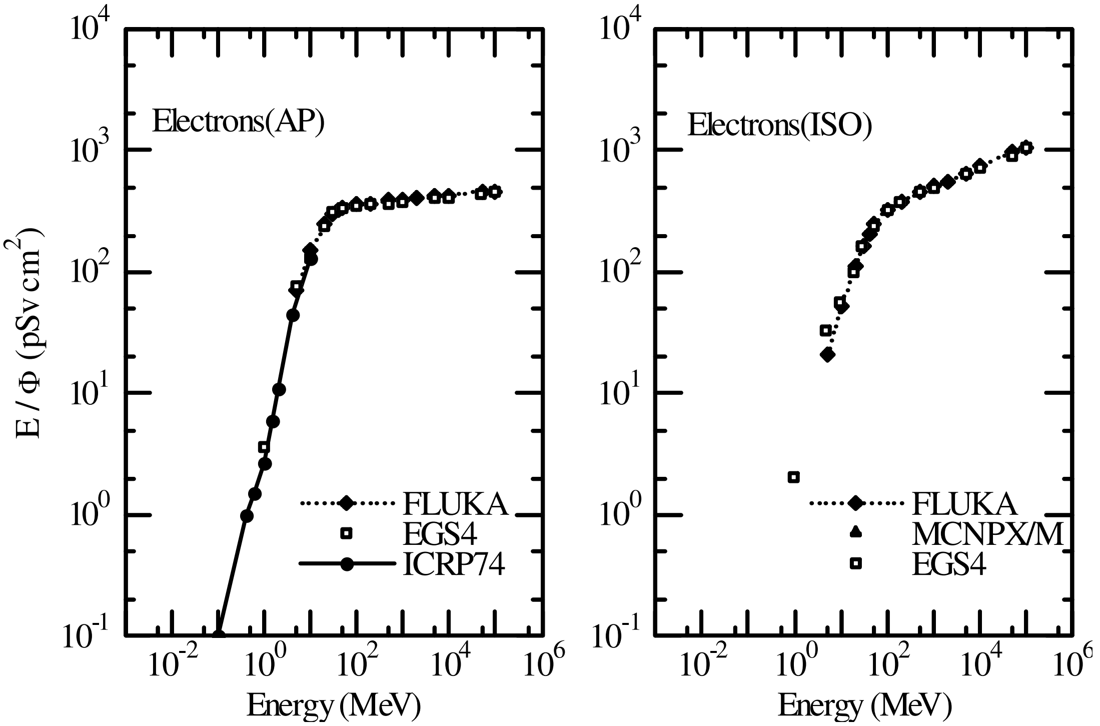

Figure 3. The effective dose conversion coefficients for high-energy neutrons at the AP and ISO irradiation geometries

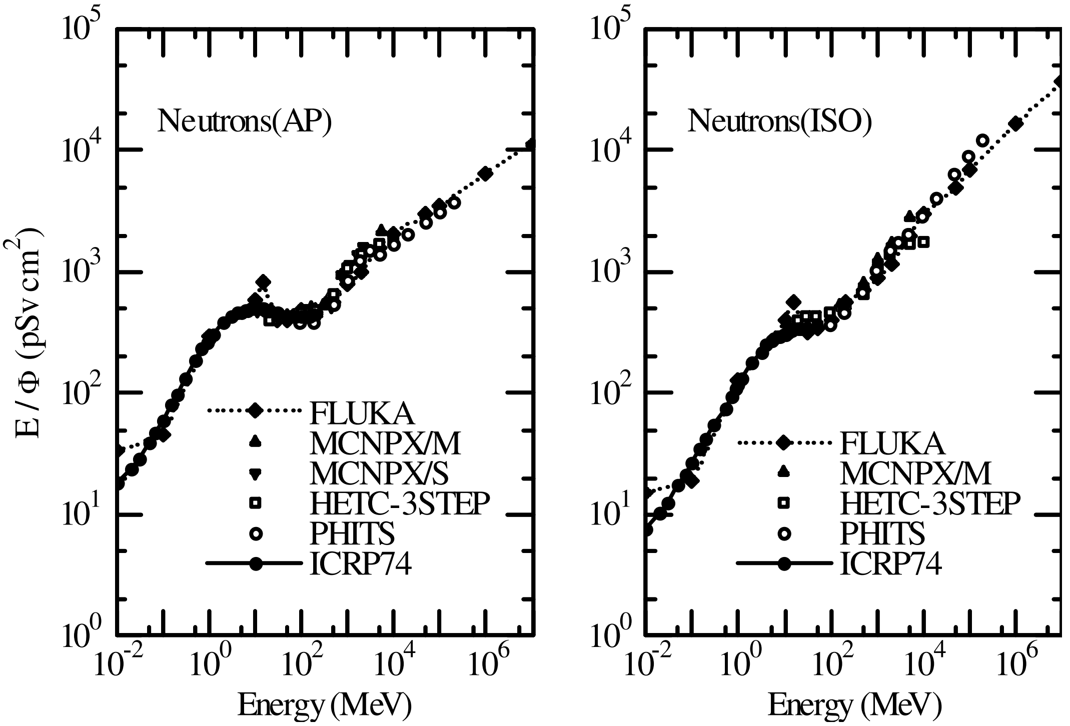

Figure 4. The effective dose conversion coefficients for high-energy protons at the AP and ISO irradiation geometries

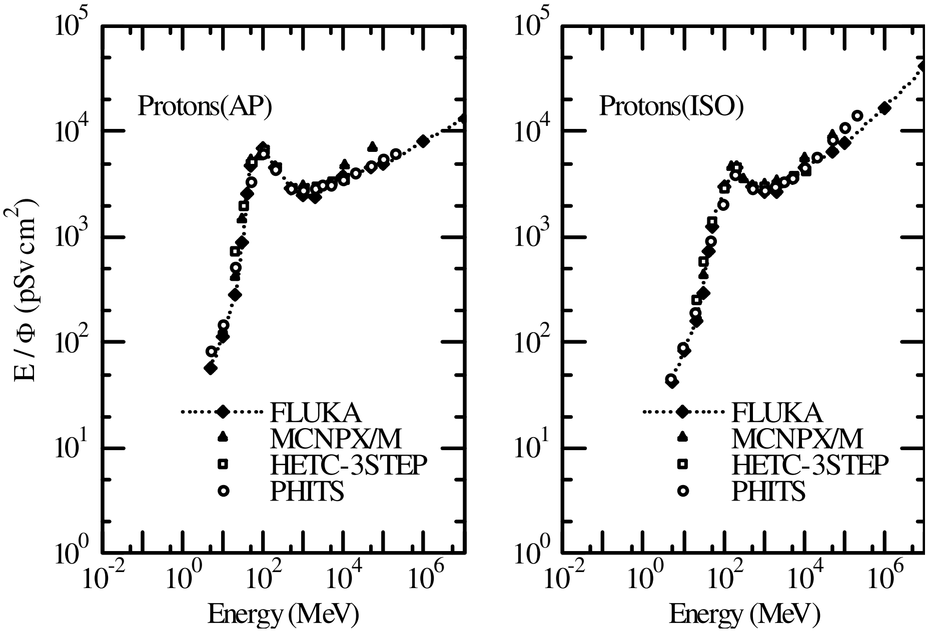

Figure 5. The effective dose conversion coefficients for high-energy alpha particles at the AP and ISO irradiation geometries

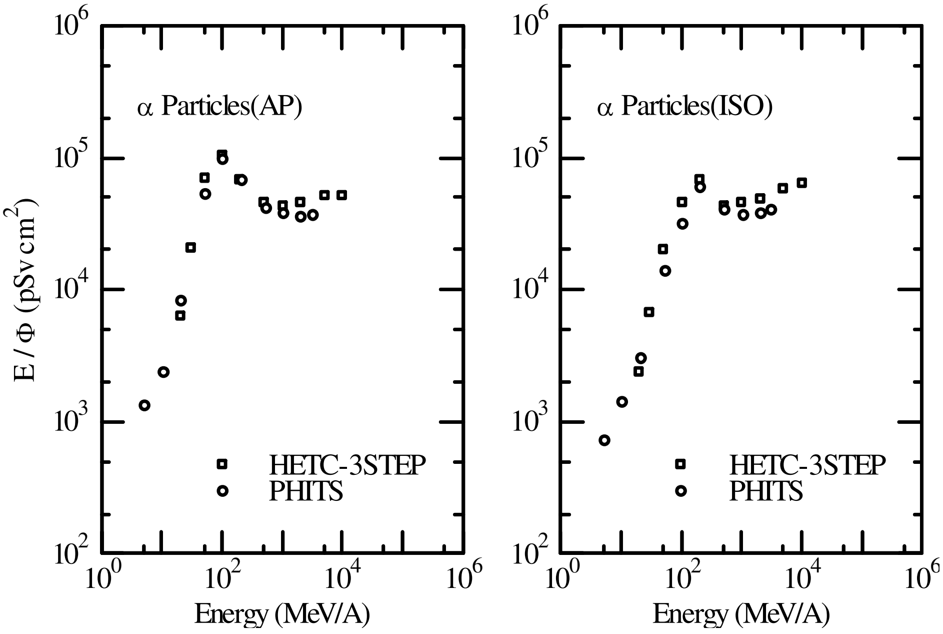

Acknowledgements

I wish to thank Dr. M. Pelliccioni (INFN), Dr. V. Mares (University of Munich), Dr. N. Yoshizawa (MRI) and Dr. T. Sato (JAERI) for their contribution to this data collection.

REFERENCES

[1] Pelliccioni, M., "Overview of Fluence-to-effective Dose and Fluence-to-ambient Dose Equivalent Conversion Coefficients for High Energy Radiation Calculated Using the FLUKA Code", *Radiation Protection Dosimetry*, Vol. 88, No. 4, pp. 279-297 (2000).

[2] Ferrari, A., M. Pelliccioni, "On the Conversion Coefficients for Cosmic Ray Dosimetry", *Radiation Protection Dosimetry*, Vol. 104, No. 3, pp. 211-220 (2003).

[3] Mares, V., H. Schraube, "The Effect of the Fluence to Dose Conversion Coefficients upon the Dose Estimation to Cosmic Radiation", *Proceedings of the 6th Meeting on Shielding Aspects of Accelerators, Targets and Irradiation Facilities (SATIF-6)*, SLAC, Stanford, CA, April 2002.

[4] Mares, V., H. Schraube, "Conversion Coefficients for Cosmic Radiation in the Atmosphere", *Proceedings of the European IRPA Congress 2002 – Towards Harmonization of Radiation Protection in Europe*, Florence, Italy, 7-11 October 2002.

[5] Sutton, M.R., N.E. Hertel, L.S. Waters, "Fluence-to-effective Dose Conversion Coefficients for High-energy Radiations Calculated with MCNPX", *Proceedings of the 5th Meeting on Shielding Aspects of Accelerators, Targets and Irradiation Facilities (SATIF-5)*, Paris, OECD/NEA, July 2000, pp. 297-311.

[6] Sutton, M.R., N.E. Hertel, L.S. Water, "High-energy Neutron Dosimetry", *Proceedings of the 9th International Conference on Radiation Shielding*, Tsukuba, Japan, 17-22 October 1999; *Journal of Nuclear Science and Technology*, Suppl. 1, pp. 753-757 (2000).

[7] Sato, T., S. Tsuda, Y. Sakamoto, Y. Yamaguchi, K. Niita, "Conversion Coefficients from Fluence to Effective Dose for Heavy Ions with Energies up to 3 GeV/A", *Radiation Protection Dosimetry*, Vol. 106, No. 2, pp. 137-144 (2003).

[8] Sato, T., S. Tsuda, Y. Sakamoto, Y. Yamaguchi, K. Niita, "Analysis of Dose-LET Distribution in the Human Body Irradiated by High Energy Hadrons", *Radiation Protection Dosimetry*, Vol. 106, No. 2, pp. 145-153 (2003).

[9] Yoshizawa, N., O. Sato, S. Takagi, S. Furihata, J. Funabiki, S. Iwai, T. Uehara, S. Tanaka, Y. Sakamoto, "Fluence to Dose Conversion Coefficients for High-energy Neutron, Proton and Alpha Particles", *Proceedings of the 9th International Conference on Radiation Shielding*, Tsukuba, Japan, 17-22 October 1999; *Journal of Nuclear Science and Technology*, Suppl. 1, pp. 865-869 (2000).

[10] Sakamoto, Y., O. Sato, S. Tsuda, N. Yoshizawa, S. Iwai, S. Tanaka, Y. Yamaguchi, "Dose Conversion Coefficients for High-energy Photons, Electrons, Neutrons and Protons", JAERI 1345, January 2003 [in Japanese].

[11] "Conversion Coefficients for Use in Radiological Protection against External Radiation", *ICRP Publication 74*, Annals of the ICRP, Vol. 26/3 (1996).

LIST OF PARTICIPANTS

GERMANY

* DITTRICH, Wolfgang
Framatome Advanced Nuclear Power GmbH
NGPS4 – Strahlenschutz
Postfach 3220
D-91050 Erlangen
Tel: +49 9131 18 96535
Fax: +49 9131 18 97507
Eml: Wolfgang.Dittrich@Framatome-ANP.com

* GOLDENBAUM, Frank
Institut für Kernphysik
Forschungszentrum Jülich GmbH
Leo Brand-Srasse
D-52428 Jülich
Tel: +49 2461 61 4250
Fax: +49 2461 61 3930
Eml: F.Goldenbaum@fz-juelich.de

LEUSCHNER, Albrecht
Deutsches Elektronen-Synchrotron
DESY
Notkestrasse 85
D-22607 Hamburg
Tel: +49 40 8998 2043
Fax: +49 40 8998 3282
Eml: Albrecht.Leuschner@desy.de

NUENIGHOFF, Kay
Institut für Kernphysik
Forschungszentrum Jülich GmbH
D-52425 Jülich
Tel: +49 2461 61 3232
Fax: +49 2461 61 3930
Eml: K.Nuenighoff@fz-juelich.de

ITALY

BARTALUCCI, Sergio
INFN
Laboratori Nazionali di Frascati
Casella Postale 56
I-00044 Frascati
Tel: +39 069 4032 754
Fax:
Eml: Sergio.Bartalucci@lnf.infn.it

BURN, Kenneth W.
ENEA
Via Martiri di Monte Sole 4
I-40129 Bologna
Tel: +39 051 6098 417
Fax: +39 051 6098 629
Eml: kburn@bologna.enea.it

---

* *Regrets not having been able to attend.*

FERNANDEZ, Jorge E.
Laboratory of Montecuccolino-DIENCA
University of Bologna
Via dei Colli 16
I-40136 Bologna
Tel: +39 051 644 1718
Fax: +39 051 644 1747
Eml: jorge.fernandez@unibo.it

JAPAN

HAYASHI, Katsumi
Hitachi, Ltd.
Power & Industrial Systems
Nuclear Systems Division
Saiwai-cho, 3-1-1
Hitachi, Ibaraki 317-8511
Tel: +81 294 55 4501
Fax: +81 294 55 9900
Eml: katsumi-a_hayashi@pis.hitachi.co.jp

HIRAYAMA, Hideo
Radiation Science Center
High Energy Accelerator Res. Org. KEK
1-1 Oho, Tsukuba-shi, Ibaraki-ken 305-0801
Tel: +81 298 64 5489
Fax: +81 298 64 1993
Eml: hideo.hirayama@kek.jp

NAKAMURA, Takashi
Dept. of Quantum Science and Energy Eng.
Tohoku University
Aramaki, Aoba-ku, Sendai-Shi
Miyagi-ken 980-8579
Tel: +81 22 217 7805
Fax: +81 22 217 7808/7809
Eml: nakamura@cyric.tohoku.ac.jp

NAKASHIMA, Hiroshi
Japan Atomic Energy Research Institute
Center for Neutron Science
Shirakata-Shirane 2-4
Tokai, Ibaraki 319-1195
Tel: +81 29 282 6144
Fax: +81 29 282 5996
Eml: nakasima@shield4.tokai.jaeri.go.jp

OISHI, Koji
Technology-Knowledge Management Center
Institute of Technology
Shimizu Corporation
4-17 Echujima 3-chome
Koto-ku, Tokyo 135-8530
Tel: +81 3 3820 6416
Fax: +81 3 3643 7260
Eml: koji_oishi@shimz.co.jp

TANIGUCHI, Shingo
Japan Synchrotron Radiation Research Inst.
Koto 1-1-1, Mihazuki-cho
Sayou-gun, Hyogo 679-5198
Tel: +81 791 58 0831
Fax: +81 791 58 0830
Eml: shingo@spring8.or.jp

KOREA (REPUBLIC OF)

LEE, Hee-Seock
Manager of Radiation Safety Group
Pohang Accelerator Laboratory
Pohang University of Science and Technology
31 Nam-gu, Pohang
Gyongbuk Province 790-784
Tel: +82 54 279 1854
Fax: +82 54 279 1799
Eml: lee@postech.ac.kr

LEE, Young-Ouk
Korea Atomic Energy Research Institute
PO Box 105
Yuseong 305-600
Daejeon
Tel: +82 42 868 2764
Fax: +82 42 868 2636
Eml: yolee@kaeri.re.kr

PORTUGAL

ALBORNOZ TRILLO, Ana Carrillo
ITN/Fisica
Estrada Nacional 10
P-2686-953 Sacavém
Tel: +351 21 994 6062
Fax: +351 21 994 1525
Eml: ana.carrillo@itn.mces.pt

CABECA MARQUES, Luis Miguel
ITN/Fisica
Estrada Nacional 10
P-2686-953 Sacavém
Tel: +351 21 994 6062
Fax: +351 21 994 1525
Eml: luis.marques@itn.mces.pt

DIAS DE OLIVEIRA, Augusto Manuel
ITN
DPRSN
Estrada Nacional 10
Apartado 21
P-2686-953 Sacavém
Tel: +351 21 994 6297
Fax: +351 21 994 1995
Eml: adoliv@itn.mces.pt

GONCALVES, Isabel F.
ITN/Fisica
Estrada Nacional 10
P-2686-953 Sacavém
Tel: +351 21 994 6054
Fax: +351 21 994 1525
Eml: ifg@itn.mces.pt

VAZ, Pedro
Instituto Tecnologico e Nuclear
Estrada Nacional 10
P-2686-953 Sacavém
Tel: +351 21 994 62 30
Fax: +351 21 994 10 39
Eml: pedrovaz@itn.mces.pt

RUSSIAN FEDERATION

BATYAEV, Vyacheslav F.
Institute for Theoretical and Exp. Physics
B. Cheremushkinskaya 25
117259 Moscow
Tel: +7 095 123 6383
Fax: +7 095 127 0543
Eml: vfb@itep.ru

TITARENKO, Yuri
Institute for Theoretical and Exp. Physics
B. Cheremushkinskaya 25
117259 Moscow
Tel: +7 095 123 6383
Fax: +7 095 127 0543
Eml: Yury.Titarenko@itep.ru

ZHIVUN, Valery M.
Institute for Theoretical and Exp. Physics
B. Cheremunshkinskaya 25
117259 Moscow
Tel: +7 095 123 6383
Fax: +7 095 127 0543
Eml: zhivun@mail.ru

SPAIN

TAIN ENRIQUEZ, Jose Luis
Instituto de Fisica Corpuscular
Universitat de València – CSIC
Edificio de Institutos de Paterna
Apartado de Correos 22085
E-46980 Paterna (València)
Tel: +34 96 398 3497
Fax: +34 96 398 3488
Eml: Jose.Luis.Tain@ific.uv.es

UNITED STATES OF AMERICA

FERGUSON, Phillip D.
Oak Ridge National Laboratory
Target Systems
Spallation Neutron Source, SNS
701 Scarboro Road
Oak Ridge, TN 37830-6474
Tel: +1 865 241 5702
Fax: +1 865 574 6080
Eml: fergusonpd@ornl.gov

GALLMEIER, Franz X.
Building 6011, MS 6474
Oak Ridge National Laboratory
PO Box 2008
Oak Ridge, TN 37830
Tel: +1 865 574 9675
Fax: +1 865 574 6080
Eml: gallmeierfz@ornl.gov

HEILBRONN, Lawrence H.
Lawrence Berkeley National Laboratory
MS 74-197
Berkeley, CA 94720
Tel: +1 510 486 4002
Fax: +1 510 486 6949
Eml: lhheilbronn@lbl.gov

HERTEL, Nolan E.
George Woodruff School of Mechanical Eng.
Georgia Institute of Technology
900 Atlantic Drive
Atlanta, GA 30332-0405
Tel: +1 404 894 3601
Fax: +1 404 894 9325
Eml: nolan.hertel@me.gatech.edu

HUGHES, Grady
Los Alamos National Laboratory
Group X-5, MS F663
Los Alamos, NM 87545
Tel: +1 505 667 5957
Fax: +1 505 665 3046
Eml: hgh@lanl.gov

KIRK, Bernadette L.
RSICC/ORNL
PO Box 2008
Bldg. 5700, MS 6171
Oak Ridge, TN 37831-6171
Tel: +1 865 574 6176
Fax: +1 865 241 4046
Eml: kirkbl@ornl.gov

LIU, James C.
Radiation Physicist
Stanford Linear Accelerator Center
SLAC, MS 48
PO Box 20450
Stanford, CA 94309
Tel: +1 650 926 4728
Fax: +1 650 926 3569
Eml: james@slac.stanford.edu

MASHNIK, Stepan G.
Diagnostics Applications Group, X-5
MS B283
Los Alamos National Laboratory
Los Alamos, NM 87545
Tel: +1 505 667 9946
Fax: +1 505 667 1931
Eml: mashnik@lanl.gov

MOKHOV, Nikolai V.
FERMILAB
MS 220
PO Box 500
Batavia, IL 60510-500
Tel: +1 630 840 4409
Fax: +1 630 840 6039
Eml: mokhov@fnal.gov

ROKNI, Sayed H.
Radiation Physicist
Stanford Linear Accelerator Center
PO Box 4349
Stanford, CA 94309
Tel: +1 650 926 3544
Fax: +1 650 926 3169
Eml: rokni@slac.stanford.edu

INTERNATIONAL ORGANISATIONS

BRUGGER, Markus
CERN TIS-RP
865-RC-0009
CH-1211 Genève 23
Switzerland
Tel: +41 22 767 6556
Fax: +41 22 767 5700
Eml: markus.brugger@cern.ch

SARTORI, Enrico
OECD/NEA Data Bank
Le Seine-Saint Germain
12 boulevard des Iles
F-92130 Issy-les-Moulineaux
France
Tel: +33 1 45 24 10 72/78
Fax: +33 1 45 24 11 10/28
Eml: sartori@nea.fr

OECD PUBLICATIONS, 2, rue André-Pascal, 75775 PARIS CEDEX 16
PRINTED IN FRANCE
(66 2005 08 1 P) No. 54073 2005